EFFECT OF GROUND ON FLOW STRUCTURE OF NON-SLENDER DELTA AND REVERSE DELTA WINGS

A THESIS SUBMITTED TO
THE GRADUATE SCHOOL OF NATURAL AND APPLIED SCIENCES
OF
MIDDLE EAST TECHNICAL UNIVERSITY

BY

GÖKTUĞ KOÇAK

IN PARTIAL FULFILLMENT OF THE REQUIREMENTS
FOR
THE DEGREE OF DOCTOR OF PHILOSOPHY
IN
MECHANICAL ENGINEERING

JANUARY 2023

Approval of the thesis:

EFFECT OF GROUND ON FLOW STRUCTURE OF NON-SLENDER DELTA AND REVERSE DELTA WINGS

submitted by **GÖKTUĞ KOÇAK** in partial fulfillment of the requirements for the degree of **Doctor of Philosophy** in **Mechanical Engineering, Middle East Technical University** by,

Prof. Dr. Halil Kalıpçılar
Dean, Graduate School of **Natural and Applied Sciences** _____

Prof. Dr. Mehmet Ali Sahir Arıkan
Head of the Department, **Mechanical Engineering Dept.** _____

Prof. Dr. Mehmet Metin Yavuz
Supervisor, **Mechanical Engineering Dept., METU** _____

Examining Committee Members:

Asst. Prof. Dr. Özgür Uğraş Baran
Mechanical Eng., METU _____

Prof. Dr. Mehmet Metin Yavuz
Mechanical Eng., METU _____

Asst. Prof. Dr. Onur Baş
Mechanical Eng., TED University _____

Asst. Prof. Dr. Hediye Atik
Aerospace Eng., Atılım Uni. _____

Asst. Prof. Dr. Mustafa Perçin
Aerospace Eng., METU _____

Date: 26.01.2023

I hereby declare that all information in this document has been obtained and presented in accordance with academic rules and ethical conduct. I also declare that, as required by these rules and conduct, I have fully cited and referenced all material and results that are not original to this work.

Name Last name : Göktuğ Koçak

Signature :

ABSTRACT

EFFECT OF GROUND ON FLOW STRUCTURE OF NON-SLENDER DELTA AND REVERSE DELTA WINGS

Koçak, Göktuğ
Doctor of Philosophy, Mechanical Engineering
Supervisor: Prof. Dr. Mehmet Metin Yavuz

January 2023, 282 pages

Flight condition of aircrafts proximity to the ground, so-called "Ground Effect" (GE), is among one of the most recent research areas since the aerodynamic performance and stability of wing in ground effect (WIG) crafts significantly vary due to the flow dynamics associated with the interaction between the wing and the surface.

In the present study, ground effect of non-slender delta wings (DW) and reversed delta wings (RDW) at static ground effect (SGE) condition in the absence of heave and pitch motion was investigated experimentally. The SGE condition was simulated with both static ground and dynamic ground conditions using an elevated ground system as well as a moving belt mechanism. The intensity of the GE and the stability characteristics of the wings were examined using force and moment, and surface pressure measurements to characterize the flow field both quantitatively and qualitatively.

The results of the present study indicate that the effect of ground has substantial impact on both aerodynamic performance and stability of the delta and reverse delta wings. As the height of the wing decreases, both drag and lift forces increase where these effects were observed to be more pronounced for higher angles of attack. The

presence of ground affects the longitudinal positions of the aerodynamic centers over the wing chord, hence results in interchanging stability characteristics varying with both height and angle of attack. The ground boundary condition tremendously affects the ground effect behavior such that dynamic ground condition results in larger areas under the lift-to-drag ratio versus angle of attack curve compared to OGE cases rather than increased peak values observed for the static ground condition whereas reduced slopes for the aerodynamic coefficients in line with different aerodynamic center positions on longitudinal axis are witnessed for both Belt On and Belt Off cases compared to the static ground condition, which might be considered as the footprints of dynamic pressure loss and flow angularity changes due to the ground boundary condition.

Keywords: Ground Effect, Delta Wing, Reversed Delta Wing, Unsteady Aerodynamics, Experimental Aerodynamics

ÖZ

YER ETKİSİNİN İNCE OLMAYAN DELTA KANAT VE TERS DELTA KANAT ÜZERİNDEKI AKIŞA ETKİSİ

Koçak, Göktuğ
Doktora, Makina Mühendisliği
Tez Yöneticisi: Prof. Dr. Mehmet Metin Yavuz

Ocak 2023, 282 sayfa

Hava araçlarının yere yakın uçuş koşullarında görülen "Yer Etkisi (YE)", kanat ve yer düzlemi arasında görülen etkileşimler üzerinden akış dinamiklerini ciddi şekilde etkilemesiyle ve de bu etkilerle birlikte yer etkisi araçlarının (YEA) aerodinamik performans ve kararlılık durumlarında ciddi değişimlere sebep olması itibariyle en güncel araştırma alanlarından biri olmuştur.

Bu çalışmada hem delta kanatlar (DK) hem de ters delta kanatlar (TDK) için yer etkisi dikey ve yunuslama hareketleri olmaksızın oluşan statik yer etkisi (SYE) koşulunda deneysel olarak incelenmiştir. SYE hem statik hem de dinamik yer koşullarında yükseltilmiş yer sistemi ve de kayar bant mekanizması ile canlandırılmıştır. Akış alanının nitel ve nicel yönden incelenmesi yer etkisi şiddeti ve kanatların kararlılık karakterlerini incelemek adına kuvvet, moment ve de yüzey basınç ölçümleri üzerinden yapılmıştır.

Bu çalışmanın sonuçları yerin delta ve ters delta kanatların hem aerodinamik performansları hem de kararlılıkları üzerinde ciddi etkileri olduğunu göstermektedir. Kanadın yerden yüksekliği azaldıkça hem sürükleme hem de taşıma kuvvetlerinde artış olduğu ve bu etkilerin yüksek hücum açılarında daha belirgin olduğu

görülmüştür. Yerin varlığı aerodinamik merkezlerin kanat veteri üzerindeki boylamsal konumlarını etkilemekte ve bu nedenle hem yüksekliğe hem de hücum açısına bağlı olarak değişken kararlılık karakterlerinin oluşmasına sebep olmaktadır. Yer sınır koşulunun hem delta hem de ters delta kanatların yer etkisindeki durumları üzerinde ciddi etkilerinin olduğu görülmüş, statik yer durumunda taşıma kuvvetinin sürükleme kuvvetine oranında görülen en yüksek değerlerin yer etkisinde yer etkisi dışındaki duruma göre artmasından farklı olarak dinamik yer durumunda taşıma kuvvetinin sürükleme kuvvetine oranının hücum açısına bağlı çizdirilmesi sonucu oluşan eğrinin altında kalan alanın yer etkisi durumunda yer etkisi dışındaki duruma göre arttığına, bununla beraber dinamik yer durumunda hem kayar bant çalışırken hem de kayar bant çalışmazken statik yer durumuna göre aerodinamik katsayıların eğimlerinde azalmanın görüldüğüne, aerodinamik merkezlerin farklı boylamsal konumlarda oluştuğuna tanıklık edilmiş ve bu etkilerin yer sınır koşulunun sebep olduğu dinamik basınç kaybı ve akış açısallığı değişimi nedenleriyle oluşabileceği değerlendirilmiştir.

Anahtar Kelimeler: Yer Etkisi, Delta Kanat, Ters Delta Kanat, Daimi Olmayan Aerodinamik, Deneysel Aerodinamik

To my family

ACKNOWLEDGMENTS

I would like to express my sincere gratitude to all people, who have devoted their time, effort, guidance and to the institutions for the support throughout my research.

I am indebted to my supervisor Prof. Dr. Mehmet Metin Yavuz for his support, and guidance throughout my undergraduate and graduate years and for giving me the opportunity to carry out my research projects as a fellow of Yavuz Research Group (YRG) where I gain precious experience and knowledge. I would like to acknowledge for his inexhaustible patience during the correction phases of our studies. I have long admired his wisdom and his trust to me in all steps of this work was the biggest encouragement and the boosting force.

I would like to express my gratitude to the committee members, Asst. Prof. Özgür Uğraş Baran, and Asst. Prof. Onur Baş for their insightful guidance, objective criticism, and continous suggestions throughout this study.

I am grateful for the funding sources that Middle East Technical University (METU) and Turkish Aerospace Industries, Inc (TA) provided to my study. This work was partially funded by Scientific Research Projects (BAP) Coordination of METU, under grant number TEZ-D-302-2021-10725 and BAP fund of TA.

My sincere thanks also go to Karaca Makina, particularly to Mr. İsmail Karaca for their help and support during the construction and integration of the moving belt mechanism to the wind tunnel of Fluids Mechanics Laboratory of Mechanical Engineering Department at METU.

I would like to thank TA BAP committee members Ayşe Şolpan Temiz, Onur Jane and Merve Ayas Özdemir and my managers from TA Aydın Birol Akdemir, and Derya Gürak for their help, support, trust and confidence in me.

I appreciate the assistance of the machine shop. I am very thankful to Mr. Mehmet Özçiftçi for his technical assistance and craftsmanship.

I would like to thank my colleague Ilgaz Doğa Okçu who helped me with 3d printing and additive manufacturing of the brackets.

Many thanks also go to my colleague Mahmut Bilgin for the technical support I have routinely received from him regarding to electronics and for his valuable opinions and suggestions.

I am forever thankful to my colleague, my teammate, and my friend Cenk Çetin for his knowledge, comments and suggestions. His moral support, contributions and support in all parts of this study are greatly appreciated.

I would like to thank my lab colleague Oğuzhan Yılmaz for his inexhaustible support and help with the experiments. We worked in harmony and shared the unforgettable moments in Fluid Mechanics Lab. I truly enjoyed each and every experiment we conducted together. He learned from me and I learned from him. I cannot image how I could complete this study without his help.

To my dearest friends, Onur Özbilgin, and Mertcan Büyüksan (a.k.a Ground Effect Ground Team), I thank you both dearly for your help and support. I feel myself extremely lucky to have you around me whenever I needed you. I was only needed for ordering the meal whenever we work together thanks to their amazing skills regarding to the mechanical design and manufacturing.

Finally, I save the greatest and deepest thank to my family, particularly my parents Meltem and İlker Koçak for their endless love, support and trust. Special thanks are due to my uncle Levent Koçak and my grandmother Meryem Urgancı who always strengthened my morale by standing by me in all situations. I would also like to thank my uncle Mehmet Mete for his inspirational ground effect vehicle models and drawings, which constantly fed my imagination and creativity. Without you, I would not be where I am right now.

Thank you so much everyone who listened to my never-ending ground effect dreams and stories!

TABLE OF CONTENTS

LIST OF TABLES

TABLES

LIST OF FIGURES

FIGURES

LIST OF ABBREVIATIONS

ABBREVIATIONS

DW: Delta Wing

GE: Ground Effect

H.S.: Height Stability

IGE: In Ground Effect

LE: Leading-Edge

METU: Middle East Technical University

OGE: Out of Ground Effect

RDW: Reverse Delta Wing

TA: Turkish Aerospace Industries, Inc.

TE: Trailing-Edge

WIG: Wing In Ground Effect

LIST OF SYMBOLS

SYMBOLS

A = surface area of the delta wing 1b

c = chord length

C_D = drag coefficient, $C_D = \frac{F_D}{\frac{1}{2}\rho U_\infty^2 A}$

CG = center of gravity

C_L = lift coefficient, $C_L = \frac{F_L}{\frac{1}{2}\rho U_\infty^2 A}$

C_L/C_D = lift-to-drag ratio

C_M = pitch moment coefficient, $C_M = \frac{M_y}{\frac{1}{2}\rho U_\infty^2 A\, L}$

C_p = pressure coefficient, $C_P = \frac{\overline{p}-p_\infty}{\frac{1}{2}\rho U_\infty^2} = \frac{\overline{p}-p_\infty}{p_{dyn}}$

F_L = lift force

F_D = drag force

h = height of the trailing-edge from the ground

H.S. = height stability of the wing in ground effect, $X_a - X_h$

L = chord length of the delta wing 1b

M_y = pitch moment

$\overline{p}$ = average surface pressure

p_{dyn} = free-stream dynamic pressure

p_∞ = free-stream static pressure

Re = Reynolds number based on chord length of the delta wing 1b, $\frac{U_\infty L}{\nu}$

s = distance equal to quarter of the wing span

S = distance equal to the wing span

t = thickness of the wing

t/c = thickness-to-chord ratio

U_∞ = free stream velocity

x = chordwise distance from the wing apex

X_a = non-dimensional location of the aerodynamic center in pitch, $\left(\frac{\partial C_M}{\partial C_L}\right)\Big|_\alpha$

X_h = non-dimensional location of the aerodynamic center in height, $\left(\frac{\partial C_M}{\partial C_L}\right)\Big|_h$

X_p = nondimensional location of the pressure center, $X|_{C_M=0}$

y = spanwise distance from wing symmetry line

α = angle of attack

α_s = static stall angle of attack

Λ = sweep angle

ρ = density of fluid

CHAPTER 1

INTRODUCTION

Aviation industry has experienced significant improvements within the last century, and it has become the driving force behind the technological innovation. The nature of the industry necessities a constant need for performance improvements as well as achieving the economic and environmental aims. The demand for better aerial vehicles further increases the complexity of the new designs. Therefore, there is an increasing need for sophisticated flight control requirements for better landing and takeoff characteristics. During the landing and takeoff phases of the operations, the aerodynamic phenomena so called "Ground Effect (GE)" is encountered by the aircrafts. Actually, any lifting surface feels the enhanced aerodynamic performance close proximity to the ground compared to the freestream condition. It eventually results in a desirable increase in lift-to-drag ratio for the aerodynamic performance of the lifting surface. This effect is also seen in the nature. For example, immigrant birds fly near the water surface in order to save energy during their journey over the ocean.

The changes in the three-dimensional flow field due to presence of the ground plane have maximum influence on the overall performance of the wing with increasing effect as the height from the ground decreases. The phenomenon becomes appreciable when the distance to the ground becomes one wing span [1], [2]. The tremendous increase in lift-to-drag ratio, which is seen proximity to the ground, eventually led the designers to build dedicated vehicles operating in ground effect (IGE), which are called "wing in ground" (WIG) crafts. They fly IGE not only at the landing and takeoff phases but also operate steadily IGE with increased efficiency compared to conventional aircrafts. As it can be seen from the earlier examples of

the Russian Ekranoplans given in Figure 1-1, they are different from the conventional airplanes, which have similar size and weight due to their distinct small aspect ratio wings, floats, as well as special take-off aids [3].

The increased aerodynamic efficiency (lift-to-drag ratio) can be as high as 20 or more compared to 3 for helicopters, 8 for hydro-airplanes and 12 for light aircraft [2]. In addition, WIG crafts present high safety travel ability since water or soil serve as continuous airports beneath the aircraft. Therefore, unique features of these crafts by means of fast, efficient and safe travel ability make WIG crafts very special vehicles since they have higher lift-to-drag ratio, lower propulsive power, wider flight range and larger payload capability with respect to an airplane of comparable size [4].

Researchers have spent great effort to fully understand the complex nature of the WIG craft aerodynamics using experimental and numerical approaches. Among the flight conditions of WIG crafts, static ground effect (SGE) condition, which is the steady cruise flight for WIG crafts in the absence of heave and pitch motions, generates quite complex flow fields dominated by the wing whereas during landing and takeoff, all aircrafts experience dynamic ground effect (DGE), where heave and pitch motions exist in vertical axis of the aircraft. General trend in practical applications states that WIG crafts are mostly designed for maritime operations on lakes, rivers, and oceans to prevent collision with structures on earth surface. The waves on water surface alters the physics of the GE and results deviate with respect to flat ground condition since the GE augmentation is strongly coupled to the height above the water.

The WIG crafts greatly suffer from hydrodynamic drag during take-off and landing resulting in excessive loads on the hull of the vehicle. In addition, they have poor longitudinal stability characteristics and often large horizontal tail, which comes with significant weight penalty, is needed for controllability purposes. Therefore, the WIG craft designers have aimed to develop optimal designs with high aerodynamic efficiency as well as superior stability characteristics.

There are three main categories of WIG crafts namely tandem wing, ram wing and reversed delta wing (RDW). Tandem wing planform can be configurable such that the design pitch angle and the geometry of the wing elements can be adjusted to resolve the problem of stability. It only operates IGE and static stability margin is reported to be sensitive to the combination of pitch angle and ground clearance [3]. Ram wing configuration provides the maximum advantage of the GE with the penalty of poor stability characteristics. However, researchers have particular interest on reverse delta wing planform in recent years since it provides inherent longitudinal stability as well as providing high lift-to-drag ratio [3]. Its unique design with built-in anhedral minimizes the hydrodynamic drag by elevating the hull with respect to the water and provides great air cushioning capability, but still remain as a compact design. Earlier design was introduced by a German aerodynamicist Alexandar Lippisch with X-112 in 1963 and later followed by X-112, X-113, X-114. Therefore, the RDW configuration is also known as Lippisch configuration or Lippisch Reversed Delta Wing. The derivatives of Lippisch configuration were later extended by Hanno Fischer, who created the famous Airfish family. Unlike the Lippisch configuration, the Airfish was designed to fly only IGE. However, it can perform temporary dynamic jumps "hop" in case of an emergency. Other RDW designs include Eska in the USSR and the XTW craft family in the People's Republic of China [3].

The non-slender delta wings, which have been employed in unmanned air vehicles (UAVs), micro air vehicles (MAVs), and unmanned combat air vehicles (UCAVs), have drawn significant attention in recent years. In Figure 1-2, some of the examples of these vehicles are provided. Although, the earlier studies focus on aerodynamic characteristics of slender delta wings [5], which have well established literature, the non-slender delta wings, with sweep angle less than 55 deg, have high potential in terms of high maneuverability and low structural-weight-to-takeoff-weight ratio [6] and offer larger surface areas suitable for flight systems equipment layout at expense of deteriorated maximum lift and stall angle [7]. The vortical flow field of the delta wings, which is mainly emanated from the leading-edges, two counter rotating

vortices greatly affect the overall performance and stability characteristics of these wings [8]. The instabilities such as vortex breakdown, shear layer instabilities, vortex wandering, and helical mode instability associated with the different flight conditions arise from the unstable vortical flow structure [9]. At sufficiently high angles of attack, vortical structure of the delta wing is lost because of the large-scale and three-dimensional surface separation [10]. The vortex breakdown phenomena, which occurs due to the sudden expansion of the leading-edge vortices (LEVs), also plays a crucial role on the performance and manueverability of the delta wings [5]. The vortex breakdown, which is represented in Figure 1-3, arises from the adverse pressure gradient, which results in the stagnation of the axial core flow with the increasing angle of attack. This stagnation causes rapid expansion of the vortex core, which introduces high velocity fluctuations and buffeting [11]. Considering the flow physics associated with the leading-edge vortex flow, comprehensive characterization of the flow physics over those planforms is necessary to address problems related to the flow instabilities and flight control since the distinct and complex flow structures around non-slender delta wings have pronounced effects on both flight performance and stability. Previous studies mainly focused on parameters such as Reynolds number, angle of attack, sweep angle, leading-edge bevel and thickness-to-chord ratio for non-slender delta wings. The flow structure of non-slender delta wings in terms of flight performance and longitudinal static stability characteristics as well as configurational parameters such as thickness-to-chord ratio and bevel leading-edge bevel have not drawn enough attention. The interaction between the flow around delta wings and the presence of the ground necessitates broader investigations, which will result in improved take-off and landing characteristics as well as potential usage of these planforms as WIG vehicles, which can be seen in Figure 1-4.

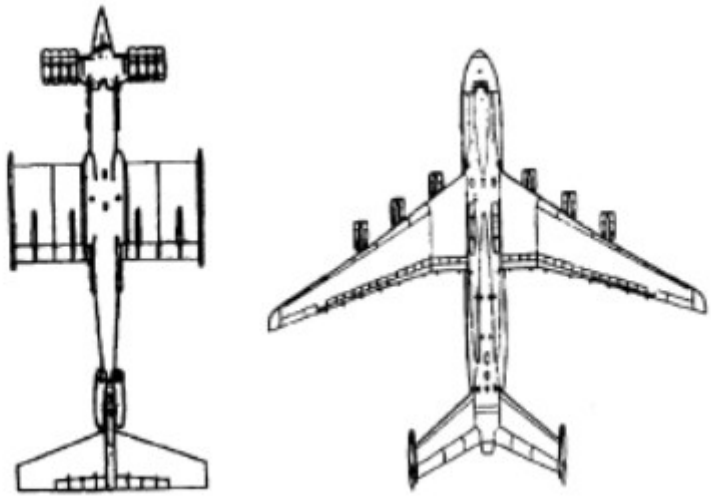

Figure 1-1 WIG vehicle Korabl Maket (KM) versus airplane Antonov Mriya (An-225) [3]

Figure 1-2 Unmanned combat air vehicles and fixed-wing micro air vehicles [6]

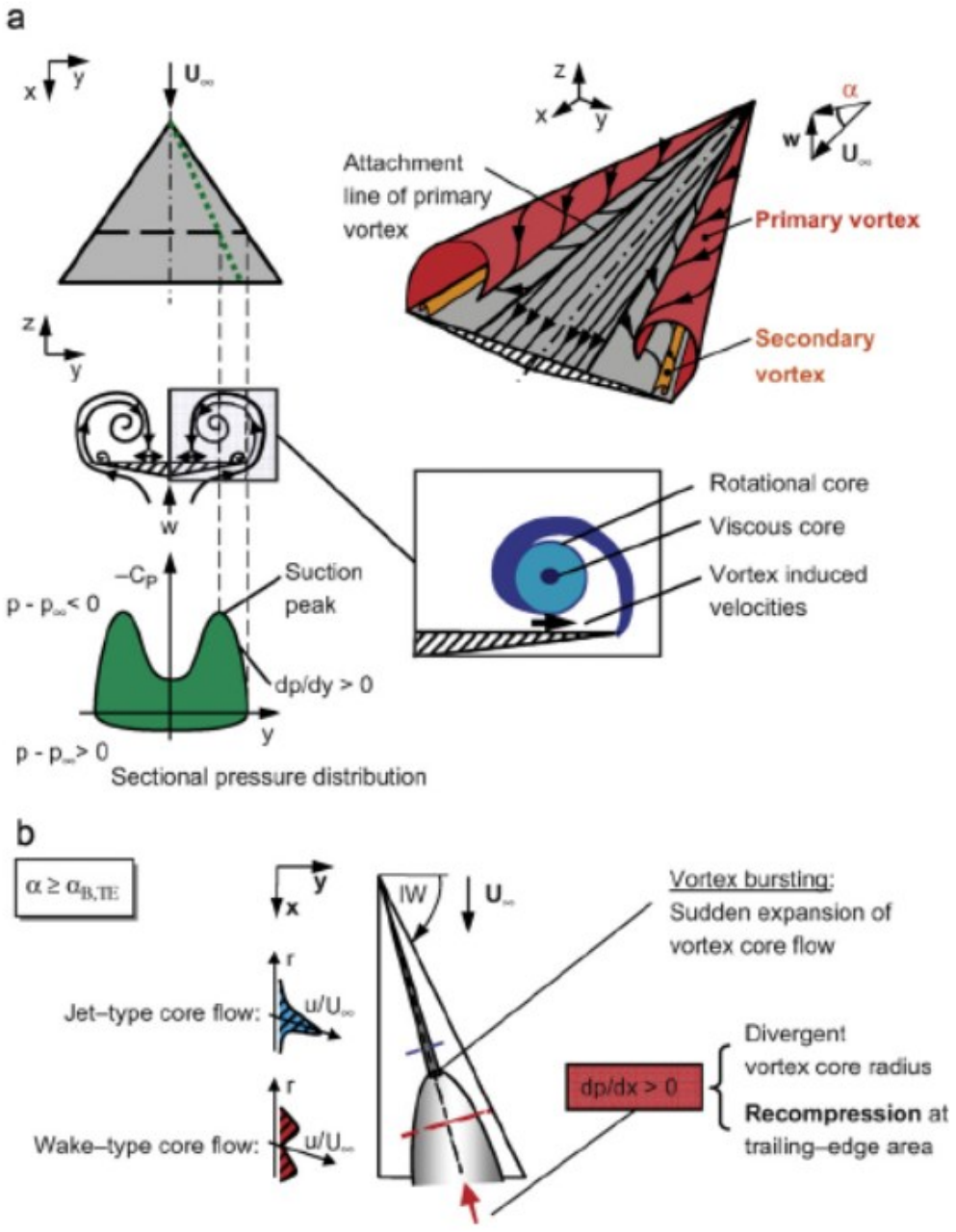

Figure 1-3 Delta wing vortex formation: main delta wing flow features (a) and vortex bursting characteristics (b) [11]

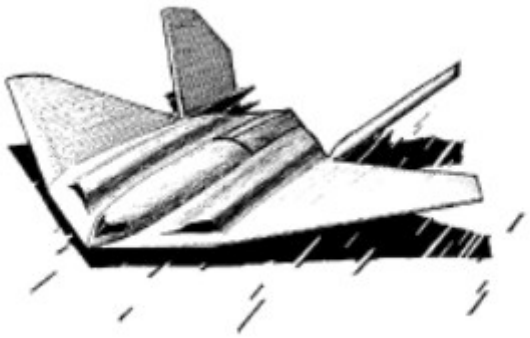

Figure 1-4 Lockheed Martin surface-effect-aircraft concept [3]

1.1 Motivation of the Study

The wing in ground effect (WIG) crafts experience quite complex and three-dimensional flow regimes during steady and unsteady flight. Therefore, understanding the global flow field and the prediction of the aerodynamic loads have become crucial in order to assess the overall figure of merit of the system as well as stability and controllability characteristics of the vehicle. Among several alternatives, the reversed delta wing (RDW) configuration has proved its potential along with its superior aerodynamic efficiency (lift-to-drag ratio) and inherent longitudinal stability characteristics compared to the other planforms such as tandem and ram type WIG crafts. Yet, there are still unclear points that further investigation is essential to understand the physics of ground effect for RDWs. Optimization of the wing in terms of aerodynamics and stability, as well as minimizing the hump drag, which is seen during takeoff and landing, are two of the major research topics for the ground effect (GE) community some of which can also be listed as dynamic ground effect (DGE), air cushion and ramp pressure mechanisms, wing vortex interaction, and tip vortices.

Very few studies have addressed the presence of the ground and its influence on the flow characteristics of delta wings. In addition, most of the existent experimental studies on non-slender delta wings do not include the longitudinal static stability

characteristics due to a lack of pitch moment data. Therefore, the current understanding of the GE on non-slender delta wings requires further investigations and comparisons to reveal landing and take-off capabilities as well as their potential to be used as WIG vehicles.

Easiness of implementing the correct boundary condition in a code is among the advantages of numerical studies. However, they greatly suffer from the numerical instabilities arising from the high turbulence levels seen in the flow field near ground. Experimental techniques are often adopted to reveal complex flow field dynamics and eliminate the uncertainties near ground but they propose rather expensive solutions since it can be challenging to construct a moving ground setup in laboratory scale. Yet, experimental studies in literature, which investigate the effect of moving ground on the complex flow fields are quite limited.

Although, several numerical and experimental studies were performed to understand the flow features associated with the delta and reverse delta wings in ground effect (IGE), further investigations and quantifications are required to characterize the effect of thickness-to-chord ratio for both of these planforms and the effect of novel design changes such as wing anhedral and cropping for the reverse delta wings on both OGE and IGE for optimized performance and stability characteristics with realistic ground effect simulations.

1.2 Aim of the Study

The aim of the present study is to characterize the ground effect flow structure of delta and reverse delta wings at static ground condition with elevated ground system and dynamic ground condition with moving belt system considering both OGE and static ground effect condition in the absence of heave and pitch motions, experimentally. The effects of thickness-to-chord (t/c) ratio, anhedral angle (δ), and cropping ratio from trailing-edge ($Cr\%$) on the aerodynamics of non-slender reverse delta wings in comparison to non-slender delta wings with sweep angle of 45 degree

were characterized in a low-speed wind tunnel using force and pressure measurements at Reynolds number of $9x10^4$. The measurements were conducted for total of 8 different delta and reverse delta wings. Two different t/c ratios of 5.9% and 1.1%, and two different anhedral angles of $\delta = 15$ and 30 degrees for non-cropped and cropped at $Cr = 30\%$ conditions were tested. The measurements were conducted for angles of attack varying between $0 \leq \alpha \leq 35$ degrees and non-dimensional heights between $3\% \leq h/c \leq 113\%$ and height stability of the wings based on aerodynamic center in pitch (X_a) and aerodynamic center in height (X_h) was constructed along with center of pressure (X_P). Ground effect simulations were conducted at three different fidelity levels, which were static and dynamic ground conditions as well as moving Belt Off condition. For that purpose, two measurement systems, which represent the static and dynamic ground conditions were constructed and integrated to the wind tunnel. The static ground condition was simulated using an elevated static ground board system, whereas the dynamic ground condition was simulated using a moving belt mechanism. For both systems, a novel model positioning system (MPS), which was used for angle of attack and height adjustments, was developed and constructed.

1.3 Structure of the Thesis

This thesis consists of six main chapters. Chapter 1 provides introductory information for the ground effect, flow over the delta and reverse delta wings as well as motivation and aim of the study.

Chapter 2 presents the details about the flow physics associated with the delta and reverse delta wings and their interaction with the ground effect along with the related studies in the literature. Chapter 3 provides technical details of the experimental system, measurement techniques, methodology as well as the uncertainty estimation and experimental matrix.

Chapter 4 summarizes the results for both OGE and IGE conditions for the static ground condition with force and pressure measurements for the delta and reverse delta wings along with global characterization with the effect of wing thickness on delta and reverse delta wings as well as the effect of wing anhedral and cropping for the reverse delta wing at OGE condition. Chapter 5 presents the results for the dynamic ground condition for the selected delta and reverse delta wings, the comparison of the different ground boundary conditions on both OGE and IGE flow fields by examining the results for static and dynamic ground conditions as well as belt status on ground effect experiments. The results provided in both Chapter 4 and Chapter 5 are discussed in terms of both aerodynamic performance as well as longitudinal axis dynamics, which is detailed with the examination of aerodynamic centers such as aerodynamic center in pitch, aerodynamic center in height and center of pressure and their contribution to the longitudinal static stability characteristics.

Chapter 6 presents the principal findings and conclusions of the present study.

CHAPTER 2

LITERATURE SURVEY

In this chapter, flow physics related with the delta and reverse delta wings along with the aerodynamic phenomenon “the Ground Effect (GE)” are provided. In the first part, the details related to the flow structures around delta wing including flow past delta wings, separated shear layer and instabilities, vortex breakdown, flow reattachment, stall and effect of thickness-to-chord ratio were given. In the second part, vortex flow structure and aerodynamics of reverse delta wings are explained together with the effect of geometrical modifications and their effects on aerodynamic performance of reverse delta wings. In the last part, many aspects related to the GE are discussed including aerodynamic efficiency, testing, operationality, controllability and stability. Several other wing planforms rather than DWs are also compared for wing in ground effect (WIG) concept. The studies, which focus on increasing overall efficiency in ground effect (IGE), are provided in this document in order to give an insight for the comprehensive aircraft design for operations close proximity to ground.

2.1 Flow Structure around a Delta Wing

2.1.1 Flow Past Delta Wings

The studies related to delta wings aerodynamics show that there are major differences between flow characteristics of the slender and non-slender delta wings. Although the earlier studies focus on aerodynamic characteristics of slender delta wings [5], researchers turned their attention to the non-slender planforms

acknowledging that these planforms have larger surface areas suitable for flight systems equipment layout at expense of deteriorated maximum lift and stall angle [7].

The flow over a delta wing is characterized by two counter-rotating vortices shed from the leading-edges [8], [12], [13], [14], [15], [16]. The strong leading-edge vortices (LEV) energize the flow, which in turn delay the stall angle of the wing. However, these vortices undergo a sudden expansion known as vortex breakdown at a sufficiently high angle of attack [5], [17], [18], which results in lift deterioration and increased pitch-up moment [19]. High vortical flow at the leeward side of the wing with low pressure at the vortex core provides suction effect and enhances the lift at the expense of high drag [5], [20], [21]. Earlier delta wing studies, which focus on vortex flows and vortex breakdown, were conducted by Werlé [22], Earnshaw and Lawford [9], Bird [23], Polhamus [24] and Erickson [25].

The flow patterns of non-slender delta wings are substantially different compared to slender ones and indicate strong reattachment of the vortex pattern [26], [27], [28]. The position of the vortex structure at low angle of attack values is closer to the wing surface for non-slender delta wings [29] causing reattachment and interaction between the vortex and the boundary layer [30], which might lead to the appearance of the second primary vortex formation [31]. This flow structure, which contains two vortices rotating in the same direction is called as “dual vortex structure” and is seen for non-slender delta wings in the main core at low angles of attack. The sketch of dual vortex structure is given in Figure 2-1. Gordnier and Visbal [31] first observed this dual vortex structure, computationally. Taylor et al. [32] and Yanıktepe and Rockwell [14] confirmed the existence of this structure with PIV measurements. The relation between the sweep angle and dual vortex structure was examined by Jin-Jun and Wang [33] and it was observed that the range of the angle of attack decreases with increasing sweep angle. The Reynolds number dependence of the flow structure, which is relatively less critical for slender delta wings [6], is significant when the secondary primary vortex appears on the non-slender planform [34].

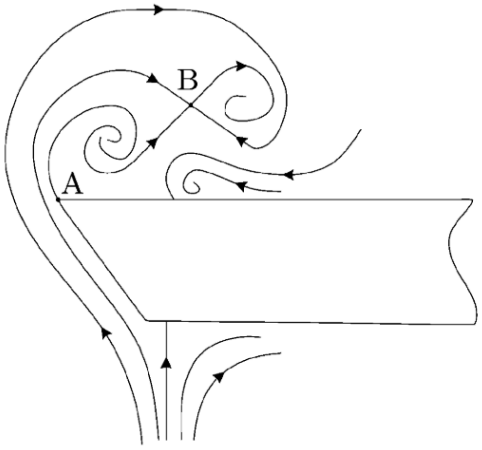

Figure 2-1 Sketch of dual vortex formation [33]

2.1.2 Separated Shear Layers and Instabilities

The interaction of the flow with a body result in adverse pressure gradient and separation of the flow occurs according to viscous flow theory. Boundary layer theory becomes invalid after the separation, which always takes place on the sharp-edge delta wings. Earnshaw [35] revealed that rotational core, viscous subcore and free shear layer are three different regions of the vortex emanating from the separation. These three regions are depicted in Figure 2-2. The classification of the vortex flow was conducted by Yanıktepe and Rockwell [14] as large-scale and small-scale patterns where the instabilities are related with the latter one. The small-scale Kelvin-Helmholtz instabilities are associated with the separation of the shear layer from the leading-edge. The small-scale vorticity concentrations were shown by Yavuz et al. [36] with PIV measurements. Özgören et al. [37] investigated the unsteady flow characteristics of a slender delta wing having sweep angle of $\Lambda = 75^{o}$, which are consistent with the instabilities observed by the Riley and Lowson [38]. Gordnier and Visbal [31] pointed out that sudden expansion of the secondary flow results in shear layer instability, which arises from the so called vortex wandering

phenomena occurring due to the interaction of surface boundary layers with primary vortex.

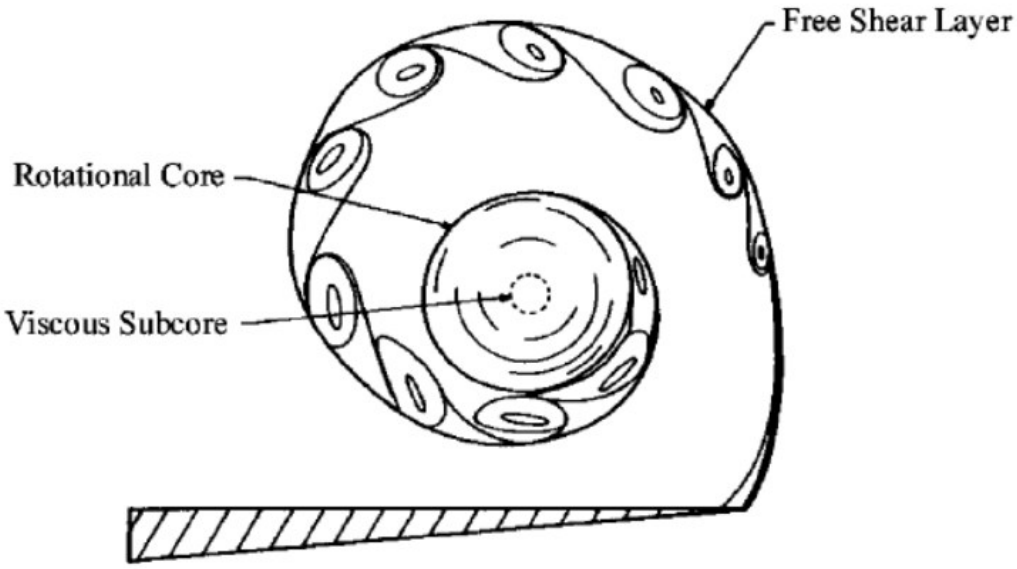

Figure 2-2 Regions of shear layer [39]

2.1.3 Vortex Breakdown

The sudden expansion of vortical structure due to the rapid deceleration of the axial velocity at the vortex core results in vortex breakdown phenomenon as a result of increasing angle of attack [40]. This phenomenon was first photographed for a slender delta wing water tunnel tests at Onera by Henri Werlé in 1954 [22]. The decrease in velocity is accompanied by pressure increase at the suction side, which eventually results in significant loss of momentum and lift. The spiral, bubble and double helix types, which are given in Figure 2-3, are seen over the delta wings, although seven different vortex breakdown types exist [41]. The spiral type vortex breakdown is generally seen over the slender delta wing planforms [24], while non-slender delta wings exhibit more conical shape of the breakdown, where swirling and reversed axial flow in the vortical core are absent [14], [35], [42]. The formation

and location of the vortex breakdown depends on two main factors; the pressure gradient and the swirl level [40]. Payne [43] showed that as the sweep angle increases, the location of the vortex breakdown shifts towards to the trailing-edge for slender delta wings. Lowson [44] reported that the vortex breakdown location fluctuates along the streamwise direction of the order to 10% over a slender delta wing whereas these fluctuations in the breakdown location of the order of to 50% were observed by Ol et al. [29] and Taylor et al. [32] for non-slender delta wings. Yavuz [45] and Gursul [40] reported that the fluctuations of the vortex breakdown phenomena may result in high buffeting loads, which are also responsible of the structural vibrations and fatigue damage as well as deteriorated stability and controllability characteristics.

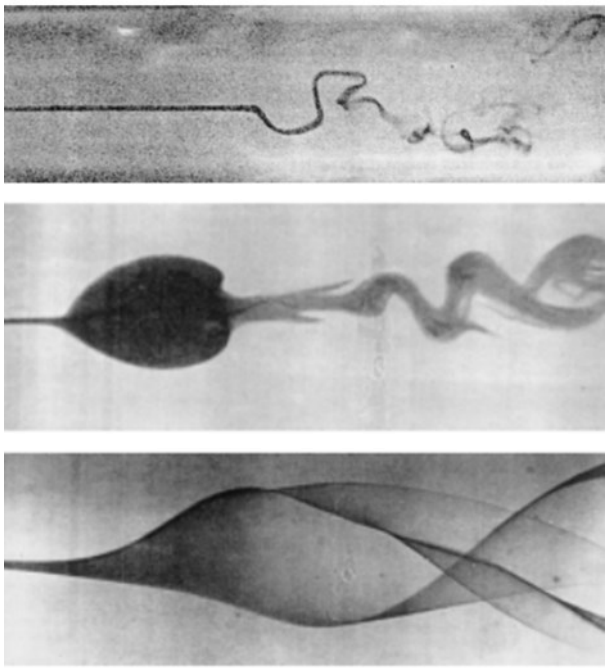

Figure 2-3 Spiral, bubble and double helix vortex breakdown types from top to bottom [41]

2.1.4 Shear Layer Reattachment & Three-Dimensional Flow Separation/Stall

Flow reattachment occurs on the delta wings due to the shear layer, which is separated from the leading-edges, attachment to the suction side of the wing and this phenomenon is observable for both slender and non-slender delta wings, although its occurrence is limited to the small incidences and its control is difficult for the former ones since flow does not attach after a certain angle of attack [26]. For the non-slender wings, the attachment of the separated flow occurs outboard of the wing symmetry plane compared to the slender ones, whereas the reattachment line approaches to the inboard of the symmetry plane as the angle of attack increases [6]. Honkan and Andreopoulos [46] experimentally studied delta wing having sweep angle of $\Lambda = 45^{o}$ and concluded that the shear layer reattachment zone and the area of secondary separation are associated with high levels of turbulence intensity. Taylor and Gursul [42] showed the movement of the reattachment line towards the centerline with increasing incidences and reattachment is observed at the symmetry plane at the stall condition. The high velocity fluctuations or turbulence intensity levels associated with the reattachment line at the wing symmetry plane are the primary source of buffeting, rather than vortex breakdown in the pre-stall regime [47].

At sufficiently high incidences, delta wing vortical structure loses its characteristics and the pre-stall regime of the non-slender delta wings is characterized by the large-scale and three-dimensional surface separation, which is governed by inward-swirling surface streamline pattern [10]. The streamlines take the whorl form due to the further increase in angle of attack in stall region, where shear layer reattachment to the planform surface can no longer be possible. The size of the stagnant region shown in Figure 2-4 on the wing surface increases [47] and low velocity fluctuations as well as buffet loads are observed [42].

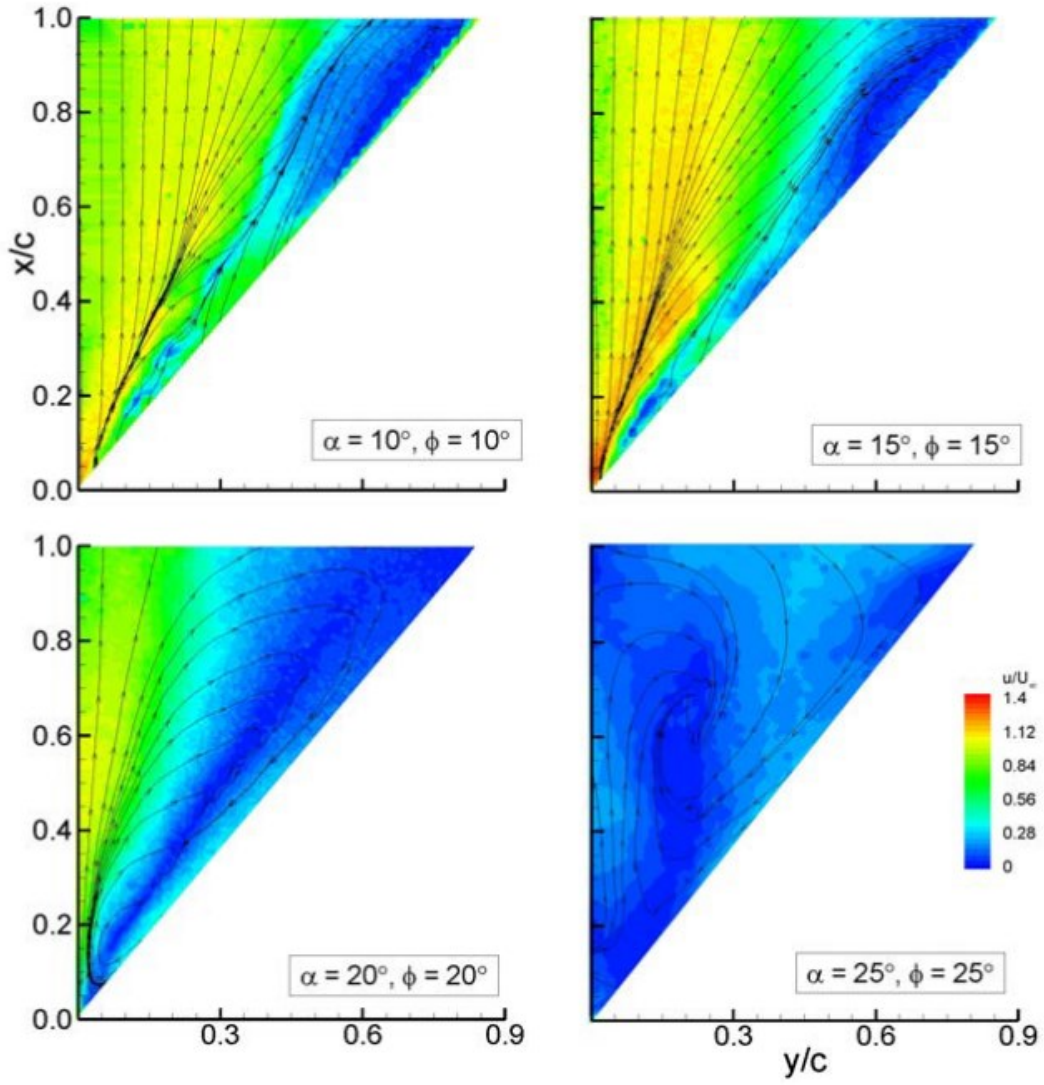

Figure 2-4 Time-averaged velocity magnitude contours and near wing surface streamline patterns [47]

2.1.5 Active and Passive Control Techniques and Geometrical Modifications for on Aerodynamic Performance of Delta Wings

To reduce the deteriorated aerodynamics and stability characteristics of non-slender delta and reverse delta wings, active and passive flow control techniques along with the geometrical modifications are utilized. Enhancing the shear layer or postponing

the vortex breakdown and eradication of disorganized three-dimensional flow characteristics on the leeward side of the wing are the primary focus for delta wings. Energizing the flow utilizing either steady or unsteady blowing or suction were utilized as active flow techniques by [48], [49], [50], [51], [52]. Passive control techniques and geometrical modifications including flexible wing structure [53], bioinspired edge modifications [54], leading-edge shape [9], [6], [55], trailing-edge attachment [56], [57], [58], thickness effect [59], [60], [61], and passive bleeding [62], [63] have been adopted and investigated thoroughly.

2.2 Flow Structure around Reverse Delta Wing

In recent years, forward-swept-wing particularly the reverse delta wing, which is an inverted form of the regular delta wing, has also been a major field of interest. These planforms, which are commonly utilized as ground effect vehicles or for ground proximity applications, offer aerodynamic benefits compared to regular delta wings in terms of generating increased lift force at low speeds, hence reducing required power and noise levels during take-off and landing [19]. In addition, the flow irregularities such as crossflow and attachment line instabilities as well as the primary modes of transition on swept wings were reported minimal on reverse delta wing configuration [64], [65]. Further, the favorable aerodynamic characteristics of the reverse delta wing for efficient supersonic flight were also endorsed [66]. A variable forward-sweep wing concept, which combines the beneficiary aspects of forward-swept wings and unswept wings, by positioning the wing between its unswept and full-forward positions, was also proposed [67]. It is stated that this versatile aircraft concept is capable of landing on short runways, having a large payload, and overcoming the increased drag at transonic and supersonic speeds while achieving desirable handling quality, control, and stability characteristics.

2.2.1 Vortex Flow Structure and Aerodynamics

The studies into the low-speed aerodynamics of delta wings go back to the pioneering work conducted by Alexander Lippisch [21], whereas early investigations into the aerodynamics of reverse delta wings conducted by NACA were dated back to 1947 [66]. Elsayed et al. [68], and Altaf et al. [69] characterized the flow of $\Lambda = 75^{o}$ delta and reverse delta wings using PIV and force measurements, in which they reported that the reverse delta wing had a higher lift-to-drag ratio resulting from the lower lift and lower drag values. The vortex flow structure and aerodynamics of a reverse delta wing having a sweep angle of $\Lambda = 65^{o}$ were investigated with PIV measurements, flow visualization, and force measurements [19]. The flow visualization results showed that leading-edge vortices seen in delta wings were replaced by a unique "arm-and-fist" leading-edge tip vortex pattern as well as the multiple spanwise vortex filaments, which caused the stall of reverse delta wings, whereas the stall of delta wings was related to the breakdown of leading-edge vortex. The PIV measurements showed that the RDW vortex was positioned above and outboard of the wing, which moved inboard the spanwise direction as it progressed downstream in contrast to the outboard movement of leading-edge-vortex of the delta wing suggesting that the upper surface acted like a wake generator and RDW vortices were not the primary source of the lift [19]. The force measurements showed that reverse delta wing had higher lift as well as the higher lift-to-drag ratio at low angle of attacks ($\alpha \leq 10^{o}$) compared to the delta wing [19]. The effect of sweep angle on the flow structure was examined by [70] and the comparison of the vortex flow and aerodynamic characteristics over slender ($\Lambda = 65^{o}$) and nonslender ($\Lambda = 50^{o}$) delta and reverse delta wings at low Reynolds number ($\mathrm{Re} = 11{,}000$) was made. It was found that reverse delta wings, when compared to delta wings, exhibited similar aerodynamic and vortex flow characteristics but lower maximum lift and delayed stall angle regardless of the slenderness.

2.2.2 The Effect of Geometrical Modifications on Aerodynamic Performance of Reverse Delta Wings

Considering the aerodynamic performance enhancements for reverse delta wings, adaptations of different geometrical features have been frequently utilized. Lee [71] adopted Gurney flap-like strips on both leading and trailing-edges with different strip heights on a reverse delta wing with sweep angle of 65 degree. The force measurement results showed that the addition of the trailing-edge strips resulted in a leftward shift of the lift curve with respect to angle of attack accompanied with significant increases in lift and lift-to-drag ratio while leading-edge strips postponed the stall with the penalty of decreased lift-to-drag ratio. Lee et al. [72] investigated the effect of anhedral on a reverse delta wing with sweep angle of 65 degree. The anhedral angle on aerodynamic characteristics showed a monotonic behavior such that as the anhedral angle increases, lowered lift and lift-to-drag ratio were obtained. Lee and He [73] reported that the contribution of the trailing-apex region of the reverse delta wing was negligible, hence cropping of the wing from the trailing-edge side might be effectively used for weight reduction without a major loss in the lift. Therefore, sole cropping of the reverse delta wing, as well as the combination of cropping, anhedral, Gurney flap-like strips, and winglets, were employed on a reverse delta wing with sweep angle of 65 degree and effects of those geometrical modifications on the vortex flow and aerodynamic characteristics were extensively investigated. The results indicated that the lift of the cropped wing could be significantly improved with the presence of Gurney flap-like trailing-edge strips [73].

2.3 Ground Effect

Ground effect is an aerodynamic phenomenon and it often results in a beneficial performance impact on aircrafts. It can be generalized such that anything flies feel an increase in lift and decrease in induced drag as it approaches to the ground (either soil or water). Not only aircrafts benefit from the GE but also large birds such as Albatross and Pelican, which is shown in Figure 2-5, save energy by utilizing the GE.

Figure 2-5 Brown pelican flying in ground effect [74]

All air vehicles experience the GE augmentation when operating very close to ground. Although, most of them are not designed for GE operations, the handling quality characteristics of any air vehicle should be adequate for operations near ground since they feel the GE either during take-off or landing.

It is known that as the aircraft gets bigger, aerodynamic efficiency induced by the GE also increases. Nebylov et al. [75] provides that as the aircraft gets bigger, the transport efficiency of the aircraft consequently gets higher. Cui and Zhang [2] summarizes that lift-to-drag ratio, which is the ultimate parameter to be improved, of various vehicles are reported such that it is 3 for helicopters, 8 for hydro-planes and 12 for light aircrafts. For WIG crafts, which are the high speed and low altitude aircrafts, it can even reach to 20 or more during flights which are close to ground less than or equal to one-fifth of the wing chord length.

Considering the categories of WIG crafts, there are three main types namely single ram wing, tandem wing (also known as Jörg) and the RDW (also known as Lippisch configuration). The types of WIG crafts are given in Figure 2-6. As reported by Urquhart et al. [76], the RDW is the only configuration that can also fly OGE.

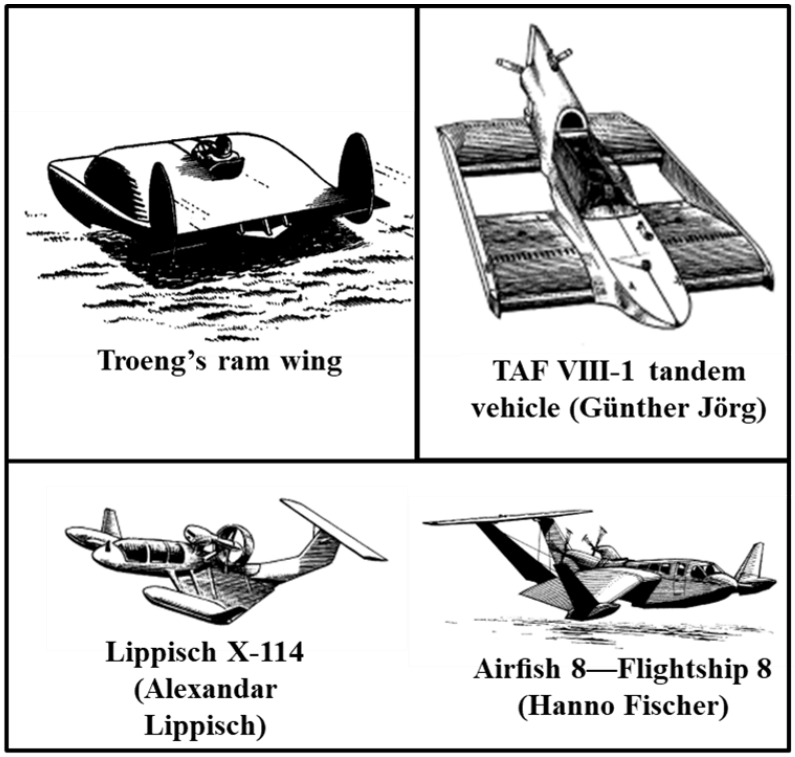

Figure 2-6 Different GE vehicles [3]

Although, the present study focuses on the reversed delta wings IGE, a brief history is also provided. However, the complete review of the WIG crafts is given by Rozhdestvensky [3]. The Russian Ekranoplans are the pioneers of the WIG crafts starting with a 550-ton WIG vehicle "the KM" shown in Figure 2-7, which is also known as the "Caspian Sea Monster".

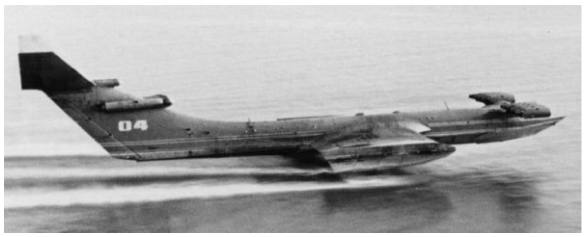

Figure 2-7 KM Caspian Sea Monster [77]

Later versions include A-90 Orlyonok, Chaika A-050. The Ekranoplans are basically large-aspect-ratio rectangular wings operating near water surface. One of the problems with WIG crafts operating near water surface is the take-off since the vehicle is partially merged in water. The excessive hydrodynamic loads, which is known as “hump drag”, have to be overcome to separate the hull of the aircraft from the water. Described by Wang et al. [78], Russian designers used “power augmented ram” (PAR) turbojet engines to overcome this problem. These engines, which are located on the tip of the fuselage, operate to increase the pressure beneath wings by tilting the jet engines and directing air exhaust over the wings.

WIG crafts suffer from longitudinal stability issues and a large high mounted horizontal tail is often needed. The Lippisch type reversed delta wing (RDW) planform is another alternative for operating near water surface. It is designed by German aerodynamicist Alexandar Lippisch. Its special design, which adopts anhedral to minimize water contact and generate significant “cushion” of the air beneath the wing, gives superiority in terms of stability and operationality with respect to rectangular wings. Earlier designs started with X-112 and later new designs are developed such as RFB X-114 and state-of-art design AirFish 8 shown in Figure 2-8.

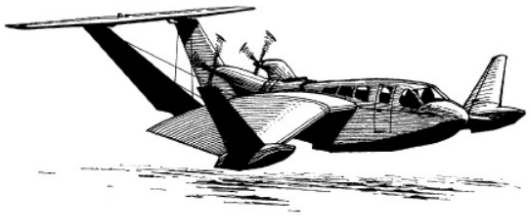

Figure 2-8 Airfish 8 [3]

Wang et al. [78] states that the Lippisch type WIG craft is reported to be only GE vehicle that has inherent stability. The RDW planform, which is adopted for the Lippisch-Type WIG crafts, became more popular in the recent years thanks to the significant developments in control theory and aerodynamics. It promises increased stability and safety for flights close proximity to the ground. An analogy is made by Lee [71] that special RDW shape is similar to gliding flight of butterflies and kites.

Tremendous amount of air pressure is confined between the wing and the ground since there is a solid boundary neglecting the depression of water beneath the wing during flights IGE over the water. This is called “Ram pressure” and utilized by GE vehicles.

As stated by Nebylov et al. [79], the WIG technology can also be employed where ships, hydrofoil vehicles and helicopters tend to be slow and dangerous. Furthermore, aircrafts do not have capability of achieving low altitude tasks. The infrared and radio signature of WIG crafts are reported to be very low. This feature gives them special stealth ability for submarine sonar. In addition, they are less risky in terms of mine threats. All these advantages prove that they can also be used for military purposes.

Provided by Qin et al. [80], the GE is categorized in two as attached flow GE of high-aspect-ratio wings for transport aircrafts and the separated flow GE for DWs for fighters. Former one is further classified as the “chord dominated GE” and latter one as the “span dominated GE”. These two types of GE are strongly related to air

cushion, downwash and tip vortices generated by the wing. The physics associated for the chord dominated GE and span dominated GE are summarized by Cui and Zhang [2]. For a typical aircraft wing, aerodynamic force consists of lift and drag components. Parallel to the flow direction, drag force is generated and it is perpendicular to lift force. Lift force is generated due to the pressure difference of its upper and lower surfaces named as suction and pressure sides. The trailing-edge vortices are generated due to the flow from high pressure side toward to the suction side. They adversely affect the lift generation of the wing since they create a spanwise distribution of downwash, which deflects the flow around the wing downward. Eventually, local flow incidence is reduced and overall lift of the wing reduces. The downward deflection of the flow results in increase in drag known as induced drag or lift dependent drag, which is proportional to the square of the lift. This is due to the fact that drag, which is equal to the product of the lift and deflection angle, is a function of the lift. In Figure 2-9, illustration of the wing tip vortices as well as induced downwash is provided.

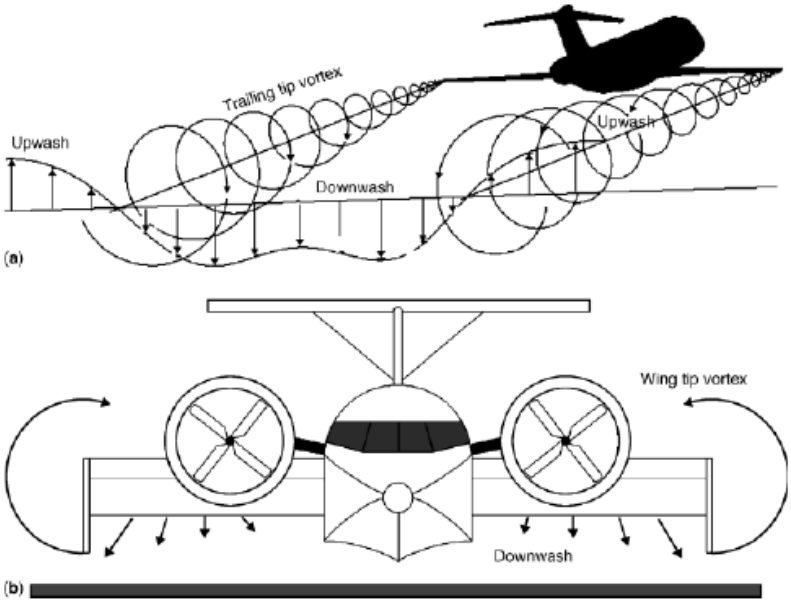

Figure 2-9 Illustration of wing tip vortices and induced downwash of a WIG aircraft. (a) Illustration of the wing tip vortices and induced downwash; (b) reduction of downwash in ground effect [2]

The span dominated GE is known for downwash generated by the wing. The downwash is blocked by the apparent ground boundary during IGE operations. This yields to a reduction of induced drag and eventually results in a favorable flight condition. It is accompanied with the disrupted wing tip vortices, which adversely affect the lift generation of the wing. In extreme GE condition such as flight height of one-fourth of wingspan, air is compressed between the wing and the ground creating air cushion which dominates the flow. For the chord dominated GE, air cushion effect is dominant and results in increased lift. Both the reduction in induced drag and increased pressure on the lower surface during air cushion results in increase in the lift-to-drag ratio. Therefore, span dominated GE is mainly due to the reduced induced drag and chord dominated GE is a consequence of increase in lift.

It is reported by Urquhart et al. [76] that height/span is important for span dominated GE and height/chord is important for chord dominated GE flows. Cui and Zhang [2] shows that for aircrafts flying close to the ground or water, the phenomenon becomes significant when the distance between the aircraft and the boundary is less than or equal to one wing span. In addition, air cushion starts to form for ground clearances less than one-fourth of the wing span for the aircrafts flying in extremely close to the ground.

Considering the application fields, the ride height may be constant resulting in “the static GE (SGE)”, whereas “the dynamic GE (DGE)” occurs when ride height changes in time**.** Their impact on the wing are different and may result in significant deviations in terms of aerodynamic characteristics. Therefore, stability of the wing also alters during SGE and DGE.

The DWs are categorized according to sweep angle. A non-slender DW is defined as the wing which has a sweep angle less or equal to 55 deg. Manshadi et al. [81] provided that the vertical flow structure is substantially different from a “slender” DW for a “non-slender” DW. In this study, flow field is examined experimentally for a generic cranked double DW and two different leading-edge shapes namely

"sharp" and "round" are examined OGE. Edge shape is reported to affect the size and location of primary vortex for DWs. The size and strength of the primary vortex reduces with increasing leading-edge radius. It also improves the longitudinal characteristics by retarding the formation of the LEV with the penalty of reduced vortex lift.

2.3.1 Delta Wing and Reverse Delta Wing IGE Studies

In this part, the DW flow features are detailed IGE and OGE as well as comparisons among DW and RDW are provided.

Qu et al. [82] investigated the aerodynamics of a sharp leading-edge with sweep angle of 65-degree delta wing IGE, numerically. Qin et al. [80] also studied a 65-degree sweep delta wing (VFE-2) with sharp leading-edge DW in SGE condition, numerically. The magnitudes of aerodynamic forces on leeward side are reported to be several times of those on windward side for a given ride height, indicating the total force is from suction force on leeward side induced by LEVs [82]. The lift, drag and nose down moment increase were observed as the height of the wing decrease at a certain angle of attack [82], [80]. The flow of the windward side expands and pushed more outboard caused by the increase in pressure of the inboard portion IGE. This increase in pressure is the famous "ramping effect" well known by the GE researchers also shows up for delta wings. It increases with decreasing flight height. In addition, LEV is enhanced IGE before the breakdown and the vortex breakdown is promoted due to the increased adverse pressure gradient. The Rosby number, which is the ratio of the local maximum axial velocity component to the local maximum circumferential velocity component, is used to determine the vortex breakdown [80]. The efficiency IGE is also addressed by Qu et al. [82] that lift-to-drag ratio slightly increases with the GE, although not as much as in the case of large-aspect-ratio wings. It is provided that for the large-aspect-ratio wings induced drag decrease is related to the decrease in wing tip vortices strength and they are pushed away from the wing due to ground's viscous dissipation and resulting in smaller

downwash angle. Therefore, it is well known that the total drag of large-aspect-ratio wings decreases in SGE [82], [80].

For DWs, tip vortices are replaced by LEVs and lift induced drag increases as flight height decreases. Another difference is seen for the variations in aerodynamic behaviors of DWs and large-aspect-ratio wings. For the former case, the changes on the windward side are relatively large and those on the leeward side are relatively small whereas for the latter case changes in aerodynamic behavior can be attributed both sides. However, it is concluded that the total forces and moments on DWs are from the leeward side which is dominated by LEVs. Qin et al. [80] studied a 65-degree sweep DW (VFE-2) with sharp leading-edge DW in SGE condition. The magnitudes of aerodynamic forces on leeward side are reported to be several times of those on windward side for a given ride height, indicating the total force is from suction force on leeward side induced by LEVs.

Lee and Ko [83] conducted force and PIV measurements for a slender delta wing with 65 deg sweep angle IGE condition. It was found that LEV was strengthened and vortex breakdown was promoted with GE induced RAM pressure, which gets stronger with decreasing height. The vortex trajectory was observed to move inboard and above the wing. Tumse et al. [17] investigated GE for a non-slender delta wing having 40 deg sweep angle with force and PIV measurements. It was provided that LEVs move outboard in spanwise direction while expanding their sizes. The level of turbulence increases with GE while lift-to-drag augmentation is higher with decreasing heights and between angles of attack of $\alpha = 5^{o}$ and 8^{o}.

In Ref. [84], same DW given in Ref. [80] is numerically studied but this time in DGE condition. Compared to SGE condition, the increments for lift, drag and nose down pitch moment seen in SGE become larger in DGE with increasing sink velocities. Except the small ride heights, the aerodynamic forces are similar to SGE for the DGE condition as long as the angle of attack values are equal. However, the aerodynamic forces are found to be much larger for DGE small ride height condition compared to SGE even though the angle of attack value is the same. In this flow regime, the SGE

and compression work effect is found to govern the flow together for DGE condition. The former one is found to be responsible for pressure increase on windward side and vortex strength enhancement while the latter one further increases the pressure on windward side but has negligible effect on the airflow over the DW or leeward side.

The examination on aerodynamic improvements through different leading-edge flaps for DW OGE is made by Ishide and Itazawa [85] using PIV and force measurements. It is outlined that stable LEV generation on the top of wings is the most important feature of DW aerodynamics. It is found that the lift-to-drag ratio with the drooping apex flap is improved in comparison with the upward deflected flap. However, the combination type leading-edge flap using both drooping apex flap, which can delay vortex breakdown, and the upward deflected flap, which induces a stronger LEV at low angles of attack, improves the aerodynamic efficiency in the post stall region.

Fluid structure interaction is often missing for numerical studies and may result in discrepancies with the experimental results. In Ref. [86], it is examined for a cropped DW. The interaction between unsteady aerodynamics and the structural response is reported to be highly nonlinear. LEV induced vibrations can cause large deformations on the wing and eventually influence the aerodynamic forces and moments.

The RDW planform is extensively investigated in Ref. [71], [87], [72], and [19]. The DW planform is also considered in order to compare the advantages of RDW both IGE and OGE. It is found Lee et al. [19] that lift generation mechanism for RDW is based on the lower side of the wing while upper portion acts like a wake generator and RDW vortices play a little role for the lift generation of the wing. In Ref. [87], the effects of cropping, anhedral, Gurney flaplike strips and winglets on the vortex flow and aerodynamic properties of slender RDW, which has 65-degree sweep angle, operating OGE are investigated experimentally. It is found that cropping, which is beneficial in terms of weight reduction and extended laminar flow region, shows a

minor change in RDW aerodynamics especially vortex flow. However, it results in promoting stall. Lee et al. [72] address only the anhedral effect on RDW OGE and anhedral has inferior effect although vortices are strengthened with respect to baseline wing. The results in Ref. [87] show that the Gurney flaplike side edge strips (SESs) increase lift, drag, and vortex strength. Lee [71] extensively investigate the SESs effect on RDW OGE and the downward LES-wing is reported to produce a lower vortex strength and lift compared to the upward counterpart. Finally, Lee et al. [87] reports that winglets have no effect on vortex flow properties. Flow properties of RDW were also examined. In addition, a unique arm-and-fist vortex flow pattern, which is originated from the pressure side surface, is seen. It is also indicated that the RDW vortices are located outboard. In other words, the lift is produced by pressure exerted on the wing's bottom surface. Comparing the LEVs of DW and RDW shows that DW vortices are more concentrated and have higher vorticity levels. In Figure 2-10, three-dimensional representation of iso-vorticity contour at $\alpha = 16^{o}$ are compared for DW and RDW. Overall, among all cropped wing configurations, joint anhedral and SESs is observed to have superior lift characteristics and their combined effect is expected to perform better IGE condition. The winglets on the RDW with anhedral are reported to help roll control rather than for conventional wingtip vortex flow control but also provide strengthened RDW vortex.

Non-slenderness of the RDW is also discussed in Ref. [19] by comparing wings with 50-degree sweep angle (DW50 and RDW50, $\Lambda = 50^{o}$). Although, RDW50 is reported to generate more lift than DW50 for $\alpha \leq 10^{o}$, no general conclusion is drawn and further investigation over the aerodynamic curves is suggested.

In Ref. [76], wake pressure survey and aerodynamic investigation of RDW is made experimentally in a wind tunnel, which has a static ground plane. It is reported that static ground plane falsely simulates the actual boundary layer at low ground clearance values. It is revealed that as the height reduces, apparent lift-to-drag ratio increase is seen. This is accompanied with increasing nose-up pitching moment.

Importantly, wake survey results indicate that tip vortex is positioned a long distance from the horizontal stabilizing tail surface. Therefore, the tip vortex has small impact on effectiveness of the tail. In addition, horizontal tail is unaffected from the decreasing height. In other words, the main wing lift and therefore pitch moment change due to higher ground effect intensity for lesser wing height. Therefore, large horizontal tail should have enough restoring moment capability to counteract the moment generated by the main wing. Obviously, as the height increases, aircraft will have better stability characteristics. In addition, Wang et al. [78] reports that the aerodynamic efficiency is not affected by the high horizontal tail configuration.

In Ref. [88], W-shaped leading-edge (referred as W-wing), RDW planform IGE is investigated with experimental and numerical techniques. Both fixed ground and moving belt methods are employed. It is reported that the shortcomings of fixed ground boundary layer are more pronounced as angle of attack increases. In the subsonic flow condition, forward sweep wing promises induced drag reduction, soft stall and higher lift-to-drag ratio. Therefore, the combination of backward and forward sweep is employed on the wing. The lift-to-drag ratio increases tremendously IGE. It is doubled IGE with respect to OGE case and reached to a value of 30. Tip vortices pushed outward IGE, which is an indication of increased effective wing aspect ratio, which means increase in lift and lift-to-drag ratio. In addition, outward movement of tip vortices suggests that their interference on the wing and any tail surface is reduced. The W-wing IGE has advantageous character during take-off since strong air cushion effect exists for the wing. As the wing moves higher from the ground, this ram effect diminishes.

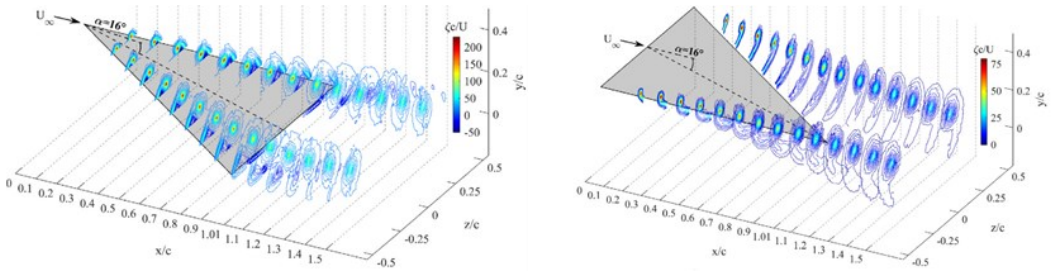

Figure 2-10 Three-dimensional representation of iso-vorticity contour at $\alpha = 16^{o}$ for DW and RDW OGE [87]

2.3.2 Aerodynamic Results

In this part, the GE aerodynamics are examined in detail in terms of the different motions, which are performed by the GE vehicles such as flapping, ditching and heaving etc. In Ref. [89], the GE phenomena is investigated numerically for flapping wing, which has NACA0012 profile. Strouhal number (St) is found to be important quantity over lift and drag aerodynamic coefficients C_L and C_D. St number IGE for flapping wing is defined in Eqn. 1 where f is the oscillating frequency, A is the amplitude of oscillation and U_∞ is the free stream velocity. Noting that as the flapping occurs over the ground, height of the wing changes. Therefore, subscript h shows the dependence of St number to the GE intensity, which changes with height of the trailing-edge. It is found that C_D monotonously decreases with increasing St and after a certain value it becomes negative indicating that thrust force is obtained. As this critical frequency is achieved, C_L increases tremendously and keeps increasing with increasing oscillating frequency. Therefore, it is noted that there exists a critical frequency of oscillation, which determines whether thrust force and positive lift force can be generated IGE.

$$St_h = \frac{2 \cdot f \cdot A}{U_\infty} \qquad 1$$

WIG vehicles are both heaving and pitching oscillating foils. In Ref. [90], the flight of WIG vehicles is simulated in a towing tank. The lower limit of the St number was

selected to ensure hydrodynamic forces with the particular experimental setup. In addition, trailing-edge of the foil is found to produce strong vortices that may entrain air. Therefore, upper limit of the St number is selected to avoid this entrainment in the wake. Thrust gradient is positive with increasing St number. However, there is a trade-off between increased efficiency and the presence of a stabilizing GE. Force measurements results show that the dynamic forces associated with a flapping foil IGE are inherently different than the case of a static wing IGE. The hydrodynamic efficiency, which is the ratio of the output power to travel with a certain speed IGE to the input power to make heave and pitch oscillatory motions IGE, is also reported to be inversely correlated to the strength of repulsion caused by the GE. That is, increased hydrodynamic efficiency can only be achieved by incurring suction force, or that the benefits of a positive GE can only be achieved at the expense of reduced efficiency. This kind of motion is also important since WIG crafts also operate in wavy waters and there is an ongoing debate over how the ideal motion should be for them. In addition, there is also no consensus over the longitudinal stability indicated by Nebylov et al. [75] such that motion can be either altitude stabilization, which dictates that the average level of disturbed sea is regarded and the vehicle moves in straight above the crests of waves with rather small clearance margin whereas the second stabilization can be based on permitting the vehicle to track partly the wave disturbance passing them. Therefore, oscillating WIG concept plays an important role in aerodynamic researches since mathematical models of the WIG vehicles heavily depend on these aerodynamic findings.

WIG vehicles also suffer from water contact during take-off or landing since these flight conditions result in high hydrodynamic forces which eventually deteriorate safety and comfort of the flight. Ditching of WIG vehicles often takes place and it may cause extreme loads by water impacts. Cheng et al. [91] shows numerically that ditching of WIG has two stages namely sliding and gliding which are analogous to the stone skipping accompanied with the angular variation. At the free glide phase, the horizontal velocity of the WIG ship remains constant, while the vertical velocity decreases linearly under the gravity. Furthermore, the water depression which is

depicted in Figure 2-11, during operation close to the water occurs which changes the effective height of the vehicle.

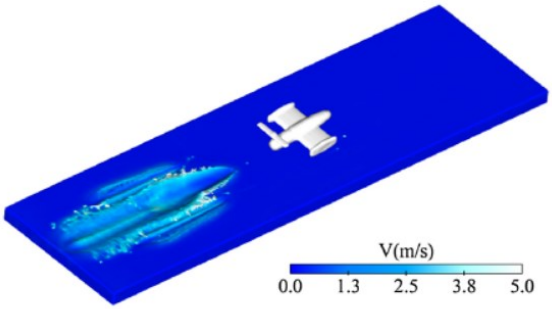

Figure 2-11 Velocity field images in the three-dimensional view during the ditching of the WIG ship [91]

2.3.3 Aerodynamic Improvements

The aerodynamic efficiency can be improved passively by changing the wing planform to some extent. In this part, these kinds of modifications are examined. In Ref. [92], effect of wing tip sails is investigated. A representative pelican wing is manufactured with and without wing tip sails. The tests are conducted in a towing tank equipped with a trailer. It is found that lift-to-drag ratio increases with respect to pelican wing IGE without tip sails at angle of attack values larger than 5^{o}. It is concluded that tip sails enlarge the wing area, decrease the size of the tip vortices and lift-to-drag ratio increase is mainly due to increase in lift not the decrease in drag.

It is known that wing tip vortices play a major role for aerodynamic efficiency. WIG aerodynamic efficiency can also be improved with the compound wing design shown in Figure 2-12, which consists of a main wing with low aspect ratio and an endplate, which can be utilized to prevent the high-pressure air escaping from the air cushion beneath the main wing, and outer wing with high aspect ratio. It is reported in Ref. [93] that endplate between main wing and outer wing reduces the influence of the tip-vortex of the main wing on the outer wing. Ref. [93] also shows that the GE both decreases tip vortices and downwash so it further enhances lift-to-drag ratio. In

addition, the main wing aerodynamic performance is improved with the inclusion of endplate. The overall lift is mainly generated from the main wing compared to outer wing whereas the main wing's role also increases with reduction of ground clearance and the same observation is valid for the pitching moment as well. The lift-to-drag ratio also increases with the inclusion of outer wing. The outer wing can also be as a horizontal stabilizer. Therefore, height stability, which will be discussed later, decreases with increasing ground clearance and improves when the outer wings shift toward the trailing-edge of the main wing.

Gurney flaps are well-known devices among aerodynamicists to achieve better aerodynamic efficiency. They are also considered for the GE applications. The aerodynamics of Gurney flaps on a rectangular, untapered and untwisted wing are experimentally investigated by Zerihan and Zhang [94] using moving belt mechanism to simulate the moving ground. The particle image velocimetry (PIV) and the laser doppler anemometry (LDA) measurements are conducted. Not only aviation industry but also car industry is interested in the GE research. Specifically, the GE technology plays a vital role for Formula 1 (F1) car design with superior aerodynamic characteristics leading to the performance enhancement of the car. The acceleration of the car is correlated with downforce generated with the following relation given in Eqn. 2 by Ref. [95], where μ_{max} is the peak coefficient of friction of the tire, M is the mass associated with that tire, and g is the gravitational acceleration and Acc. is the acceleration of the car. A typical car is viewed as a low aspect ratio (AR = 0.38) bluff body operating in ground effect (gap/chord = 0.005).

$$\text{Acc.} = g \cdot \mu_{max} + \frac{\text{downforce} \cdot \mu_{max}}{M} \qquad 2$$

In Ref. [94], Tyrrell 026 F1 car front wing is utilized and two different sizes of Gurney flaps are tested. It is shown that adding a Gurney flap IGE increases the lift (or downforce for car industry applications) more significantly than OGE. In addition, increasing the incidence angle of the wing results in a reduction in

sensitivity to ground height. Increasing the size of the Gurney IGE reduces the frequency of vortex shedding but it increases the St number asymptotically reaching to its maximum for the largest Gurney.

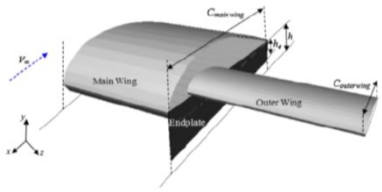

Figure 2-12 Schematic for 3D geometry of the compound WIG [93]

2.3.4 Control and Stability

Control and stability are two important issues accompanied with the GE since the flight safety, handling quality and comfort are as important as achieving superior aerodynamic efficiency for a successful design. In this part, these two topics and terminology are briefly covered. IGE there is a stability term called height stability (H.S.). It is defined by two neutral aerodynamic centers for WIG. There is a point where the moment does not vary with the angle of attack and another neutral point where moment is independent of flying height. These neutral points are the aerodynamic center in pitch (X_a) and the aerodynamic center in height (X_h). These points can be determined using the lift and moment coefficient curves with respect to angle of attack and the ground clearance. As reported by Tavakoli Dakhrabadi and Seif [93] and proposed by Irodov [96], the longitudinal static stability of height of a WIG dictates that the WIG has the static stability if the aerodynamic center in height is located upstream of the aerodynamic center in pitch. Mathematically, it can be expressed by Relation 3, where positive x direction is from leading-edge to trailing-edge.

$$H.S. = \frac{C_{M_\alpha}}{C_{L_\alpha}} - \frac{C_{M_h}}{C_{L_h}} = X_a - X_h \geq 0 \qquad 3$$

Kornev and Matveev [97] provided that the center of gravity (X_{CG}) should be located between X_h and X_a, which is defined by Relation 4. However, it is desired that X_{CG} is located closer to the X_h with respect to the X_a. The favorable locations are given in Figure 2-13

$$X_a \geq X_{CG} \geq X_h \quad (4)$$

They further suggested that H.S. is to be between 0.05 and 0.15, which is provided by Relation 5.

$$0.05 \leq H.S. \leq 0.15 \quad (5)$$

Large horizontal tail obviously improves the longitudinal stability. Regarding the economics, it is reported that large horizontal tail is not a good option since it introduces structural weight and drag but as shown in Ref. [93] that outer wing can be a good option to reduce the horizontal tail area and moment arm of the tail. One drawback is the somehow decreased overall lift force of the compound wing as the side wing moves back. However, it is seen that aft placement of side wing improves the stability of the wing. Wang et al. [78] shows that high tail configuration improves longitudinal stability by shifting X_h forward and X_a to backward.

Hahn et al. [98] reported that air speed, angle of attack and height are reported to be important variables for the control of the WIG craft. In addition, “pitch up tendency” due to increased ram pressure during GE flights creates an inherent danger, which is a longitudinal instability because of the shift in aerodynamic center. In addition to these, Cui and Zhang [2] reports that wingspan, chord length, and the wing loading, which is the aircraft weight per unit area of wing, are the other factors affecting the performance of the WIG. Stability analysis conducted by Aminzadeh and Khayatian [99] shows that without any disturbance, the GE problem is linear time invariant control problem for cruise condition whereas under wavy surface and gust,

aerodynamics and stability derivatives are reported to be changing. In addition, the effects of wave amplitude, wavelength, course angle of wave, wave speed and gust velocity have different influences on control of the WIG. Their importance on the aerodynamics are also reported in Ref. [2]. The strong influence on airfoil forces due to the phase angle between the wave and airfoil motion is specifically emphasized.

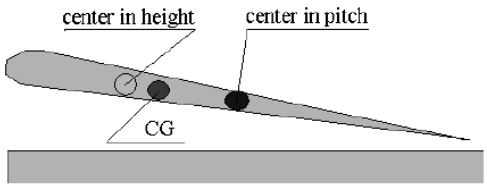

Figure 2-13 Favorable positions of the aerodynamic center in pitch (X_a), aerodynamic center in height (X_h), and CG [97]

2.3.5 Ground Effect Testing

The ground effect testing is a challenging task since it is hard to simulate the correct boundary condition at the ground level. Barber [100] stated that numerical and experimental results show significant discrepancies due to incorrect specification of the ground surface boundary condition. In addition, without taking into account the viscous effects, efficiency values are overpredicted. It also questions whether the rigid ground assumption is valid for vehicles operating over water since water depression occurs. The aerodynamic pressure on the water surface has influence on the water boundary condition. In real flight, water surface sags under the vehicle. Therefore, aerodynamic coefficients found from numerical and experimental simulations have some variations from the real flights. The difficulty to simulate this strong coupling between hydrostatics and aerodynamics is well documented in Ref. [100]. It is indicated that matching the Re number for aerodynamics and Froud (Fr) number for naval architecture problems simultaneously is very hard. Therefore, CFD

shows its usefulness at this point for WIG vehicle testing. Noting the chord dominated GE, Re and Fr numbers are given by Eqn. 6 and Eqn. 7.

$$\mathrm{Re} = \frac{\mathrm{Uc}}{\nu} \tag{6}$$

$$Fr = \frac{U}{\sqrt{gL}} \tag{7}$$

Ref. [100] claims that water depression occurs due to wing tip vortices not because of the aerodynamic pressure that has been assumed at very beginning of that study. In the real flight, considering the relative velocity of the ground and air indicate that ground should has slip condition, which refers to zero shear stress at the ground among aerodynamicists and CFD practitioners as outlined by Barber [100]. The mirror image model condition dictates setting the lower boundary to a symmetry condition by placing the exact replica of the model, which is also challenging to achieve, in wind tunnel testing. Zhang et al. [95] reported that the image method is considered as inviscid GE simulation since the velocity of the dividing streamline among two models determine the velocity of the ground plane. It loses the real physics to some degree since the velocity gradient at the boundary disappears unlike the normal operating condition. Barber [100] also describes the difference between image and slip wall methods such that for the former one, all normal gradients are zero whereas the latter indicates only the normal component of the velocity is zero. The dynamic ground plane testing, where the ground moving at the freestream velocity, is physically correct condition for the GE simulations. Moving belt system constructed for a F1 car testing is depicted in Figure 2-14.

Figure 2-14 Image of a race car model in a low-speed wind tunnel equipped with a moving belt system [95]

Ground moving condition is numerically easy to implement but experimentally it is very challenging. Zhang et al. [95] describes that the vibration problems of the rollers, possible lateral movement of the belt, the need for a cooling system for long runs as well as the lift of the belt due to the suction generated by the negative pressure field of the model are some of the problems associated with this method. In addition, surface vibration problems and electrical noise interference with the measurements in the region close to the wall also reported by Yoshioka et al. [101] as the drawbacks of the moving belt system.

Moving belt mechanism is shown in Figure 2-15 (belt having wind tunnel airspeed) together with suction slot to remove the oncoming boundary layer. Another system to suck the belt from below to a flat surface are often employed for the GE testing.

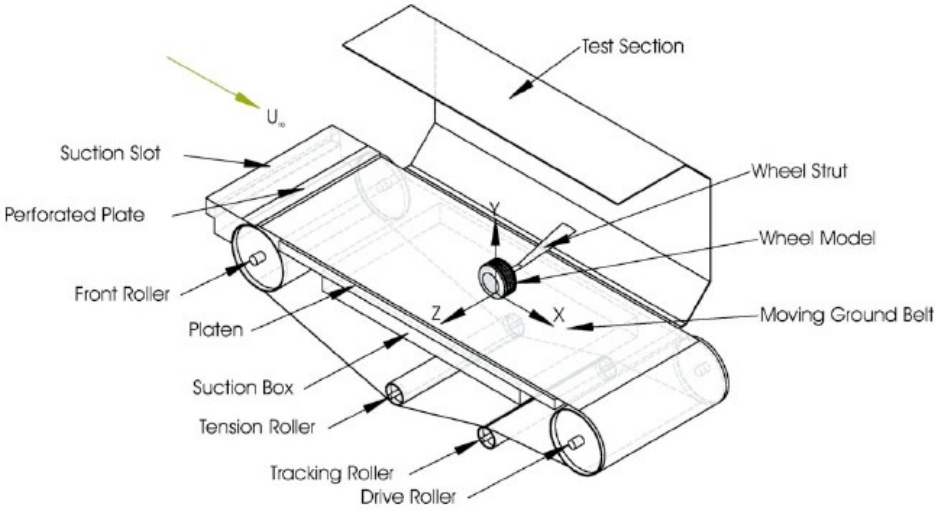

Figure 2-15: Schematic of the moving belt system with a side mounted wheel model [95]

Jones [77] addressed the necessity to employ dynamic GE testing and concluded that spanwise lift coefficient and height above the ground are two distinct parameters whether moving belt is required or not. The conditions requiring moving belt ground plane is given in Figure 2-16.

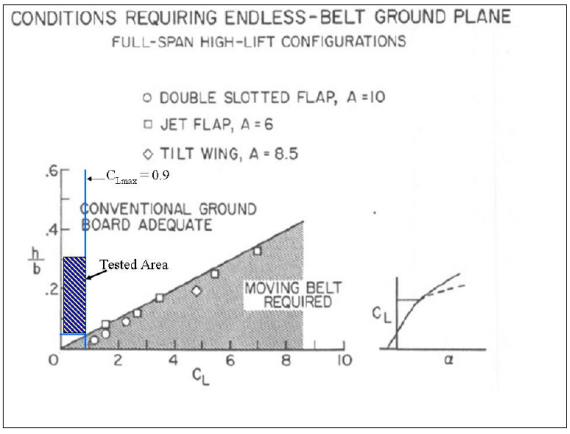

Figure 2-16 Conditions requiring moving belt ground plane [77]

The differences for the velocity profiles due to different ground boundary conditions are given in Figure 2-17. Barber [100] stated that combination of both experimental and numerical techniques reveal confirm the ground stationary condition (or static ground testing) predicts continuous increase for lift-to-drag ratio as the ground clearance lessens whereas the realistic condition of ground moving model shows lower lift-to-drag ratio predictions.

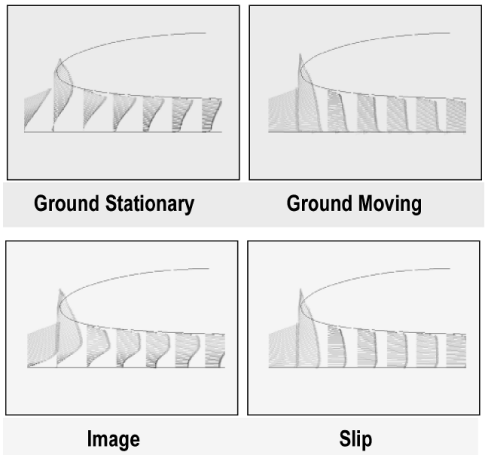

Figure 2-17 Velocity profiles for different ground surface boundary conditions [100]

In Figure 2-18, percent increase in lift coefficient IGE vs aspect ratio (AR) for various aircrafts including DWs is given by Jones [77]. In this figure, both the static and the dynamic ground testing results are provided. For the latter one, landing approach and take-off maneuver was simulated by manually or mechanically moving the model towards the ground plane. It is seen that ground effect augmentation is overestimated for DWs with static ground testing. In addition, overprediction for increase in lift coefficient monotonically increases with increased delta wing sweep angle.

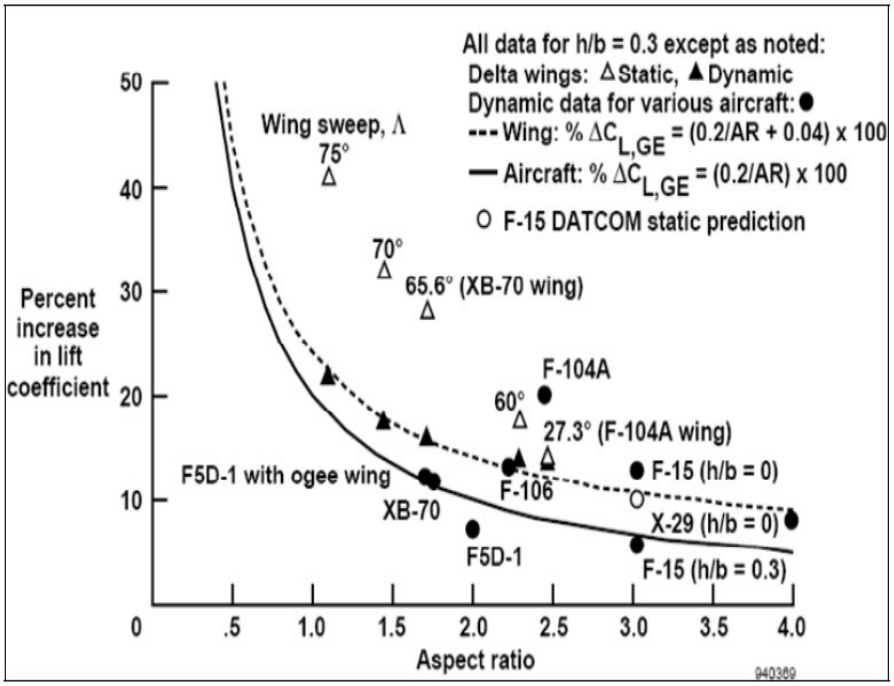

Figure 2-18 Percent increase in lift coefficient IGE vs AR for various aircrafts [77]

Lee et al. [102] examined F-106B and XB-70 aircraft models with static and dynamic GE test cases in wind tunnel. Similarly, dynamic GE testing yielded to lower increments in lift and drag coefficients, which was primarily emanating from the absence of the vortex motion, compared to the static GE testing condition. The static GE testing results showed significant improvements in the longitudinal static stability, which were mainly attributed to the refinements in flow field around wing tip region. The combined effect of increased LEV strength as well as more outboard positioning of these vortices with reducing ground heights resulted in more nose-down moment as a consequence of more positively loaded wing tip region.

Wind tunnel test data are compared with the flight test data by Schweikhard [103]. It was provided that lift, drag, and nose-down moment for the same lift coefficient are enhanced in ground effect (IGE). The nose-down moment is counteracted by the downforce generated by the tailed aircrafts and delta wings, hence the increment in lift for trimmed flight will be lesser than the untrimmed model tests in wind tunnel [103].

In automotive industry, three different research tools are used for GE aerodynamics. These are full scale track tests, CFD simulation and wind tunnel model tests. In Ref. [95], it is provided that full scale tests are often employed as the final assessment for the performance whereas CFD simulation gets increasingly valuable. The wind tunnel experiments again are reported to have incorrect boundary layer problems. Suction of the oncoming flow to get rid of the distorted boundary layer is considered as an expensive method whereas tangential blowing to inject flow close to the ground at the wind tunnel airspeed is similar and again expensive. A flat board, which is placed a short distance upstream of the model, is reported to be a relatively simple method.

Towing model in water channel is another option. Synchronizing flow visualization and quantitative measurement instrumentations to the setup is one of the biggest challenges accompanying with this technique. Measuring equipment are moved with the model while measuring or recording the flow field as well as measuring force and moment. In Ref. [92], experimental investigation of the wing with tip sails IGE is made. Their experimental setup is provided in Figure 2-19 with sketch of the towing tank.

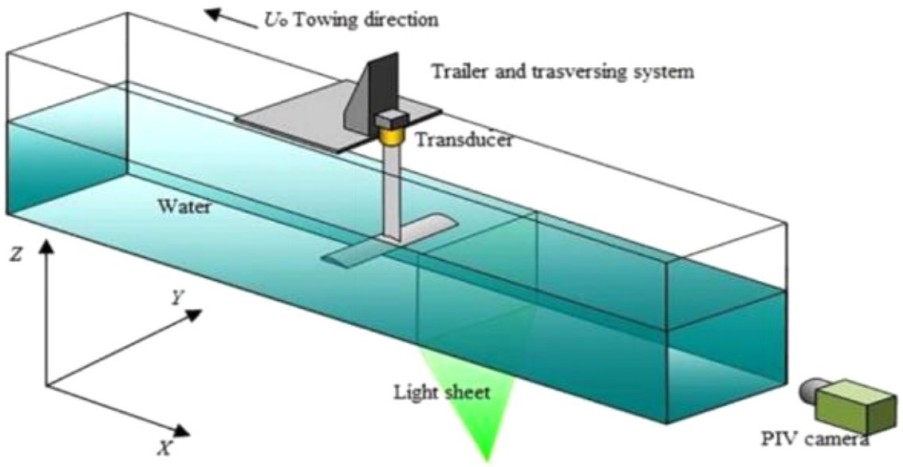

Figure 2-19 Towing tank and ground effect test setup [92]

In Ref. [101], the highly complex flow between a steady surface and a moving model is reported to be quantified in “HART” facility in Japan, which is a towing wind tunnel facility without the moving belt system and provided in Figure 2-20. A testing model moves in still air on a testing track. It is also noted that high Re number experiments can be conducted in such a test facility. Unfortunately, this facility with 6.9 km in length and 3.46 m in width comes with the huge economic penalty.

For the DGE, experiments are even harder since vertical motion as well as the pitch angle should be varied. A special floor boundary layer removal system is used in Ref. [1] as well as vertical travel and pitch are automatically controlled for testing at various sink rates and angle of attack values. The GE is quantified in terms of lift and pitching moment measurements.

Figure 2-20 Snapshot of HART vehicle in test section [101]

CHAPTER 3

EXPERIMENTAL SET-UP AND MEASUREMENT TECHNIQUES

In this chapter, experiemental system, methodology, measurement techniques, experimental matrix and uncertainty estimation are presented. For that purpose, wind tunnel, wing models, model positioning system (MPS), angle of attack measurement, and ground effect simulation techniques are further detailed. For the sake of brevity, some of the images regarding to the wind tunnel, MPS, static and dynamic ground systems are provided in Appendix D.

3.1 Wind Tunnel

Experiments were performed in a low-speed, suction type, and open-circuit wind tunnel, located in Fluids Mechanics Laboratory of Mechanical Engineering Department at Middle East Technical University. The wind tunnel consists of five main parts, which are settling chamber, contraction cone, test section, diffuser, and fan. The tunnel facility is shown in Figure 3-1.

The wind tunnel has a test section of 750 mm wide, 510 mm deep, and 2000 mm long, with a contraction ratio of 8:1. The transparency of the test section, which is given in Figure 3-2, is achieved by utilizing plexiglass walls at all sides, thereby allowing the optical flow measurement methods. The uniform flow as well as minimal turbulence intensity in the test section are created by utilizing a honeycomb and additional three fine-mesh screens, which are installed along the 2700 mm long settling chamber. A 7300 mm long diffuser expands and decelerate the high-speed flow leaving the tunnel section to increase static pressure, hence decrease the required power of the wind tunnel. The maximum freestream velocity of the test section is equal to 30 m/s. The desired tunnel speed can be adjusted with a remote

frequency control unit, which governs an axial fan and a 10 kW AC motor assembly mounted at the exit of the tunnel.

The Reynolds number, which calculated based on Eqn. 8, of $\mathrm{Re} = 9\mathrm{x}10^4$ was used for the experiments, calculation of which was based on the delta wing 1b chord length of 135 mm regardless of the cropping condition.

$$\mathrm{Re} = \frac{U_\infty c}{\nu} \qquad 8$$

The maximum blockage ratio was below 2.7% at the highest angle of attack over the entire test matrix.

Figure 3-1 View from the wing tunnel facility

Figure 3-2 View from the test section of the wind tunnel

3.1.1 Wind Tunnel Characterization

The wind tunnel characterization was conducted using Laser Doppler Anemometry (LDA) and Pitot-Static Tube measurements [104]. These measurements were also validated for the present study with pitot-static tube measurements. Environmental conditions such as temperature, humidity, and elevation were taken into account for the dynamic pressure calculation of the Pitot-Static Tube measurements. The average velocity with respect to tunnel power as well as turbulence intensity values are provided in Figure 3-3. The linearity of the tunnel velocity versus fan power starts above 4%. It is reported that maximum difference among the LDA and Pitot-Static Tube measurement techniques is around 3%. The maximum turbulence intensity was found to be less than 1% at the free stream velocity for the corresponding $\mathrm{Re} = 9\mathrm{x}10^4$.

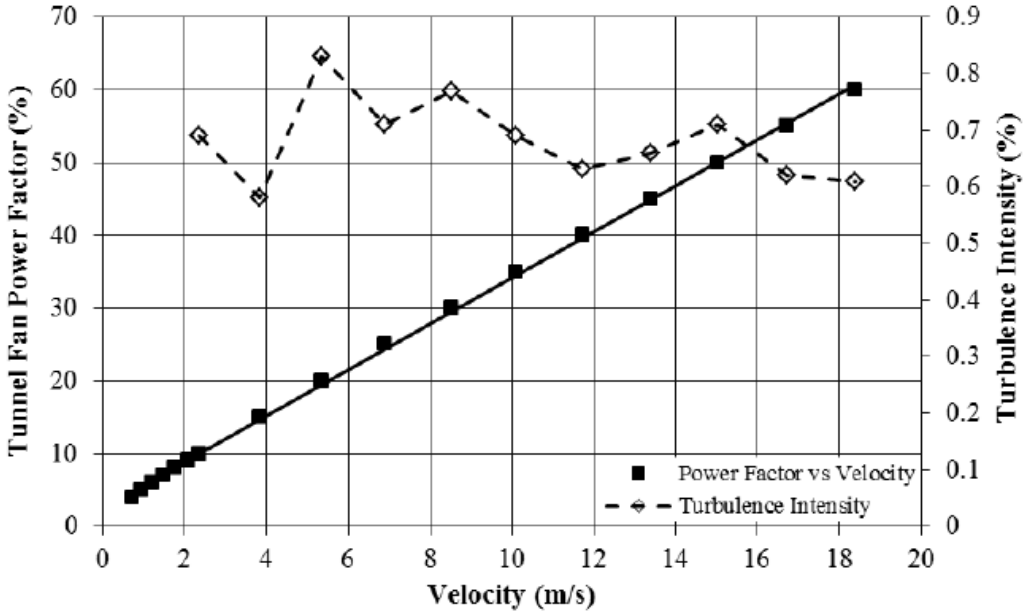

Figure 3-3 Wind tunnel calibration graph [104]

3.1.2 Structural Vibration Characterization

The structural vibration characterization of the low-speed wind tunnel was made using 3-Space Sensor^{TM} USB v2.0 Inertial Measurement Unit (IMU) sensor, which is a miniature, high-precision, high reliability, Attitude and Heading Reference System (AHRS). It offers up to 1 kHz sampling frequency. The aim of the test was to measure vibration levels of the wind tunnel over acceleration values. The schematic representation of the vibration measurements is shown in Figure 3-4. The IMU sensor was placed at the ceiling of the test section. It was energized from a laptop using a USB cable. The IMU sign convention follows left hand rule such that x axis toward starboard side, z axis towards forward and y axis towards up. Therefore, y acceleration is measured close to gravity when the tunnel does not operate, hence measurements follow this sign convention.

For the vibration test campaign, wind tunnel speed was incrementally increased. Total 12 tests were performed such that the tunnel fan power was swept between 0 to 55%. The model mount mechanism as well as pitot tube were kept mounted for all tests. Each test was performed for 60 seconds durations. In Figure 3-5, mean values of the acceleration data are shown with respect to the tunnel fan power factor. The acceleration data are given in gravitational acceleration (g). Considering Figure 3-5, the acceleration values are constant for x and z axes (drag and side force) channels at fan power values greater than 15%. For the y axis (lift force or gravity), acceleration mean value decreases up to 20% fan power and increases monotonically up to 45%. Therefore, vibration level is only correlated with freestream velocity in this direction. However, results show that structural vibration levels alter insignificantly up to 55% fan power for all three directions.

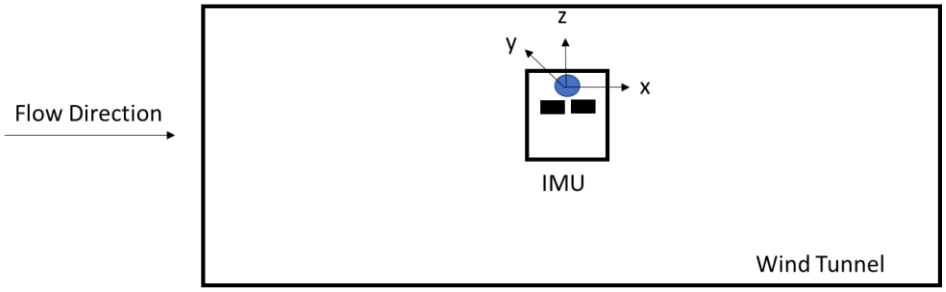

Figure 3-4 Top view of the wind tunnel and sign convention (left-handed) for IMU measurement axes

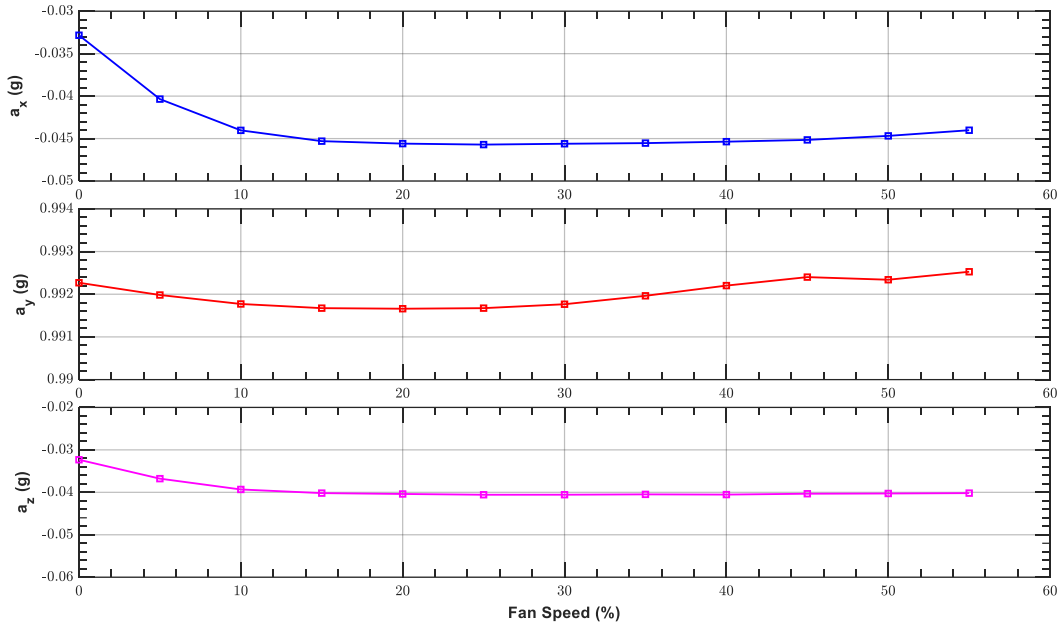

Figure 3-5 Mean values of the time history of acceleration data

3.2 Wing Models

Eight different wings with a sweep angle of 45 degree were used. The wing geometries are detailed in Figure 3-6 where wings are labelled with numbers 1 and 2 for delta wings and reverse delta wings, respectively. The first two columns of Figure 3-6 provide geometric parameters including the wing thickness, edge type, anhedral angle (δ) and cropping ratio (Cr%), while the third column defines the parameters such as base wingspan (S), quarter-span (s), base wing chord line (c), cropped chord line (c_{cr}), sweep angle, cropping percentage (Cr%), and indicates freestream directions for delta and reverse delta wings. Anhedral angle and wing cropping are explained on the bottom right schematic of Figure 3-6. Anhedral angle is the downward angle from the chord or cropped chord lines. The wings 2c and 2d configurations are the anhedraled reverse delta wings in absence of cropping whereas the 2e and 2f configurations are the cropped versions of the wings 2c and 2d. The cropped trailing-apex region is shown with the dashed area. The uncropped wings had a chord length of 135 mm and span of 270 mm whereas cropped wings had a

chord length of 94.5 mm. Base delta wings and base reverse delta wings were geometrically identical for thick (1a and 2a) and thin (1b and 2b) configurations, respectively. The geometrical properties of the wings are given in Table 3-1. These properties are detailed in Appendix A.

Thicknesses of the wings were 8 mm and 1.5 mm with corresponding thickness-to-chord ratios of t/c = 5.9% and 1.1% for thick and thin configurations. The base thick wings (1a and 2a) were manufactured using rapid prototyping of fine polyamide PA2200 with a thickness of 0.15 mm. All three edges of these two wings are sharp and beveled symmetrically with a 45-degree angle. Only base thick delta wing (1a) has 18 pressure taps distributed symmetrically at the chordwise distance of x/c=0.5. The symmetric bevel condition enables that both sides of the wing can be used as suction and pressure sides. Therefore, 1a wing has pressure taps, which are present on only one side of the wing. The diameter of these taps on the surface of the wing is 1.5 mm. The thin wings (1b, 2b, 2c, 2d, 2e, 2f) were made of an aluminum flat plate and had sharp and cut edges at all sides with no bevel on both leading and trailing-edges.

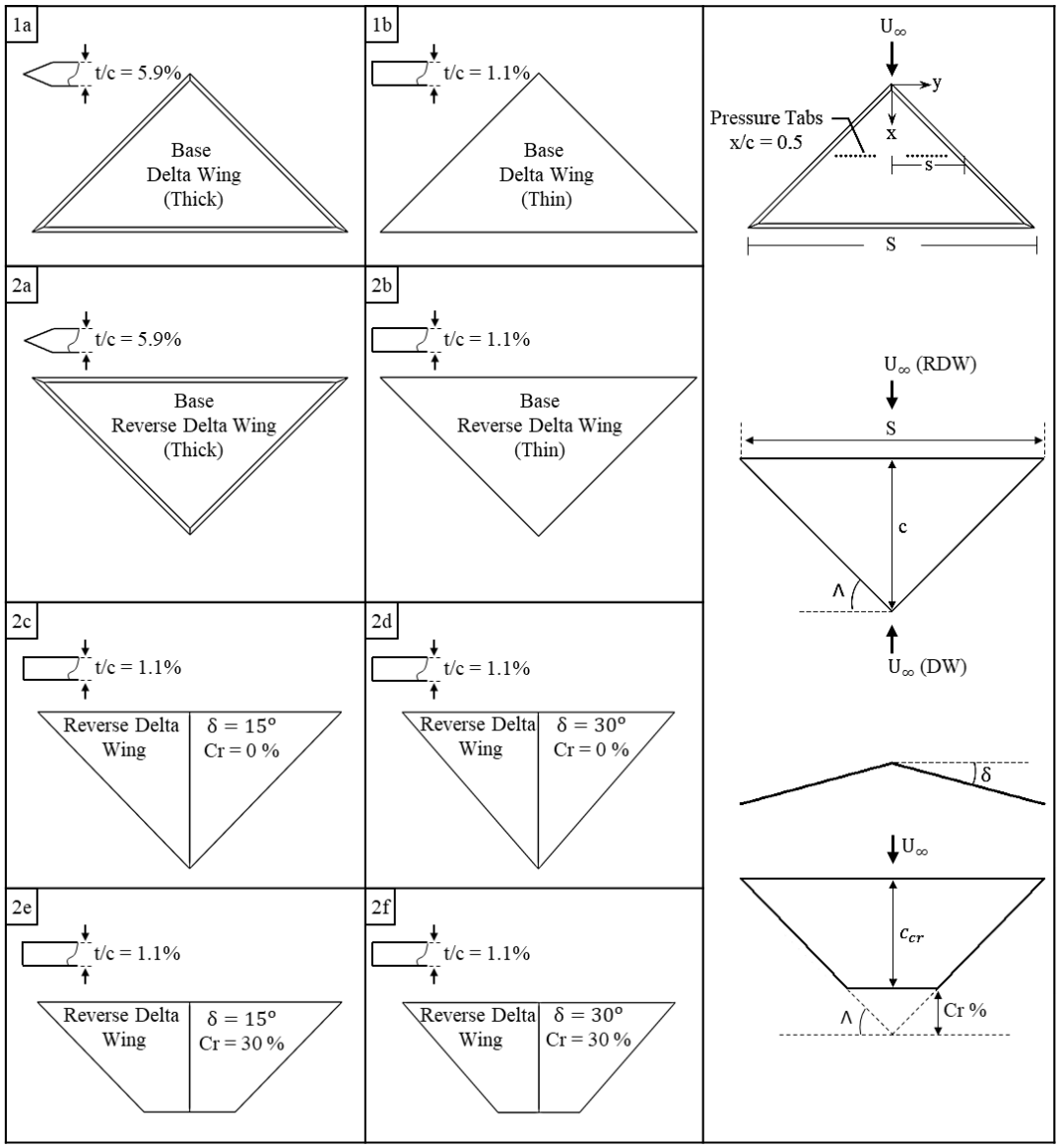

Figure 3-6 Schematic representations of the wings including delta wing, reverse delta wing, anhedraled and cropped

Table 3-1 Wing configurations and geometric parameters

Wing Model	Λ (deg)	t/c (%)	δ (deg)	Cr% (%)	c_{eff} (m)	b_{eff} (m)	A_{BW} (m^2)	A (m^2)	Area Ratio (nd)	AR (nd)	α_{eff} (deg)	h_{min} (mm)
DW (1a)	45	5.9	0	0	0.135	0.2700	0.0182	0.0182	1.0000	4.0000	0	0
DW (1b)	45	1.1	0	0	0.135	0.2700	0.0182	0.0182	1.0000	4.0000	0	0
RDW (2a)	45	5.9	0	0	0.135	0.2700	0.0182	0.0182	1.0000	4.0000	0	0
RDW (2b)	45	1.1	0	0	0.1350	0.2700	0.0182	0.0182	1.0000	4.0000	0	0
RDW (2c)	45	1.1	15	0	0.1350	0.2608	0.0182	0.0176	0.9659	3.8637	14.51	34.94
RDW (2d)	45	1.1	30	0	0.1350	0.2338	0.0182	0.0158	0.8660	3.4641	26.57	67.50
RDW (2e)	45	1.1	15	30	0.0945	0.2608	0.0182	0.0160	0.8790	4.2458	14.51	34.94
RDW (2f)	45	1.1	30	30	0.0945	0.2338	0.0182	0.0144	0.7881	3.8067	26.57	67.50

3.3 Model Positioning System (MPS)

The model positioning system (MPS) was designed to overcome the challenges imposed by the ground effect testing. Therefore, a generic positioning system was aimed so that it can be used for both ground effect and out of ground effect tests as well as it does not impose any limitations such as model dependency or exceeding the sensible ranges of the sensor, which is integrated to the MPS, due to increase in load path.

The accuracy of the parametric tests with different delta and reverse delta wings relies on the correct positioning of the wing in the wind tunnel test section. It necessitates correct measurement of the aerodynamic forces, precise assessment of

aerodynamic centers varying with angle of attack and height as well as selection of the optimal area of the wing operating near ground.

During the test campaign, orientation of the model is needed to be altered to simulate different scenarios. These scenarios include testing of different models at different heights measured from the ground plane as well as at different angle of attack values. The schematic representations of the MPS working principle with static and dynamic ground tests are given in Figure 3-7. The ground plane can be simulated with static condition using the tunnel wall or a stationary plane, which is placed beneath the wing by elevating a solid surface. Dynamic ground condition is planned to be simulated using a moving belt mechanism. For all ground scenarios, the height of the model is measured from the trailing-edge of the model. Therefore, the height of the model (distance between trailing-edge and ground plane) should not change for different angle of attack tests for the sake of easiness and speed of conducting the consecutive experiments.

All these requirements are fulfilled with the designed the MPS. It is a mechanical solution where user can change the angle of attack and the height of the model without interrupting the running wind tunnel or reopening the transparent walls to adjust the attitude angles of the model. In addition to requirements defined by the ground effect tests, ergonomics of the overall design was taken into account considering easy access of the operator, who controls the orientation of the model by adjusting the height and angle of attack prior to subsequent tests. The MPS was decided to be placed near the side wall since bottom wall of the wind tunnel is preserved for simulating the ground plane, which can be both at static and dynamic conditions. The isometric view of the global position of the MPS is given in Figure 3-8.

The MPS has sub-components such as height adjustment and sensor assembly adaptors, angle setting disks, an inner adaptor, model positioning rods and a fixed frame to place the overall system at the desired location in the laboratory.

Two adaptors connecting the angle setting disks to the height rods are used for height adjustment in the wind tunnel. Custom interface adaptors had to be designed according to the fastener patterns on the sensor. Therefore, two interface plates as the sensor assembly adaptors are used to mount the sensor rigidly to the ground, which is a fixed surface positioned outside the tunnel and stands on the laboratory ground plane, and to the tooling side adaptor of the sensor which is attached to the aerodynamic load that is to be measured. The angle setting disks are used as mechanical coupling to change the angle of attack at a certain amount. The inner adaptor, which is connected to the mechanical coupling, transmits the change in angle of attack to the sensor assembly adaptors. Finally, model positioning rods connected to the sensor tooling side adaptor transmits the change in angle of attack to the model from the trailing-edge of the model since the rotation axes of the model trailing-edge and inner adaptor are coincident. In addition, model positioning rods are connected to the model with the help of a bracket using fasteners and nuts. The model positioning rod is threaded on each side and fitted in the hole on the bracket. Therefore, built-in yaw angle can be introduced to the model inside the wind tunnel for future research projects.

The MPS can be mounted to the wind tunnel outer walls. However, the MPS was isolated from the wind tunnel walls to prevent vibration of measurement system, which can be affected from the structural vibration of the wind tunnel walls. For that purpose, the MPS is located inside a chassis, which stands on the laboratory floor and adjacent to the side wall. Therefore, the MPS is elevated to the test section of the wind tunnel using this rigid frame. The halfway of the transparent side wall of the wind tunnel is cut to open a slot in which model positioning rods can be move up and down. The procedure is based on performing the subsequent angle of attack runs before changing the height of the model for the dynamic ground condition or vice and versa for the static ground condition tests. This can be illustrated for the dynamic ground condition tests such that user tests the model for different angle of attack values after fixing the desired height from the ground plane. For these runs, the slot is closed using tapes except at the hole where model positioning rod enters

the wind tunnel so that suction of the air from the open slot does not distort the flow field.

The MPS was further improved and modified for the dynamic ground condition tests with the inclusion of height traverse to adjust the height of the model. The modified MPS can be seen in Figure 3-9. For the desired height, the operator positions the MPS at the desired height by rotating the volant wheel on the left side in Figure 3-9. After this procedure, open slot on the sidewall of the wind tunnel is taped and consecutive angle of attack runs are conducted. The procedure is iterated for the next height. The inclusion of the height traverse to the MPS significantly reduced the run time of the dynamic ground condition experiments, since there is no need to remove the fasteners to change the elevation of the MPS first and then tighten the fasteners again. This way the overall system, which include the angle setting disks, interface plates, sensor, struts and wing model, is rigidly installed and mounted to the MPS chassis and can move up and down with the height traverse. The elevation of the static ground board was changed with the static ground system, hence it does not require height traverse feature of the MPS.

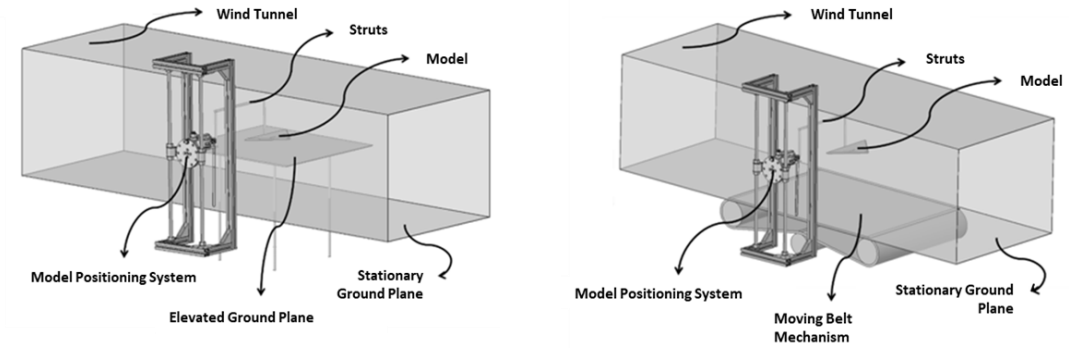

Figure 3-7 Schematic representation of the MPS with static and dynamic ground conditions

Figure 3-8 Isometric view showing the global position of the MPS

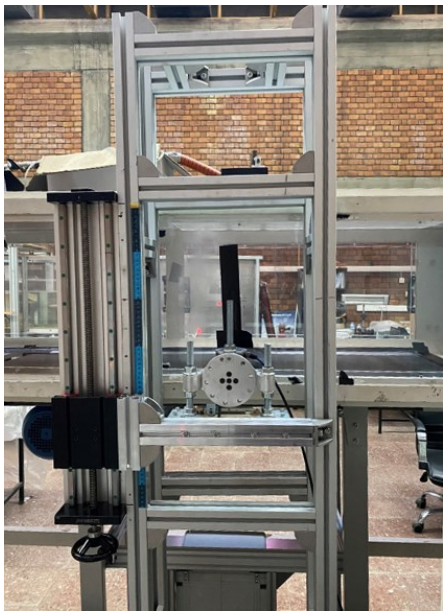

Figure 3-9 Modified MPS with the inclusion of height traverse

3.4 Geometric Angle of Attack Measurement

The angle of attack setting in all tests were performed using a digital inclinometer. Although, the MPS mechanically guarantees the 2-degree increment at successive angle of attack changes, operator controls the actual angle by manually placing a digital inclinometer after each angle of attack adjustments, which are made in order to eliminate the small deviations from the target angle of attack.

After the preliminary tests, an Inertial Measurement Unit (IMU) sensor of 3-Space Sensor™ USB v2.0 was integrated at the upper surface of the sensor ground adaptor to observe the angle of attack value in real-time. The attached sensor can be seen from two different perspectives in Figure 3-10. The IMU sensor was coupled with Matlab® software to digitize spatial data of the sensor. The angular orientation of the wing is the same with the force sensor. Therefore, measuring the orientation of the IMU sensor, which is taped to the upper surface of the sensor, provides the orientation of the wing inside the wind tunnel.

The built-in Matlab® function of "ahrsfilter" was used to obtain the orientation from the accelerometer, gyroscope, and magnetometer readings. This function uses an indirect Kalman filter, which returns the sensor fusion of the accelerometer, gyroscope, and magnetometer data to estimate device orientation and angular velocity. However, only the angle which corresponds to the angle of attack of the wing was used for the visualization of the actual orientation of the sensor. With the inclusion of the IMU sensor, the resolution of the angle of attack is set to 0.01 degree, which was previously 0.1 deg with the digital inclinometer used for the preliminary tests. The sampling rate is set such that operator can easily follow the actual angle on the computer screen without having a major delay penalty.

Figure 3-10 The IMU sensor attached to the sensor ground adaptor plate

3.5 Ground Effect Simulation

In this chapter, ground effect simulation techniques are provided for static and dynamic ground conditions.

3.5.1 Static Ground System

The ground plane can be simulated at the static condition using the tunnel wall (or stationary moving belt at Belt Off Condition) or a stationary plane, which is placed beneath the wing by elevating a surface. The latter one offers higher fidelity ground effect simulation since it is free from wind tunnel wall boundary layer distortion. Although, dynamic ground offers higher fidelity ground effect testing capability, the fidelity difference may vary at different ground effect intensity level, which is proportional to the height of the model. The shape of the model may also deviate this difference. Therefore, static ground tests were evaluated by comparing the results with dynamic ground results to address this issue. For all ground scenarios, the height of the model is measured from the trailing-edge of the model. Therefore, the height of the model (the distance between the trailing-edge and ground plane) do not change

for different angle of attack tests. The MPS and brackets designed for the wing-strut connection mechanically satisfy this requirement, which is broadly discussed in Appendix B.

In Figure 3-11, the schematic representation and isometric view of the elevated ground test rig are given. The wing (1) is positioned on the middle of the static ground plane (2). A plexiglass flat plate serving as the ground plane has dimensions of 540 mm in length, 475 mm in width and 9 mm thickness. The leading-edge of the flat plate is beveled at 26.25^{o}. The ground plane is rigidly connected to the push rods (4) using hinge joints (3) and flange nuts. The wind tunnel floor (5) is drilled at 3 positions at which the push rods can enter the wind tunnel test section. The structural chassis (6), which can move up and down on a 1D traverse mechanism (7), is the main supporting frame to which all the sigma profiles are attached to the system outside the wind tunnel so that any oscillatory motion is damped at the laboratory ground connection (8). The user manually changes the position of the ground plane by rotating the volant wheel of the traverse. Therefore, during the static ground condition tests, the wing is always fixed in height and the angle of attack of the wing is change using the MPS. In Figure 3-12, the top view of the ground elevation system is given, which shows the dimensions and relative positions of the wind tunnel floor (1), elevated ground (2), and wing (3). In Figure 3-13, schematic representations of the top and side views for the force measurement system are given for static ground condition. The static plane is placed such that the midsection of the ground plane in the flow direction is coincident with the mid-chord $(x/c = 0.5)$ of the wing at zero angle of attack condition. At this condition, distances between wing apex and leading-edge of the plexiglass flat plate as well as wing trailing-edge and plate trailing-edge are both 1.5c as detailed in Figure 3-13. The distances between the plate and sidewalls of the wind tunnel were one chord. The OGE test of the wing was conducted with ground plate installed as well as without ground plate (bare wind tunnel test section) configurations to confirm that the blockage associated with the ground plate was negligible. Further details are provided in Appendix B with Figure B - 11 and Figure B - 12.

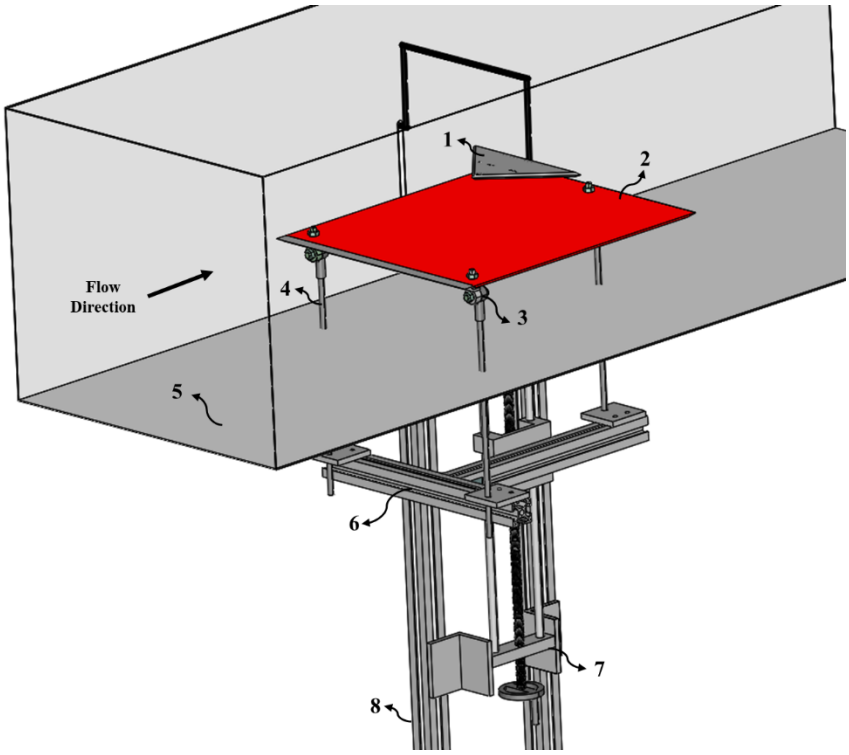

Figure 3-11 The elevated ground test rig, 1) wing, 2) static ground plane, 3) hinge joints, 4) push rods, 5) wind tunnel floor, 6) structural chassis, 7) height adjustment traverse, 8) ground connection

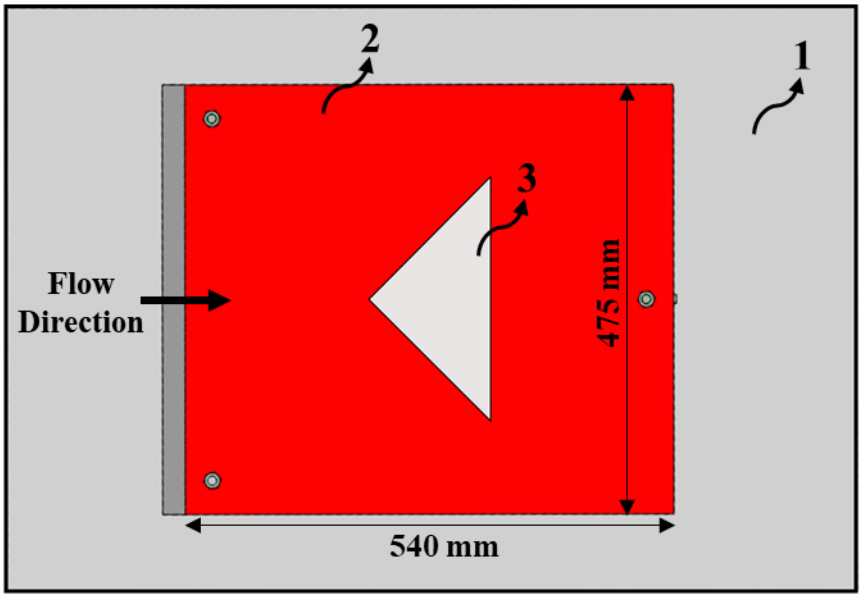

Figure 3-12 Top view of the ground effect test rig with the elevated ground system, 1) wind tunnel bottom floor, 2) static ground plane, 3) wing

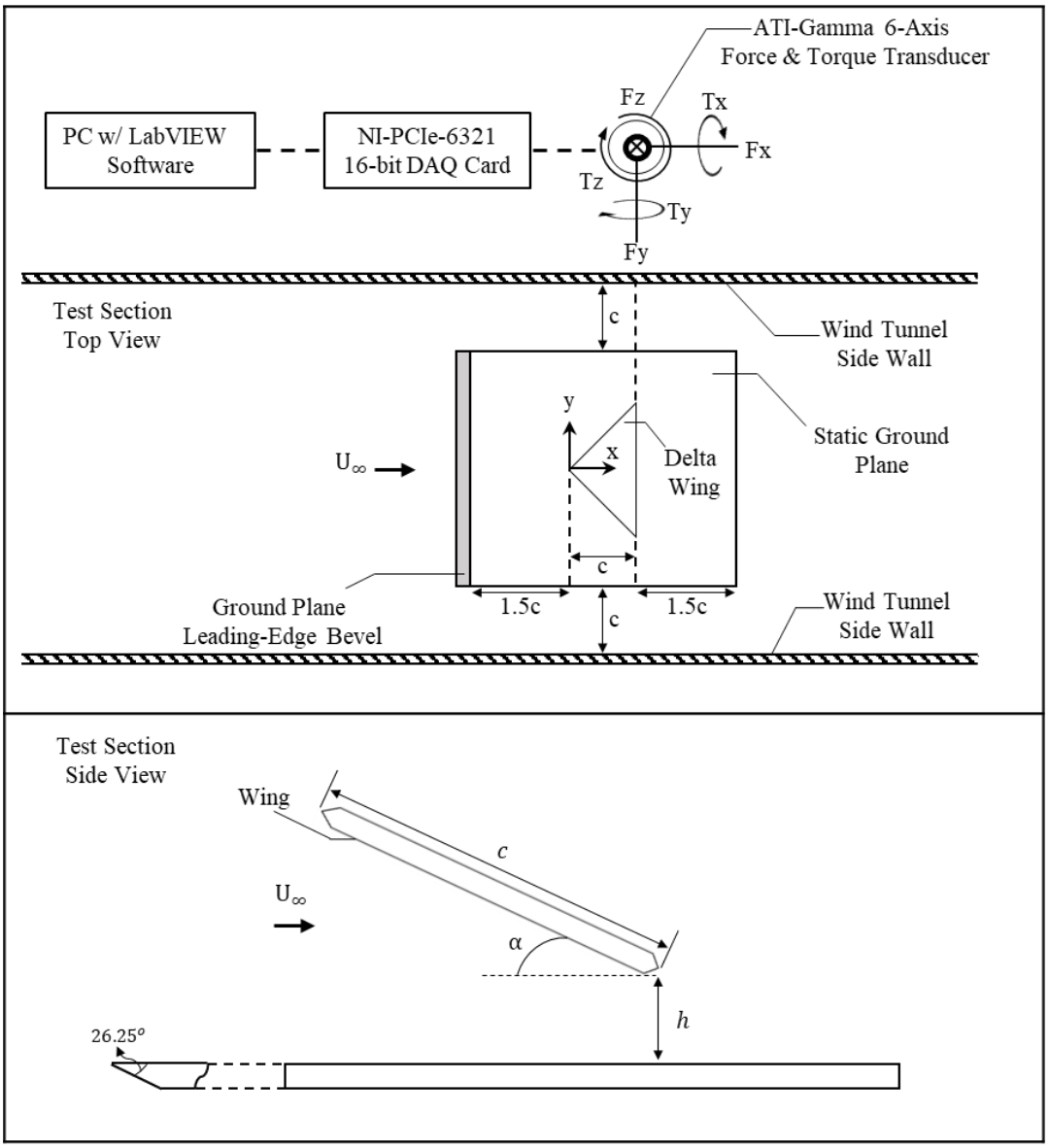

Figure 3-13 Schematic representations of the top and side views for the force measurement set-up with the static ground system

3.5.2 Moving Ground System

The moving ground system was constructed using a moving belt mechanism. For that purpose, a conveyor, and its subcomponents were integrated to the wind tunnel. Operating speed of the tunnel for this study was determined to be 12 m/s at most considering the desired Re number. Therefore, the maximum speed of the conveyor was selected as 12 m/s. In addition, speed of the conveyor is desired to be adjustable by the operator so that tests can also be performed for different operating speeds less than 12 m/s, which eventually results in different Reynolds (Re) numbers.

The moving ground system includes a steel structural chassis with a polyvinyl chloride (PVC) belt having 475 mm width and 1500 mm length. Motor with a reductor is used and speed can be adjusted manually with the electronic control unit of the system. The trigger belt was used for the transmission of power. The legs of the moving belt mechanism were designed such that the height of the belt can be adjusted in a range from 1100 mm to 1400 mm with respect to the laboratory ground plane. Therefore, this mechanism can be used for future projects with different tunnel test sections, which are shorter or higher than the current one.

In Figure 3-14 and Figure 3-15, isometric and top views of the initial design are given. In these figures, some of the important subcomponents are also shown. All these subcomponents are flush to the surface of the tunnel test section bottom floor so that the flow distortions were minimized. The sensitivity studies were conducted to address the issues such as vibration, warming of the belt, and speed control. The vibration of the mechanism and its interference with the tunnel test section, warming of the belt and variation of the belt speed were found to be negligible for all the conducted tests.

The complete ground effect test rig is given in Figure 3-16. The model positioning system for IGE and OGE tests was previously designed and manufactured. It is elevated to the tunnel test section using the model positioning system tower (1). Angle of attack of the wing is altered about the trailing-edge, which is parallel to the

rotation axis of the MPS shown by red dashed line (11), using angle setter disks (2), which are also part of the MPS. The wing (3) is positioned inside the wind tunnel test section (5) and mounted to the strut, which is formed from AISI 321 round tubes (4) with 10 mm diameter. The moving belt (6), which simulates the physically correct boundary condition, is shown inside the dashed lines. The other parts belonging to the moving belt mechanism, such as belt tension roller (7), motor (8), and trigger belt (9) are also shown together with the stationary wind tunnel floor (10).

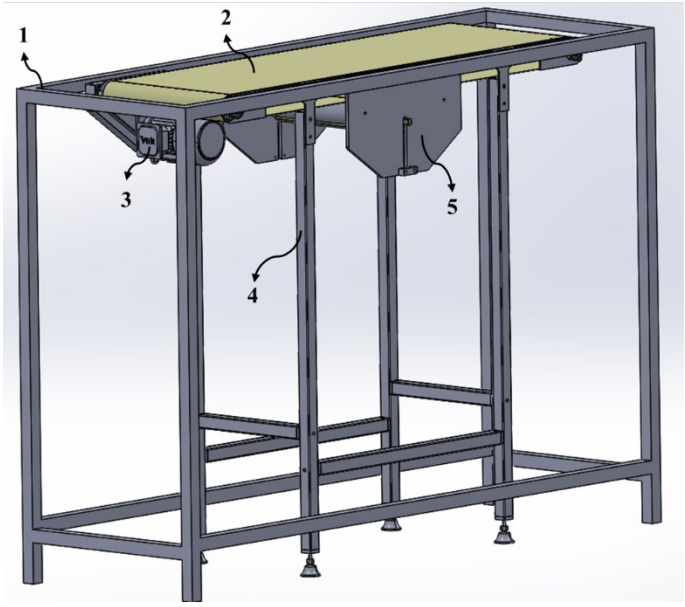

Figure 3-14 Schematic representation of the moving belt mechanism, 1) wind tunnel bottom floor, 2) moving belt, 3) motor, 4) moving ground plane height adjustment legs, 5) belt tension adjustment tool

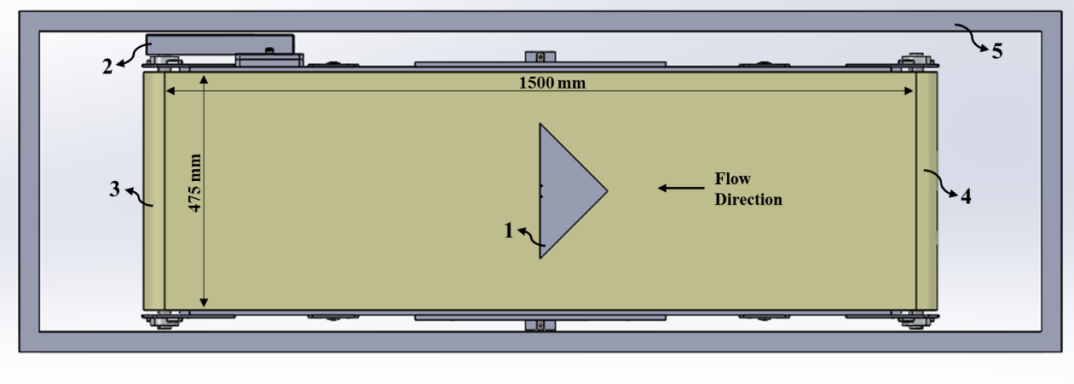

Figure 3-15 Top view of the moving belt mechanism, 1) wing, 2) trigger belt, 3) back roller, 4) front roller, 5) test section boundary

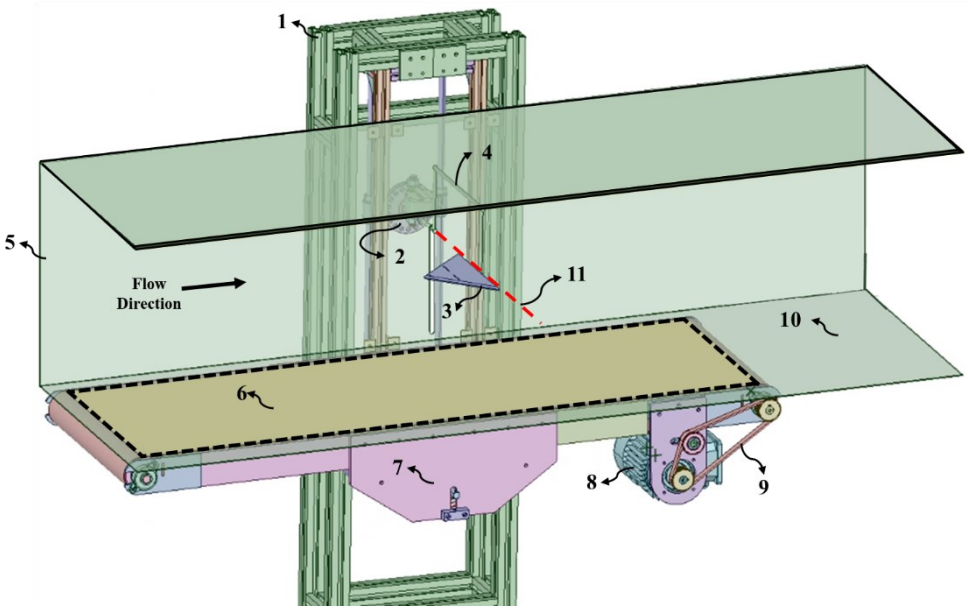

Figure 3-16 The ground effect test rig with moving belt mechanism and model positioning system, 1) model positioning system tower, 2) angle setter disks, 3) wing, 4) struts, 5) wind tunnel test section, 6) moving belt, 7) belt tension roller, 8) motor, 9) trigger belt, 10) wind tunnel floor, 11) rotation axis of angle of attack change

3.5.2.1 Moving Belt Calibration

The calibration of the moving belt mechanism was conducted using a Geevorks contact tachometer. The calibration was conducted to convert control panel reading to the linear belt speed. The belt speed is matched with the freestream speed for the

desired Re number. The calibration curve is given in Figure 3-17. The linear curve fit was performed for the measurements and linear relation with belt speed in m/s and control panel reading in Hz was given in Eqn. 9. The belt speed can be altered with 0.1 Hz increments for the desired condition.

$$\text{Belt Speed} = 0.2692 \cdot \text{Control Panel Reading} + 0.2097 \qquad 9$$

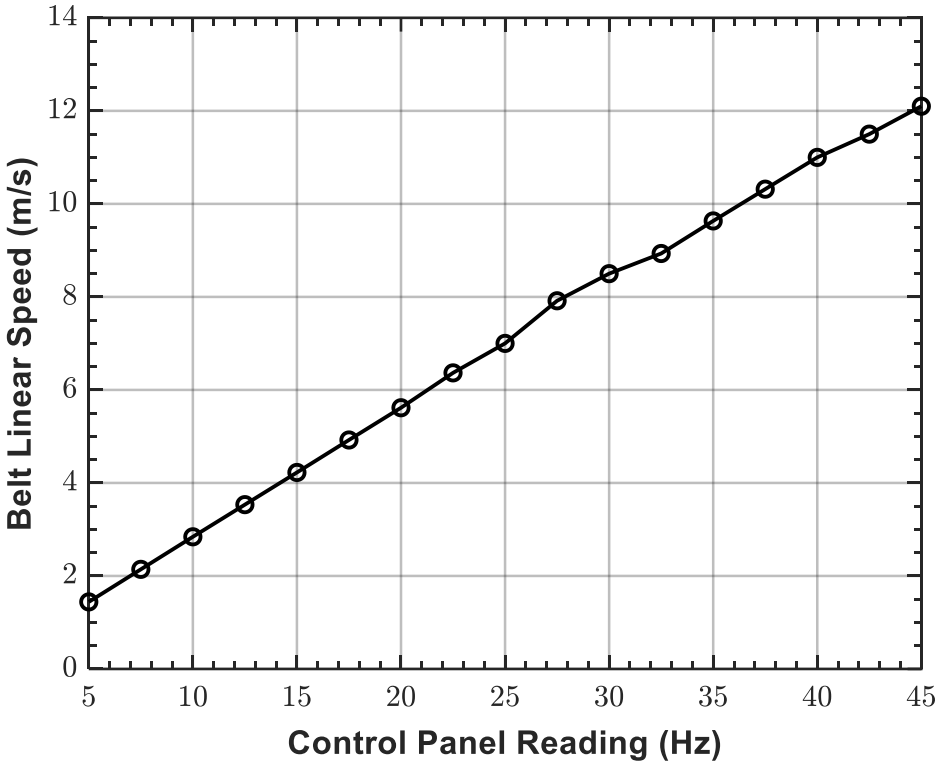

Figure 3-17 Belt calibration curve with respect to control panel reading

3.6 Measurement Techniques

In this chapter, the surface pressure and force measurement techniques, which were adopted for the present study, are detailed.

3.6.1 Surface Pressure Measurement

The surface pressure measurements on both suction and pressure sides of the base thick delta wing were conducted using a 16-channel Netscanner 9116 Intelligent Pressure Scanner, which was equipped with a 16-piezo-resistive transducer with the range of 0-2.5 kPa. The pressure scanner results were validated with respect to manometer readings, although manufacturer provided the pre-calibration results. The scanner had a resolution of $\pm 0.003\%$ FS (full scale) and an accuracy of $\pm 0.05\%$ FS considering the combined errors arising from non-linearity, hysteresis, and non-repeatability. The pressure data were collected at a sampling rate of 500 Hz for 10 seconds. The noise values were acquired before each experiment and subtracted from the actual measurements to obtain refined data. Preliminary tests were carried out to ensure the symmetry along with the spanwise pressure distribution, hence the measurements for only one half of the wing were performed. These tests were also conducted at different ambient conditions to ensure repeatability of the results. Non-dimensional pressure coefficient C_P was calculated using Eqn. 10.

$$C_P = \frac{\bar{p} - p_\infty}{\frac{1}{2}\rho U_\infty^2} = \frac{\bar{p} - p_\infty}{p_{dyn}} \qquad 10$$

The surface pressure measurement IGE for the delta wing 1a at static ground condition along with the pitot-static system is shown in Figure 3-18.

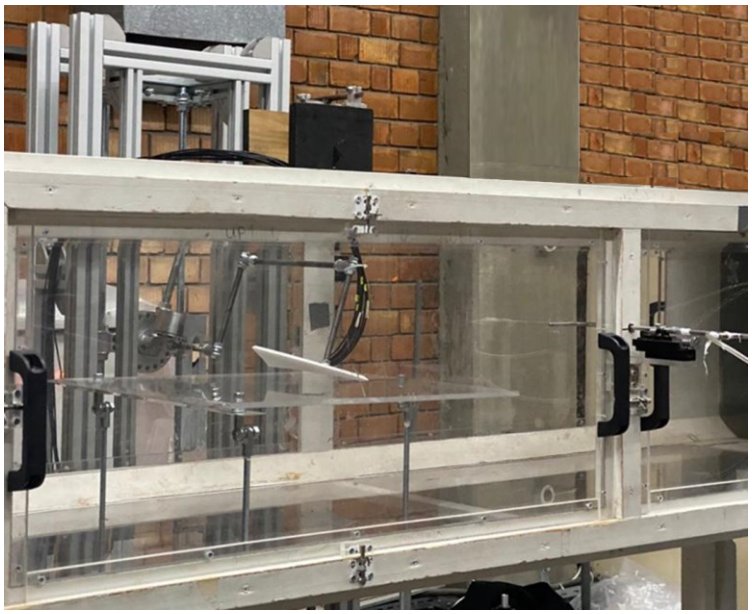

Figure 3-18 The surface pressure measurement IGE for the delta wing 1a at static ground condition

3.6.2 Force Measurement

Aerodynamic forces and moments were measured using an external force balance system. ATI Gamma Series 6-Axis Force and Torque sensor, which was calibrated according to SI-32-2.5 scheme, was installed out of the wind tunnel near the sidewall and attached to the wing with a strut to obtain drag, lift, and pitch moment. In Figure 3-19, schematic representations of the top and side views for the force measurement system are given. The aerodynamic and inertial forces and moments existing over the bare strut were also measured for each angle of attack. These loads were subtracted from the measurements for the wings to exclude the effect of the strut on force and moment measurements. The pitch axis was the trailing-edge or trailing-apex of the wing. The force and moment data were collected for the angles of attack $0 \leq \alpha \leq 35$ degrees. The non-dimensional force and moment coefficients were calculated using Eqn. 11 and 12. For all eight wings, reference area A and reference length L were the surface area and the chord length of the base delta wing 1b and equivalent to 0.0182 m^2 and 0.135 m, respectively. National Instrument NI-PCIe-

6321 16-bit data acquisition (DAQ) card was equipped and coupled to LabVIEW software for digitization of the raw voltage data, which were collected at 10 kHz for 10 seconds for each data point. The preliminary tests were conducted to validate that the blockage associated with the ground plate was negligible and to ensure repeatability of the force measurements at different ambient conditions. The repeatability tests were also repeated with different wing planforms, which were not tested in the scope of this study.

The aerodynamic forces are presented as C_L versus α, C_L/C_D versus α, C_D versus α and drag polar curve C_L versus C_D. The longitudinal stability characteristics are evaluated by utilizing pitch moment data, where the positive moment acts to pitch the wing in the nose-up direction. For that purpose, four different charts are constructed. In the first chart, C_M data is expressed at the trailing-edge and plotted with respect to angle of attack. In the second chart, C_M expressed at trailing-edge is plotted versus C_L. The slope of this curve is equal to the aerodynamic center in pitch X_a, which is the point where pitch moment is independent of angle of attack and expressed as Eqn. 13. It provides the non-dimensional distance of the aerodynamic center of the associated wing from its trailing-edge, which is positive if the aerodynamic center lies between the leading-edge and trailing-edge of the wing and negative if the point lies downstream of the trailing-edge. In the third chart, the pitch moment at the associated wing center of gravity is plotted with respect to angle of attack. The slope of this curve measures the static margin of the wing and must be negative to possess positive longitudinal static stability for OGE condition. For the fourth chart, the non-dimensional center of pressure location, which is the point where C_M is equal to zero and expressed in Eqn. 14, is plotted with respect to angle of attack. It provides the non-dimensional location, normalized by the chord length c or cropped chord length c_{cr} depending on whether the wing is cropped or not, which in turn indicates 0 and 1 limiting values representing the leading-edge and trailing-edge of the corresponding wing. Likewise, ground effect parameters, which are aerodynamic center in height X_h, and H.S. are also expressed in Eqn. 15 and Eqn. 16.

$$C_D, C_L = \frac{F_D,\ F_L}{\frac{1}{2}\rho U_\infty^2 A} \quad (11)$$

$$C_M = \frac{M_y}{\frac{1}{2}\rho U_\infty^2 A\, L} \quad (12)$$

$$X_a = \left(\frac{\partial C_M}{\partial C_L}\right)\Big|_\alpha \quad (13)$$

$$X_P = X|_{C_M=0} \quad (14)$$

$$X_h = \left(\frac{\partial C_M}{\partial C_L}\right)\Big|_h \quad (15)$$

$$H.S. = X_a - X_h \quad (16)$$

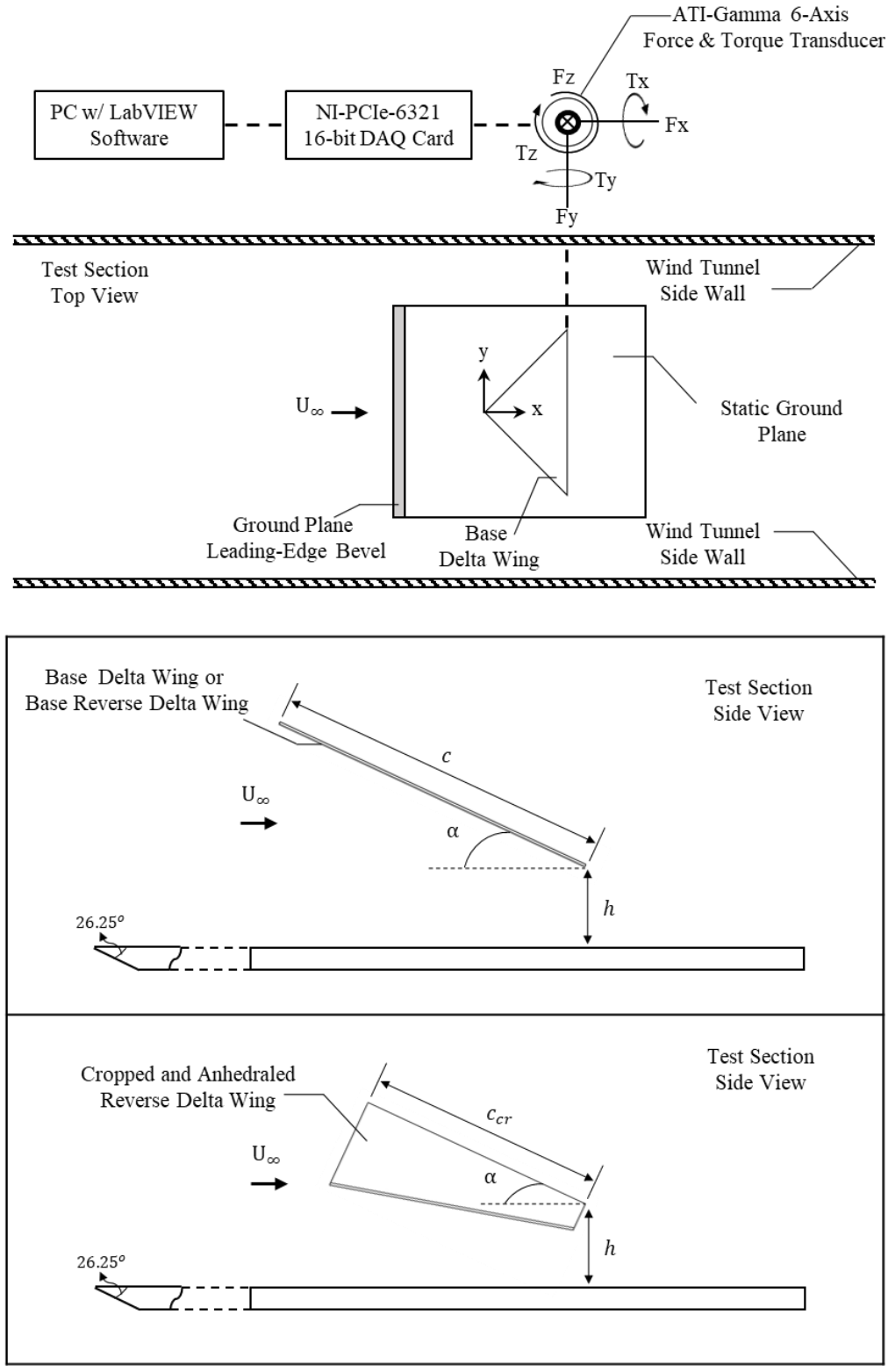

Figure 3-19 Schematic representations of the top and side views for the force measurement set-up

3.6.2.1 The DAQ card

Prior to the force measurements, a new DAQ card, which is NI PCIe-6321, X Series DAQ card from National Instruments, was acquired first and used for the digitization of the raw data, although the facility already had NI PCI-6024E-16 channel 12-bit DAQ card. Some of the important features of the old and new DAQ cards are summarized in Table 3-2. Both of these DAQ cards are compatible with the Labview® software. Considering the force and moment measurements, the former one introduces noticeable resolution improvement (16 times better), although the accuracy windows are the same for both cards. The overall performance of the force measurement unit in terms of sensible range, resolution and measurement uncertainty are summarized in Table 3-3. Therefore, the values given in Table 3-3 is valid for all the results reported in this study.

Table 3-2 The comparison of the technical features of the DAQ cards installed in the laboratory

	Description	Bus Type	Front Connector	Life Cycle Status	Input - Output
NI PCI-6024E	Multifunction I/O Device	PCI	SCSI-II type	Obsolete	16 AI[1] (12-bit, 200 kS/s), 2 AO[2], 8 DIO[3]
NI PCIe-6321	Multifunction I/O Device	PCI Express	VHDCI type	Active	16 AI (16-bit, 250 kS/s), 2 AO (900 kS/s), 24 DIO

[1] Analog Input
[2] Analog Output
[3] Digital Input-Output

Table 3-3 Sensible range, resolution and measurement uncertainty values of the Gamma transducer with 16-bit NI PCIe-6321 DAQ card

	Fx (N)	Fy (N)	Fz (N)	Tx (N-m)	Ty (N-m)	Tz (N-m)
Range	±32	±32	±100	±2.5	±2.5	±2.5
Resolution	0.0063	0.0063	0.0125	0.0005	0.0005	0.0005
Uncertainty	0.2400	0.2400	0.7500	0.0250	0.0310	0.0370

3.6.2.2 Methodology for Force Measurements

For all tests, there are 4 different measurements at each angle of attack values to obtain the aerodynamic loads generated by the wing. These tests are classified according to the measured loads in Table 3-4 with respect to the configuration, which is mounted to the MPS, and the wind tunnel status, which is “on” when the tunnel operates at the related Re number and “off” when the tunnel does not operate. The first two tests are the measurements of inertial and combined inertial and aerodynamic forces and moments when both wing and strut mounted during the tunnel statues are both off and on. The other two tests are the measurements of inertial and combined inertial and aerodynamic forces and moments when only the strut is mounted during the tunnel statue are both off and on. By subtracting these four different tests from each other, the necessary taring is made and results in the aerodynamic forces and moments generated by the wing only case can be found.

Table 3-4 The measured loads according to the configuration and wind tunnel status

ID	Configuration	Wind Tunnel Status	Measured Forces and Moments
1	Wing + Strut	Off	Wing Inertial Strut Inertial
2	Wing + Strut	On	Wing (Inertial + Aerodynamics) Strut (Inertial + Aerodynamics)
3	Strut	Off	Strut Inertial
4	Strut	On	Strut (Inertial + Aerodynamics)

The subtraction operations of different tests and measured loads after these operations are given below. Since the exact weight of the wing is known, the results in B can also be generated without actually conducting the tests Test ID 1 and Test ID 3.

A = Test ID 2 – Test ID 4 = Wing (Inertial + Aerodynamics)

B = Test ID 1 – Test ID 3 = Wing Inertial

C = A-B = Wing Aerodynamics

The configurations are also detailed in Appendix B with Figure B - 13.

3.6.2.3 Axis Frames

The coordinate frames are provided in this chapter. These axis frames are wind and body frames. The wind frame, which is shown in Figure 3-20, is stationary and does not vary with angle of attack changes whereas the body frame is positioned on the sensor and rotating with the sensor when the angle of attack is altered. The loads on all 6 channels are measured on the sensor in the body frame. The body (red) and wind frame (magenta) axes are also shown in Figure 3-21 at a certain angle of attack

value. Both frames follow the right-hand rule. Therefore, the y axis for body frame is not shown for the sake of visualization. Respective angle of attack (α) between these axis frames is the angle between the yellow lines. In addition, nature of the model positioning system (MPS) and sensor rotation around wind frame y axis yield that the resolution of the force measurement in the wind frame z axis improves as the angle of attack increases. This is because sensor resolution of the measured forces in the x and y axis of body frame is twice better than the z axis as provided in Table 3-3.

Measured loads can be transformed into the wind frame and translated to any point inside the wind tunnel. Since the measured forces do not carry any location information, the appropriate translation of the forces in wind frame enables finding the moment coefficients on the wing surface. By doing so, the pressure center and the aerodynamic centers in pitch and height can be found and the stability assessment in longitudinal axis can be made.

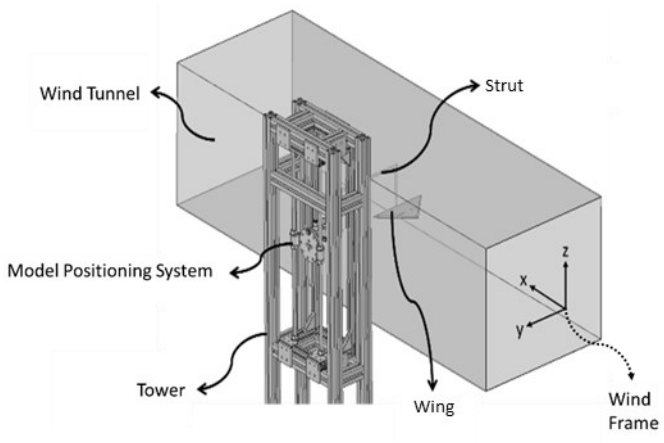

Figure 3-20 Test ring and wind frame

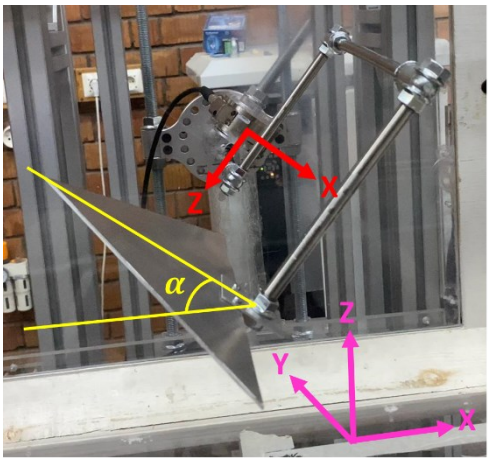

Figure 3-21 Body frame (red), wind frame (magenta), and angle of attack (yellow)

The necessary transformation from body frame to wind frame is conducted using the following formulas, where subscripts b and w denote the body and wind frame;

$$F_{x,w} = +\left(F_{x,b} \cdot \cos(\alpha) - F_{z,b} \sin(\alpha) \right)$$

$$F_{y,w} = -\left(F_{y,b} \right)$$

$$F_{z,w} = -\left(F_{x,b} \cdot \sin(\alpha) + F_{z,b} \cos(\alpha) \right)$$

$$M_{x,w} = +\left(M_{x,b} \cdot \cos(\alpha) - M_{z,b} \sin(\alpha) \right)$$

$$M_{y,w} = -\left(M_{y,b} \right)$$

$$M_{z,w} = -\left(M_{x,b} \cdot \sin(\alpha) + M_{z,b} \cos(\alpha) \right)$$

In the above formulas, $F_{x,w}$, $F_{y,w}$ and $F_{z,w}$ are the wind frame drag, side and lift forces whereas $M_{x,w}$, $M_{y,w}$ and $M_{z,w}$ are the wind frame roll, pitch and yaw moments, respectively.

3.6.2.4 Alignment, Weight and Geometric Data

Prior to tests, alignment was conducted by using the wing-strut configuration since the strut configuration does not offer a measurement surface inside the wind tunnel.

Therefore, angle of attack can be measured inside the wind tunnel using wing-strut configuration thanks to the available wing surface. The wing-strut configuration was positioned at zero angle of attack value and model was disassembled from the wing-strut to obtain the strut configuration at zero angle of attack.

The tower shown in Figure 3-20 is positioned parallel to the wind tunnel walls to align the whole setup in yaw axis. In addition, an extra degree of freedom is available inside the wind tunnel. The user uses two flange nuts for mounting the model bracket to the model positioning rod. Without locking these nuts, the bracket can freely rotate around the free end of the vertical rod, on which the model is mounted. Therefore, any built-in yaw angle can be introduced.

The mass values of the subcomponents mounted on the sensor are measured and provided in Table 3-5. The measured values are used in order to control the alignment indirectly using Test ID 1 and Test ID 3. In other words, Fz value at zero angle of attack at tunnel off status should be equal to the total weights for the wing-strut and strut for the Test ID 1 and Test ID 3. In addition, the Fz value at tunnel off status should be the same for the angle of attack values if their absolute values are the same. The maximum values of Fz and Mx should be at zero angle of attack value because the maximum force along gravity vector is read at this configuration.

Table 3-5 Mass values

	Mass (gr)
Model	83
Tooling	572
Sensor tooling side adaptor	71
Sensor	255
Total	981

The distances between the geometric centroid of the sensor and the mid plane of the bracket nuts as well as height of the mid plane of the bracket nuts were measured.

These distances are provided in Table 3-6 and shown in Figure 3-22. At zero angle of attack value, the difference in measured Mx between Test ID 1 and Test ID 3 is the moment due to the weight of the model. Therefore, dividing the difference in measured Mx into dy value has to be equivalent to the weight of the model. In this manner, the yaw angle of the model with respect to sensor can be controlled because any misalignment in the yaw angle results in a different moment value due to difference in the distance from center of mass of the model to the sensor in the y direction.

Table 3-6 The distances between the sensor centroid and midplane of the bracket nuts for a sample alignment test

Distances (mm)			
dx	dy	dz	h
0	471	29	230

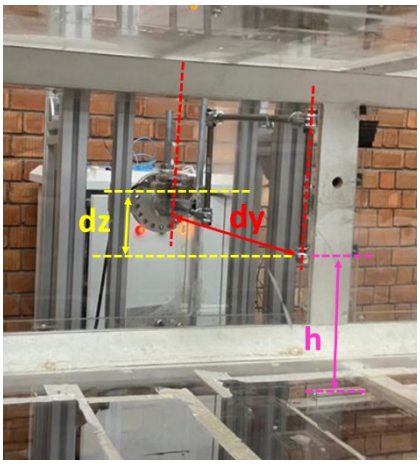

Figure 3-22 The measured distances for a sample alignment test

3.6.2.5 Wind Frame Moments, Pressure Center in Longitudinal Axis, and Aerodynamic Center in Pitch and Aerodynamic Center in Height

An external balance adopted for load measurements is positioned near the side wall. Therefore, moment values can be obtained by translating the forces and summing them with the measured moments on the sensor. Once the body frame to wind frame conversion is conducted, moments in the wind frame at any location apart from the sensor can be found according to equations given below;

$$M_{x,w} = +F_{y,w} \cdot dz - F_{z,w} \cdot dy + M_{x,w_{sensor}}$$

$$M_{y,w} = -F_{x,w} \cdot dz + F_{z,w} \cdot dx + M_{y,w_{sensor}}$$

$$M_{z,w} = +F_{x,w} \cdot dy - F_{y,w} \cdot dx + M_{z,w_{sensor}}$$

The distances in all three directions (dx, dy, dz) are defined according to the wind frame locations of the arbitrary point and sensor.

$$dx = x_{point} - x_{sensor}$$

$$dy = y_{point} - y_{sensor}$$

$$dz = z_{point} - z_{sensor}$$

If the sensor global position inside the laboratory is selected as the origin ($x_{sensor} = 0, y_{sensor} = 0, z_{sensor} = 0$);

- dx is positive if the point is apart from the sensor in drag direction
- dy is positive if the point is on the starboard side of the sensor when viewed from the wind tunnel fan location
- dz is positive if the point is above the sensor when viewed from sidewalls of the tunnel

The pressure center in longitudinal axis (X_p, where $M_{y,w} = 0$) can be found using following relation:

$$X_p = \frac{\left(-\left(M_{y,w}\right)_{sensor} + F_{x,w} \cdot dz\right)}{F_{z,w}}$$

The aerodynamic center in pitch (X_a) is defined in the linear region of the aerodynamic lift force and pitch moment coefficients. It is found by diving the slope of the pitch moment curve slope to the lift curve slope. Therefore, it is a normalized quantity and the chord length is used for normalization. The location is measured from the apex of the wing, where 1 is equal to the leading-edge of the wing and 0 is equal to the trailing-edge of the wing.

$$X_a = 1 - \frac{C_{M,\alpha}}{C_{L,\alpha}}$$

Aerodynamic center in pitch can be easily found using the formula method. However, it is hard to find slope of the C_M versus height and C_L versus height curves since the aerodynamic behavior is highly nonlinear. In order to minimize the slope reading errors and generalize the calculation of the stability derivatives X_a and X_h, definitions of these points are used. For that purpose, longitudinal axis is discretized with the calculated C_M value at all the points from trailing-edge to leading-edge at a given height, and this procedure is repeated at each angle of attack. With this method, the aerodynamic center in pitch can be found, figuratively. The curves intersect each other at X_a considering the C_M versus x/c plot. Likewise, the aerodynamic center in height can be found by calculating the C_M value at all the points from trailing-edge to leading-edge at a given angle of attack, the procedure is repeated for each height. This procedure is illustrated for the results of the delta wing 1b in Figure 3-23 and Figure 3-24, where X_a and X_h are shown on these figures at the intersection points of these curves at OGE condition and $\alpha = -6^o$. Intersection points are calculated in the post-process code by finding the minimum value of the standard deviation of the values of these curves. The discretization of the apex and trailing-edge is made with 1000 nodes such that the nodal increment is 0.001, which is equal to 0.135 mm.

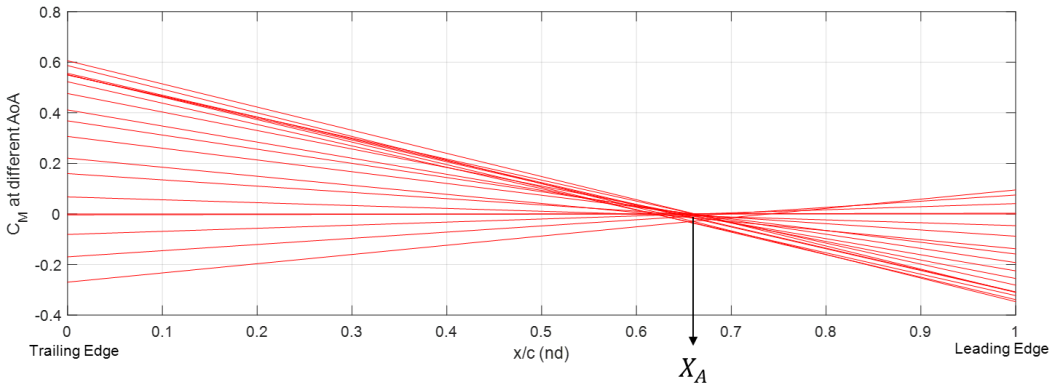

Figure 3-23 The delta wing 1b C_M data at all coordinates from trailing-edge to apex on the wing for all angle of attack values at OGE condition

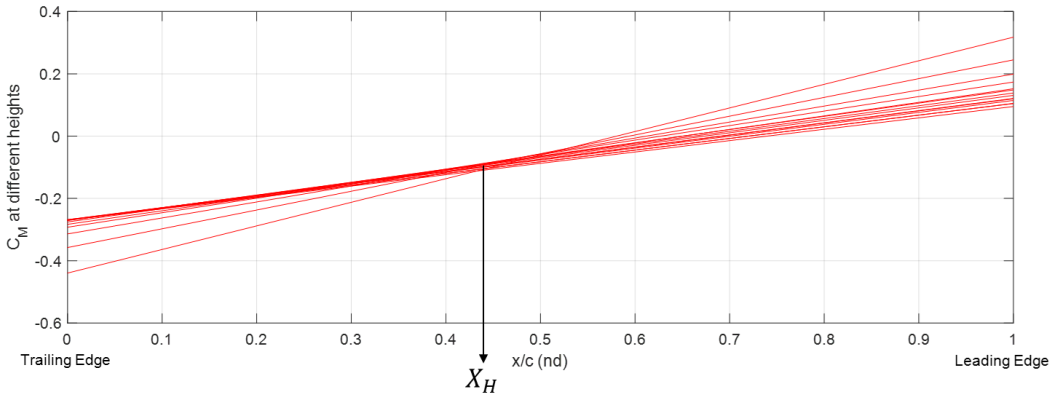

Figure 3-24 The delta wing 1b C_M data at all coordinates from trailing-edge to apex on the wing for all height values at $\alpha = -6^o$

3.6.2.6 Wind Frame Coefficients

The aerodynamic coefficients are found with the measured aerodynamic forces (drag, side, and lift) and moments (roll, pitch, and yaw) using the following formulas where ρ is the air density, V_∞ is the free-stream velocity, A is the characteristic area, L is the characteristic length, S is the wingspan and c is the chord length.

$$C_D = \frac{F_{x,w}}{\frac{1}{2}\cdot\rho\cdot V_\infty^2\cdot A},\ C_Y = \frac{F_{y,w}}{\frac{1}{2}\cdot\rho\cdot V_\infty^2\cdot A},\ C_L = \frac{F_{z,w}}{\frac{1}{2}\cdot\rho\cdot V_\infty^2\cdot A}$$

$$C_R = \frac{M_{x,w}}{\frac{1}{2}\cdot\rho\cdot V_\infty^2\cdot A\cdot L},\ C_M = \frac{M_{y,w}}{\frac{1}{2}\cdot\rho\cdot V_\infty^2\cdot A\cdot L},\ C_N = \frac{M_{z,w}}{\frac{1}{2}\cdot\rho\cdot V_\infty^2\cdot A\cdot L}$$

$$A = \frac{1}{2} \cdot S \cdot c$$

$$L = c$$

$$\text{Dynamic Pressure} = \frac{1}{2} \cdot \rho \cdot V_{\infty}^{2}$$

3.6.2.7 Testing Methodology

Initially, wing-strut configuration was tested since it was easier to align this configuration due to the available wing suction side surface for angle measurements in the roll and pitch axes. The strut configuration tests were conducted after the wing-strut configuration tests. All of the tests were conducted in an angle of attack range from a negative angle (usually between -6 to -2 degree) to a positive angle (around +35 degree) with +2-degree increments. For each test points, steady state data were collected for 10 seconds. Once the wind tunnel and moving belt were switched on, 5 minutes were waited in order to make sure that the overall system and the flow field have reached the steady state condition.

3.7 Experimental Matrix

The present study consists of both the static and dynamic ground conditions, which are characterized by force and pressure measurements at various heights, which are discretized at both OGE and IGE conditions, as well as angles of attack. The thick delta wing 1a is particularly examined with pressure measurements to characterize this wing at both IGE and OGE conditions and their effect on vortical flow field around suction (leeward) and pressure (windward) sides. The dynamic ground condition is only investigated with the thick delta wing 1a and the reverse delta wing 2e. Further characterization of ground boundary condition on both OGE and IGE performance and longitudinal axis dynamics is examined with static versus dynamic ground conditions as well as the effect of belt status on aerodynamic forces and

moments of the delta wing 1a and the reverse delta wing 2e. Experimental matrix is given in Figure 3-25.

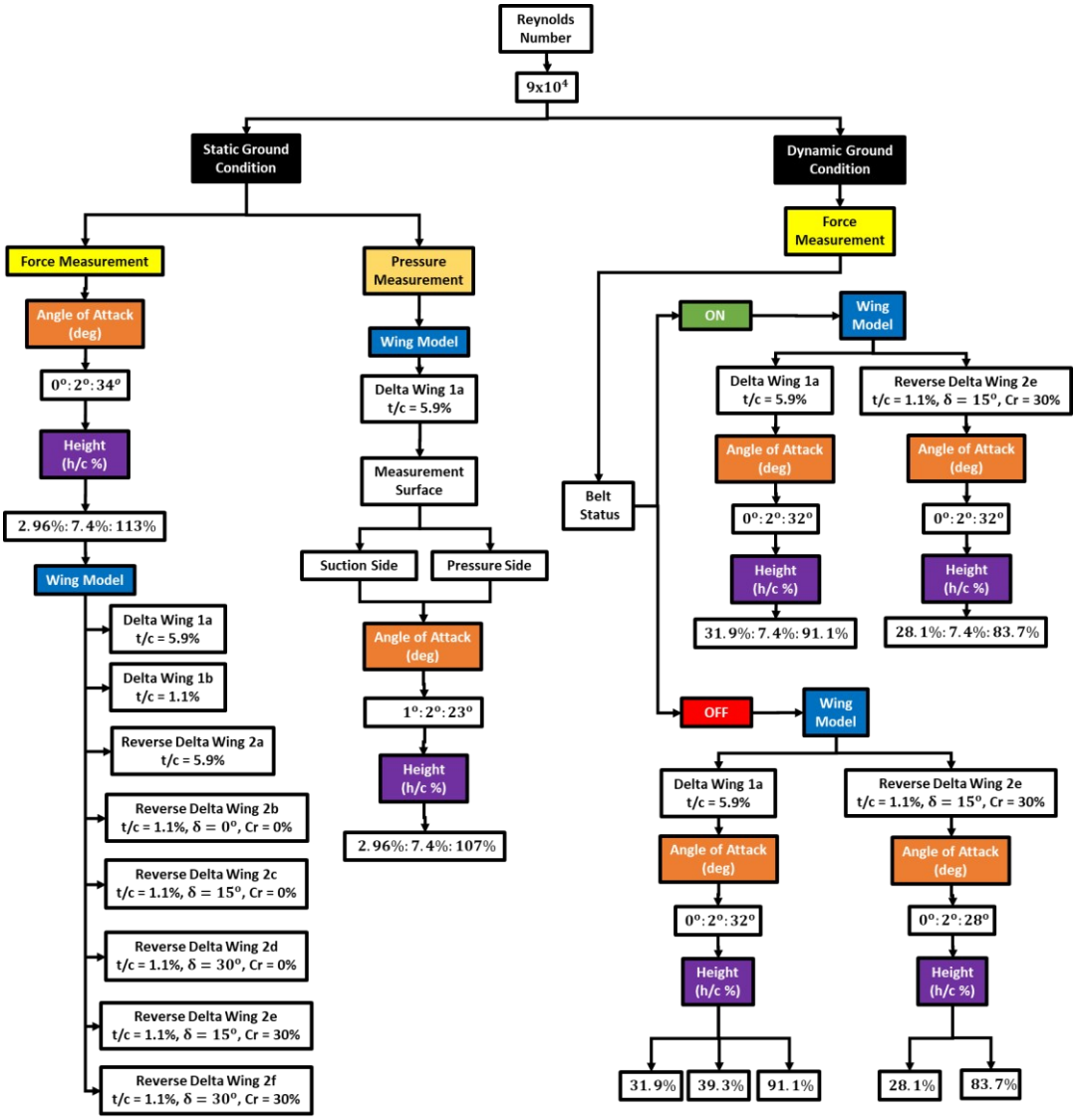

Figure 3-25 Experimental Matrix

3.8 Uncertainty Estimates

Experimental uncertainties inherently exist for any kind of experimental data arising either from the experimental system or physical phenomenon and its random nature. The uncertainties associated with measured quantities are addressed in this chapter.

The calculation of the best estimate uncertainty of a result R, which is a function of n number of measured variables is given by Eqn. 17 by Wheeler and Ganji [105].

$$\omega_R = \left[\left(\omega_{x_1}\frac{\partial R}{\partial x_1}\right)^2 + \left(\omega_{x_2}\frac{\partial R}{\partial x_2}\right)^2 + \cdots + \left(\omega_{x_n}\frac{\partial R}{\partial x_n}\right)^2\right]^{1/2} \quad 17$$

In Eqn. 17, ω_{x_i} stands for the uncertainty estimate of each measured variable. Likewise, the relative uncertainty of each result or measured variable is found using Eqn. 18.

$$u_R = \frac{\omega_R}{R} \quad 18$$

The relative uncertainty values of each results for force and pressure measurements are given as follows.

Forces and moments: Measured with load cell

P: Dynamic pressure, measured with pitot-static system

A: Area is measured by ruler

α: Angle of attack, measured by IMU

The relative and absolute uncertainty calculations for force and pressure coefficients are provided in chapters from 3.8.1.1.1 to 3.8.1.1.5 and shown with equations from 19 to 33.

3.8.1.1.1 Lift coefficient uncertainty calculation

$$C_L = \frac{L}{P_{dyn} A}$$

$$C_L = \frac{-(F_x \sin(\alpha) + Fz \cos(\alpha))}{P_{dyn} A}$$

$$C_L = C_L(F_x, F_z, \alpha, P_{dyn}, A)$$

$$u_{C_L} = \pm \left[\left(\frac{F_x}{C_L} \frac{\partial C_L}{\partial F_x} u_{F_x} \right)^2 + \left(\frac{F_z}{C_L} \frac{\partial C_L}{\partial F_z} u_{F_z} \right)^2 + \left(\frac{\alpha}{C_L} \frac{\partial C_L}{\partial \alpha} u_\alpha \right)^2 + \left(\frac{P_{dyn}}{C_L} \frac{\partial C_L}{\partial P_{dyn}} u_{P_{dyn}} \right)^2 + \left(\frac{A}{C_L} \frac{\partial C_L}{\partial A} u_A \right)^2 \right]^{1/2} \quad (19)$$

$$u_{C_L} = \pm \left[\left(\frac{F_x}{C_L} \left(-\frac{\sin(\alpha)}{P_{dyn}\, A} \right) u_{F_x} \right)^2 + \left(\frac{F_z}{C_L} \left(-\frac{\cos(\alpha)}{P_{dyn}\, A} \right) u_{F_z} \right)^2 + \left(\frac{\alpha}{C_L} \left(-\frac{F_x \cos(\alpha) - F_z \sin(\alpha)}{P_{dyn}\, A} \right) u_\alpha \right)^2 + \left(\frac{P_{dyn}}{C_L} \left(\frac{F_z \cos(\alpha) + F_x \sin(\alpha)}{(P_{dyn})^2\, A} \right) u_{P_{dyn}} \right)^2 + \left(\frac{A}{C_L} \left(\frac{F_z \cos(\alpha) + F_x \sin(\alpha)}{P_{dyn}\, A^2} \right) u_A \right)^2 \right]^{1/2} \quad (20)$$

$$\omega_{C_L} = \pm\left[\left(\omega_{F_x}\left(-\frac{\sin(\alpha)}{P_{dyn}\,A}\right)\right)^2 + \left(\omega_{F_z}\left(-\frac{\cos(\alpha)}{P_{dyn}\,A}\right)\right)^2 + \left(\omega_{\alpha}\left(-\frac{F_x\cos(\alpha) - F_z\sin(\alpha)}{P_{dyn}\,A}\right)\right)^2 + \left(\omega_{P_{dyn}}\left(\frac{F_z\cos(\alpha) + F_x\sin(\alpha)}{(P_{dyn})^2\,A}\right)\right)^2 + \left(\omega_{A}\left(\frac{F_z\cos(\alpha) + F_x\sin(\alpha)}{P_{dyn}\,A^2}\right)\right)^2\right]^{1/2} \quad (21)$$

3.8.1.1.2 Drag coefficient uncertainty calculation

$$C_D = \frac{D}{P_{dyn}A}$$

$$C_D = \frac{(F_x\cos(\alpha) - Fz\sin(\alpha))}{P_{dyn}A}$$

$$C_D = C_D(F_x, F_z, \alpha, P_{dyn}, A)$$

$$u_{C_D} = \pm\left[\left(\frac{F_x}{C_D}\frac{\partial C_D}{\partial F_x}u_{F_x}\right)^2 + \left(\frac{F_z}{C_D}\frac{\partial C_D}{\partial F_z}u_{F_z}\right)^2 + \left(\frac{\alpha}{C_D}\frac{\partial C_D}{\partial \alpha}u_{\alpha}\right)^2 + \left(\frac{P_{dyn}}{C_D}\frac{\partial C_D}{\partial P_{dyn}}u_{P_{dyn}}\right)^2 + \left(\frac{A}{C_D}\frac{\partial C_D}{\partial A}u_A\right)^2\right]^{1/2} \quad (22)$$

$$u_{C_D} = \pm\left[\left(\frac{F_x}{C_D}\left(\frac{\cos(\alpha)}{P_{dyn}\,A}\right)u_{F_x}\right)^2 + \left(\frac{F_z}{C_D}\left(-\frac{\sin(\alpha)}{P_{dyn}\,A}\right)u_{F_z}\right)^2 + \left(\frac{\alpha}{C_D}\left(-\frac{F_x\sin(\alpha)+F_z\cos(\alpha)}{P_{dyn}\,A}\right)u_{\alpha}\right)^2 + \left(\frac{P_{dyn}}{C_D}\left(-\frac{F_x\cos(\alpha)-F_z\sin(\alpha)}{(P_{dyn})^2\,A}\right)u_{P_{dyn}}\right)^2 + \left(\frac{A}{C_D}\left(-\frac{F_x\cos(\alpha)-F_z\sin(\alpha)}{P_{dyn}\,A^2}\right)u_A\right)^2\right]^{1/2} \quad (23)$$

$$\omega_{C_D} = \pm\left[\left(\omega_{F_x}\left(\frac{\cos(\alpha)}{P_{dyn}\,A}\right)\right)^2 + \left(\omega_{F_z}\left(-\frac{\sin(\alpha)}{P_{dyn}\,A}\right)\right)^2 + \left(\omega_{\alpha}\left(-\frac{F_x\sin(\alpha)+F_z\cos(\alpha)}{P_{dyn}\,A}\right)\right)^2 + \left(\omega_{P_{dyn}}\left(-\frac{F_x\cos(\alpha)-F_z\sin(\alpha)}{(P_{dyn})^2\,A}\right)\right)^2 + \left(\omega_A\left(-\frac{F_x\cos(\alpha)-F_z\sin(\alpha)}{P_{dyn}\,A^2}\right)\right)^2\right]^{1/2} \quad (24)$$

3.8.1.1.3 Lift-to-drag ratio uncertainty calculation

$$C_L/C_D = \frac{L}{D}$$

$$C_L/C_D = \frac{-(F_x \sin(\alpha) + Fz\cos(\alpha))}{(F_x \cos(\alpha) - Fz\sin(\alpha))}$$

$$u_{C_L/C_D} = \pm\left[\left(\frac{F_x}{C_L/C_D}\frac{\partial C_L/C_D}{\partial F_x}u_{F_x}\right)^2 + \left(\frac{F_z}{C_L/C_D}\frac{\partial C_L/C_D}{\partial F_z}u_{F_z}\right)^2 + \left(\frac{\alpha}{C_L/C_D}\frac{\partial C_L/C_D}{\partial \alpha}u_\alpha\right)^2\right]^{1/2} \quad (25)$$

$$u_{C_L/C_D} = \pm\left[\left(\frac{F_x}{C_L/C_D}\left(\frac{F_z}{(F_x\cos(\alpha) - Fz\sin(\alpha))^2}\right)u_{F_x}\right)^2 + \left(\frac{F_z}{C_L/C_D}\left(-\frac{F_x}{(F_x\cos(\alpha) - Fz\sin(\alpha))^2}\right)u_{F_z}\right)^2 + \left(\frac{\alpha}{C_L/C_D}\left(-\frac{F_x^2 + F_z^2}{(F_x\cos(\alpha) - Fz\sin(\alpha))^2}\right)u_\alpha\right)^2\right]^{1/2} \quad (26)$$

$$\omega_{C_L/C_D} = \pm\left[\left(\omega_{F_x}\left(\frac{F_z}{(F_x\cos(\alpha) - Fz\sin(\alpha))^2}\right)\right)^2 + \left(\omega_{F_z}\left(-\frac{F_x}{(F_x\cos(\alpha) - Fz\sin(\alpha))^2}\right)\right)^2 + \left(\omega_\alpha\left(-\frac{F_x^2 + F_z^2}{(F_x\cos(\alpha) - Fz\sin(\alpha))^2}\right)\right)^2\right]^{1/2} \quad (27)$$

3.8.1.1.4 Pitch moment coefficient uncertainty calculation

$$C_M = \frac{M_y}{P_{dyn} A\, L}$$

$$C_M = C_M(M_y, P_{dyn}, A, L)$$

$$u_{C_M} = \pm \left[\left(\frac{M_y}{C_M} \frac{\partial C_M}{\partial M_y} u_{M_y} \right)^2 + \left(\frac{P_{dyn}}{C_M} \frac{\partial C_M}{\partial P_{dyn}} u_{P_{dyn}} \right)^2 + \left(\frac{A}{C_M} \frac{\partial C_M}{\partial A} u_A \right)^2 + \left(\frac{L}{C_M} \frac{\partial C_M}{\partial L} u_L \right)^2 \right]^{1/2} \quad (28)$$

$$u_{C_M} = \pm \left[\left(\frac{M_y}{C_M} \left(\frac{1}{P_{dyn}\, A\, L} \right) u_{M_y} \right)^2 + \left(\frac{P_{dyn}}{C_M} \left(-\frac{M_y}{P_{dyn}^2\, A\, L} \right) u_{P_{dyn}} \right)^2 + \left(\frac{A}{C_M} \left(-\frac{M_y}{P_{dyn}\, A^2\, L} \right) u_A \right)^2 + \left(\frac{L}{C_M} \left(-\frac{M_y}{P_{dyn}\, A\, L^2} \right) u_L \right)^2 \right]^{1/2} \quad (29)$$

$$\omega_{C_M} = \pm \left[\left(\omega_{M_y} \left(\frac{1}{P_{dyn}\, A\, L} \right) \right)^2 + \left(\omega_{P_{dyn}} \left(-\frac{M_y}{P_{dyn}^2\, A\, L} \right) \right)^2 + \left(\omega_A \left(-\frac{M_y}{P_{dyn}\, A^2\, L} \right) \right)^2 + \left(\omega_L \left(-\frac{M_y}{P_{dyn}\, A\, L^2} \right) \right)^2 \right]^{1/2} \quad (30)$$

3.8.1.1.5 Pressure coefficient uncertainty calculation

$$C_P = \frac{P - P_{static}}{P_{total} - P_{static}}$$

$$C_P = C_P(P, P_{static}, P_{total})$$

$$u_{C_P} = \pm \left[\left(\frac{P}{C_P} \frac{\partial C_P}{\partial P} u_P \right)^2 + \left(\frac{P_{static}}{C_P} \frac{\partial C_P}{\partial P_{static}} u_{P_{static}} \right)^2 + \left(\frac{P_{total}}{C_P} \frac{\partial C_P}{\partial P_{total}} u_{P_{total}} \right)^2 \right]^{1/2} \quad (31)$$

$$u_{C_P} = \pm \left[\left(\frac{P}{C_P} \left(- \frac{1}{P_{static} - P_{total}} \right) u_P \right)^2 + \left(\frac{P_{static}}{C_P} \left(\frac{P - P_{total}}{(P_{static} - P_{total})^2} \right) u_{P_{static}} \right)^2 + \left(\frac{P_{total}}{C_P} \left(- \frac{P - P_{static}}{(P_{static} - P_{total})^2} \right) u_{P_{total}} \right)^2 \right]^{1/2} \quad (32)$$

$$\omega_{C_P} = \pm \left[\left(\omega_P \left(- \frac{1}{P_{static} - P_{total}} \right) \right)^2 + \left(\omega_{P_{static}} \left(\frac{P - P_{total}}{(P_{static} - P_{total})^2} \right) \right)^2 + \left(\omega_{P_{total}} \left(- \frac{P - P_{static}}{(P_{static} - P_{total})^2} \right) \right)^2 \right]^{1/2} \quad (33)$$

The absolute uncertainty values of the measured quantities are provided in Table 3-7.

Table 3-7 Absolute uncertainty values of the measured quantities

Variable	Nominal Values	ω_R
Fx, Mx	From the test	0.0032 N, 0.00025 Nm
Fz, Mz	From the test	0.01 N, 0.00025 Nm
My	From the test	0.0005 Nm
α	From the test	0.1 degree
P_{dyn}	From the test	2500x0.05/100x2=2.5 Pa
A (wing 1a)	0.0182	$4x10^{-4}$ m^2
P	From the test	2500x0.05/100x1=1.25 Pa

3.8.1.1.6 Uncertainty results

The absolute uncertainty values for all wings were constructed. For that purpose, the uncertainty values at OGE condition, at the closest height of the static ground condition as well as the maximum absolute uncertainty values considering all the heights and angle of attack points at static ground condition are provided. The comparison of the C_L results of the thick delta wing 1a and the thin delta wing 1b with respect to related studies in literature are also presented in this chapter. Considering the time history of all measured parameters such as surface pressure measurements as well as force and moment measurements, the RMS values of each test point were found. It was ensured that RMS values are smaller than the accuracy windows of the related parameter of the pressure transducer and force and torque transducer. For the OGE results, maximum uncertainty results considering all the 8 wings are summarized in Table 3-8.

The detailed explanation of the trends for the absolute uncertainty levels are explained considering the delta wing 1a as a function of angle of attack. In Figure 3-26, the combined uncertainty levels of C_P for suction and pressure sides at $x/c =$

0.5 and $y/s = 0.77$ location together with $h/c = 107\%$ and 10.4% for $0 \leq \alpha \leq 25$ degrees are given in the first row, whereas the combined uncertainty levels of C_D, C_L, C_L/C_D, and C_M are given in the $h/c = 107\%$ and $h/c = 6.67\%$ for $0 \leq \alpha \leq 30$ degrees are provided in the second and third rows. Considering the C_P charts in the first row, the uncertainty levels on pressure side do not vary much with angle of attack and are around 0.02 for all angles of attack at two different heights values representing the out of ground effect (OGE) condition and high GE intensity condition whereas uncertainty levels on the suction side increase up to $\alpha = 15^o$ for $h/c = 107\%$ to the 0.0467 and $\alpha = 13^o$ for $h/c = 10.4\%$ to the 0.0562, respectively. Considering the charts force and moment coefficients as well as C_L/C_D, the maximum uncertainty levels are reached at the angle where the corresponding parameter reaches its maximum value for the angle of attack interval. Therefore, maximum uncertainty levels are reached at the highest angle of attack $\alpha = 30^o$ for C_D and equal to 0.044 and 0.034. At the stall angles, which are at $\alpha = 20^o$ and $\alpha = 22^o$, the maximum levels are equal to 0.074 and 0.059 for C_L, and 0.053 and 0.045 for C_M. The maximum C_L/C_D values appear at angles of attack $\alpha = 8^o$ and $\alpha = 10^o$, and the corresponding maximum uncertainty levels are equal to 0.087 and 0.058 for $h/c = 103\%$ and $h/c = 6.67\%$ cases, respectively.

The trends of the uncertainty values as a function of angle of attack and results of the maximum uncertainty values at OGE, the closest height to the static ground and for all heights for static ground condition of the delta and reverse delta wings are provided from Figure C - 17 to Figure C - 23 and, from Table C - 1 to Table C - 8 in Appendix C. The force coefficients of other delta and reverse delta wings show similar trends with both angle of attack and ground height.

In Figure 3-27, the C_L values of the current study for the thick delta wing 1a and the thin delta wing 1b are also compared with the results of [7], [9], [59], [60], [63], and which utilize delta wings having 45^o sweep angle with different t/c ratios, Reynolds number and leading-edge shapes.

The comparison of the C_L results of the thick delta wing 1a with respect to related studies in literature is presented in the upper chart of Figure 3-27. Earnshaw and Lawford [9] studied a delta wing having a slight stream-wise camber, whereas Ghazijahani and Yavuz [60] and Kestel et al. [63] studied a sharp-edged delta wing with 45 deg bevel angle on the windward side of the wing. Considering the C_L distributions, the lift curve slopes of all four results are similar whereas the maximum attainable C_L as well as maximum C_L at $\alpha = 0^o$ are achieved in the study of [9], which can be attributed to leading-edge shape of the wing. The nonzero C_L values at $\alpha = 0^o$ for [60] and [63] are also expected to be due to asymmetric bevel conditions. At lower chart of Figure 3-27, the C_L distribution of the thin delta wing 1b is compared with the results of [7], [59] and [60]. Taylor et al. [7] and Ghazijahani and Yavuz [60] adopted a sharp-edged 45 deg bevel angle on the windward side whereas Kawazoe et al. [59] utilized rounded and semicircular leading-edge shape. Kawazoe et al. [59] states that rounded leading-edge shape is responsible of delaying stall and attributed it to the primary attachment line, which reaches to the wing centerline at higher angle of attack. The stall characteristics of the present study is similar to the results of [59] and both wings stall at the same angle of attack $\alpha = 20^o$, which might be associated with the delaying stall mechanism due to the symmetric bevel. Considering the charts on the second row together for the consistency assessment of the results of the current study, the C_L distributions of the present study are quite in line with the representative studies in literature in terms of C_L slopes, maximum C_L values, and stall angles even though the studies include variation in leading-edge shapes and Reynolds numbers.

Table 3-8 Maximum uncertainty values at OGE condition for all delta and reverse delta wings

	Condition	Maximum Uncertainty Value (ω_R)	
Pressure Measurements	$\alpha \geq 5^o$	Suction Side, Cp	$\omega_{C_p} = \pm 0.0509$
		Pressure Side, Cp	$\omega_{C_P} = \pm 0.0275$
Force Measurements	$\alpha \geq 1.5^o$	C_D	$\omega_{C_D} = \pm 0.0398$
		C_L	$\omega_{C_L} = \pm 0.0629$
		C_L/C_D	$\omega_{C_L/C_D} = \pm 0.3055$
		C_M	$\omega_{C_M} = \pm 0.0629$

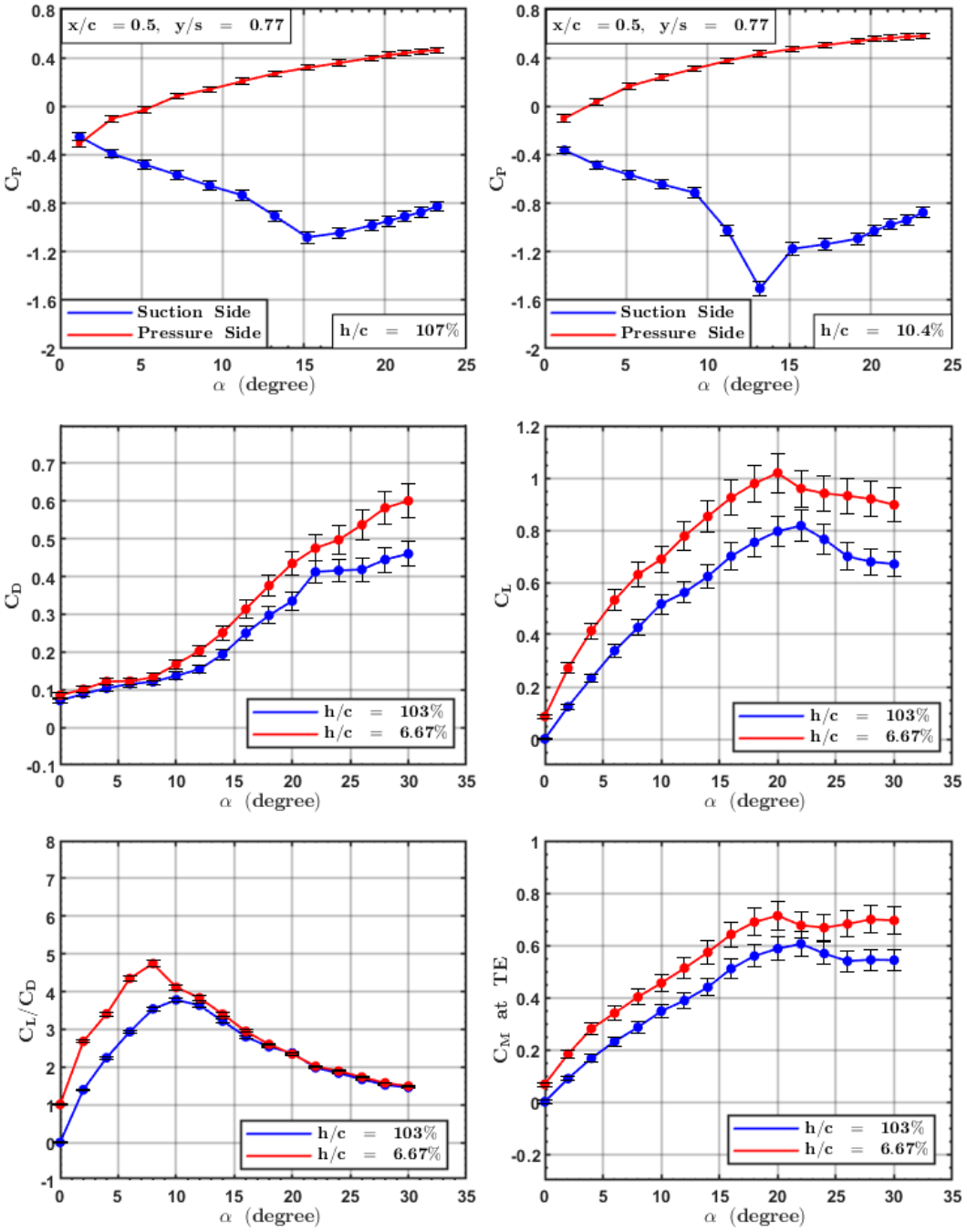

Figure 3-26 The absolute uncertainty levels of C_P, C_D, C_L, C_L/C_D, and C_M of the delta wing 1a as a function of angle of attack

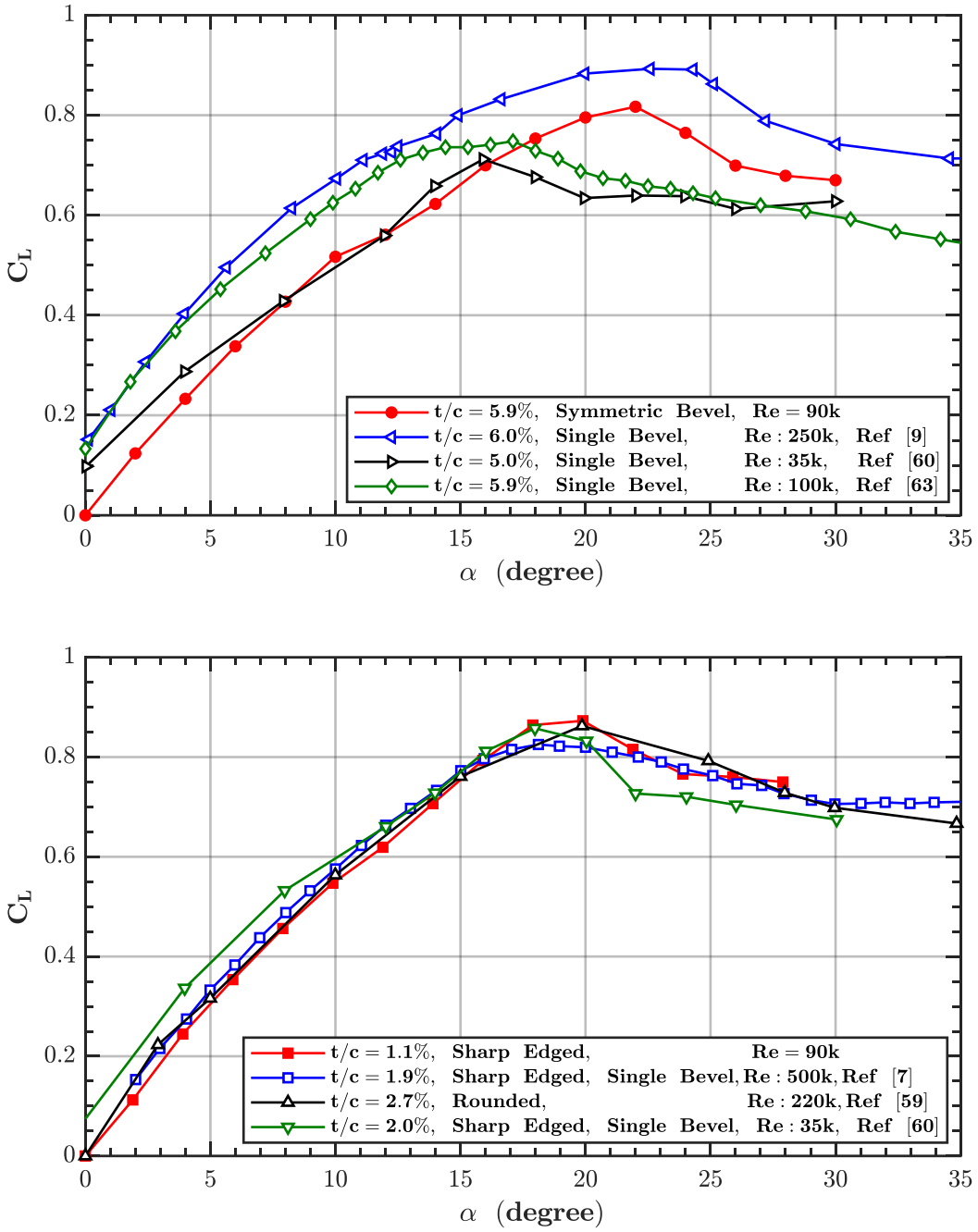

Figure 3-27 The comparison of lift coefficient of thick (1a) and thin (1b) delta wings with the results of [7], [9], [59], [60], and [63].

CHAPTER 4

EFFECT OF STATIC GROUND CONDITION

In this chapter, the results with the static ground condition are provided. The vortical flow field of the delta wing 1a is examined with pressure measurements, which are provided with surface measurements on both suction and pressure sides, whereas the effect of wing thickness on delta and reverse delta wings as well as the effect of wing anhedral and cropping are particularly discussed for OGE results of the delta and reverse wings 1a, 1b, 2a, 2b, 2c, 2d, 2e, and 2f.

The schematic representations of the wings, geometrical details and the locations of the pressure tabs are provided again in Figure 4-1 for the sake of understanding, although these parameters are detailed in Chapter 3.2.

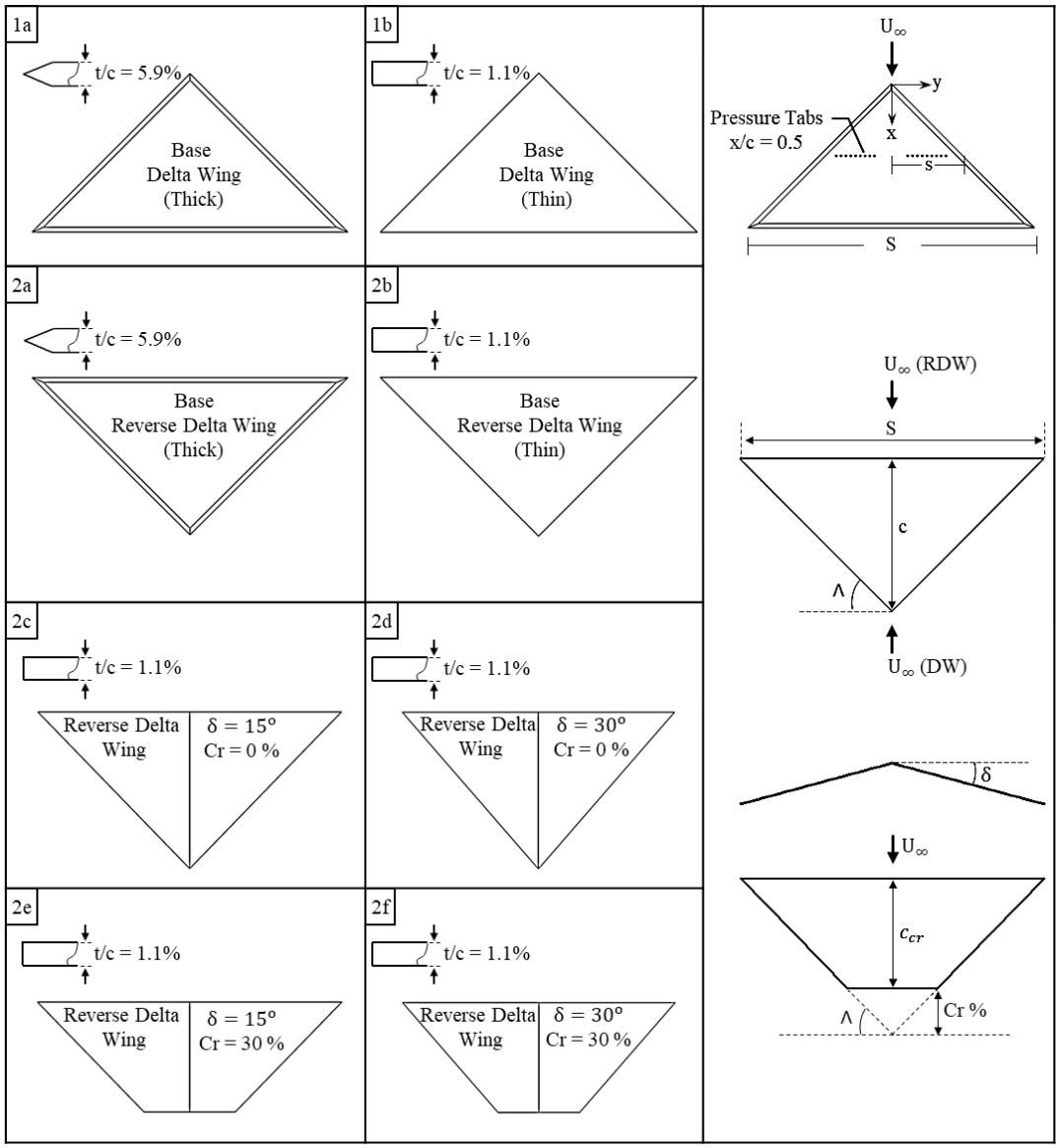

Figure 4-1 Schematic representations of the wings including delta wing, reverse delta wing, anhedraled and cropped

4.1 Out of Ground Effect Results

The results at OGE condition of all eight wings are discussed in this chapter.

4.1.1 Results of Surface Pressure Measurements

In Figure 4-2, C_P distributions at suction and pressure sides of the thick delta wing (1a) at chordwise location of $x/c = 0.5$ and at angles of attack of $\alpha = 5, 9, 13, 17, 20,$ and 23 degrees are given. The horizontal axis of the charts indicates the spanwise distance at the chordwise location of $x/c = 0.5$, which is normalized with the corresponding local half span length.

Considering the suction side curves (in blue), the location of the lowest C_P value is an indicator of the projection of possible location of vortex core on wing surface, while the location of the highest C_P value represents the reattachment location of the vortex to the wing surface, when vortex dominant flow appears on the planform. These minimum and maximum values of C_P (ΔC_P) indicate the strength of the leading-edge vortex such that the strength of the vortex increases up to the angle of attack $\alpha = 17^o$ and deteriorates following that. ΔC_P values are $0.40, 0.59, 0.69, 1.02, 0.64,$ and 0.13 at angles of attack of $\alpha = 5, 9, 13, 17, 20,$ and 23 degrees, respectively. The C_P distribution turns into nearly a flat distribution at $\alpha = 23^o$, which is indicating an appearance of three-dimensional surface separation on the planform and quite in line with the stall condition of the wing that will be discussed in the following section. Considering the pressure side curves (in red), positive C_P distributions are evident on the planform, which are linearly increasing toward the leading-edge having slopes monotonically increase as the angle of attack increases. In addition, considering both the suction and pressure side curves, the area enclosed by the curves is the footprint of the normal force, which has the contribution from both the lift and drag forces.

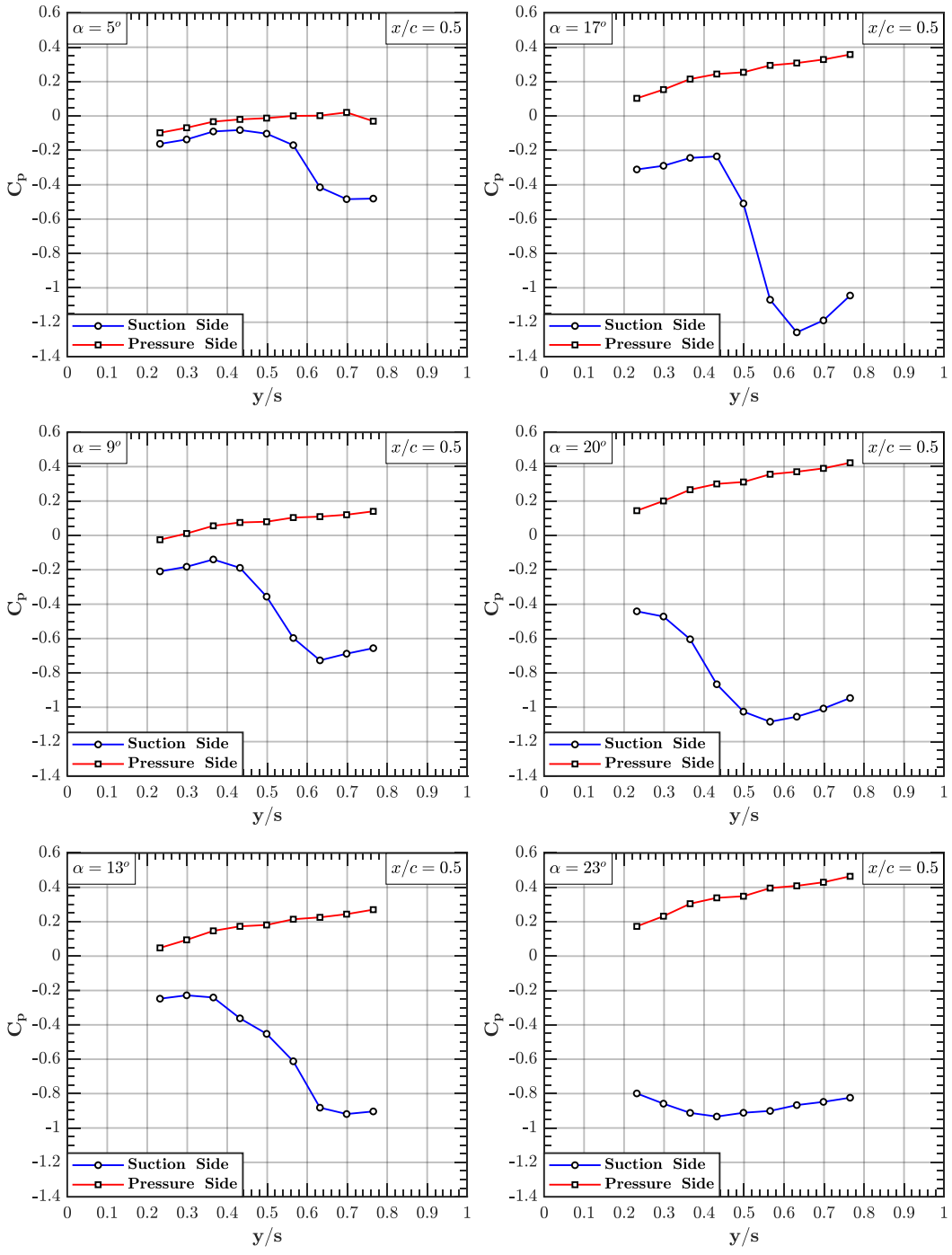

Figure 4-2 C_P distributions at suction and pressure sides of the delta wing (1a) at chordwise location of $x/c = 0.5$ for the angles of attack of $\alpha = 5, 9, 13, 17, 20$ and 23 degrees at $Re = 9x10^4$

4.1.2 Results of Force Measurements

4.1.2.1 Effect of Wing Thickness

In Figure 4-3, distributions of drag coefficient C_D, lift-to-drag ratio C_L/C_D, lift coefficient C_L as a function of angle of attack and drag polar for thick and thin delta wings (1a, 1b) and thick and thin reverse delta wings (2a, 2b) are given, respectively.

Considering the drag coefficient C_D shown in the upper left chart, for both delta and reverse delta configurations the thick wings demonstrate higher C_D values with lower rate of change at low angles of attack up to $\alpha = 10^o$ compared to the thin wings. For delta wing configurations, similar drag coefficients are observed between $\alpha = 10^o$ and 20^o. However, the thick delta wing 1a exhibits sudden drag increase, which is absent for the thin delta wing 1b, at the stall angle, which can be deduced from either the pressure results in Figure 4-2 or C_L chart in Figure 4-3, and roughly to be between $\alpha_s = 22^o - 23^o$. Comparing the drag coefficients of the thick 2a and thin 2b reverse delta wings, the drag coefficients linearly increase with angle of attack and the thick configuration always exhibits higher drag coefficients at all angles of attack.

Considering the lift coefficient C_L shown in upper right chart, the delta wings exhibit typical stall behavior with a sudden loss in lift, whereas the lift coefficients of the reverse delta wings reveal that the lift curve starts to indicate flat distribution after a certain angle of attack. The thin delta wing 1b has a stall angle of $\alpha_s = 20^o$ whereas stall onset is postponed to $\alpha_s = 22^o$ for the thick delta wing 1a with a relatively less maximum C_L. For the thick reverse delta wing 2a, lift curve flattens around the maximum C_L value. The thin reverse delta configuration 2b possesses consistent increase in lift coefficient, however, the rate of increase in C_L reduces dramatically after $\alpha = 10^o$. Considering the lift curve slopes of all four wings, thin configurations 1b and 2b have higher rate of increase in lift compared to thick ones 1a and 2a. Finally, lift prediction based on the theory defined in Ref. [24] gives good correlation with the results for the delta wings 1a and 1b up to the angle of attack $\alpha = 5^o$,

whereas deviation between the prediction of the theory and results of the delta wings increases at higher angles. The leading-edge suction analogy, which is adopted by the aforementioned theory, is particularly successful for the prediction of the lift of the slender delta wings but fails to estimate the lift for the non-slender delta wings, which is dominated by the vortical flow over the suction side of the wing and quite sensitive to the sweep angle.

The C_L/C_D distribution is shown in the lower left chart and primarily presents the aerodynamic performance of the wings. Considering the thickness effect, the thin wings 1b and 2b demonstrate superior aerodynamic performances compared to thick wings 1a and 2a at all angles of attack, where the thin reverse delta indicates the best performance among all configurations. Considering the slope of C_L/C_D distributions for all four wings, the rate of increase of C_L/C_D for reverse delta wings 2a and 2b are higher compared to ones for the delta wings 1a and 1b up to the angle of attack where the maximum C_L/C_D appears. In addition, the peak values of C_L/C_D for delta wings 1a and 1b are postponed to higher angles of attack compared to reverse delta wings 2a and 2b.

The drag polar shown at the lower right chart of Figure 4-3, presents the ability of the wing to generate additional lift without increasing the drag, hence having a higher slope is desired. Comparing the delta wings 1a and 1b in the pre-stall region and the reverse delta wings 2a and 2b for all angles of attack, the drag polar demonstrates that thin configurations 1b and 2b generate relatively less drag for the same lift coefficient compared to thick configurations 1a and 2a. The behavior of the reverse delta wing 2b significantly deteriorates after $C_L = 0.6$ and lift generation ability comes with a high drag generation penalty while 2a cannot generate additional lift after $C_L = 0.71$. The slopes of the drag polar curves of the delta wings 1a and 1b are quite similar between $C_L = 0.6$ and 0.86 suggesting that amount of the drag drawback is similar for the same amount of additional lift.

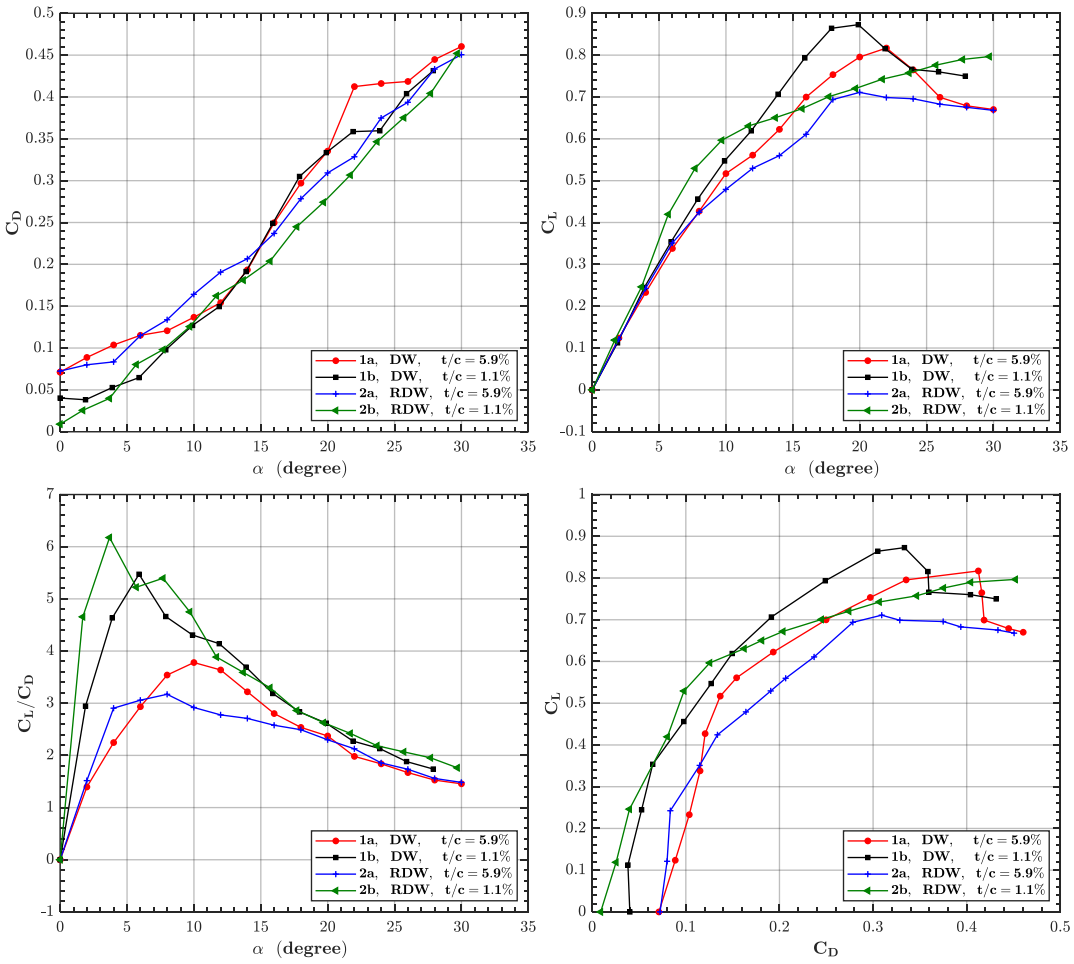

Figure 4-3 Distributions of drag coefficient C_D, lift-to-drag ratio C_L/C_D, lift coefficient C_L as a function of angle of attack and drag polar for the delta wings (1a), (1b) and the reverse delta wings (2a), (2b)

In Figure 4-4, variation of moment coefficient C_M at trailing-edge (TE) and center of gravity (CG) as functions of angle of attack and lift coefficient C_L, and non-dimensional center of pressure coordinate X_P as a function of angle of attack for delta wings 1a and 1b and reverse delta wings 2a and 2b are given.

Considering the distribution of C_M at trailing-edge shown in the upper left chart, the thick configurations 1a and 2a induces lower slopes up to $\alpha = 14^o$ compared to the corresponding thin wings 1b and 2b. For the delta wings 1a and 1b, the slope of C_M distribution decreases significantly and becomes negative at the stall angle. However, this behavior is not evident for the reverse delta wings 2a and 2b since the

rate of change of C_M is always positive. In addition, reverse delta wings 2a and 2b, possess relatively higher C_M compared to the delta wings. The center of pressure X_P location, which will be further discussed along with the lower right chart of Figure 4-4, might be effective on this behavior since X_P located close to leading-edge results in higher trailing-edge moments for the same amount of lift. Therefore, the location of X_P is tremendously important over the longitudinal stability characteristics of the wings.

The distribution of C_M at the trailing-edge as a function of C_L is demonstrated in the bottom left chart of Figure 4-4. The location of the aerodynamic center in pitch X_a can be found with respect to the trailing-edge from the slope of the curve and the corresponding values of X_a are given in Table 4-1. The highest slope is seen for the thin reverse delta wing 2b demonstrating the most forward X_a position and located in the vicinity of the leading-edge ($X_a = 0.033$). The reverse delta wings 2a and 2b have X_a positions closer to the leading-edge compared to delta wings 1a and 1b. The thickness has negligible effect on X_a position for delta wings 1a and 1b, both of which have similar values around $X_a = 0.3$, whereas X_a appears closer to the leading-edge for the thin reverse delta wing 2b compared to thick reverse delta wing 2a.

Table 4-1 The aerodynamic center in pitch X_a, $X_a = 0$ and 1 correspond to the leading-edge/apex and trailing-edge/apex, respectively

Parameter	Wing			
	1a	1b	2a	2b
X_a (x/c)	0.317	0.333	0.15	0.033

Considering the C_M at wing center of gravity (CG) as a function of α shown at upper right corner of Figure 4-4, all four wings 1a, 1b, 2a, 2b have positive slopes and positive C_M, which in turn result in unstable longitudinal stability characteristics. As the slope of this curve approaches to zero, the wing becomes insensitive to possible disturbances due to incremental changes in angle of attack. The wing thickness does not affect the stability characteristics of the delta wings 1a and 1b, accompanied by

similar amount of moment around the CG as well as demonstrating similar slopes. The slope of the curve for reverse delta wing 2b is similar to the delta wings 1a and 1b up to $\alpha = 5^o$, whereas for higher angle of attack, reverse delta wings 2a and 2b demonstrate similar slopes with C_M curve of the thin wing 2b shifted upwards. Therefore, reverse delta wings 2a and 2b have higher stability margin compared to delta wings 1a and 1b. The stability in longitudinal axis can be assured utilizing a negative C_M source such as a horizontal stabilizer generating nose-down moment around CG. Considering the overall maneuverability and controllability requirements, desired behavior can be adjusted with the position of CG as well as the control power generated by the horizontal stabilizer. The moment generated by the horizontal stabilizer is directly proportional to the area of the wing and the thick reverse delta wing 2a has the lowest C_M. This can be interpreted as an advantage of the thick reverse delta wing 2a compared to other three wings 1a, 1b and 2b in terms of weight reduction since it needs the smallest negative moment around CG generated by the horizontal stabilizer, which can be achieved by a smaller horizontal stabilizer. In addition, a smaller horizontal stabilizer at the same longitudinal position results in smaller shift of the CG towards trailing-edge.

Considering the X_P as function of angle of attack demonstrated in lower right corner of Figure 4-4, the wing thickness is effective on reverse delta wings such that the thick reverse delta wing 2b has X_P position closer to the leading-edge compared to the wing 2a for all angles of attack while a negligible shift toward leading-edge is seen for the thick delta wing 1a compared to thin delta wing 1b. As the angle of attack increases, X_P gets closer to the leading-edge for the thick reverse delta wing 2a whereas no remarkable movement of the X_P is seen for other three wings 1a, 1b and 2b. Considering the delta wings 1a and 1b, center of pressure is around $x/c = 0.35$ and does not change with angle of attack. The aerodynamic centers of these two wings are X_a =0.317 and 0.333 and quite close to X_P. Considering the "thin airfoil theory" and neglecting the small changes in X_P with angle of attack, the combined behavior of X_a and X_P demonstrate 2D symmetric airfoil characteristics such that center of pressure is coincident with aerodynamic center in pitch and it does not

change with angle of attack, although $X_a \cong X_P = 0.35$ for delta wings 1a and 1b but the "thin airfoil theory" dictates that $X_a = X_P = 0.25$.

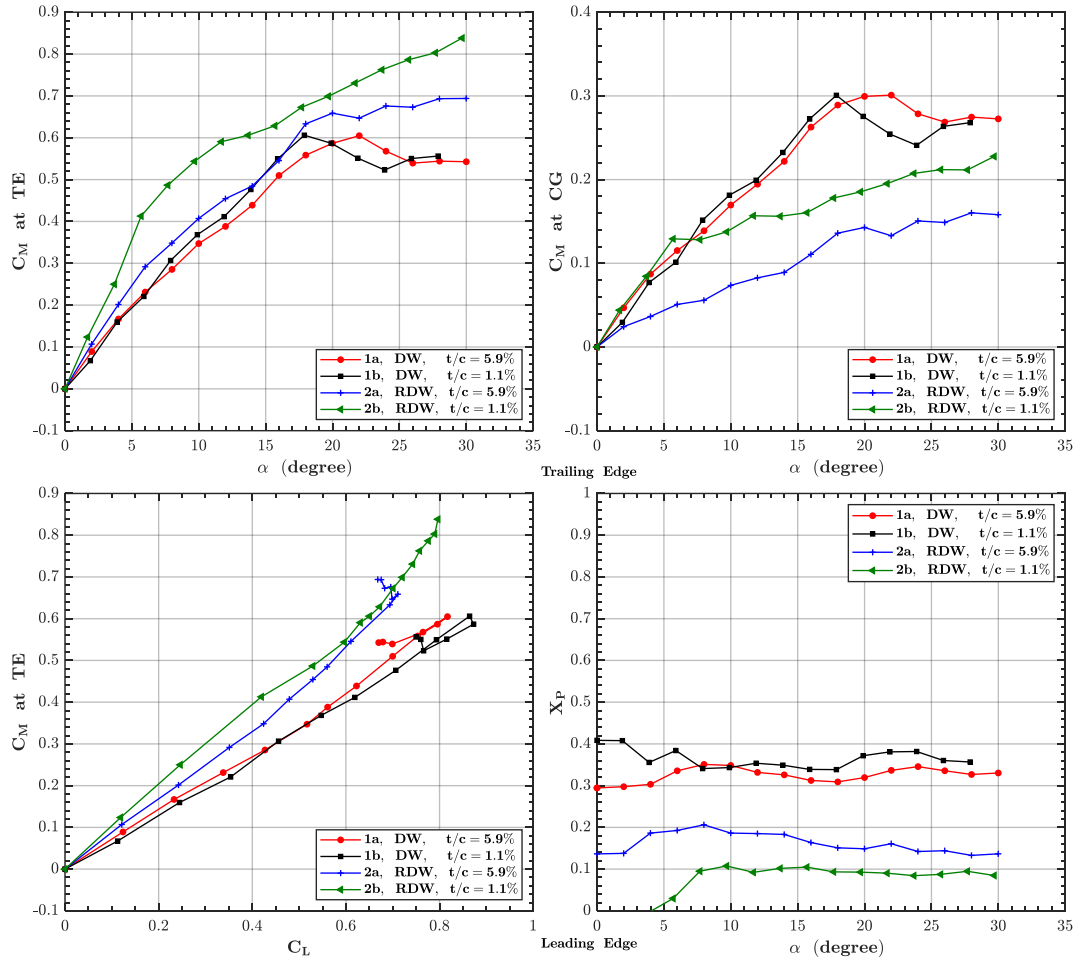

Figure 4-4 Distributions of moment coefficient C_M at trailing-edge (TE) and center of gravity (CG) as functions of angle of attack and lift coefficient C_L, and non-dimensional center of pressure coordinate X_P as a function of angle of attack for the delta wings (1a), (1b) and the reverse delta wings (2a), (2b)

4.1.2.2 Aerodynamic Characteristics of Reverse Delta Wings

In Figure 4-5, distributions of drag coefficient C_D, lift-to-drag ratio C_L/C_D, lift coefficient C_L as a function of angle of attack and drag polar for reverse delta wings (2b, 2c, 2d, 2e, and 2f) are given, respectively.

Considering the C_D shown in the upper left chart, the sole effect of the anhedral angle on the reverse delta wing does not have a monotonic trend on drag since the anhedraled wing ($\delta = 15^o$) 2c has higher C_D distributions nearly for all angles of attack, but further increase in anhedral angle to $\delta = 30^o$decreases C_D and the anhedraled wing ($\delta = 30^o$) 2d has C_D values in between the reverse delta wing 2b and the anhedraled wing 2c. When considering the wings 2c and 2e as well as the wings 2d and 2f separately, the sole effect of the cropping results in decreased C_D distributions for both anhedral angles $\delta = 15^0$ and 30^0 and downward shift of C_D curves, where the lowest C_D distributions are achieved with 2f wing configuration of $\delta = 30^0$ and $Cr = 30\%$. Considering the angle of attack range up to $\alpha = 5^0$, the drag values of the reverse delta wing 2e do not show a monotonic behavior with increasing angle of attack. The decrease in drag values up to $\alpha = 4^0$ might be due to the combined effect of decreasing wetted area with increasing angle of attack and decreasing wing surface area with anhedral and cropping and their associated effects on the flow fields over the pressure and suction sides of the wing. The drag increase with increasing angle of attack is negligibly small for the reverse delta wing 2d, which might only be attributed to the anhedral angle $\delta = 30^0$ this time.

Considering the C_L distributions shown in upper right chart, the characteristic lift coefficient trend for the reverse delta wing 2b is witnessed in all configurations such that lift curve slope decreases as the angle of attack increases without clear indications of stall formation and reduction in lift coefficient. The highest C_L values and lift curve slopes are achieved with the reverse delta wing 2b. As the anhedral angle increases, both the lift coefficient and its rate of change decrease. Considering the effect of cropping at $\delta = 30^o$ for wing configurations 2d and 2f, two different

trends are observed for relatively low and high angles of attack. The cropped wing 2f indicates higher C_L slopes compared to non-cropped wing 2d for angles of attack up to $\alpha = 12^o$, on the contrary, the trend is complete opposite for higher angles of attack.

Considering the C_L/C_D shown in the lower left chart, aerodynamic performance of anhedraled and cropped wing 2e is superior compared to the other configurations. The maximum efficiency angle of attack of all five wings are close to each other and around $\alpha = 5^o$. The sole effect of anhedral results in deterioration of the wing performance since C_L/C_D distributions of the wings 2c and 2d are quite close to each other and the corresponding maximum value is significantly less than the one achieved with the reverse delta wing 2b. Cropping tremendously improves the performance of the anhedraled wings 2c and 2d and results in higher C_L/C_D for both wings 2e and 2f while the improvement is more prominent for $\delta = 15^o$ with respect to $\delta = 30^o$.

Considering the drag polar chart demonstrated at the lower left corner, overall distributions of the wings 2b, 2c, and 2d indicate that drag penalty increases with increasing δ for the same amount of lift. Cropping causes significant improvement up to $C_L = 0.6$ and reverses the adverse effects of anhedral such that similar drag polar distributions are obtained among the wings 2b, 2e, and 2f. However, the ability of generating lift without drag penalty deteriorates and distribution becomes nearly horizontal after $C_L = 0.6$.

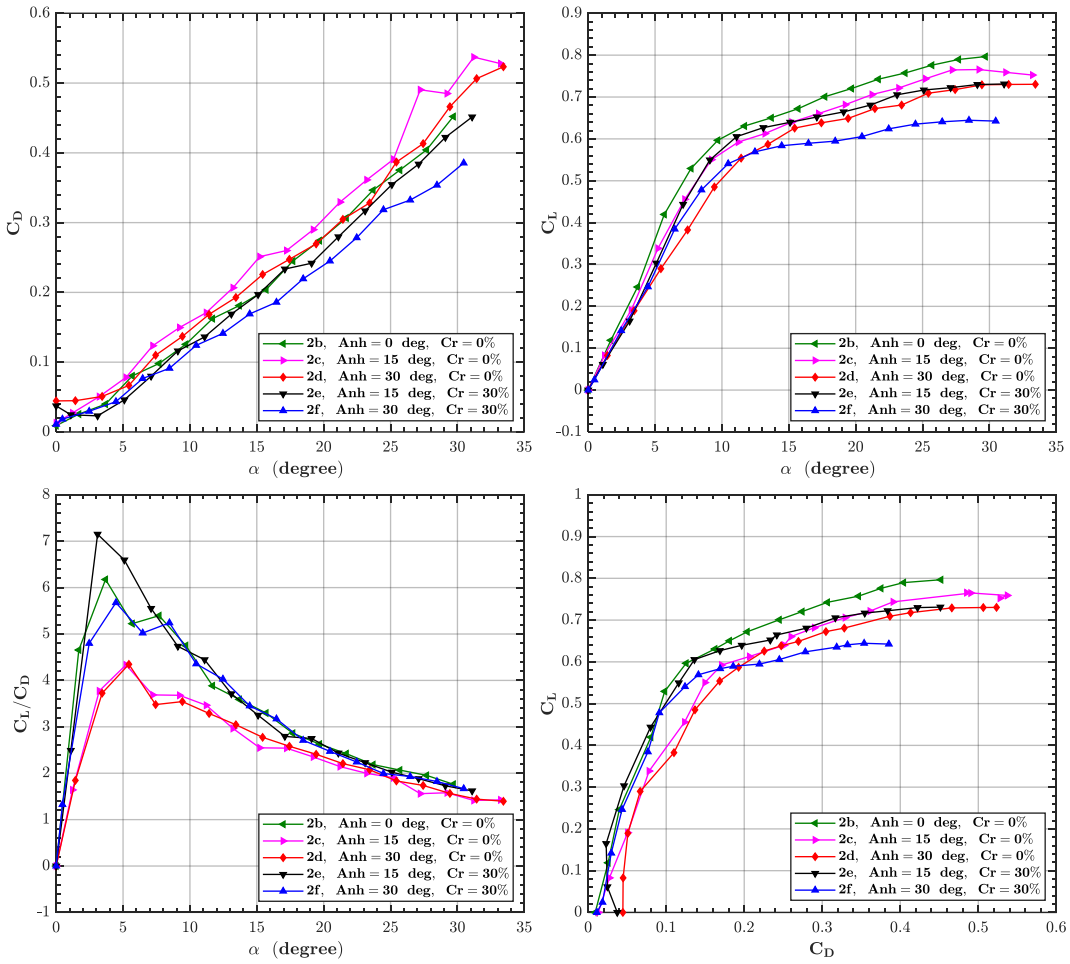

Figure 4-5 Distributions of drag coefficient C_D, lift-to-drag ratio C_L/C_D, lift coefficient C_L as a function of angle of attack and drag polar for different reverse delta wing configurations (2b), (2c), (2d), (2e), (2f)

In Figure 4-6, variation of moment coefficient C_M at trailing-edge (TE) and center of gravity (CG) as functions of angle of attack and lift coefficient C_L, and non-dimensional center of pressure coordinate X_P as a function of angle of attack for reverse delta wings (2b, 2c, 2d, 2e, and 2e) are given, respectively.

Considering the C_M at trailing-edge shown in the upper left chart, both the C_M and its slope decrease due to the increase in nose-down moment with the inclusion of anhedral for the wings 2c and 2d compared to the reverse delta wing 2b. Similarly, the cropping for the wings 2e and 2f causes significant drop in C_M and its slope compared to the reverse delta wing 2b and anhedraled wings 2c and 2d.

The C_M at trailing-edge as a function of C_L is demonstrated in the bottom left chart. The locations of the aerodynamic center in pitch X_a of the reverse delta wings are given in Table 4-2. The location of the aerodynamic center in pitch X_a is at the maximum forward position with respect to trailing-edge for the reverse delta wing 2b. As the anhedral angle increases to $\delta = 15^o$ from the $\delta = 0^o$ for the wing 2b, X_a moves towards the trailing-edge $X_a = 0.112$ for the wing 2c while further increase in anhedral angle results in movement of the X_a towards the leading-edge $X_a = 0.089$ for the wing 2d. However, cropping results in monotonic shift of X_a towards to the trailing-edge of the wings 2e and 2f compared to ones 2c and 2d. Among all five wings, wing 2e with $\delta = 15^o$ and $Cr = 30\%$ induces the most aft positioned aerodynamic center X_a, which is $X_a = 0.195$.

Considering the C_M at wing CG as a function of α shown at upper right corner of Figure 4-6, all five wings 2b, 2c, 2d, 2e, and 2f have positive slopes and positive C_M, hence possess unstable longitudinal static stability characteristics. The inclusion of anhedral decreases the C_M at CG compared to the reverse delta wing 2b. However, further increase in anhedral angle from $\delta = 15^o$ to $\delta = 30^o$, comparing the configurations 2c and 2d, do not induce further reduction in moment coefficient for angle of attack higher than $\alpha = 10^o$. Cropping has a complex influence on anhedraled wings 2c and 2d such that it shifts the curve of the anhedraled wing 2c downward without changing the slope and results in a distribution seen for the wing 2e while it has no effect for the wing 2f compared to the wing 2d up to $\alpha = 5^o$ but decreases C_M between $\alpha = 5^o$ and 30^o with significant decrease in the slope. Therefore, cropping has stabilizing effect for angle of attack higher than $\alpha = 5^o$ for anhedraled wing $\delta = 30^o$ but has no effect for the wing with $\delta = 15^o$. Considering the concepts of longitudinal static stability and aforementioned aerodynamic efficiency, the wing 2e offers the highest aerodynamic efficiency without any deterioration in longitudinal stability characteristics compared to the other four reverse delta wings 2b, 2c, 2d, and 2f.

The center of pressure X_P as function of angle of attack is presented in the lower right corner of Figure 4-6. X_P does not change with α for the reverse delta wing 2b, while it moves toward to the leading-edge for the anhedraled wings 2c and 2b as well as the anhedraled and cropped wings 2e and 2f as the angle of attack increases. The slope of the X_P is steeper for the cropped wings 2e and 2f compared to the non-cropped wings 2c and 2d. In addition, cropped wings 2e and 2f have the X_P positions closest to trailing-edge among all wing configurations.

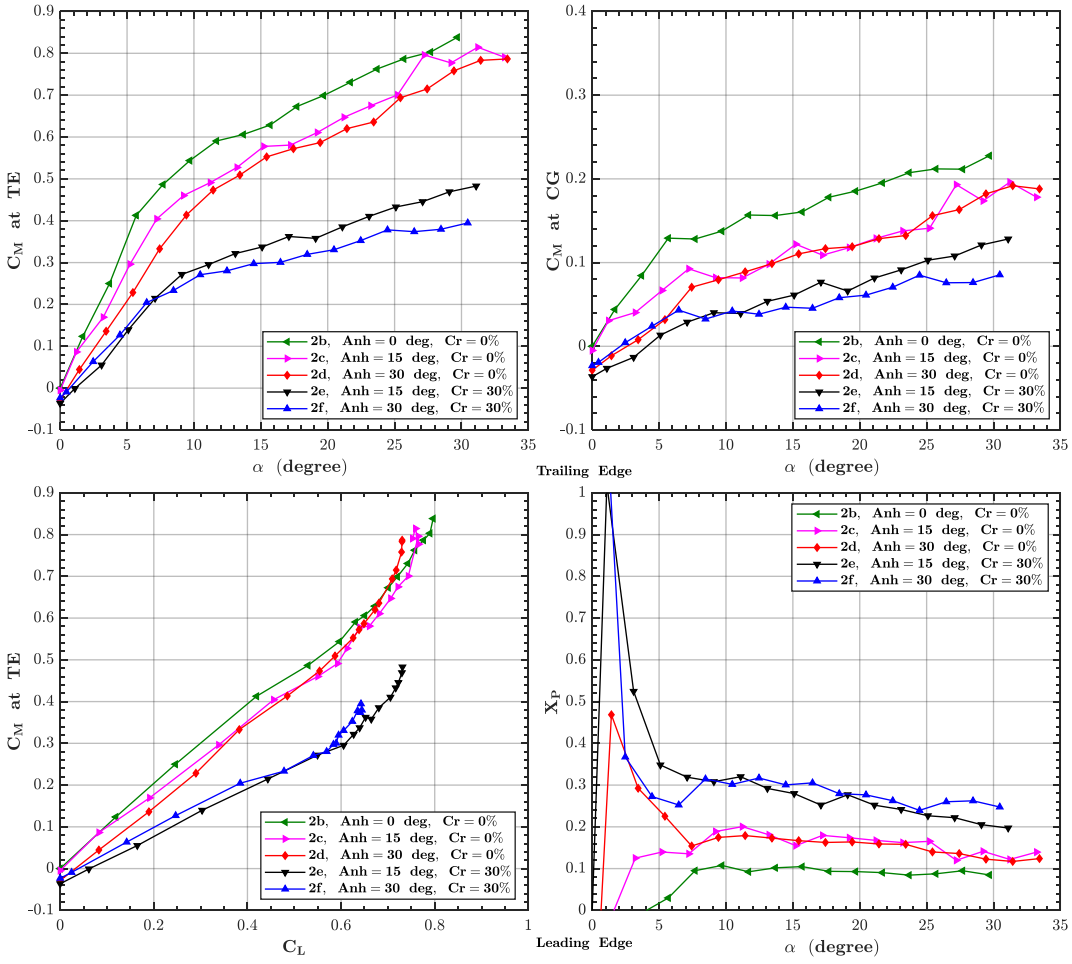

Figure 4-6 Distributions of moment coefficient C_M at trailing-edge (TE) and center of gravity (CG) as a function of angle of attack and lift coefficient C_L, and non-dimensional center of pressure coordinate X_P as a function of angle of attack for different reverse delta wing configurations (2b), (2c), (2d), (2e), (2f)

Table 4-2 The aerodynamic center in pitch X_a, $X_a = 0$ and 1 correspond to the leading-edge and trailing-edge/apex, respectively

Parameter	Wing				
	2b	2c	2d	2e	2f
X_a (x/c)	0.033	0.112	0.089	0.195	0.153

4.2 In Ground Effect Results

The boundary layer state of the ground plate at the wing trailing-edge location is expected to be laminar, since the local Reynolds number is significantly less than the critical Reynolds number. The boundary layer thickness at the corresponding location was calculated as 3.55 mm. Considering the minimum height values of the trailing-edge for pressure and force measurements, which were equal to 4 mm ($h/c = 2.96\%$) and 9 mm ($h/c = 6.67\%$), respectively, the wing was positioned outside the boundary layer for all test points.

4.2.1 Results of Surface Pressure Measurements for the Delta Wing 1a

In Figure 4-7, C_P distributions at suction and pressure sides, which are shown with solid and dashed lines of the delta wing 1a at chordwise location of $x/c = 0.5$ and at angles of attack of $\alpha = 5, 9, 13, 17, 20,$ and 23 degrees are given for 15 different non-dimensional height values varying from $h/c = 2.96$ to 107%. The horizontal axis of the charts indicates the spanwise distance at the chordwise location of $x/c = 0.5$, which is normalized with the corresponding local half span length.

Considering the suction side curves (solid lines), the location of the lowest C_P value is an indicator of the projection of possible location of vortex core on wing surface, while the location of the highest C_P value represents the reattachment location of the vortex to the wing surface, when vortex dominant flow appears on the planform. These minimum and maximum values of C_P (ΔC_P) indicate the strength of the LEV such that the strength of the vortex increases up to the angle of attack $\alpha = 17^o$ and

deteriorates following that. The $\alpha = 13^{o}$ results show distinct features such that as the GE intensity increases, reattachment of the vortex is promoted since the minimum values of the C_P are nearly linear and around -0.3 up to $y/s = 0.6$. This might be an indication of the more outboard located LEV, which is stretched in spanwise direction considering the reattachment of the vortex up to $y/s = 0.6$. The GE on suction side of the wing is non-linear such that its effectiveness for $\alpha = 9^{o}$ is minor since the solid curves are nearly coincident whereas GE shows significant effects on LEV reattachment at $\alpha = 13^{o}$ as well as strength at $\alpha = 17^{o}$ and 20^{o} both of which are affected monotonically with increasing GE intensity. For $\alpha = 17^{o}$, GE tremendously changes spanwise C_P distribution such that effect is higher around the region $y/s = 0.4$ whereas the most inboard and the most outboard regions have similar C_P values. As the ground effect intensity increases, monotonically, C_P distribution becomes more negative on suction side of the wing. Considering $\alpha = 20^{o}$, the negative C_P values at outboard spanwise locations significantly deviates for the highest ground effect intensity cases, hence lift augmentations with GE increase with decreasing heights are different for the smallest height values. The lift and drag coefficient results in Figure 4-8 also confirms this non-linear behavior, which is discussed in Chapter 4.2.2.

Considering the pressure side curves (dashed lines), upward shift of C_P distributions is evident on the planform for decreasing heights, whereas the amount of shift increases with both decreasing heights and increasing angles of attack. The pressure side curves are linearly increasing toward the leading-edge up to $\alpha = 20^o$ while both inboard and outboard regions are affected similarly. The spanwise distributions for $\alpha = 20^o$ and 23^o show that inboard regions are greatly influenced by the presence of the ground with respect to the region close to the leading-edge since the upward shift of the C_P is higher for the region close to $y/s = 0.2$. In addition, considering both the suction and pressure side curves, the area enclosed by the curves is the footprint of the normal force, which has the contribution from both the lift and drag forces. Considering the suction side curves, the apparent hump-like behaviors at all heights up to $\alpha = 20^o$ indicate the occurrence of the LEV whereas C_P distribution turns into nearly a flat distribution at $\alpha = 23^o$ for all heights, which is indicating an appearance of three-dimensional surface separation on the planform and quite in line with the stall condition of the wing that will be discussed in the following section.

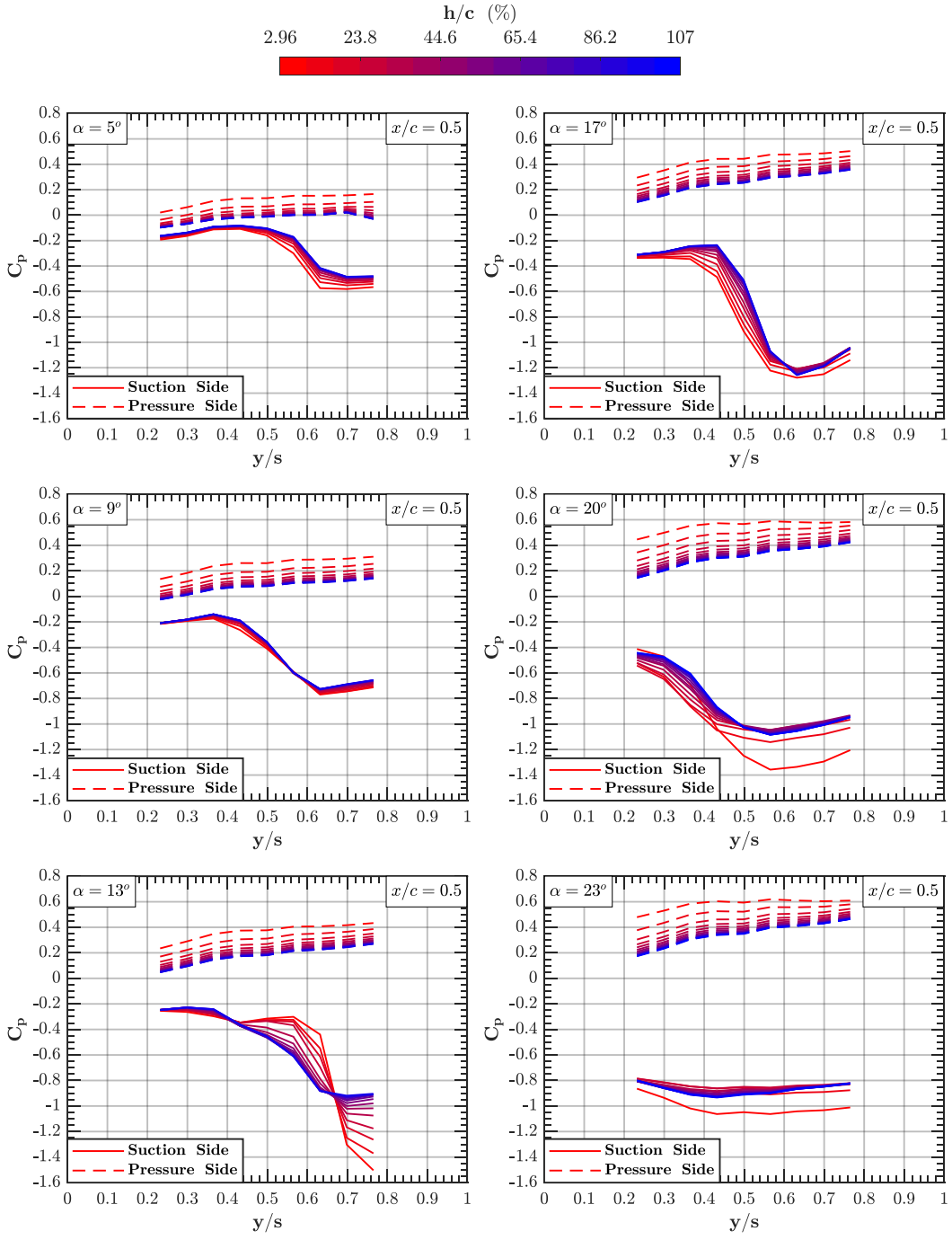

Figure 4-7 C_P distributions at suction and pressure sides of the delta wing 1a at chordwise location of $x/c = 0.5$ and at angles of attack of $\alpha = 5, 9, 13, 17, 20$ and 23 degrees at Re = 9 x 10^4

4.2.2 Results of Force Measurements

In this chapter, ground effect force measurements results for the static ground condition are given as a function of angle of attack for all eight delta and reverse delta wings. For the sake of brevity, the results as function of non-dimensional height values are not discussed, but they are provided with the figures from Figure C - 1 to Figure C - 16 in Appendix C.

4.2.2.1 Results of Force Measurements for the Delta Wing 1a

In Figure 4-8, distributions of drag coefficient C_D, lift-to-drag ratio C_L/C_D, lift coefficient C_L as a function of angle of attack and drag polar for the delta wing 1a are given for 14 different non-dimensional height values varying from $h/c = 6.67\%$ to 102.96%. Considering the drag coefficient C_D shown in the upper left chart, the wing demonstrates higher C_D values with increasing GE intensity. However, the rate of change of drag coefficient increases with increasing angle of attack. The drag coefficient linearly increases with angle of attack between $\alpha = 12^o$ and 20^o for all heights, whereas the drag increase no longer exists around the stall angle for heights close to OGE condition, which can be deduced from either the pressure results in Figure 4-7 or C_L chart in Figure 4-8, and roughly to be between $\alpha_s = 20^o - 23^o$. However, further increase in GE intensity also results in drag increase around stall angle.

Considering the lift coefficient C_L shown in upper right chart, the delta wing exhibits typical stall behavior with a sudden loss in lift. The delta wing has a stall angle of $\alpha_s = 22^o$ for OGE condition whereas earlier stall onset at $\alpha = 20^o$ exits for the IGE cases with higher maximum C_L values. However, increase in lift coefficient is observed for all angles with increasing GE intensity in both low and high angles. The lift curve slope increases with decreasing height and is the highest for the smallest height, hence the rate of increase in C_L increases dramatically with increasing angle of attack as the wing approaches to the ground. Around $\alpha = 10^o$ for OGE case, lift

curve slope is reduced. Not only the stall angle but the angle, where the decrease in lift curve slope is seen, also decreases with the increasing GE intensity.

The C_L/C_D distribution is shown in the lower left chart and primarily presents the aerodynamic performance of the wings. Considering the GE, the performance of the wing is improved at all angles of attack up to $\alpha = 17^o$. The improvement is considerably larger for small angles up to $\alpha = 7^o$, which is due to the lift increase without drag increase penalty. Therefore, favorable condition with GE is more pronounced up to this angle. In addition, the peak values of C_L/C_D for the delta wing is seen around $\alpha = 7^o$, where the peak values for height values close to OGE condition are postponed to higher angles of attack close to $\alpha = 10^o$.

The drag polar shown at the lower right chart of Figure 4-8, presents the ability of the wing to generate additional lift without increasing the drag, hence having a higher slope is desired. The slopes of the drag polar curves of the delta wing are quite similar up to $C_D = 0.14$ and maximum C_L is increased at this drag coefficient value for increased GE intensity. The slopes of the curves, which significantly decrease, hence deteriorate in terms of efficiency, are quite similar with decreasing heights. However, the additional lift with the increasing GE intensity is observed and the effect is more pronounced with increasing heights.

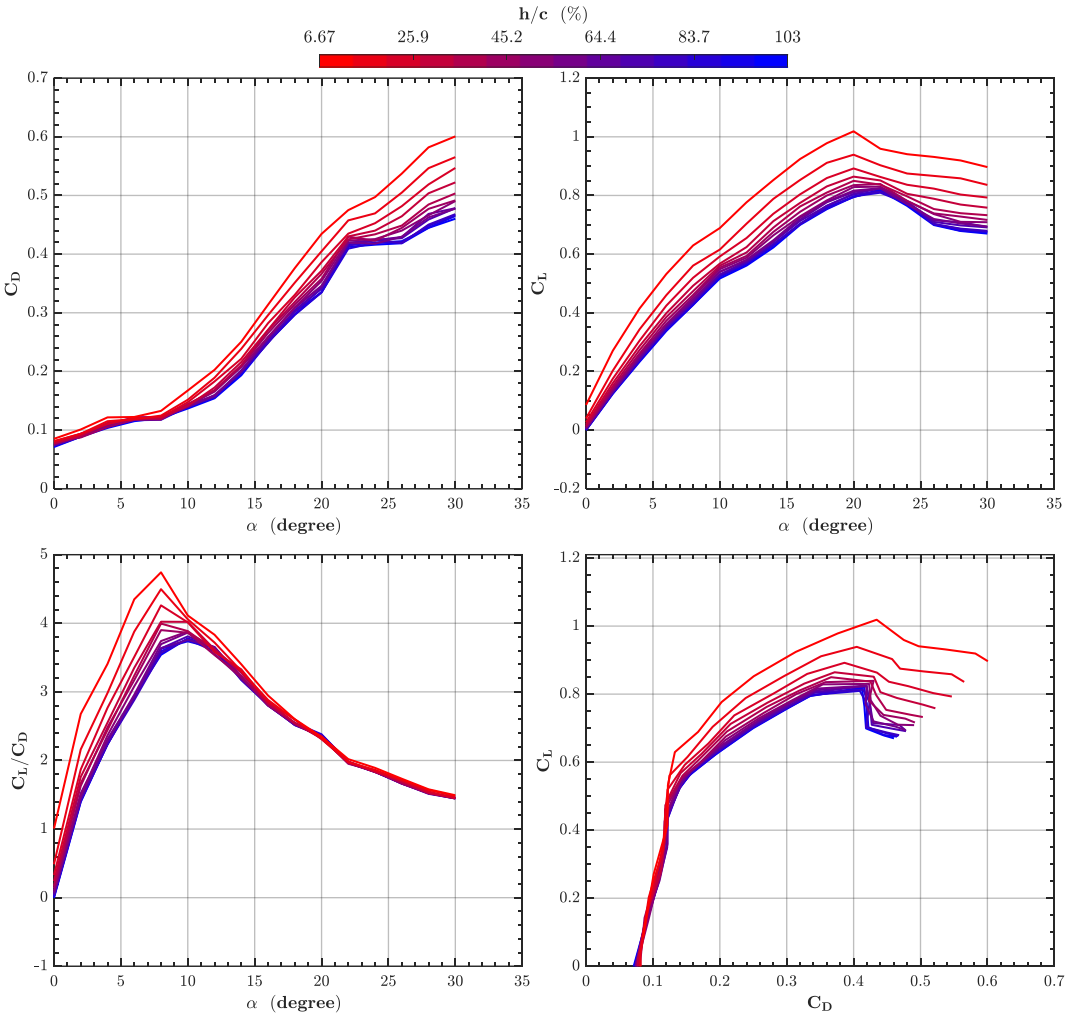

Figure 4-8 Variation of Drag coefficient C_D, Lift-to-Drag ratio C_L/C_D, Lift coefficient C_L as a function of angle of attack and Drag Polar for the delta wing 1a

In Figure 4-9, variation of moment coefficient C_M at trailing-edge (TE) and center of gravity (CG) as functions of angle of attack and lift coefficient C_L, and non-dimensional center of pressure coordinate X_P as a function of angle of attack for the delta wing 1a are given for different height values. Considering the distribution of C_M at trailing-edge shown in the upper left chart, the moment coefficients at all angles increased as the height decreases. However, the rate of change of the pitch-up moment is also increasing with GE intensity and becomes maximum for the closest distance to the ground. As the wing stalls at various heights, the slope of the

moment curve becomes negative. Therefore, stall angles at various height values can also be deduced from the moment curves.

The distribution of C_M at the trailing-edge as a function of C_L is demonstrated in the bottom left chart of Figure 4-9 for different height values. The location of the aerodynamic center in pitch X_a can be found with respect to the trailing-edge from the slope of the curve and the corresponding values of X_a are explicitly shown in Figure 4-24. The highest slope is seen for the OGE condition, whereas the aerodynamic center in pitch slightly shifts towards to the trailing-edge of the wing as the height decreases.

Considering the C_M at wing center of gravity (CG) as a function of α shown at upper right corner of Figure 4-9, all curves at different heights pose positive slopes and positive C_M values. The moment balance around CG can be assured with a nose-down moment source such as horizontal stabilizer, hence the control power generated by the horizontal stabilizer increases as the wing approaches to the ground. Although, positive moment curve slope at aircraft CG is interpreted as unstable aircraft at OGE condition, the overall longitudinal static stability analysis can be conducted with the inclusion of the aerodynamic center in height, X_h, which will be detailed in the next chapter. For the sake of data interpretation, only the moment curves at constant height and at various angles of attack are shown.

Considering the X_P as function of angle of attack demonstrated in lower right corner of Figure 4-9, GE shifts the center of pressure X_P toward trailing-edge of the wing, whereas no remarkable movement of the X_P is seen for the different height values close to the OGE condition considering the associated angle of attack. For all heights, the center of pressure is located between $x/c = 0.3$ and $x/c = 0.4$.

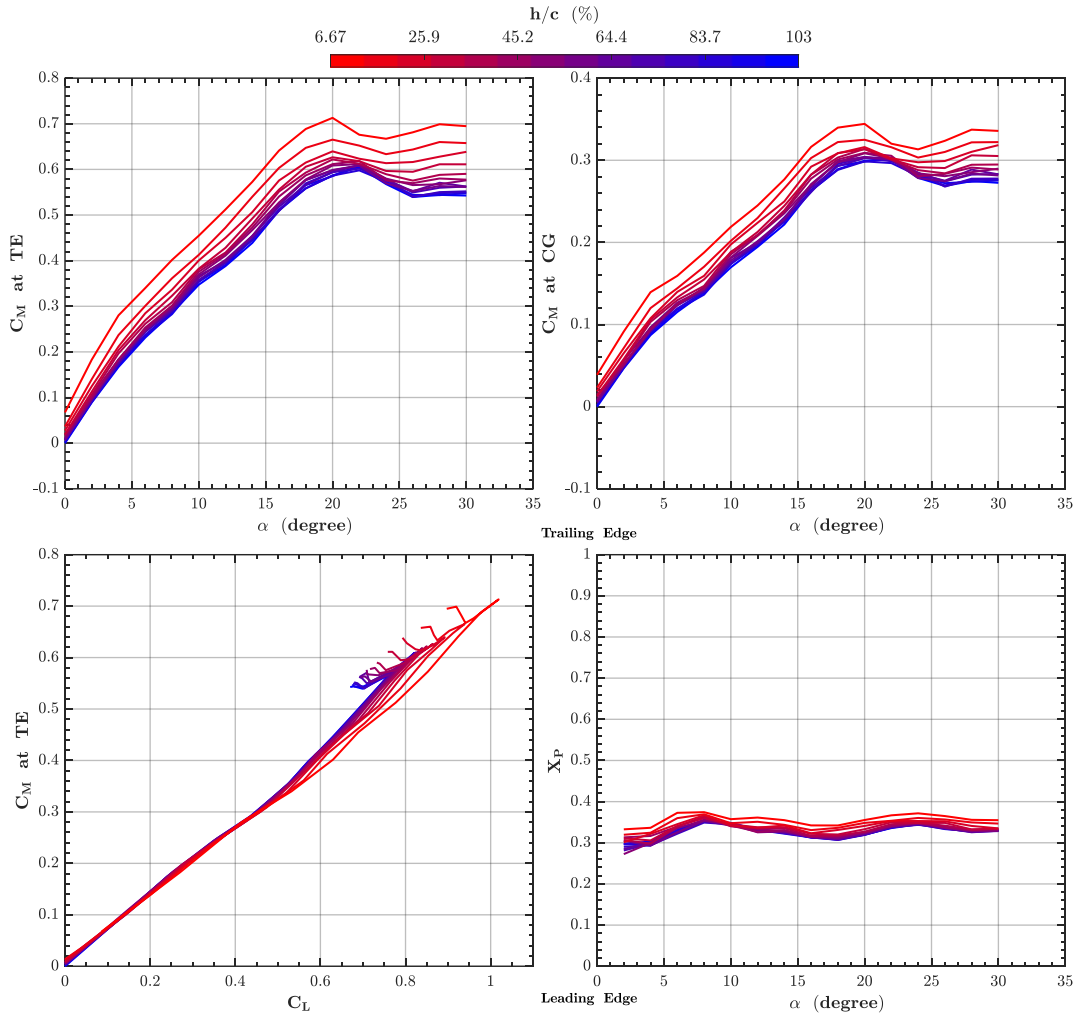

Figure 4-9 Variation of Moment coefficient C_M at trailing-edge (TE) and center of gravity (CG) as a function of angle of attack and Lift coefficient C_L, and Non-Dimensional Pressure Center coordinate X_P as a function of angle of attack for the delta wing 1a

4.2.2.2 Results of Force Measurements for the Delta Wing 1b

In Figure 4-10, distributions of drag coefficient C_D, lift-to-drag ratio C_L/C_D, lift coefficient C_L as a function of angle of attack and drag polar for the delta wing 1b are given for different non-dimensional height values varying from $h/c = 11.1\%$ to 107%. Considering the drag coefficient C_D shown in the upper left chart, similar findings are observed compared to delta wing 1a such that the wing demonstrates higher C_D values with increasing GE intensity and the rate of change of drag coefficient increases with increasing angle of attack. The drag increase is observed nearly all angles, which is reduced for height values close to OGE condition. However, drag curve slope is significantly increased with increasing ground effect intensity.

Considering the lift coefficient C_L shown in upper right chart, the delta wing 1b also exhibits typical stall behavior with a sudden loss in lift. The delta wing has a stall angle of $\alpha_s = 20^o$ for OGE condition whereas slightly earlier stall onset at $\alpha = 18^o$ exits for the IGE cases with higher maximum C_L values. However, increase in lift coefficient is observed for all angles with increasing GE intensity in both low and high angles. The lift curve slope increases for small angles with decreasing height and is the highest for the smallest height, hence the rate of increase in C_L increases dramatically with increasing angle of attack as the wing approaches to the ground. Around $\alpha = 10^o$ for OGE case, lift curve slope is reduced, which is also observed for all heights but occurs at smaller angles. Not only the stall angle but the angle, where the decrease in lift curve slope is seen, also decreases with the increasing GE intensity and there is negligible or no lift loss particularly for the smallest heights with increasing angle of attack value after stall.

Considering C_L/C_D distribution shown in the lower left chart, the performance of the wing is improved at all angles of attack up to $\alpha = 18^o$. The improvement is considerably larger for small angles up to $\alpha = 6^o$, which is due to the lift increase without drag increase penalty. Therefore, favorable condition with GE is more

pronounced up to this angle. In addition, the peak values of C_L/C_D for the delta wing is seen around $\alpha = 4^o$, where the peak values for height values close to OGE condition are postponed to higher angles of attack close to $\alpha = 6^o$. Comparing the maximum C_L/C_D values between OGE at $h/c = 107\%$ case and the most intense ground effect case at $h/c = 11.1\%$, the performance is improved by 20% for the latter case.

Considering the drag polar shown at the lower right chart, the slopes of the drag polar curves of the delta wing are increasing with increasing ground effect intensity, which is higher between $C_D = 0.2$ and $C_D = 0.3$ interval and becomes flat after stall for the smallest height values.

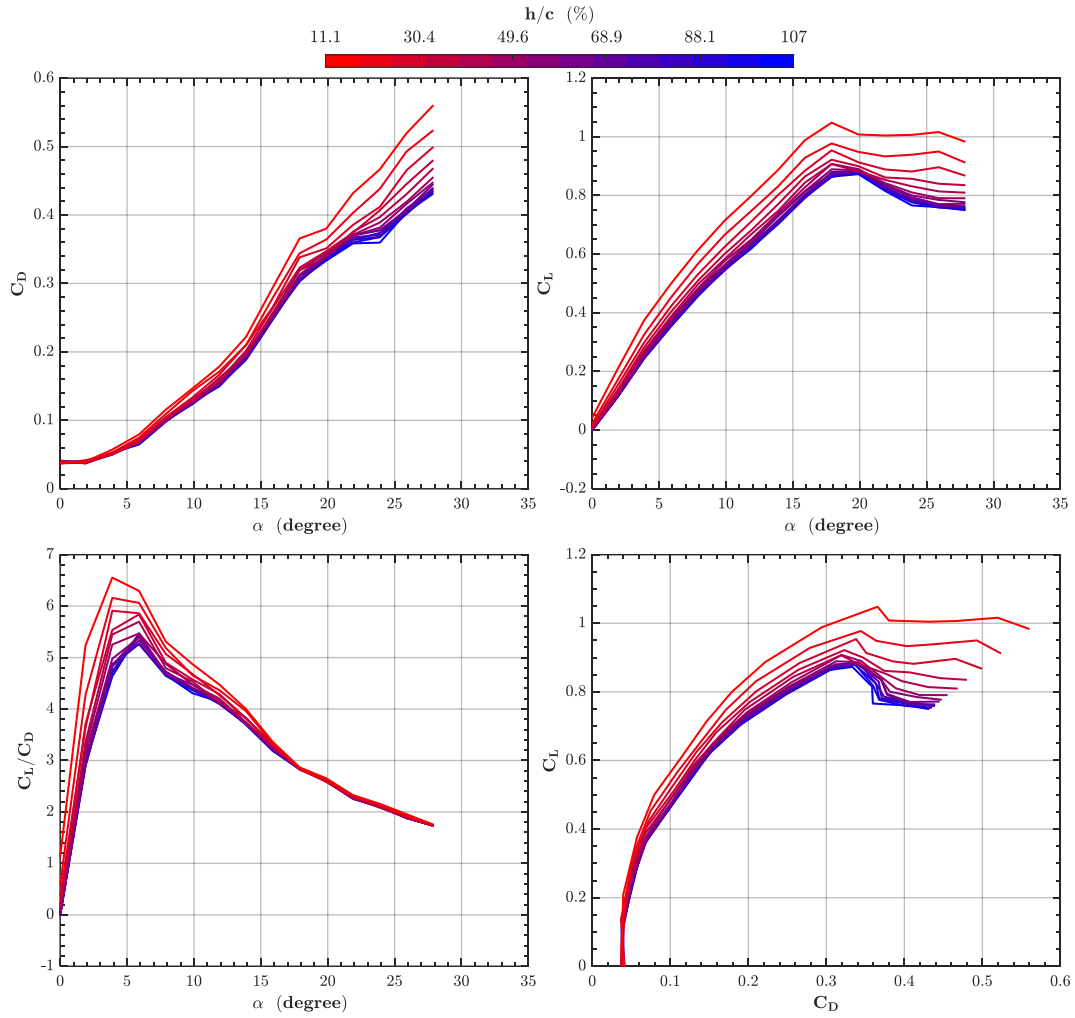

Figure 4-10 Variation of Drag coefficient C_D, Lift-to-Drag ratio C_L/C_D, Lift coefficient C_L as a function of angle of attack and Drag Polar for the delta wing 1b

In Figure 4-11, variation of moment coefficient C_M at trailing-edge (TE) and center of gravity (CG) as functions of angle of attack and lift coefficient C_L, and non-dimensional center of pressure coordinate X_P as a function of angle of attack for the delta wing 1b are given for different height values. Considering the distribution of C_M at trailing-edge shown in the upper left chart, similar findings are observed for the delta wing 1b compared to results of the delta wing 1a such that the moment coefficients at all angles increased as the height decreases and the rate of change of

the pitch-up moment is also increasing with GE intensity and becomes maximum for the closest distance to the ground.

The distribution of C_M at the trailing-edge as a function of C_L is demonstrated in the bottom left chart. The highest slope is also seen for the OGE condition, whereas the aerodynamic center in pitch slightly shifts towards to the trailing-edge of the wing as the height decreases.

Considering the C_M at wing center of gravity (CG) as a function of α shown at upper right corner, all curves at different heights pose positive slopes and positive C_M values. As the height of the wing decreases $C_{M_{cg}}$ is increased monotonically, which indicates larger longitudinal control authority need for trim.

Considering the X_P as function of angle of attack demonstrated in lower right corner, GE shifts the center of pressure X_P toward trailing-edge of the wing, whereas no remarkable movement of the X_P is seen for the different height values close to the OGE condition considering the associated angle of attack. For all heights, the center of pressure is located between $x/c = 0.3$ and $x/c = 0.42$.

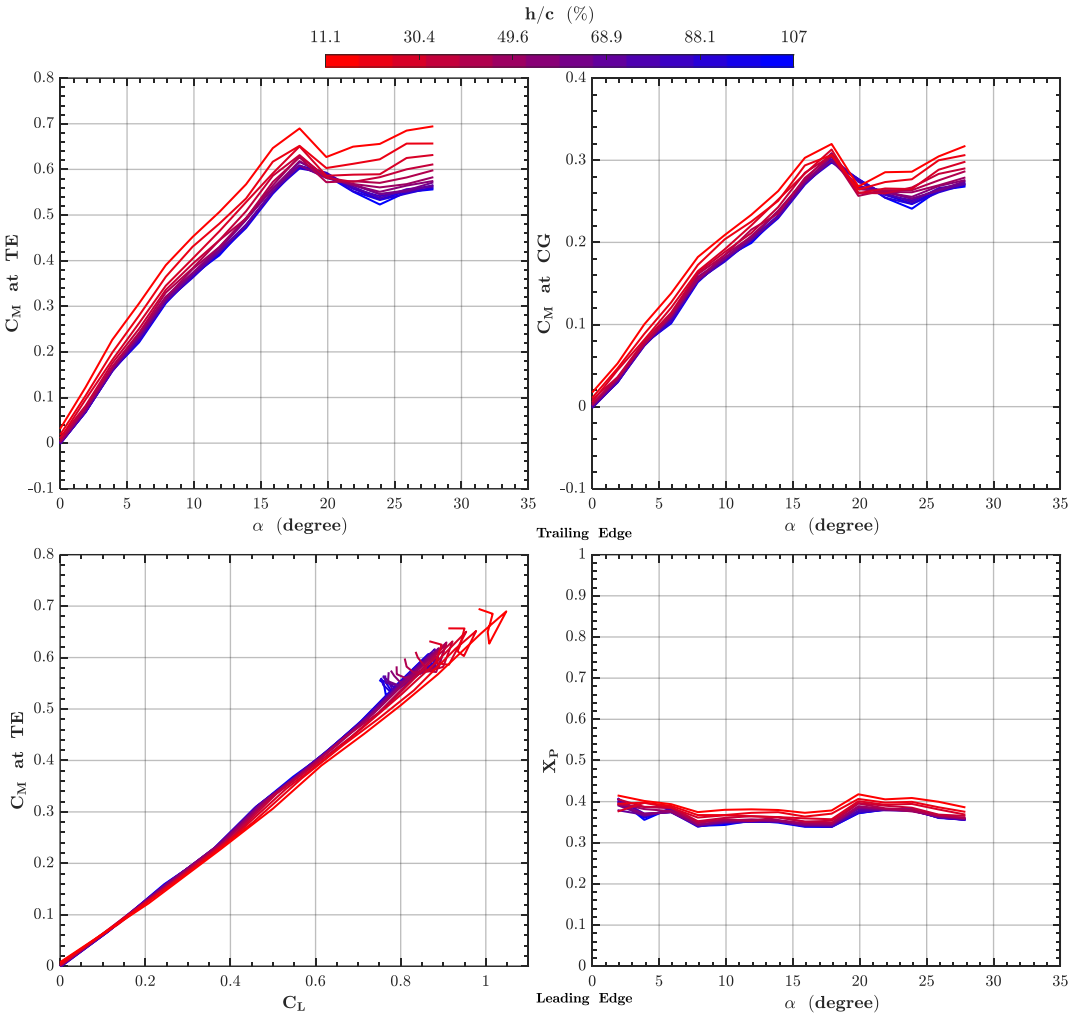

Figure 4-11 Variation of Moment coefficient C_M at trailing-edge (TE) and center of gravity (CG) as a function of angle of attack and Lift coefficient C_L, and Non-Dimensional Pressure Center coordinate X_P as a function of angle of attack for the delta wing 1b

4.2.2.3 Results of Force Measurements for the Reverse Wing 2a

In Figure 4-12, distributions of drag coefficient C_D, lift-to-drag ratio C_L/C_D, lift coefficient C_L as a function of angle of attack and drag polar for the reverse delta wing 2a are given for different non-dimensional height values varying from $h/c = 2.96\%$ to 107%. Considering the drag coefficient C_D shown in the upper left chart, drag curve slope is significantly increased with increasing ground effect intensity whereas there is no clear evidence of stall considering all height values including OGE condition.

Considering the lift coefficient C_L shown in upper right chart, the reverse delta wing 2a exhibits a unique stall behavior, which is characterized by small or negligible lift loss after stall angle. The reverse delta wing has a stall angle of $\alpha_s = 18^o$ for OGE condition whereas significantly earlier stall onset at $\alpha = 14^o$ exits for the smallest height IGE case with higher maximum C_L values. However, increase in lift coefficient is observed for all angles with increasing GE intensity in both low and high angles. The lift curve slope increases for small angles with decreasing height and is the highest for the smallest height, hence the rate of increase in C_L increases dramatically with increasing angle of attack as the wing approaches to the ground. Around $\alpha = 5^o$, lift curve slope is reduced, which is observed for all heights. The stall angle monotonically decreases with increasing GE intensity and becomes minimum for the closest distance to ground at $h/c = 2.96\%$. After the stall angle, lift curve slope becomes nearly zero and slightly negative and tends to be flat for the highest GE intensity cases.

Considering C_L/C_D distribution shown in the lower left chart, the performance of the wing is improved at all angles of attack up to $\alpha = 18^o$. The improvement is considerably larger for small angles up to $\alpha = 8^o$, which is due to the higher lift increase compared to drag increase. In addition, the peak values of C_L/C_D for the delta wing is seen around $\alpha = 4^o$, where the peak values for height values close to OGE condition are postponed to higher angles of attack close to $\alpha = 8^o$. Comparing

the maximum C_L/C_D values between OGE at $h/c = 107\%$ case and the most intense ground effect case at $h/c = 2.96\%$, the performance is improved by 45% for the latter case.

Considering the drag polar shown at the lower right chart, the slopes of the drag polar curves of the delta wing are increasing with increasing ground effect intensity, which is higher between $C_D = 0.1$ and $C_D = 0.25$ interval and becomes flat after stall for the smallest height values. The slope is unchanged up to $C_D = 0.088$ for all heights.

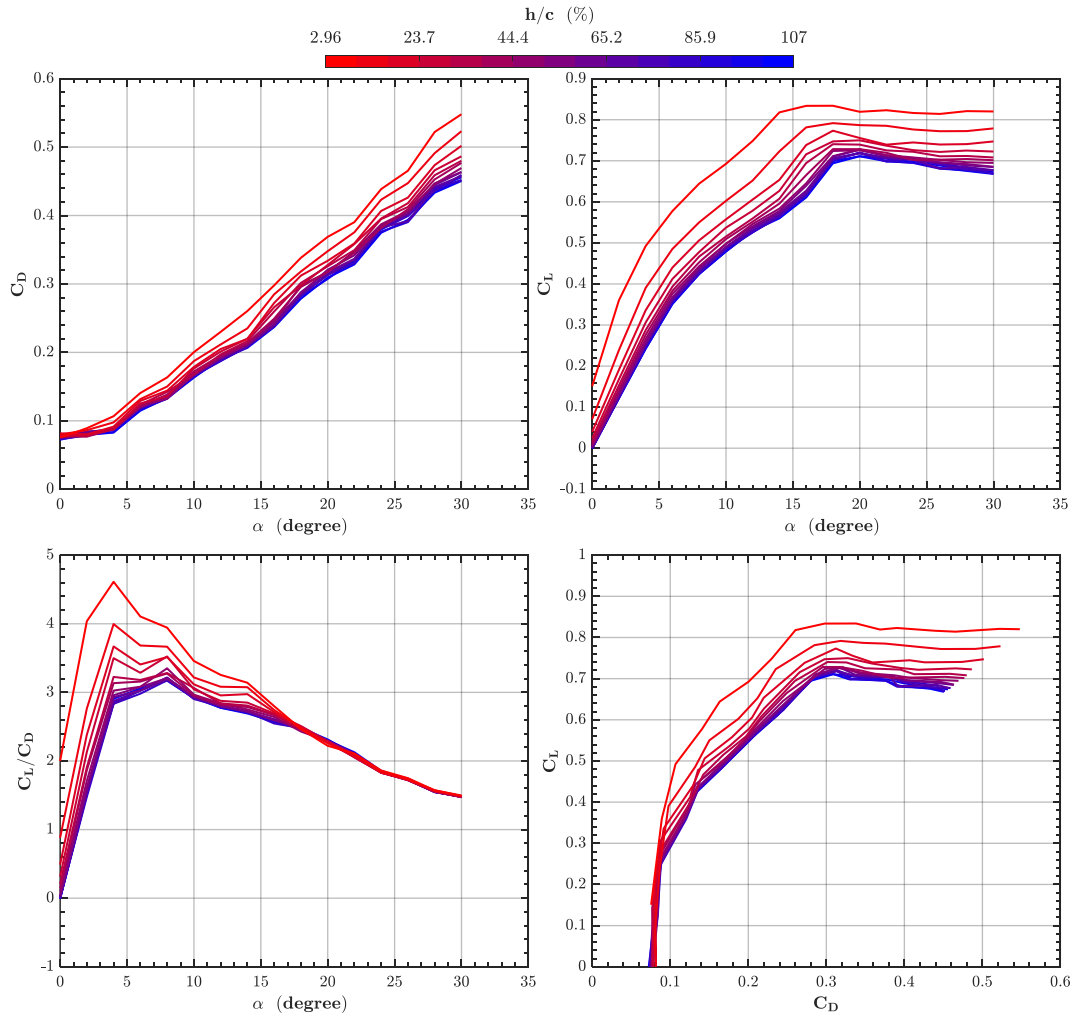

Figure 4-12 Variation of Drag coefficient C_D, Lift-to-Drag ratio C_L/C_D, Lift coefficient C_L as a function of angle of attack and Drag Polar for the reverse delta wing 2a

In Figure 4-13, variation of moment coefficient C_M at trailing-edge (TE) and center of gravity (CG) as functions of angle of attack and lift coefficient C_L, and non-dimensional center of pressure coordinate X_P as a function of angle of attack for the reverse delta wing 2a are given for different height values. Considering the distribution of C_M at trailing-edge shown in the upper left chart, the moment coefficients at all angles increased as the height decreases and the rate of change of the pitch-up moment is also increasing with GE intensity up to stall angles after which sudden pitch moment curve slope decrease occurs for all heights. After stall, as the GE intensity increases, pitch moment curve slope increases.

The distribution of C_M at the trailing-edge as a function of C_L is demonstrated in the bottom left chart. The highest slope is also seen for the OGE condition, whereas the slope of the curve remains nearly unchanged up to $C_L = 0.4$ value. After the this point, aerodynamic center in pitch monotonically shifts towards to the trailing-edge of the wing as the height decreases, whereas shift in aerodynamic center in pitch gets bigger for the higher the GE intensity values.

Considering the C_M at wing center of gravity (CG) as a function of α shown at upper right corner, all curves at different heights pose positive slopes and positive C_M values. As the height of the wing decreases $C_{M_{cg}}$ is increased monotonically, but increase in moment is negligible after $\alpha = 18^o$ for all heights.

Considering the X_P as function of angle of attack demonstrated in lower right corner, GE shifts the center of pressure X_P toward trailing-edge of the wing for all angles, whereas no remarkable movement of the X_P is seen for the different height values close to the OGE condition considering the associated angle of attack. The center of pressure movement is the minimum at $\alpha = 14^o$ for all heights, whereas the center of pressure is located between $x/c = 0.13$ and $x/c = 0.23$.

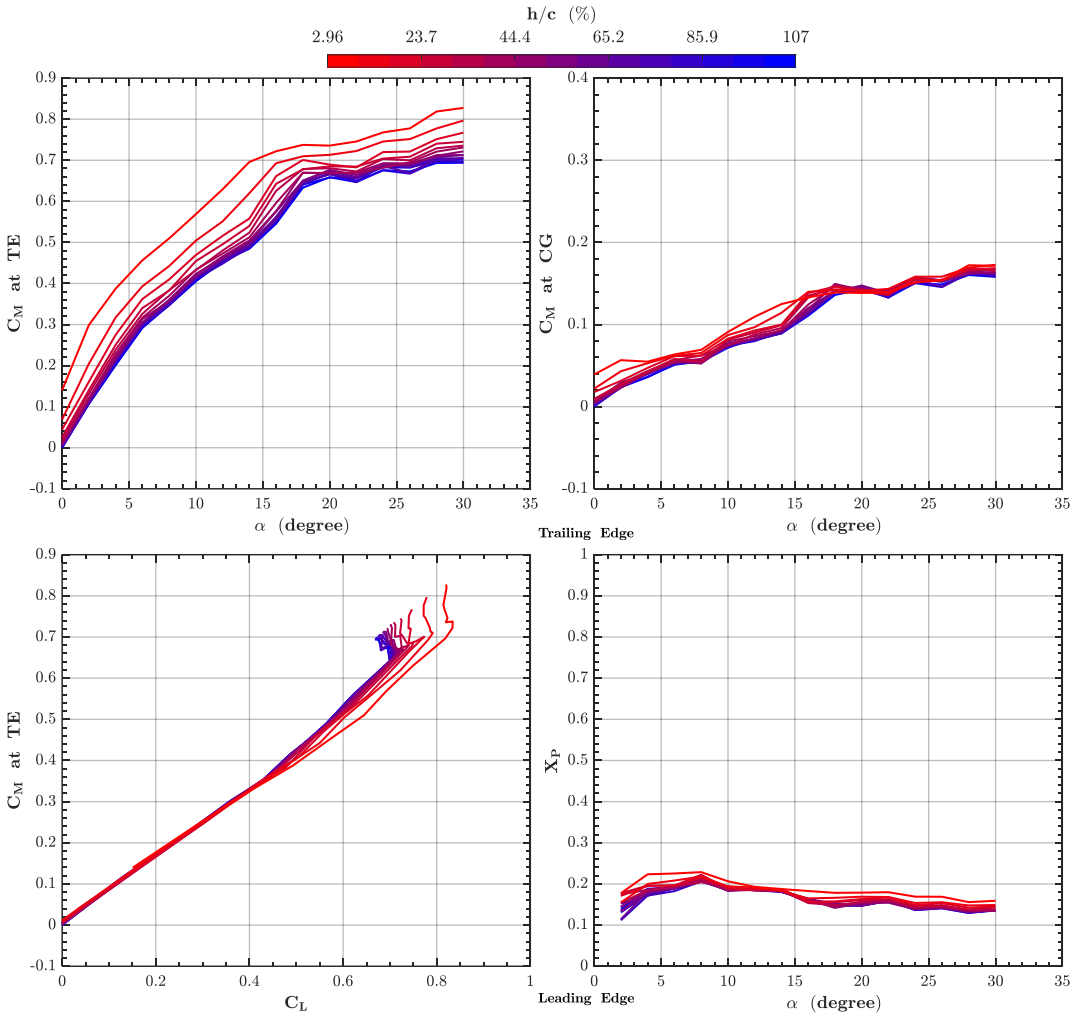

Figure 4-13 Variation of Moment coefficient C_M at trailing-edge (TE) and center of gravity (CG) as a function of angle of attack and Lift coefficient C_L, and Non-Dimensional Pressure Center coordinate X_P as a function of angle of attack for the reverse delta wing 2a

4.2.2.4 Results of Force Measurements for the Reverse Wing 2b

In Figure 4-14, distributions of drag coefficient C_D, lift-to-drag ratio C_L/C_D, lift coefficient C_L as a function of angle of attack and drag polar for the reverse delta wing 2b are given for different non-dimensional height values varying from $h/c = 5.93\%$ to 102%. Considering the drag coefficient C_D shown in the upper left chart, drag curve slope is also significantly increased with increasing ground effect intensity and higher at all heights compared to drag curve slopes of the reverse delta wing 2a. There is also no clear evidence of stall considering all height values including OGE condition.

Considering the lift coefficient C_L shown in upper right chart, the reverse delta wing 2b exhibits a different stall behavior compared to reverse delta wing 2a, which is accompanied by significant lift curve slope decrease. Although, there is significant slope decrease, it remains positive and slopes are quite similar after stall for all heights. The reverse delta wing has a stall angle of $\alpha_s = 10^o$ for OGE condition whereas significantly earlier stall onset at $\alpha = 6^o$ exists for the smallest height IGE case with higher maximum C_L values. However, increase in lift coefficient is observed for all angles with increasing GE intensity in both low and high angles. The lift curve slope increases for small angles with decreasing height and is the highest for the smallest height, hence the rate of increase in C_L increases dramatically with increasing angle of attack as the wing approaches to the ground and becomes maximum around $\alpha = 5^o$. The stall angle monotonically decreases with increasing GE intensity and becomes minimum for the closest distance to ground at $h/c = 5.93\%$.

Considering C_L/C_D distribution shown in the lower left chart, the performance of the wing is improved at all angles of attack up to $\alpha = 13^o$. The improvement is considerably larger for small angles up to $\alpha = 4^o$, which is due to the higher lift increase compared to negligible drag increase. In addition, the peak values of C_L/C_D for the reverse delta wing is seen around $\alpha = 3.6^o$, where the angles for the peak

values for different heights remain unchanged no matter how low the GE intensity is. Comparing the maximum C_L/C_D values between OGE at $h/c = 102\%$ case and the most intense ground effect case at $h/c = 5.93\%$, the performance is improved by 40% for the latter case.

Considering the drag polar shown at the lower right chart, the slopes of the drag polar curves of the delta wing are increasing with increasing ground effect intensity, which is higher between $C_D = 0.04$ and $C_D = 0.1$ interval and becomes flat after stall for the smallest height values. The slope is unchanged up to $C_D = 0.04$ for all heights.

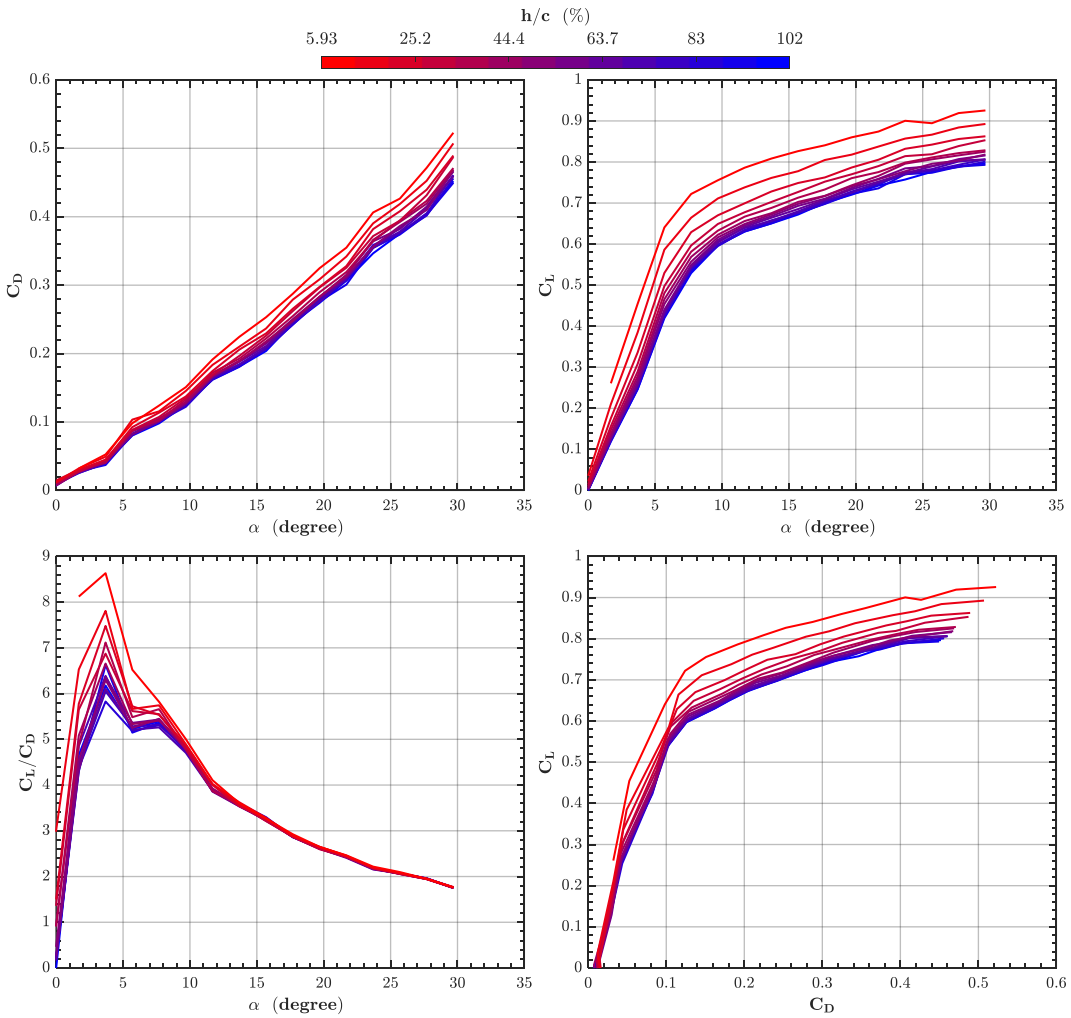

Figure 4-14 Variation of Drag coefficient C_D, Lift-to-Drag ratio C_L/C_D, Lift coefficient C_L as a function of angle of attack and Drag Polar for the reverse delta wing 2b

In Figure 4-15, variation of moment coefficient C_M at trailing-edge (TE) and center of gravity (CG) as functions of angle of attack and lift coefficient C_L, and non-dimensional center of pressure coordinate X_P as a function of angle of attack for the reverse delta wing 2b are given for different height values. Considering the distribution of C_M at trailing-edge shown in the upper left chart, the moment coefficients at all angles increased as the height decreases and the rate of change of the pitch-up moment is also increasing with GE intensity up to stall angles and after which sudden pitch moment curve slope decrease occurs for all heights. After stall, as the GE intensity increases, pitch moment curve shifts upward in y axis, whereas no slope change is observed.

The distribution of C_M at the trailing-edge as a function of C_L is demonstrated in the bottom left chart. The slope of the curve remains unchanged up to $C_L = 0.6$ value for all heights. After this point, aerodynamic center in pitch monotonically shifts towards to the trailing-edge of the wing as the height decreases, whereas shift in aerodynamic center in pitch gets bigger for the higher the GE intensity values.

Considering the C_M at wing center of gravity (CG) as a function of α shown at upper right corner, all curves at different heights pose positive slopes and positive C_M values. As the height of the wing decreases $C_{M_{cg}}$ is increased monotonically, but increase in moment with increasing GE intensity is relatively the same for all angles.

Considering the X_P as function of angle of attack demonstrated in lower right corner, GE shifts the center of pressure X_P toward trailing-edge of the wing for all angles, whereas the movement of the X_P is more remarkable at low angles of attack. The center of pressure movement is the minimum at $\alpha = 14^o$ for all heights, whereas the center of pressure is located between $x/c = 0$ and $x/c = 0.14$, hence travels in a range, which is very close to leading-edge of the wing.

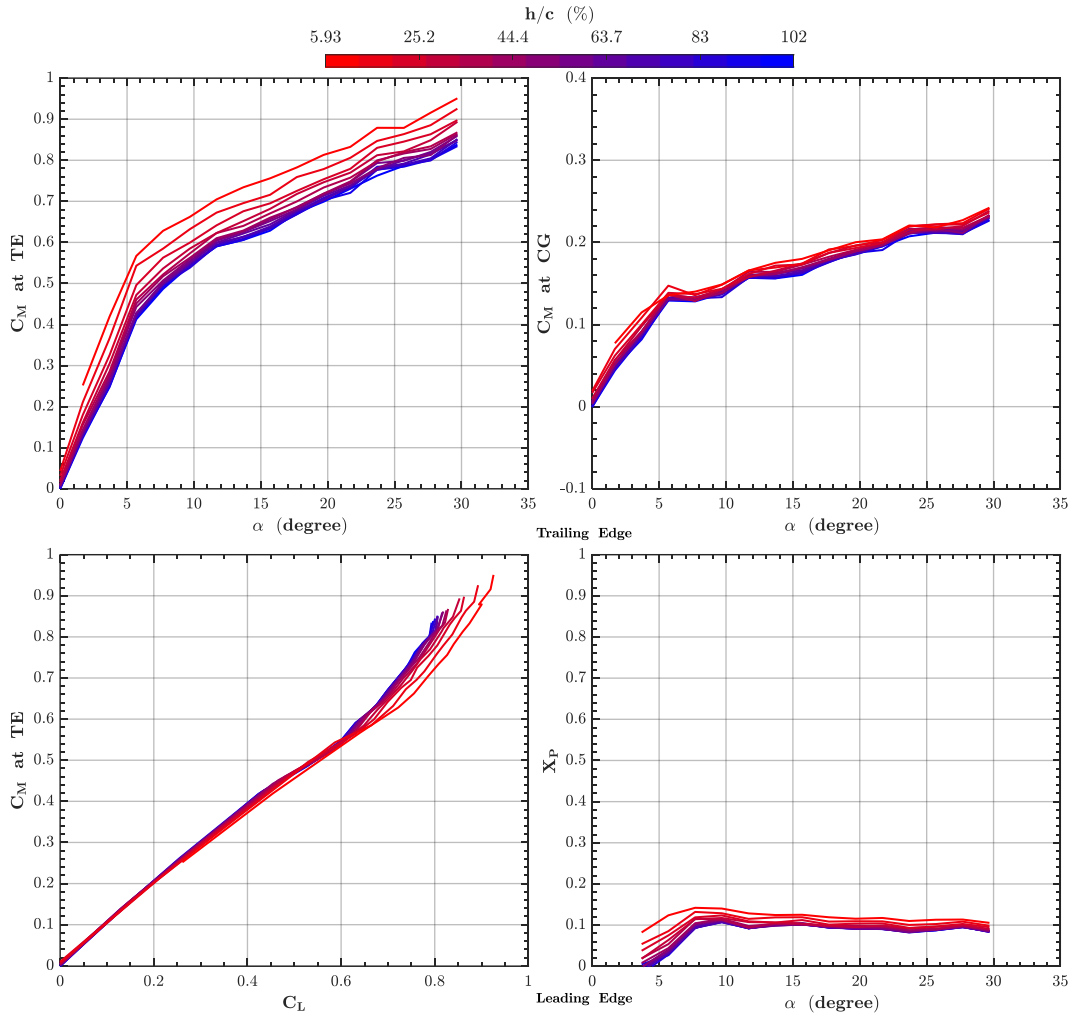

Figure 4-15 Variation of Moment coefficient C_M at trailing-edge (TE) and center of gravity (CG) as a function of angle of attack and Lift coefficient C_L, and Non-Dimensional Pressure Center coordinate X_P as a function of angle of attack for the reverse delta wing 2b

4.2.2.5 Results of Force Measurements for the Reverse Wing 2c

In Figure 4-16, distributions of drag coefficient C_D, lift-to-drag ratio C_L/C_D, lift coefficient C_L as a function of angle of attack and drag polar for the reverse delta wing 2c are given for different non-dimensional height values varying from $h/c = 5.93\%$ to 113%. The wing anhedral permits testing of the wing at lower angles of attack at small heights due to the risk of wing tip contact to the ground plane. Therefore, some of the angles for high GE cases are missing since these points were not tested. Considering the drag coefficient C_D shown in the upper left chart, drag values are increasing with increasing angle of attack and ground effect intensity whereas there is no clear evidence of stall considering all height values including OGE condition.

Considering the lift coefficient C_L shown in upper right chart, lift curve slope decreases significantly after stall. However, lift increase is persistent and the decrease in slope becomes more significant with increasing GE intensity. The reverse delta wing has a stall angle of $\alpha_s = 9^o$ for OGE condition whereas stall onset is not much affected by increasing GE intensity. However, increase in lift coefficient is observed for all angles with increasing GE intensity in both low and high angles. The lift curve slope for small angles increases with decreasing height and is the highest for the smallest height, hence the rate of increase in C_L increases dramatically with increasing angle of attack as the wing approaches to the ground. Around $\alpha = 7^o - 9^o$, lift curve slope is reduced, which is observed for all heights. After the stall angle, lift curve slope reduces more and more, which eventually becomes flat.

Considering C_L/C_D distribution shown in the lower left chart, the performance of the wing is improved at all angles of attack up to $\alpha = 11^o$. The improvement is considerably larger for small angles up to $\alpha = 7^o$, which is due to the higher lift increase compared to drag increase. In addition, the peak values of C_L/C_D for the delta wing is seen around $\alpha = 5^o$, where the angles for the peak values for different heights do not change with decreasing heights. Comparing the maximum C_L/C_D

values between OGE at $h/c = 113\%$ case and the most intense ground effect case at $h/c = 5.93\%$, the performance is improved by 15% for the latter case.

Considering the drag polar shown at the lower right chart, the slopes of the drag polar curves of the delta wing are increasing with increasing ground effect intensity, which is higher between $C_D = 0.2$ and $C_D = 0.6$ interval and becomes more negative after stall for the smallest height values, which indicates drag increase cannot be accompanied with lift increase. The slope is unchanged up to $C_D = 0.085$ for all heights.

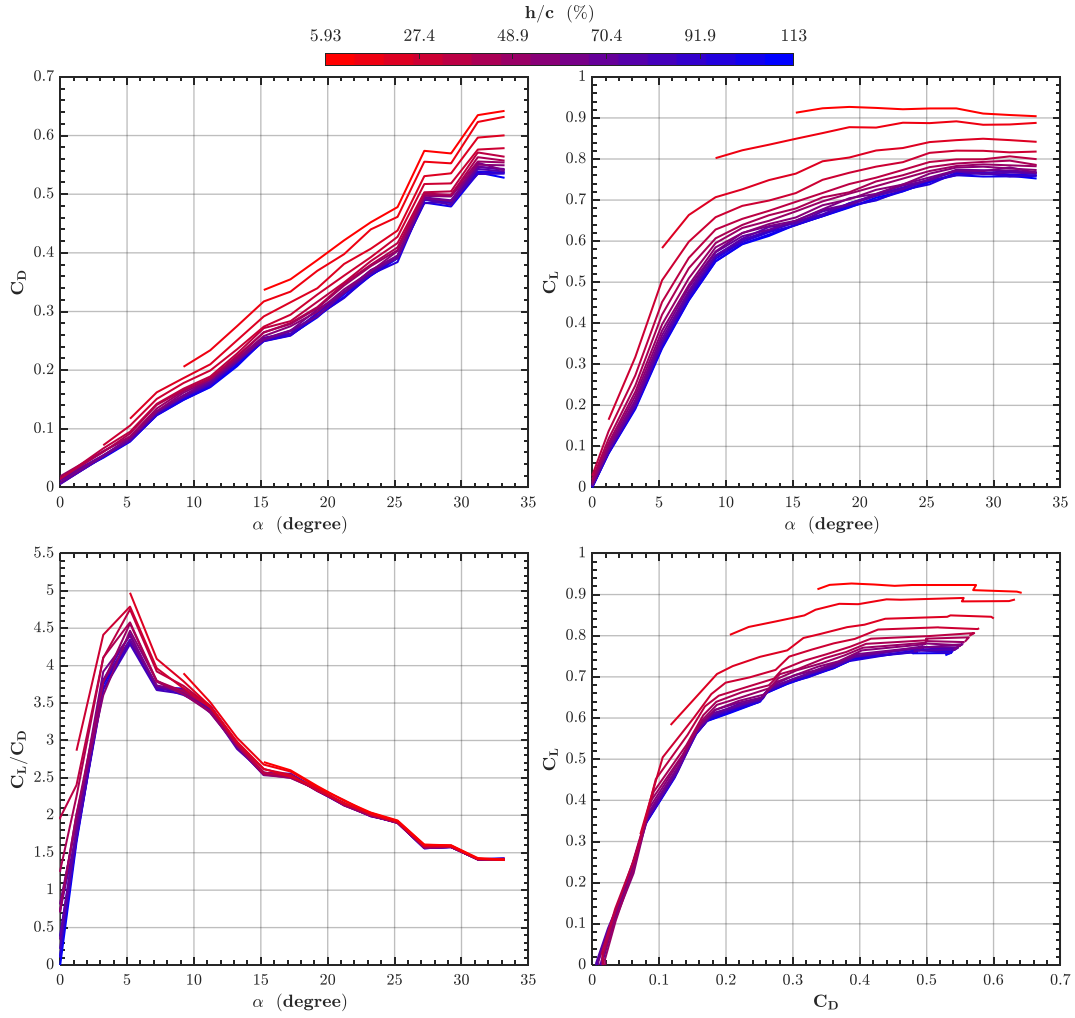

Figure 4-16 Variation of Drag coefficient C_D, Lift-to-Drag ratio C_L/C_D, Lift coefficient C_L as a function of angle of attack and Drag Polar for the reverse delta wing 2c

In Figure 4-17, variation of moment coefficient C_M at trailing-edge (TE) and center of gravity (CG) as functions of angle of attack and lift coefficient C_L, and non-dimensional center of pressure coordinate X_P as a function of angle of attack for the reverse delta wing 2c are given for different height values. Considering the distribution of C_M at trailing-edge shown in the upper left chart, the moment coefficients at all angles increased as the height decreases and the rate of change of the pitch-up moment is also increasing with GE intensity up to stall angles and after which sudden pitch moment curve slope decrease occurs for all heights. After stall, pitch moment curve slope decreases as the GE intensity increases.

The distribution of C_M at the trailing-edge as a function of C_L is demonstrated in the bottom left chart. The slope of the curve remains nearly unchanged up to $C_L = 0.6$ value. After this point, aerodynamic center in pitch monotonically shifts towards to the trailing-edge of the wing as the height decreases, whereas shift in aerodynamic center in pitch gets bigger for the higher the GE intensity values. The slope change is also postponed to higher C_L values with increasing GE intensity.

Considering the C_M at wing center of gravity (CG) as a function of α shown at upper right corner, all curves at different heights pose positive slopes and positive C_M values (except for a small region around $\alpha = 0^o$). As the height of the wing decreases $C_{M_{cg}}$ is increased monotonically, but increase in moment is negligible after $\alpha = 5^o$ for all heights.

Considering the X_P as function of angle of attack demonstrated in lower right corner, GE shifts the center of pressure X_P toward trailing-edge of the wing for all angles, whereas no remarkable movement of the X_P is seen for the different height values close to the OGE condition considering the associated angle of attack. The center of pressure is located between $x/c = 0.14$ and $x/c = 0.22$ considering all angles and height values.

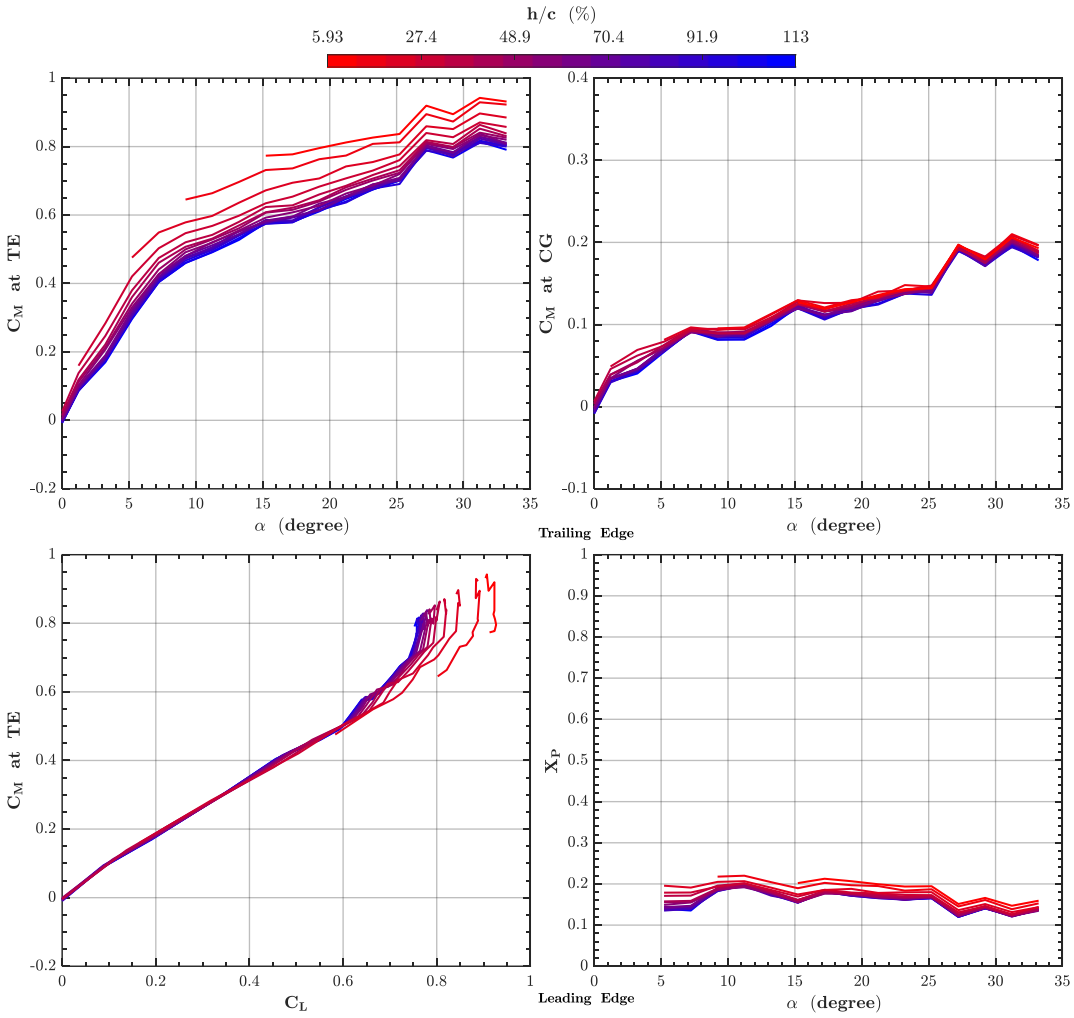

Figure 4-17 Variation of Moment coefficient C_M at trailing-edge (TE) and center of gravity (CG) as a function of angle of attack and Lift coefficient C_L, and Non-Dimensional Pressure Center coordinate X_P as a function of angle of attack for the reverse delta wing 2c

4.2.2.6 Results of Force Measurements for the Reverse Wing 2d

In Figure 4-18, distributions of drag coefficient C_D, lift-to-drag ratio C_L/C_D, lift coefficient C_L as a function of angle of attack and drag polar for the reverse delta wing 2d are given for different non-dimensional height values varying from $h/c = 3.7\%$ to 107%. Some of the angles for high GE cases are also missing since these points were not tested due to anhedral angle of the wing as mentioned before. Considering the drag coefficient C_D shown in the upper left chart, drag curve slope is increasing with increasing ground effect, which is more pronounced after $\alpha = 15^o$. However, the slopes are lesser than the ones for the reverse delta wing 2c at the same heights considering the effect of increased anhedral angle.

Considering the lift coefficient C_L shown in upper right chart, lift curve slope decreases significantly after stall. However, lift increase is not persistent and may even result in decrease in lift as seen for the highest GE cases. The decrease in slope becomes more pronounced with increasing GE intensity. The reverse delta wing has a stall angle of $\alpha_s = 11^o$ for OGE condition whereas stall onset is not much affected by increasing GE intensity. However, increase in lift coefficient is observed for all angles with increasing GE intensity in both low and high angles. The lift curve slope increases for small angles with decreasing height and is the highest for the smallest height, hence the rate of increase in C_L increases with increasing angle of attack as the wing approaches to the ground. Around $\alpha = 11^o$, lift curve slope is reduced, which is observed for all heights. After the stall angle, lift curve slope reduces more and more, which eventually becomes negative for the smallest height values. Just like the drag curves, the lift slopes are lesser than the ones for the reverse delta wing 2c at the same heights considering the effect of increased anhedral angle.

Considering C_L/C_D distribution shown in the lower left chart, the performance of the wing is improved at all angles of attack up to $\alpha = 11^o$. The improvement is not considerable with increasing GE intensity. The peak values of C_L/C_D for the reverse delta wing is seen around $\alpha = 5^o$, where the angles for the peak values for different

heights do not change with decreasing heights. Comparing the maximum C_L/C_D values between OGE at $h/c = 107\%$ case and the most intense ground effect and available case at $h/c = 63\%$, the performance is improved by 7.55% for the latter case.

Considering the drag polar shown at the lower right chart, the slopes of the drag polar curves of the delta wing are increasing with increasing ground effect intensity, which is only considerable between $C_D = 0.067$ and $C_D = 0.13$ and $C_D = 0.13$ and $C_D = 0.4$ intervals and becomes more negative after stall for the smallest height values, which indicates drag increase cannot be accompanied with lift increase and even become negative at the smallest height values due to the lift loss.

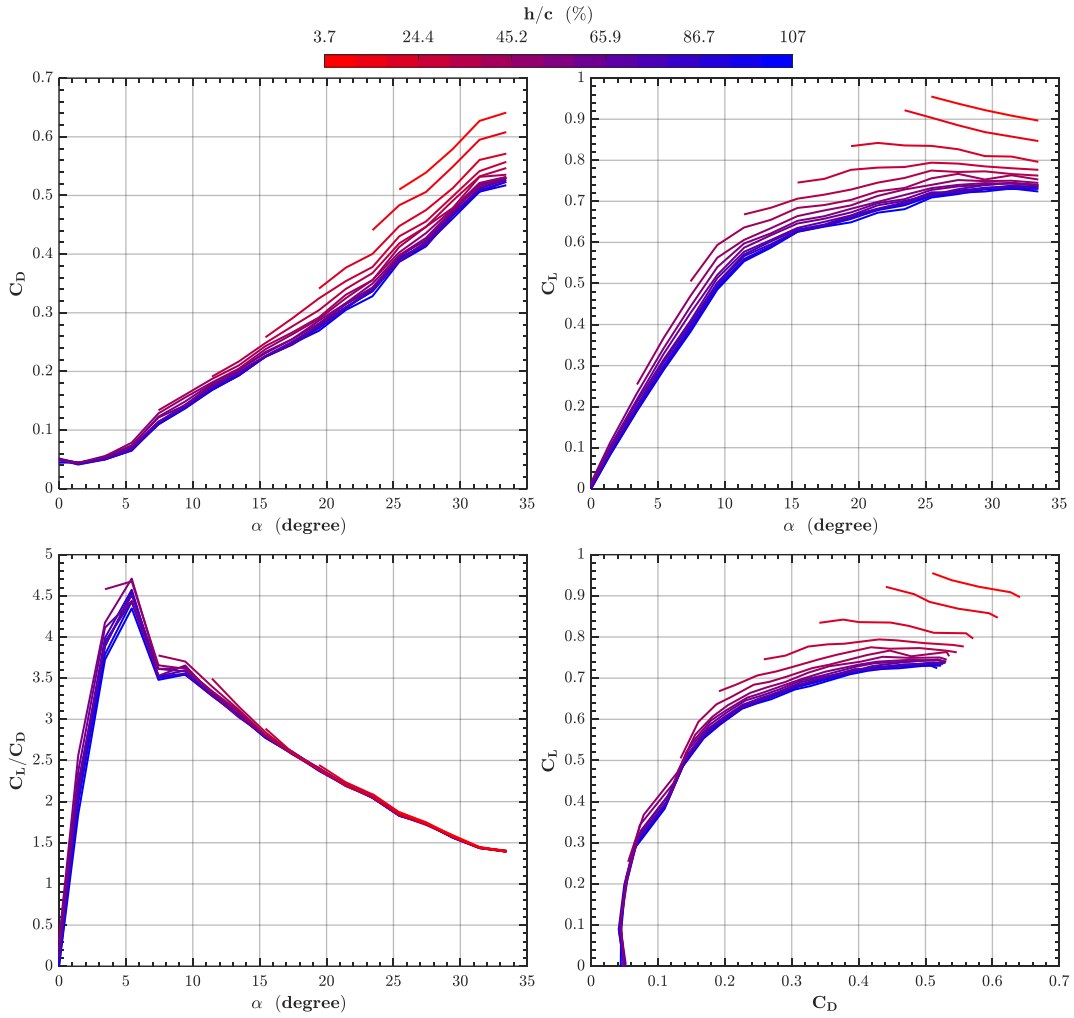

Figure 4-18 Variation of Drag coefficient C_D, Lift-to-Drag ratio C_L/C_D, Lift coefficient C_L as a function of angle of attack and Drag Polar for the reverse delta wing 2d

In Figure 4-19, variation of moment coefficient C_M at trailing-edge (TE) and center of gravity (CG) as functions of angle of attack and lift coefficient C_L, and non-dimensional center of pressure coordinate X_P as a function of angle of attack for the reverse delta wing 2d are given for different height values. Considering the distribution of C_M at trailing-edge shown in the upper left chart, the moment coefficients at all angles increased as the height decreases and the rate of change of the pitch-up moment is also increasing with GE intensity up to stall angles and after

which sudden pitch moment curve slope decrease occurs for all heights. After stall, pitch moment curve slope decreases as the GE intensity increases.

The distribution of C_M at the trailing-edge as a function of C_L is demonstrated in the bottom left chart. Similar to the results of the reverse delta wing 2c, the slope of the curve remains nearly unchanged up to $C_L = 0.6$ value. After this point, aerodynamic center in pitch monotonically shifts towards to the trailing-edge of the wing as the height decreases, whereas shift in aerodynamic center in pitch gets bigger for the higher the GE intensity values. The slope change is also postponed to higher C_L values with increasing GE intensity.

Considering the C_M at wing center of gravity (CG) as a function of α shown at upper right corner, all curves at different heights pose positive slopes and positive C_M values after $\alpha = 2.8^o$. As the height of the wing decreases $C_{M_{cg}}$ is increased monotonically, but increase in moment is limited for all angles considering different heights.

Considering the X_P as function of angle of attack demonstrated in lower right corner, GE shifts the center of pressure X_P toward trailing-edge of the wing for all angles greater than $\alpha = 7^o$, whereas just the opposite situation occurs for smaller angles such that GE shifts the center to the leading-edge. In addition, no remarkable movement of the X_P is seen up to $\alpha = 20^o$ for the different height values. The center of pressure is located between $x/c = 0.12$ and $x/c = 0.18$ considering all height values and angles after $\alpha = 7^o$.

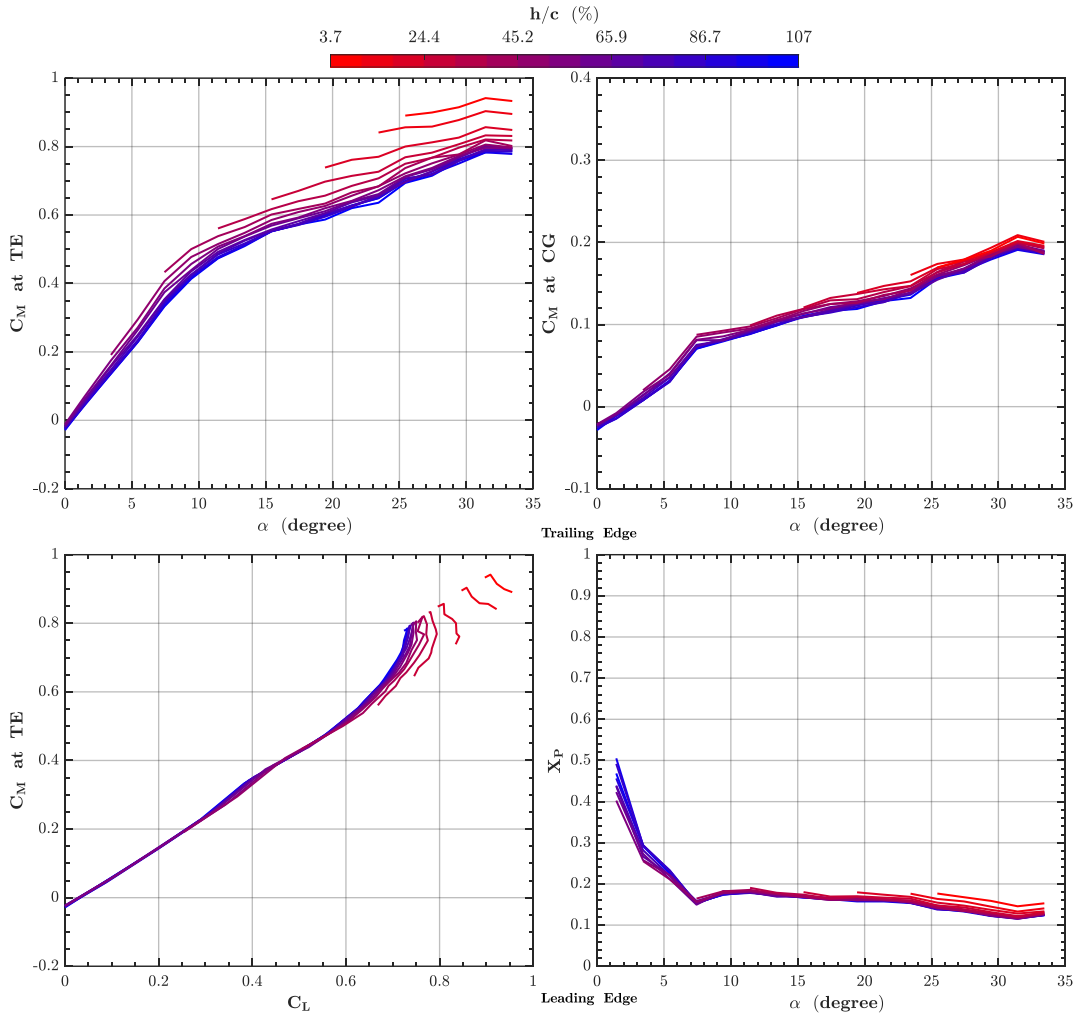

Figure 4-19 Variation of Moment coefficient C_M at trailing-edge (TE) and center of gravity (CG) as a function of angle of attack and Lift coefficient C_L, and Non-Dimensional Pressure Center coordinate X_P as a function of angle of attack for the reverse delta wing 2d

4.2.2.7 Results of Force Measurements for the Reverse Wing 2e

In Figure 4-20, distributions of drag coefficient C_D, lift-to-drag ratio C_L/C_D, lift coefficient C_L as a function of angle of attack and drag polar for the reverse delta wing 2e are given for different non-dimensional height values varying from $h/c = 9.63\%$ to 113%. Considering the drag coefficient C_D shown in the upper left chart, drag values are increasing with increasing angle of attack and ground effect intensity whereas there is no clear evidence of stall considering all height values including OGE condition. The increase in drag curve slope is more pronounced after $\alpha = 11^o$.

Considering the lift coefficient C_L shown in upper right chart, lift curve slope decreases significantly after stall. However, lift increase is persistent and the decrease in slope becomes more significant with increasing GE intensity. The reverse delta wing has a stall angle of $\alpha_s = 9^o$ for OGE condition whereas stall onset is not much affected by increasing GE intensity. However, increase in lift coefficient is observed for all angles with increasing GE intensity in both low and high angles. The lift curve slope for small angles increases with decreasing height and is the highest for the smallest height, hence the rate of increase in C_L increases significantly with increasing angle of attack as the wing approaches to the ground. Around $\alpha = 9^o$, lift curve slope is reduced, which is observed for all heights. After the stall angle, lift curve slope reduces more and more, which eventually becomes flat for the $h/c = 9.63\%$.

Considering C_L/C_D distribution shown in the lower left chart, the performance of the wing is improved at all angles of attack up to $\alpha = 11^o$. The improvement is considerably larger for small angles up to $\alpha = 7^o$, which is due to the higher lift increase compared to drag increase. In addition, the peak values of C_L/C_D for the delta wing is seen around $\alpha = 3^o$, where the angles for the peak values for different heights do not change with decreasing heights. Comparing the maximum C_L/C_D values between OGE at $h/c = 113\%$ case and the most intense ground effect case at $h/c = 24.4\%$, the performance is improved by 21% for the latter case, which

yields the maximum performance value achieved considering all wings tested in this study.

Considering the drag polar shown at the lower right chart, the slopes of the drag polar curves of the reverse delta wing are increasing with increasing ground effect intensity, which gets higher at $C_D = 0.03$ and becomes more negative after stall for the smallest height values and eventually becomes flat for the $h/c = 9.63\%$ case.

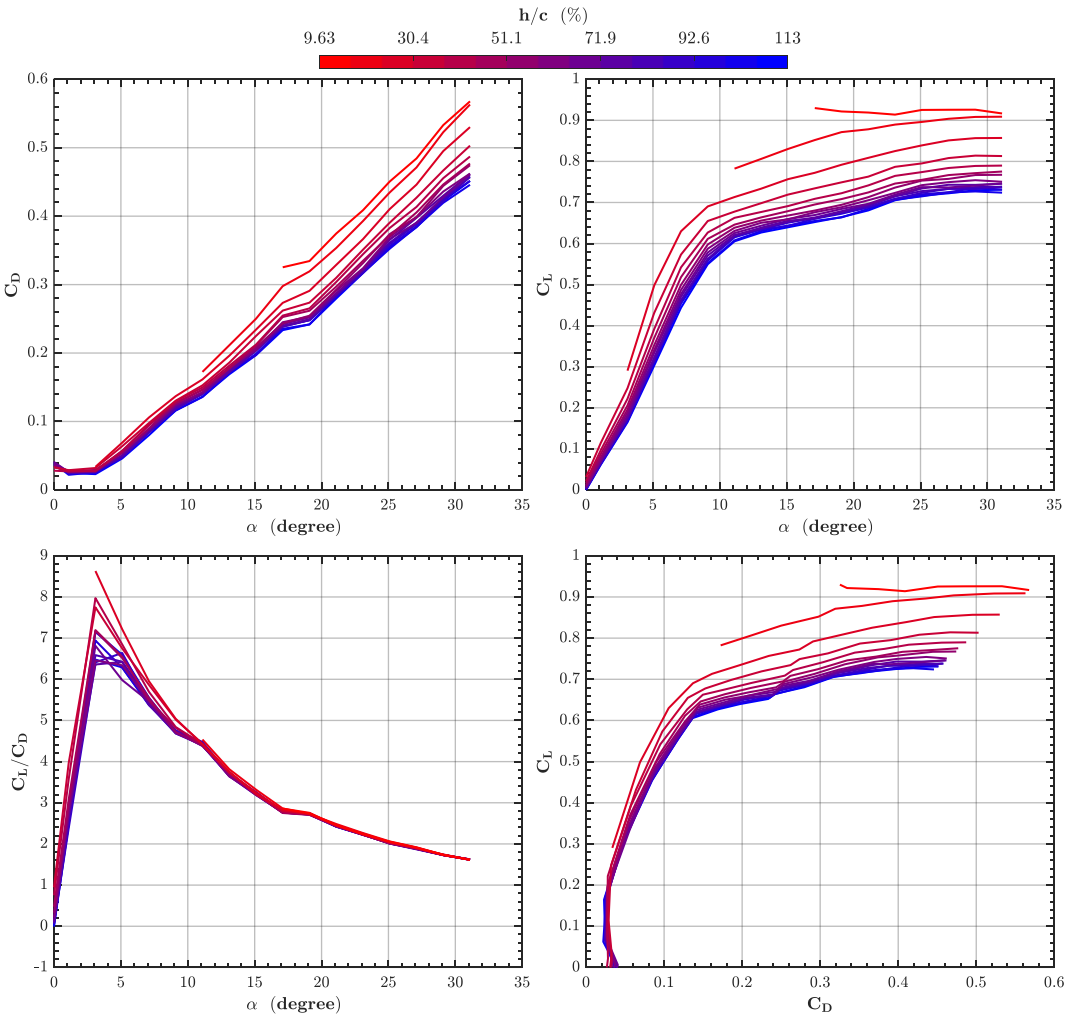

Figure 4-20 Variation of Drag coefficient C_D, Lift-to-Drag ratio C_L/C_D, Lift coefficient C_L as a function of angle of attack and Drag Polar for the reverse delta wing 2e

In Figure 4-21, variation of moment coefficient C_M at trailing-edge (TE) and center of gravity (CG) as functions of angle of attack and lift coefficient C_L, and non-dimensional center of pressure coordinate X_P as a function of angle of attack for the reverse delta wing 2e are given for different height values. Considering the distribution of C_M at trailing-edge shown in the upper left chart, the moment coefficients at all angles increased as the height decreases and the rate of change of the pitch-up moment is also increasing with GE intensity up to stall angles and after which sudden pitch moment curve slope decrease occurs for all heights. After stall, pitch moment curve slope remains the same with increasing GE intensity.

The distribution of C_M at the trailing-edge as a function of C_L is demonstrated in the bottom left chart. The slope of the curve remains nearly unchanged up to $C_L = 0.6$ value. After this point, aerodynamic center in pitch monotonically shifts towards to the trailing-edge of the wing as the height decreases, whereas shift in aerodynamic center in pitch gets bigger for the higher the GE intensity values. The slope change is also postponed to higher C_L values with increasing GE intensity.

Considering the C_M at wing center of gravity (CG) as a function of α shown at upper right corner, all curves at different heights pose positive slopes and positive C_M values (except for a small region around $\alpha = 0^o$). As the height of the wing decreases $C_{M_{cg}}$ is increased monotonically, but slopes of the curves remain quite similar for all heights.

Considering the X_P as function of angle of attack demonstrated in lower right corner, GE clearly shifts the center of pressure X_P toward trailing-edge of the wing after $\alpha = 10^o$, whereas no remarkable movement of the X_P is seen for the different height values close to the OGE condition considering the associated angle of attack. The center of pressure is located between $x/c = 0.19$ and $x/c = 0.34$ considering all height values and angles greater than $\alpha = 5^o$ whereas at lower angles, GE shifts X_P to the leading-edge of the wing. In $\alpha = 0^o$ to $\alpha = 5^o$ interval X_P is located between $x/c = 0.5$ and $x/c = 0.3$ for different heights.

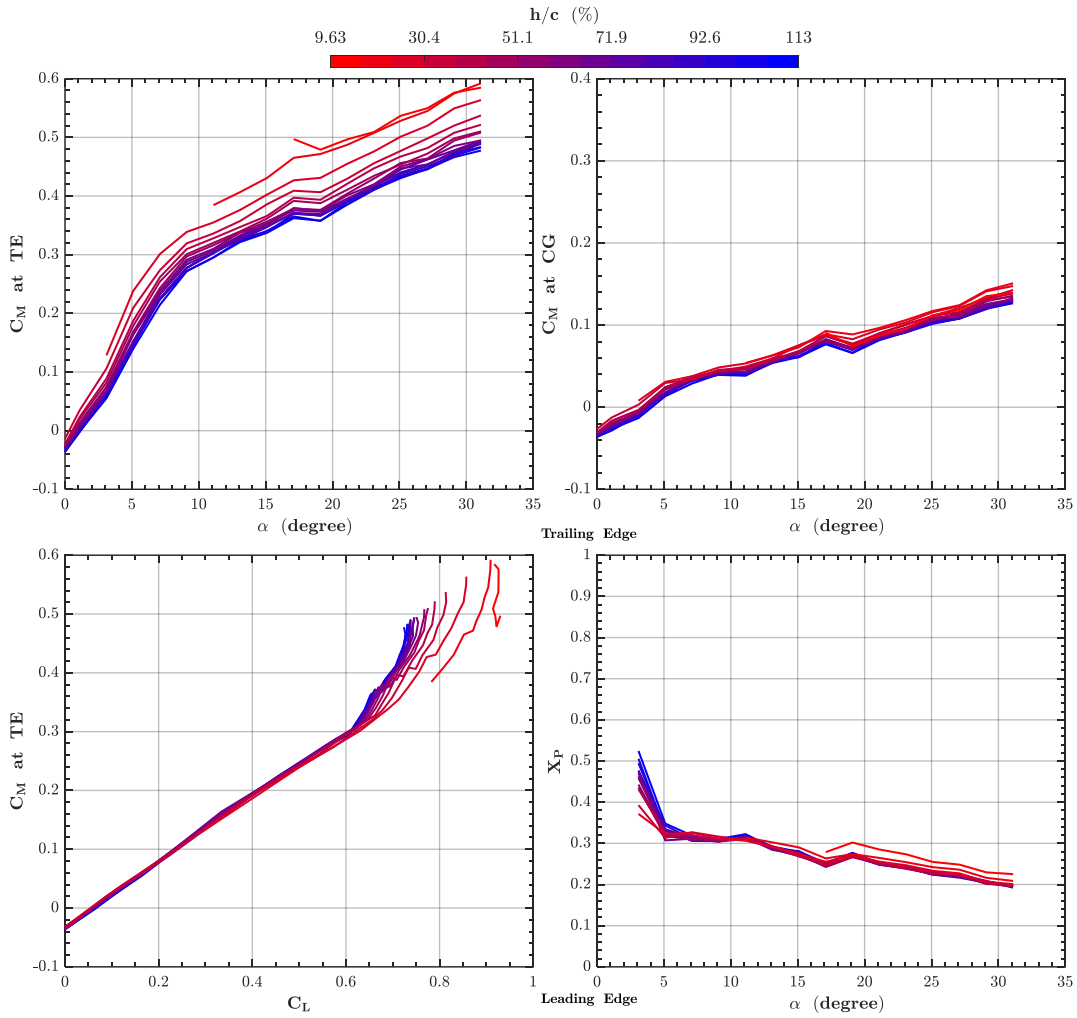

Figure 4-21 Variation of Moment coefficient C_M at trailing-edge (TE) and center of gravity (CG) as a function of angle of attack and Lift coefficient C_L, and Non-Dimensional Pressure Center coordinate X_P as a function of angle of attack for the reverse delta wing 2e

4.2.2.8 Results of Force Measurements for the Reverse Wing 2f

In Figure 4-22, distributions of drag coefficient C_D, lift-to-drag ratio C_L/C_D, lift coefficient C_L as a function of angle of attack and drag polar for the reverse delta wing 2f are given for different non-dimensional height values varying from $h/c = 15.6\%$ to 112%. Considering the drag coefficient C_D shown in the upper left chart, drag values are increasing with increasing angle of attack and ground effect intensity whereas there is no clear evidence of stall considering all height values including OGE condition. The increase in drag curve slope is more pronounced after $\alpha = 15^o$, whereas increase in drag is also very limited up to this angle. However, the slopes are lesser than the ones for the reverse delta wing 2e at the same heights considering the effect of increased anhedral angle.

Considering the lift coefficient C_L shown in upper right chart, lift curve slope decreases significantly after stall. However, lift increase is persistent and the decrease in slope becomes more significant with increasing GE intensity. The reverse delta wing has a stall angle of $\alpha_s = 10^o$ for OGE condition whereas stall onset is not much affected by increasing GE intensity. However, increase in lift coefficient is observed for all angles with increasing GE intensity in both low and high angles. The lift curve slope for small angles increases with decreasing height and is the highest for the smallest height, hence the rate of increase in C_L increases significantly with increasing angle of attack as the wing approaches to the ground. Around $\alpha = 10^o$, lift curve slope is reduced, which is observed for all heights. After the stall angle, lift curve slope reduces more and more, which eventually becomes flat for the $h/c = 15.6\%$. Just like the drag curves, the lift slopes are lesser than the ones for the reverse delta wing 2e at the same heights considering the effect of increased anhedral angle.

Considering C_L/C_D distribution shown in the lower left chart, the performance of the wing is improved at all angles of attack up to $\alpha = 8^o$. The improvement is considerably larger for small angles up to $\alpha = 5^o$, which is due to the higher lift increase compared to drag increase. In addition, the peak values of C_L/C_D for the

delta wing is seen around $\alpha = 4.5^{o}$, where the angles for the peak values for different heights do not change with decreasing heights. Comparing the maximum C_L/C_D values between OGE at $h/c = 113\%$ case and the most intense ground effect and available case at $h/c = 45.22\%$, the performance is improved by 13% for the latter case.

Considering the drag polar shown at the lower right chart, the slopes of the drag polar curves of the delta wing are increasing with increasing ground effect intensity, which gets higher after $C_D = 0.1$ and becomes more negative after stall for the smallest height values and eventually becomes flat for the $h/c = 15.6\%$ case.

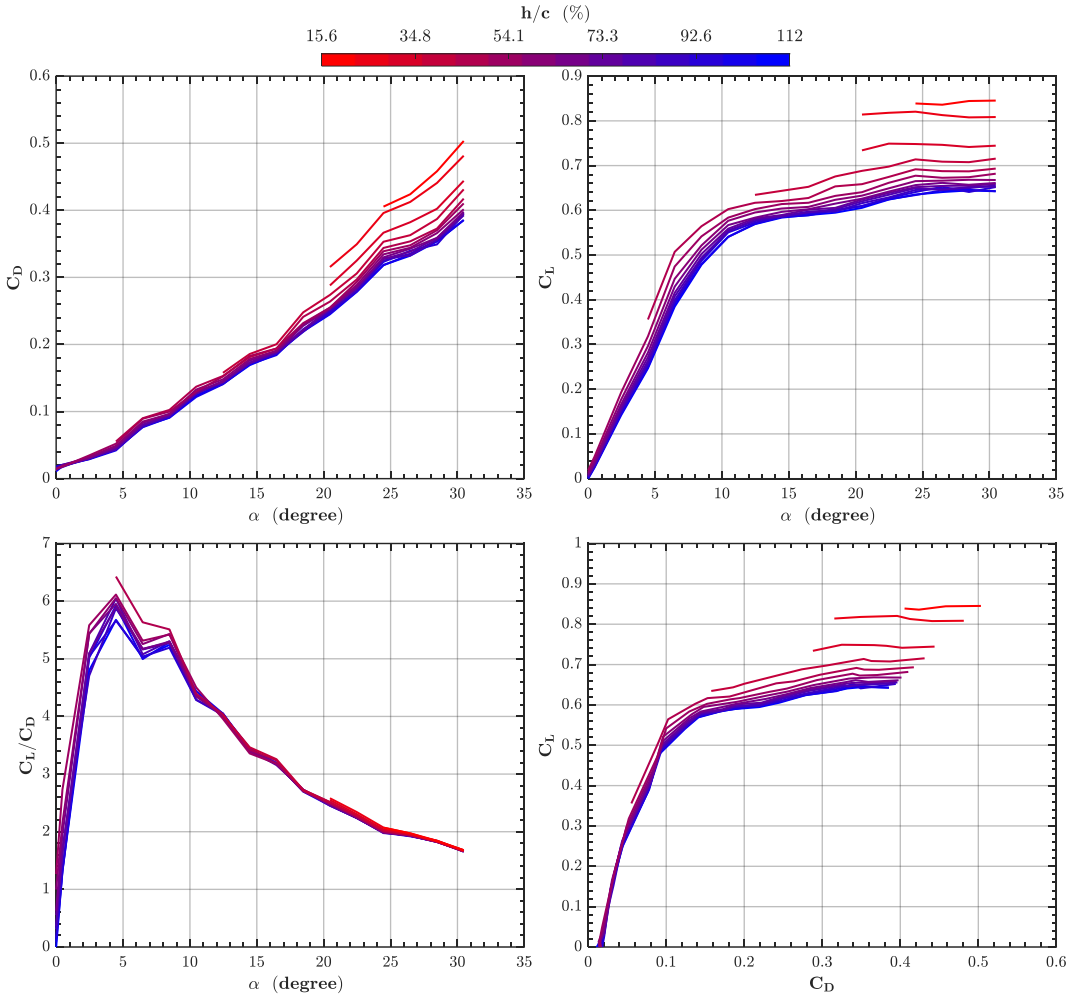

Figure 4-22 Variation of Drag coefficient C_D, Lift-to-Drag ratio C_L/C_D, Lift coefficient C_L as a function of angle of attack and Drag Polar for the reverse delta wing 2f

In Figure 4-23, variation of moment coefficient C_M at trailing-edge (TE) and center of gravity (CG) as functions of angle of attack and lift coefficient C_L, and non-dimensional center of pressure coordinate X_P as a function of angle of attack for the reverse delta wing 2f are given for different height values. Considering the distribution of C_M at trailing-edge shown in the upper left chart, the moment coefficients at all angles increased as the height decreases and the rate of change of the pitch-up moment is also increasing with GE intensity up to stall angles and after which sudden pitch moment curve slope decrease occurs for all heights. After stall, pitch moment curve slope remains the same with increasing GE intensity.

The distribution of C_M at the trailing-edge as a function of C_L is demonstrated in the bottom left chart. The slope of the curve remains nearly unchanged up to $C_L = 0.6$ value. After this point, aerodynamic center in pitch monotonically shifts towards to the trailing-edge of the wing as the height decreases, whereas shift in aerodynamic center in pitch gets bigger for the higher the GE intensity values. The slope change is also postponed to higher C_L values with increasing GE intensity.

Considering the C_M at wing center of gravity (CG) as a function of α shown at upper right corner, all curves at different heights pose positive slopes and positive C_M values (except for a small region around $\alpha = 0^o$). As the height of the wing decreases $C_{M_{cg}}$ is slightly and monotonically increased, but slopes of the curves remain quite similar for all heights. After $\alpha = 20^o$, increase in $C_{M_{cg}}$ is more pronounced.

Considering the X_P as function of angle of attack demonstrated in lower right corner, neither a remarkable movement nor a monotonic trend of the X_P is observed. At lower angles, GE shifts X_P to the leading-edge of the wing. In $\alpha = 0^o$ to $\alpha = 5^o$ interval X_P is located between $x/c = 0.36$ and $x/c = 0.3$ for different heights. Considering all heights and angles, X_P is located between $x/c = 0.36$ and $x/c = 0.23$.

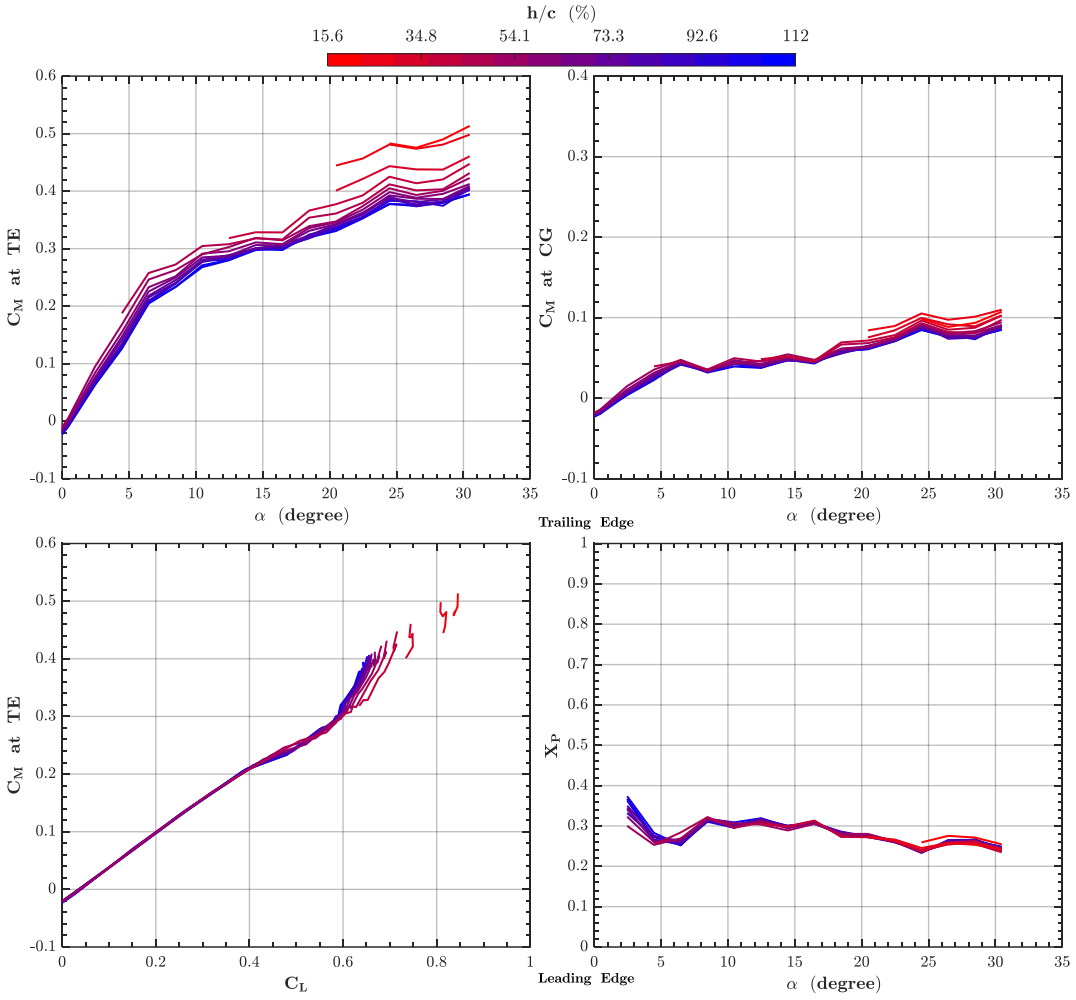

Figure 4-23 Variation of Moment coefficient C_M at trailing-edge (TE) and center of gravity (CG) as a function of angle of attack and Lift coefficient C_L, and Non-Dimensional Pressure Center coordinate X_P as a function of angle of attack for the reverse delta wing 2f

4.2.3 Results of Longitudinal Static Stability

In this chapter, longitudinal static stability assessment (Height Stability H.S.) of the wings is made based on Irodov's Criteria given in Relation 3. First, the height stability assessment is detailed for the delta wing 1a. Then, effect of thickness and H.S. assessments as well as comparisons among delta and reverse delta configurations are made for delta and reverse delta wings 1a, 1b, 2a, and 2b. Finally, effect of anhedral, and cropping on the H.S. of the reverse delta wings are examined for reverse delta wings 2b, 2c, 2d, 2e, and 2f.

4.2.3.1 Results of Longitudinal Static Stability for the Delta Wing 1a

The longitudinal static stability characteristics of the delta wing 1a are examined by constructing the height stability, H.S. and utilizing the aerodynamic center in pitch, X_a and aerodynamic center in height, X_h. In Figure 4-24, the X_a distribution is provided with respect to non-dimensional height, whereas the X_h is given with respect to angle of attack in Figure 4-25. In Figure 4-26, height stability contours with respect to angle of attack and non-dimensional height for the delta wing are provided by utilizing Eqn. 3.

Considering Figure 4-24, there is no considerable movement of the X_a until $h/c = 45\%$. Further decrease in height results in downstream movement of the X_a. For the high GE intensity region between $h/c = 45\%$ and $h/c = 7\%$, a larger shift of X_a is observed towards trailing-edge of the wing. The maximum aft position of the X_a is observed at $x/c = 0.38$. The overall movement of the X_a with respect to height can be considered as quite linear. However, the wing is unstable in terms of the H.S. since the X_a is always positioned at a more fore position with respect to X_{CG} and Relation 4 is violated for all heights. Utilization of the horizontal tail or blended body concepts, which incorporate tip twist, may be considered in order to shift the X_a to a more aft position with respect to X_{CG}.

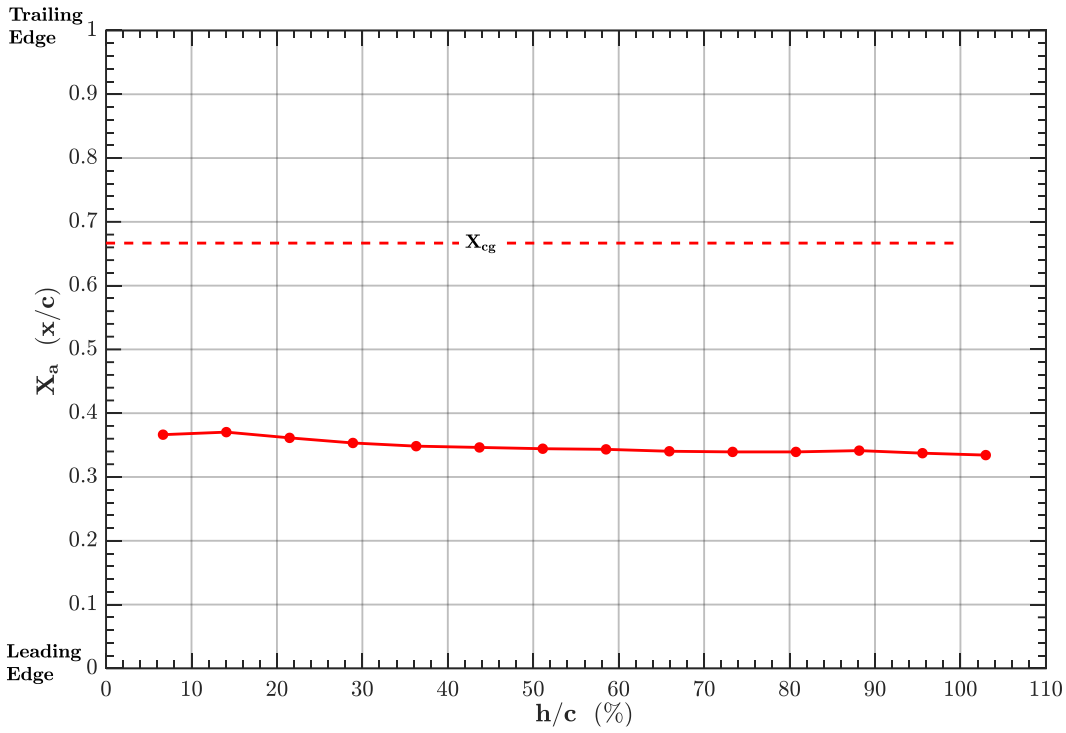

Figure 4-24 Aerodynamic center in pitch X_a with respect to non-dimensional height h/c for the delta wing 1a

Considering Figure 4-25, the movement of the X_h in longitudinal axis is quite non-linear. For the low angle of attack region between $0^o \leq \alpha \leq 7^o$, the X_h moves downstream from $x/c = 0.24$ to $x/c = 0.46$. Then, it moves upstream to $x/c = 0.38$ between $7^o \leq \alpha \leq 10^o$ and then slightly shifts toward to leading-edge until $\alpha = 16^o$. From this angle up to the stall region around $\alpha = 22^o$, it travels to $x/c = 0.54$ downstream, whereas its direction changes sign after stall and it moves toward $x/c = 0.42$ location. Since the upstream shift of the X_h is desired for the H.S. and the relative positions of the X_h and X_{CG} require that X_h has to be positioned in more upstream position, the overall trend observed for the X_h in $0^o \leq \alpha \leq 22^o$ interval is not desired. Therefore, as the angle of attack increases up to stall angle, the wing tends to be more unstable considering the sole effect of the X_h.

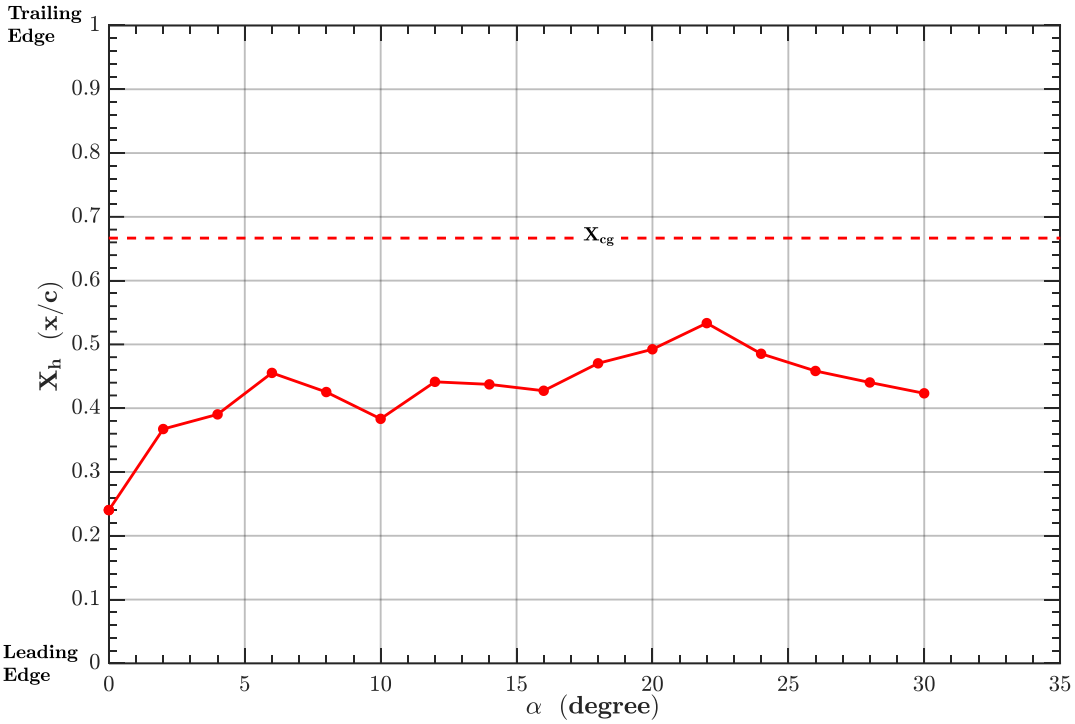

Figure 4-25 Aerodynamic center in height X_h with respect to angle of attack α for the delta wing 1a

Considering the sole effect of the H.S., hence combined behavior of the two aerodynamic centers in Figure 4-26, the wing is unstable for the majority of the test envelop, whereas it is stable at low angle of attack values for $\alpha \leq 3^o$ for all heights. For a particular region, where $\alpha \leq 3^o$ and $h/c \leq 40$, the H.S. reaches the maximum values. For the unstable region between $6^o \leq \alpha \leq 8^o$, the wing tends to become more stable as the height reduces from $h/c \leq 70$, which is primarily driven by the gradual movement of the X_a toward the trailing-edge.

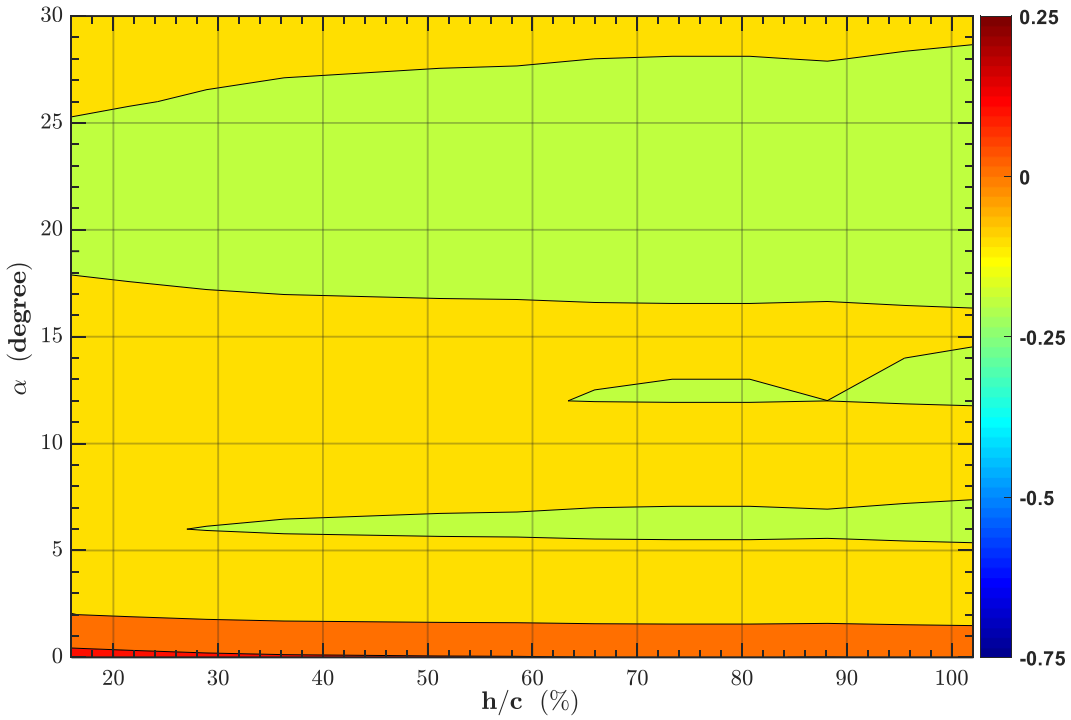

Figure 4-26 Height stability H.S. with respect to angle of attack and non-dimensional height for the delta wing 1a

4.2.3.2 Results of Longitudinal Static Stability for the Delta Wings 1a, 1b, and Reverse Delta Wings 2a, 2b

In Figure 4-27, the X_a distribution is provided with respect to non-dimensional height, whereas the X_h is given with respect to angle of attack in Figure 4-28. In Figure 4-29, height stability contours with respect to angle of attack and non-dimensional height for the delta and reverse delta wings 1a, 1b, 2a, and 2b are provided.

Considering Figure 4-27 for the delta wings 1a and 1b, which are given by red and black curves, there is no considerable movement of the X_a until $h/c = 45\%$ for both wings whereas further decrease in height results in downstream movement of the X_a, which is more pronounced for the thin delta wing 1b. For the high GE intensity region between $h/c = 45\%$ and $h/c = 7\%$, a larger shift of X_a is observed towards trailing-edge of the wing for both delta wings. The position of the X_a of the delta wing 1b is more aft positioned with respect to the position of the X_a of the delta wing 1a for all heights. The maximum aft position of the X_a for the delta wing 1b is observed at $x/c = 0.41$. However, both wings are unstable in terms of the H.S. since the X_a is always positioned at a more fore position with respect to X_{CG} and Relation 4 is violated for all heights for both wings. Considering the static margin of two wings, the delta wing 1b has a more favorable X_a position compared to the thick counterpart. Considering the results for the reverse delta wings 2a, and 2b, which are given by blue and green curves, there is also no considerable movement of the X_a until $h/c = 35\%$ for both wings whereas further decrease in height results in downstream movement of the X_a, which is again more pronounced for the thin reverse delta wing 2b. Contrary to the delta wing thickness effect on the position of the X_a, the position of the X_a of the reverse delta wing 2a is more aft positioned with respect to the position of the X_a of the reverse delta wing 2b for all heights and difference between the positions of the X_a for two reverse delta wings are higher at all height values compared to the difference between delta wings counterparts. Similar to delta wings, both the thick and thin reverse delta wings 2a and 2b wings

are unstable in terms of the H.S. since the X_a is always positioned at a more fore position with respect to X_{CG} and Relation 4 is violated for all heights for both wings. Considering the static margin of two wings, the delta reverse wing 2a has a more favorable X_a position compared to the thick counterpart.

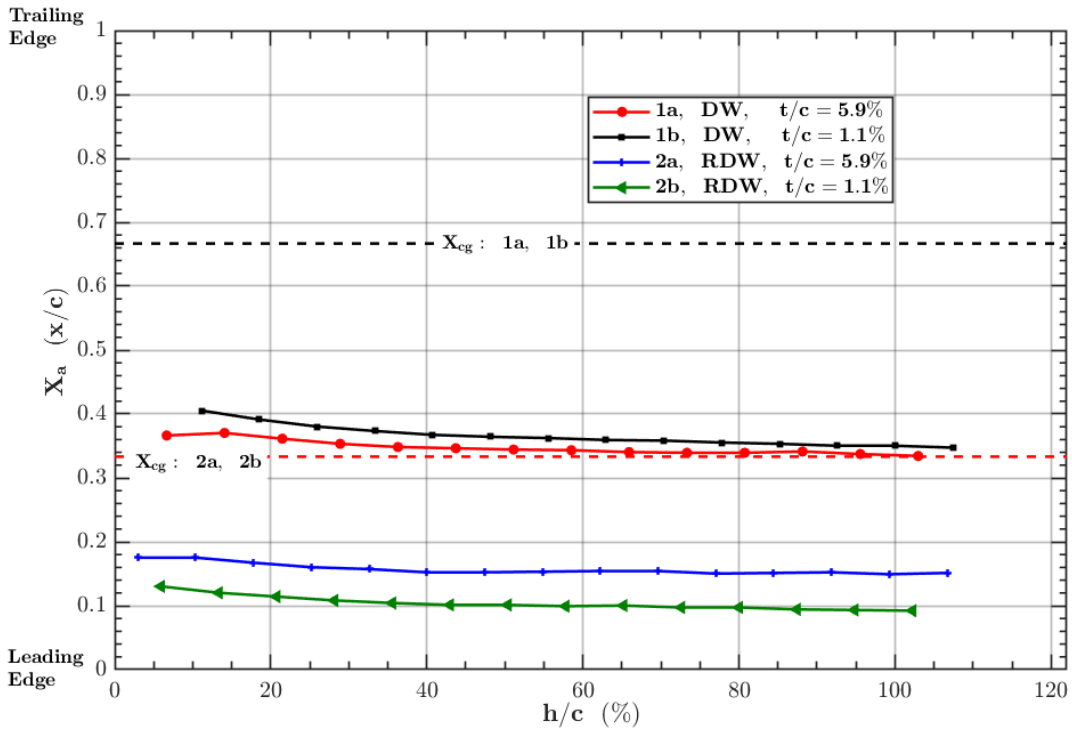

Figure 4-27 Aerodynamic center in pitch X_a with respect to non-dimensional height h/c for the delta and reverse delta wings 1a, 1b, 2a, 2b

Considering Figure 4-28 for the delta wings 1a and 1b, which are given by red and black curves, the movement of the X_h in longitudinal axis is quite non-linear. For the low angle of attack region between $0^o \leq \alpha \leq 7^o$, the X_h moves downstream for the delta wing 1a, which occurs in a smaller α range $0^o \leq \alpha \leq 4^o$ for the delta wing 1b. Then, it moves upstream to $x/c = 0.38$ between $7^o \leq \alpha \leq 10^o$ and then slightly shifts toward to leading-edge until $\alpha = 16^o$ and from this angle up to the stall region around $\alpha = 22^o$, it travels to $x/c = 0.54$ downstream, whereas its direction changes sign after stall and it moves toward $x/c = 0.42$ location for delta wing 1a. For the delta wing 1b, X_h movement is much more limited compared to the thick delta wing 1a in angle of attack region between $4^o \leq \alpha \leq 16^o$. However, from this angle up to

the stall region around $\alpha = 20^o$, the movement of the X_h is much more aggressive compared to the delta wing 1a since it travels to $x/c = 0.71$ downstream, whereas its direction again changes sign after stall and it moves toward $x/c = 0.48$ location for delta wing 1b. Since the upstream shift of the X_h is desired for the H.S. and the relative positions of the X_h and X_{CG} require that X_h has to be positioned in more upstream position, the overall trend observed for the X_h in $0^o \leq \alpha \leq 22^o$ interval is not desired. Therefore, as the angle of attack increases up to stall angle, both wings tend to be more unstable considering the sole effect of the X_h. Compared to its thin counterpart, the delta wing 1a has a more favorable X_h position with respect to the X_{CG} since its X_h is positioned at more forward positions for all angles excluding $\alpha = 6^o$ and $\alpha = 22^o$. Considering the results for the reverse delta wings 2a, and 2b, which are given by blue and green curves, the X_h moves downstream for both reverse delta wings between $0^o \leq \alpha \leq 6^o$. Then, it slightly shifts toward to leading-edge until $\alpha = 30^o$ for the reverse delta wing 2b. Although, similar downstream movement is observed for the reverse delta wing 2a between $6^o \leq \alpha \leq 16^o$, a reversal in X_h movement occurs at $\alpha = 16^o$ and it travels to $x/c = 0.38$ downstream, whereas its direction changes sign one more time after $\alpha = 20^o$and it moves toward $x/c = 0.25$. Considering the trends as well as the angles where the direction change occurs for the movement of the X_h of the delta wing 1b and the reverse delta wing 2a, the two wings show similar characteristics between $16^o \leq \alpha \leq 30^o$. Although, favorable upstream movement of the X_h between $6^o \leq \alpha \leq 16^o$ are much more pronounced compared to the delta wings 1a and 1b, which is observed particularly for the reverse delta wing 2a, as the angle of attack increases up to stall angle, both reverse delta wings tend to be more unstable similarly to the delta wings counterparts 1a and 1b.

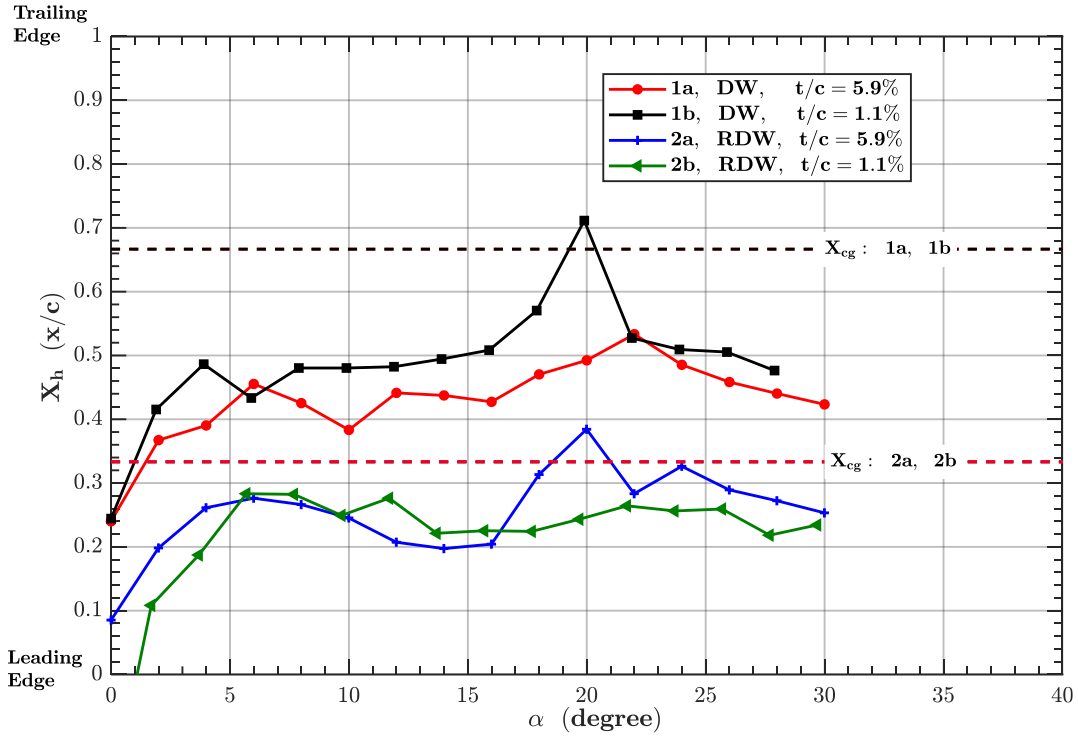

Figure 4-28 Aerodynamic center in height X_h with respect to angle of attack α for the delta and reverse delta wings 1a, 1b, 2a, 2b

Considering the sole effect of the H.S., hence combined behavior of the two aerodynamic centers in Figure 4-29, the delta wings 1a, 1b and reverse delta wings 2a, 2b are unstable for the majority of the test envelop. Considering the delta wings 1a and 1b for the low angles, the maximum values for the H.S. (provided with red contours) are further extended to $h/c \leq 80\%$ for $\alpha \leq 3^o$. For the unstable region between $6^o \leq \alpha \leq 8^o$ of the delta wing 1a are expanded and shifted to the $3^o \leq \alpha \leq 5^o$ for the delta wing 1b, the wing tends to become more stable as the height reduces from $h/c \leq 60$, which is again driven by the movement of the X_a toward the trailing-edge, which is greater for the delta wing 1b compared to delta wing 1a, since the movement of X_h is even more unfavorable than the X_h movement of the delta wing 1a. Considering H.S. contours of the reverse delta wings 2a and 2b, the stable zone for the reverse delta wing 2a is limited to the $\alpha \leq 2^o$ region and slightly expands toward to for the height values $h/c \leq 40\%$. Contrary to the thick counterpart, the H.S. values are significantly improved for the $\alpha \leq 4^o$. The stable zone for the

reverse delta wing 2b is also limited to the $\alpha \leq 2^{o}$ region, but the H.S. values are significantly improved for all height values, which is a result of the more upstream positioned X_h considering its unfavorable and more upstream positioned X_a. In addition, the X_a has a steeper shift towards to the trailing-edge in $h/c \leq 30\%$, hence the increased H.S. values for this highest GE intensity zone arises from the combined behaviors of favorable movements of the X_a and the X_h.

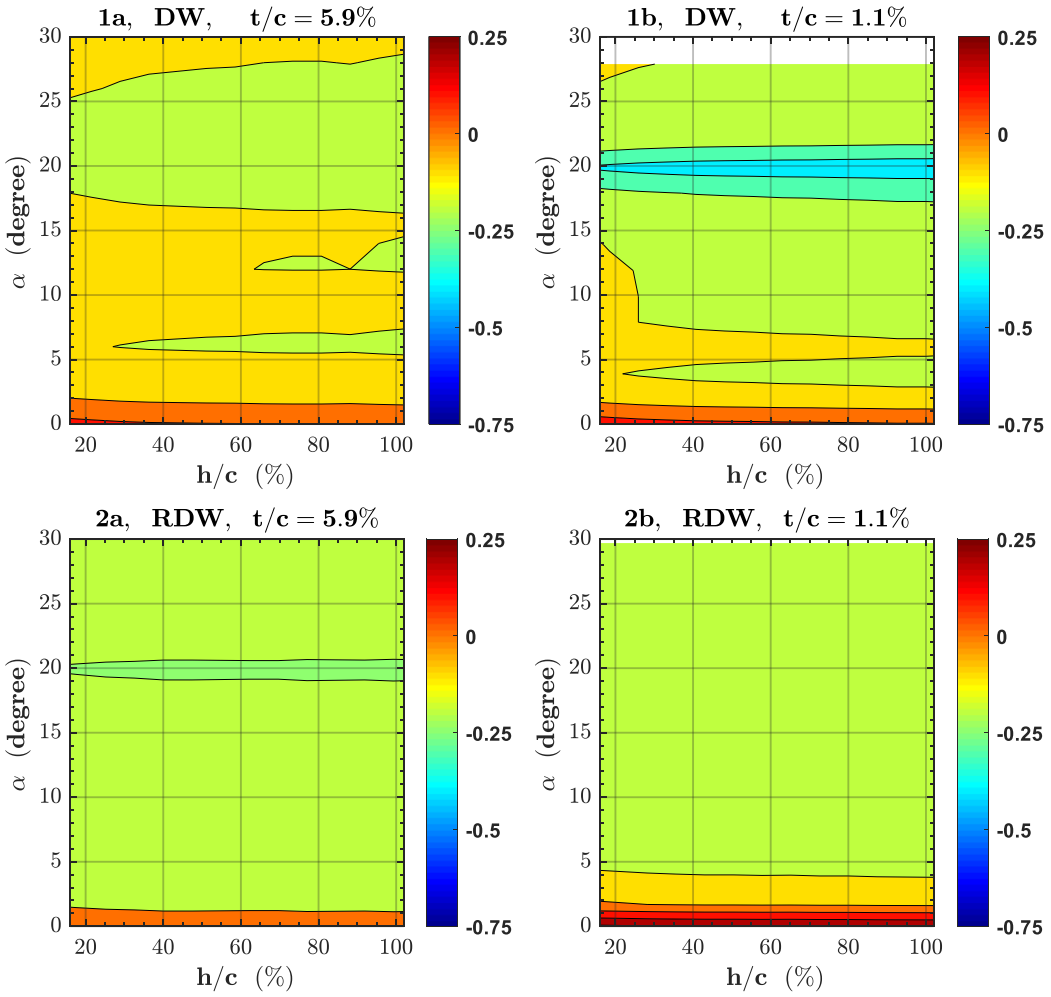

Figure 4-29 Height stability H.S. with respect to angle of attack and non-dimensional height for the delta wings 1a, 1b, and the reverse delta wings 2a, 2b

4.2.3.3 Results of Longitudinal Static Stability for the Reverse Delta Wings 2b, 2c, 2d, 2e, and 2f

In Figure 4-30, the X_a distribution is provided with respect to non-dimensional height, whereas the X_h is given with respect to angle of attack in Figure 4-31. In Figure 4-32, height stability contours with respect to angle of attack and non-dimensional height for the reverse delta wings 2b, 2c, 2d, 2e, and 2f are provided.

Considering Figure 4-30 for the reverse delta wings 2b, 2c and 2d, which are given by green, magenta and red curves, the X_a is shifted to more downstream positions for $\delta = 15^o$ considering the sole effect of the anhedral but this effect is not observed for $\delta = 30^o$ since the X_a positions of the reverse delta wing 2b and 2d are almost the same. The favorable aft shift observed with $\delta = 15^o$ is reversed for the high GE intensity zone since the X_a of the reverse delta wing 2c is significantly shifted upstream for $h/c \leq 25\%$. The undesired reversal of the X_a is also observed for the reverse delta wing 2d and $\delta = 30^o$ resulted in earlier reversal since the upstream shift of the X_a occurs for $h/c \leq 55\%$. Considering the sole effect of cropping with the reverse delta wings 2c and 2e, as well as 2d and 2f, a favorable situation is observed for the reverse delta wing 2d since Cr=30% resulted in significantly downstream shift of the X_a as it can be seen with the reverse delta wing 2f. In addition, intensity of the reversal in X_a position with increasing GE intensity is much stronger for the reverse delta wing 2f to lower h/c values. However, cropping has negligible impact on the reverse delta wing 2c since the X_a position of the reverse delta wing 2e is almost at the same position. Considering the primary reason for the instability of the reverse delta wings, the X_a is always positioned at a more fore position with respect to X_{CG} and Relation 4 is violated for all heights for all reverse delta wings. This undesired behavior gets stronger as the GE intensity increases.

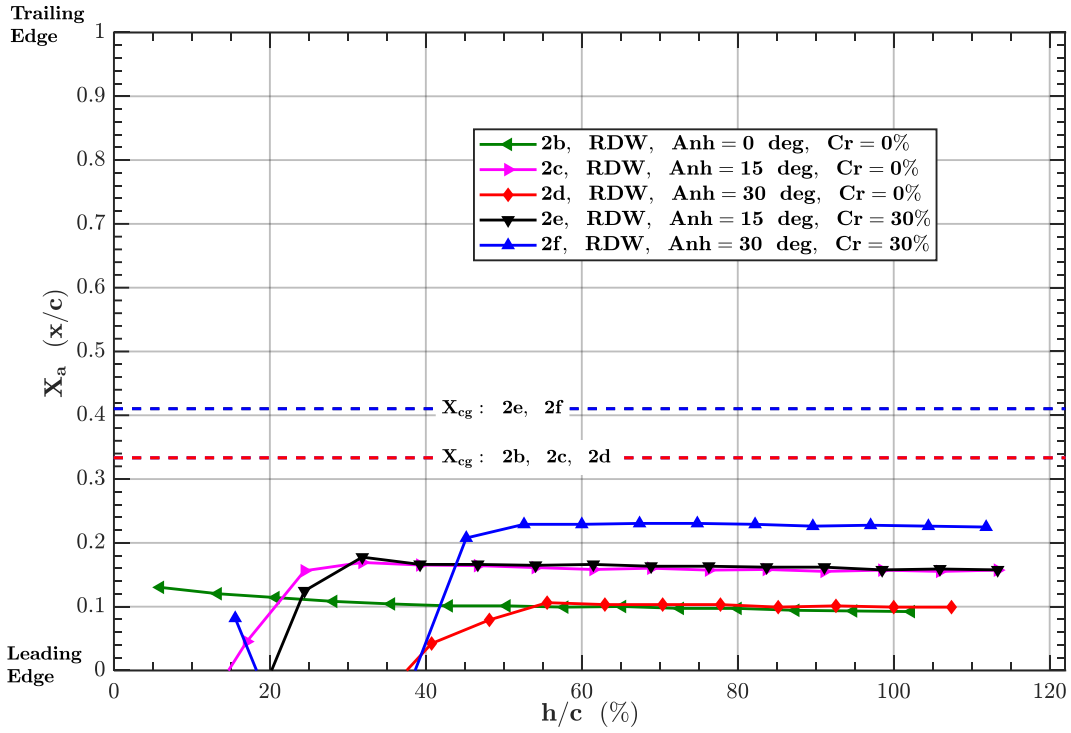

Figure 4-30 Aerodynamic center in pitch X_a with respect to non-dimensional height h/c for the reverse delta wings 2b, 2c, 2d, 2e, 2f

Considering Figure 4-31 for the reverse delta wings 2b, 2c and 2d, which are given by green, magenta and red curves, the movement of the X_h in longitudinal axis becomes more linear between $5^o \leq \alpha \leq 33^o$ for the reverse delta wing 2c with $\delta = 15^o$ and unfavorable downstream shift is observed, whereas slope of the X_h is increased for the reverse delta wing 2d with $\delta = 30^o$ particularly for $3^o \leq \alpha \leq 11^o$. For the low angle of attack region between $0^o \leq \alpha \leq 5^o$, the X_h moves downstream for all the reverse delta wings, whereas the reverse delta wing 2e is best performing for $\alpha \leq 3^o$. For the angle of attack interval $3.5^o \leq \alpha \leq 13.5^o$, $\delta = 30^o$ is quite beneficial since it significantly moves the X_h towards to leading-edge, which is more pronounced for the low angles in this range. The X_h positions of the reverse delta wings 2c and 2d are quite similar in $0^o \leq \alpha \leq 3^o$ interval, where the reverse delta wing 2c with $\delta = 15^o$ performs slightly better than the reverse delta wing 2d with $\delta = 30^o$. Considering the sole effect of cropping with the reverse delta wings 2c and 2e, as well as 2d and 2f, cropping mostly results in unfavorable downstream shift of

the X_h for both the reverse delta wing 2c and 2d for $5^o \leq \alpha \leq 33^o$. In addition, cropping greatly amplified back and forth movement of the X_h, which occurs in $5^o \leq \alpha \leq 20^o$ interval. The reverse delta wing 2f with $\delta = 30^o$ and Cr=30% particularly shows this characteristic.

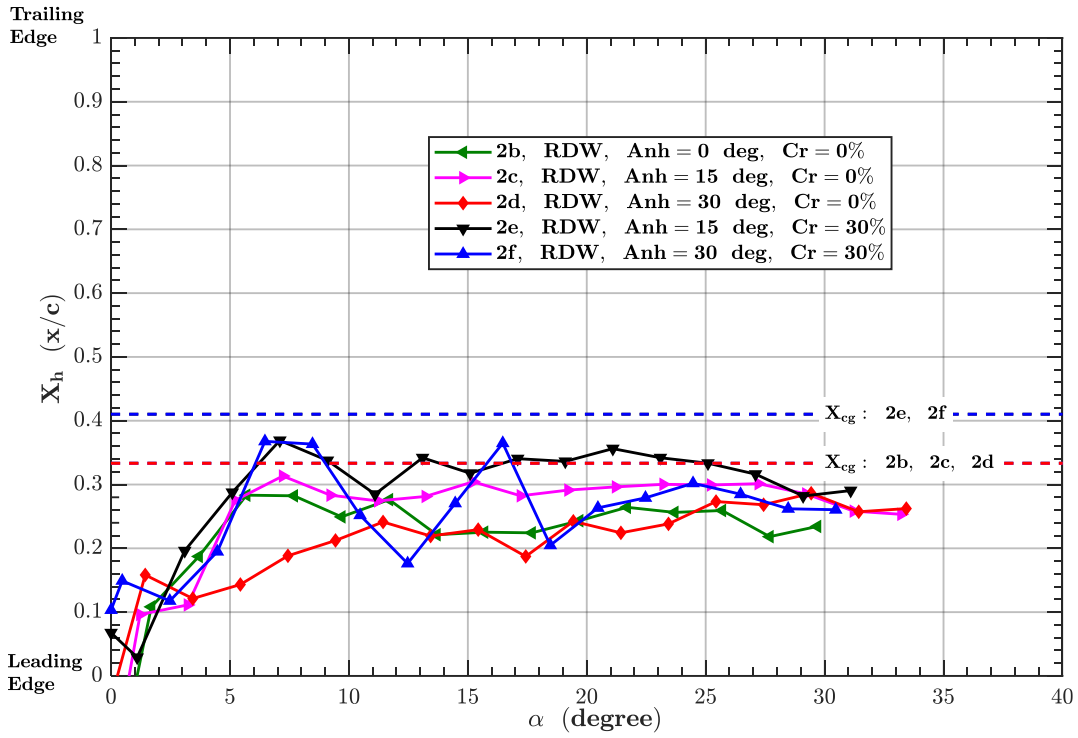

Figure 4-31 Aerodynamic center in height X_h with respect to angle of attack α for the reverse delta wings 2b, 2c, 2d, 2e, 2f

Considering the sole effect of the H.S., hence combined behavior of the two aerodynamic centers in Figure 4-32, all of the reverse delta wings are unstable for the majority of the test envelop. Considering the anhedral on the H.S. by comparing the reverse delta wings 2b, 2c, and 2d, $\delta = 15^o$ improves the H.S. $\alpha \leq 4^o$ for all heights except a small portion below $h/c \leq 20\%$ and $\alpha \geq 1^o$, which is observed with the reverse delta wing results 2c, whereas further increase in anhedral results in significantly deteriorated H.S. characteristics since H.S. remains positive only for $\alpha \leq 1^o$ for the reverse delta wing 2d. The sole effect of cropping is beneficial for the

reverse delta wing 2c with $\delta = 15^{o}$ in terms of increasing the maximum H.S. values at low angles as it can be seen with the results of the reverse delta wing 2e, whereas cropping for the reverse delta wing 2d with $\delta = 30^{o}$ results in expanding the stabile zone for $40 \leq h/c \leq 110\%$ up to angles $\alpha \leq 5^{o}$ and it creates additional stabile zones around $\alpha = 12^{o}$ and $\alpha = 18^{o}$ for $h/c \geq 40\%$. The H.S. can be assured for all reverse delta wings by design changes, which should aim to shift of the X_a to more downstream positions since this is the primary reason of the instability observed for both OGE and IGE conditions. This might be achieved with the inclusion of a horizontal tail. Considering the operational envelope, it can be properly scheduled such that its effectiveness may be increased at different angles of attack and heights by methods such as variable cambering or variable incidence which yields increased effectiveness both for OGE and IGE conditions.

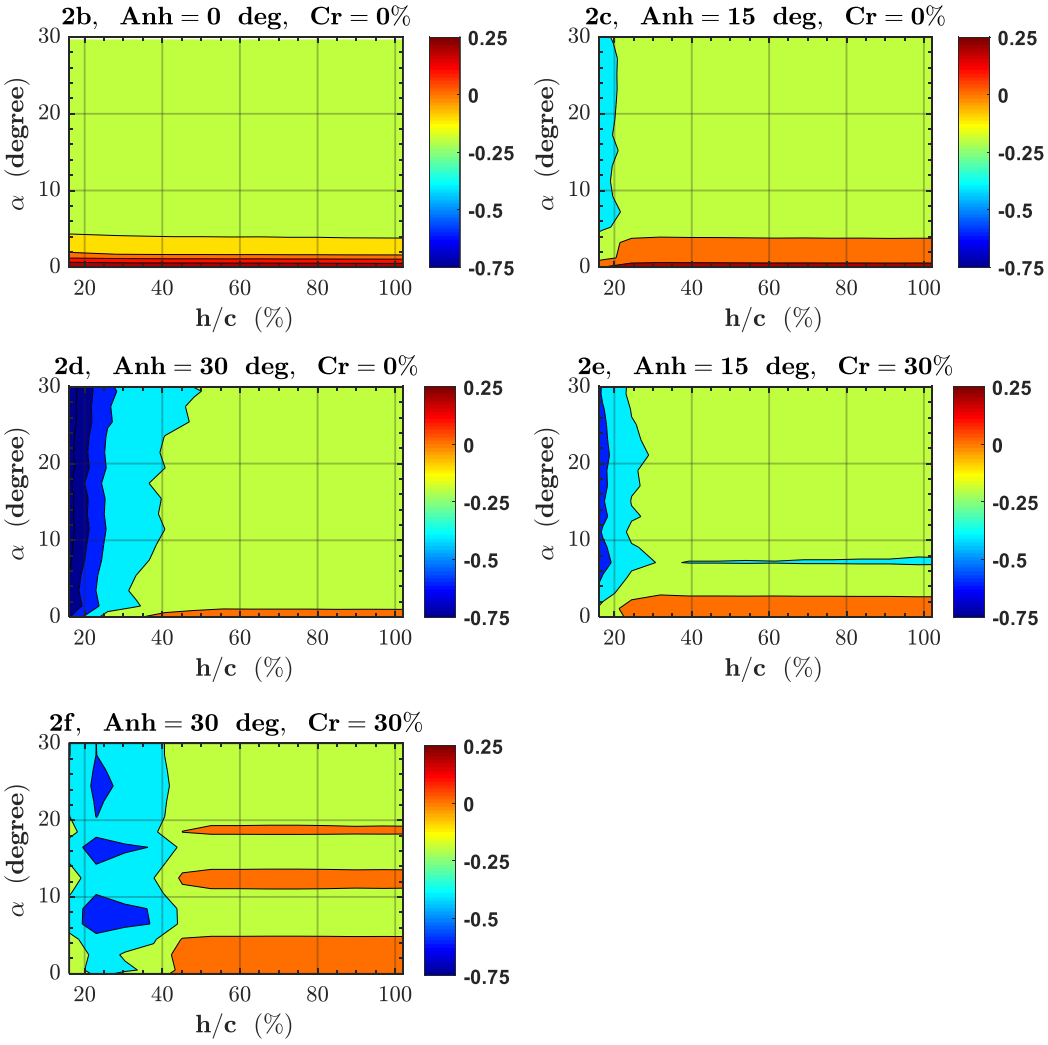

Figure 4-32 Height stability H.S. with respect to angle of attack and non-dimensional height for the reverse delta wings 2b, 2c, 2d, 2e, and 2f

CHAPTER 5

EFFECT OF DYNAMIC GROUND CONDITION

In this chapter, the results of the dynamic ground condition are provided for the delta wing 1a and the reverse delta wing 2e utilizing the force measurements. For both wings, the results obtained with the static ground condition are compared with the results of the dynamic ground condition tests along with the comparison of different belt statuses with Belt On versus Belt Off cases of the associated moving belt integrated IGE tests.

5.1 Out of Ground Effect and In Ground Effect Results

5.1.1 Results of Force Measurements

In this chapter, ground effect force measurements results for the dynamic ground condition are given as a function of function of angle of attack for the delta wing 1a and the reverse delta wing 2e.

5.1.1.1 Results of Force Measurements for the Delta Wing 1a

In Figure 5-1, distributions of drag coefficient C_D, lift-to-drag ratio C_L/C_D, lift coefficient C_L as a function of angle of attack and drag polar for the delta wing 1a are given for different non-dimensional height values varying from $h/c = 31.9\%$ to 91.1%.

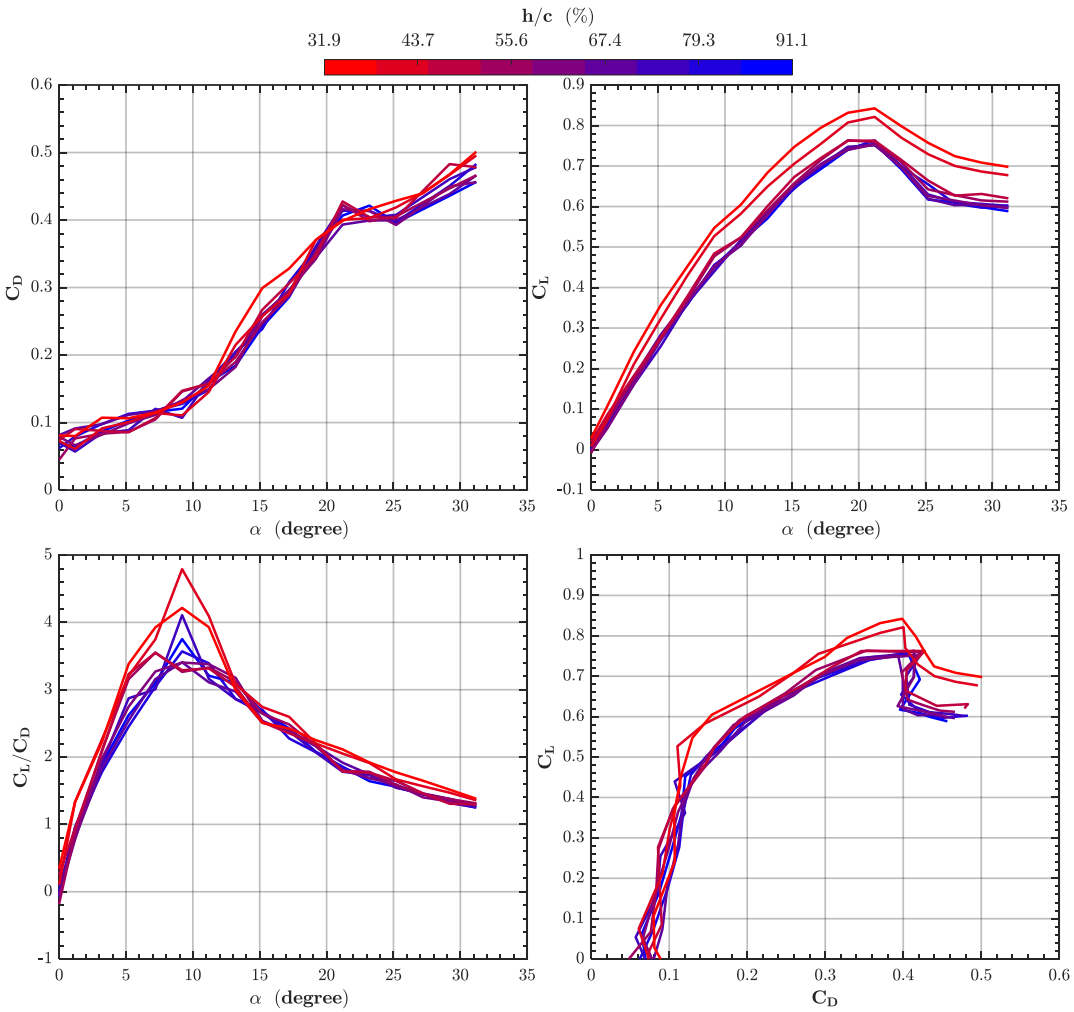

Figure 5-1 Variation of Drag coefficient C_D, Lift-to-Drag ratio C_L/C_D, Lift coefficient C_L as a function of angle of attack and Drag Polar for the delta wing 1a

Considering the drag coefficient C_D shown in the upper left chart, drag curves exhibit similar magnitudes for angles less than 20 deg, whereas slopes are quite similar except for the most intense ground effect case at $h/c = 31.9\%$ where the slope is

also significantly increased. Local decrease at drag values are observed for the angles near stall, although a sudden increase is observed for all cases after $\alpha = 25^{o}$.

Considering the lift coefficient C_L shown in upper right chart, the delta wing exhibits typical stall behavior with a sudden loss in lift. The delta wing has a stall angle of $\alpha_s = 21.2^{o}$ for OGE condition, which is quite similar for the case with the static ground condition, whereas earlier stall onset is not observed this time. However, increase in lift coefficient is observed for all angles with increasing GE intensity in both low and high angles. The lift curve slope increases with decreasing height and is the highest for the smallest height, hence the rate of increase in C_L increases dramatically with increasing angle of attack as the wing approaches to the ground. The increase in lift curve slope is particularly more appreciable for the most intense two cases at $h/c = 31.9\%$ and $h/c = 39.3\%$. Around $\alpha = 10^{o}$, lift curve slope is reduced for all cases, although the decrease is more pronounced with increased ground effect intensity.

The C_L/C_D distribution is shown in the lower left chart. Considering the GE especially for the most intense three cases at $h/c = 31.9\%$, $h/c = 39.3\%$ and $h/c = 46.7\%$, the performance of the wing is improved at all angles of attack excluding the $\alpha = 9^{o}$, where lift loss and drag increase has significant impact such that it does not show a monotonous character with ground effect. The improvement is considerably larger for small angles up to $\alpha = 9^{o}$, which is due to the significant lift increase without drag increase penalty. Therefore, favorable condition with GE is more pronounced up to this angle. In addition, the peak values of C_L/C_D for the delta wing is seen around $\alpha = 9^{o}$, where the peak values for height values close to OGE condition are not postponed, which is the case for the static ground condition.

The drag polar shown at the lower right chart of Figure 5-1, the slopes of the drag polar curves of the delta wing are quite similar up to $C_D = 0.11$ and maximum C_L is increased at this drag coefficient value for increased GE intensity. Increasing ground effect intensity results in shift in y axis for the region after $C_D = 0.11$ for the cases

at $h/c = 31.9\%$, $h/c = 39.3\%$, although similar slopes are observed for all curves in this region, which is also characterized by reversal in the slope at the stall angles.

In Figure 5-2, variation of moment coefficient C_M at trailing-edge (TE) and center of gravity (CG) as functions of angle of attack and lift coefficient C_L, and non-dimensional center of pressure coordinate X_P as a function of angle of attack for the delta wing 1a are given for different height values.

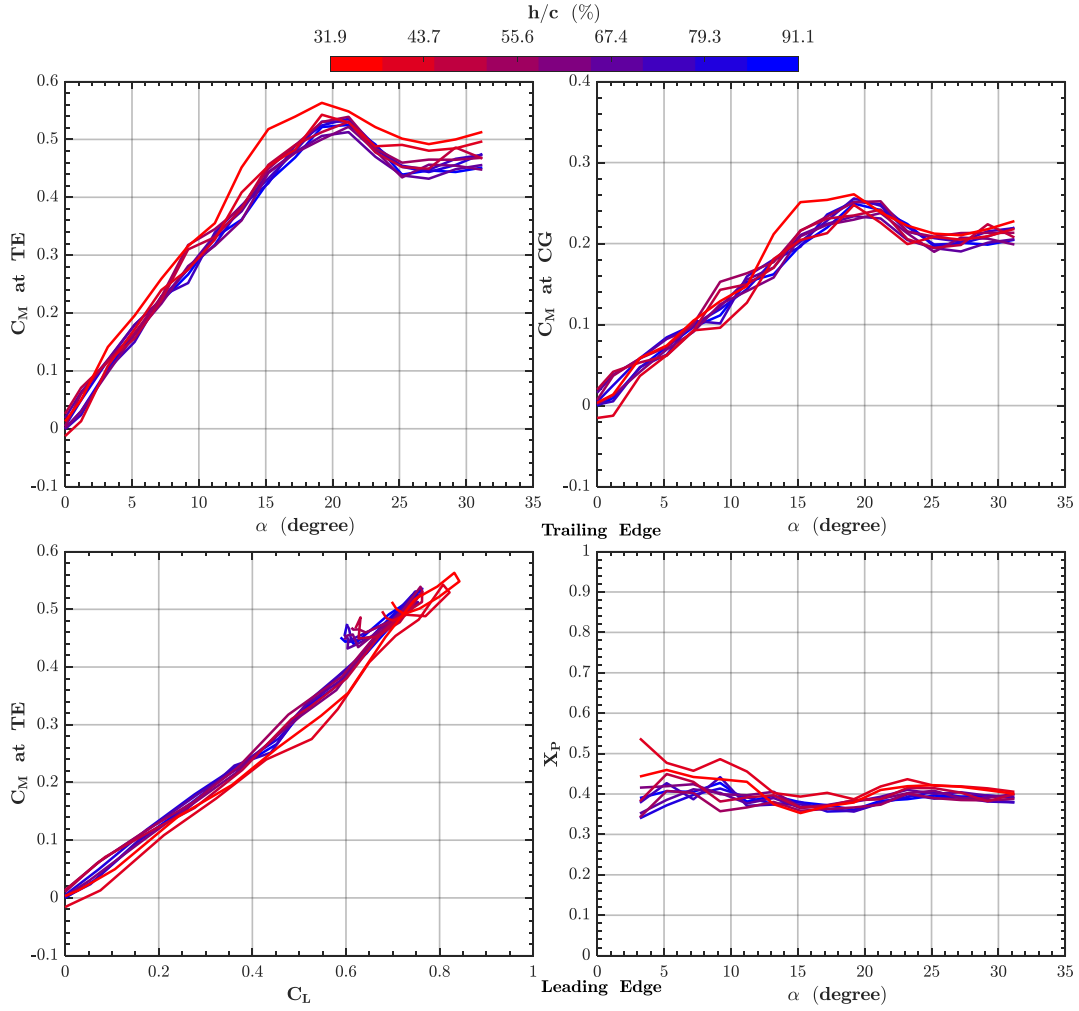

Figure 5-2 Variation of Moment coefficient C_M at trailing-edge (TE) and center of gravity (CG) as a function of angle of attack and Lift coefficient C_L, and Non-Dimensional Pressure Center coordinate X_P as a function of angle of attack for the delta wing 1a

Considering the distribution of C_M at trailing-edge shown in the upper left chart, curves are almost identical up to $h/c = 61.5\%$, after which the rate of change of the pitch-up moment is increasing with GE intensity and becomes maximum for the closest distance to the ground. For the maximum ground effect case, the slope of the moment curve is further increased after $\alpha = 11^o$

The distribution of C_M at the trailing-edge as a function of C_L is demonstrated in the bottom left chart of Figure 5-2 for different height values. The highest slope is seen for the OGE condition, whereas the aerodynamic center in pitch slightly shifts towards to the trailing-edge of the wing as the height decreases.

Considering the C_M at wing center of gravity (CG) as a function of α shown at upper right corner of Figure 5-2, all curves at different heights pose positive slopes and positive C_M values. Excluding the $\alpha = 9^o$ case for different height values, only the most intense ground condition poses increased slope between $\alpha = 11^o$ and $\alpha = 15^o$, whereas all curves pose similar slope and magnitude around CG.

Considering the X_P as function of angle of attack demonstrated in lower right corner of Figure 5-2, GE shifts the center of pressure X_P toward trailing-edge of the wing as it can be seen for the $h/c = 31.9\%$ and $h/c = 39.3\%$, whereas no remarkable movement of the X_P is seen for the different height values close to the OGE condition considering the associated angle of attack. For all heights, the center of pressure is located around $x/c = 0.4$.

5.1.1.2 Results of Force Measurements for the Reverse Wing 2e

In Figure 5-3, distributions of drag coefficient C_D, lift-to-drag ratio C_L/C_D, lift coefficient C_L as a function of angle of attack and drag polar for the reverse delta wing 2e are given for different non-dimensional height values varying from $h/c = 28.1\%$ to 83.7%.

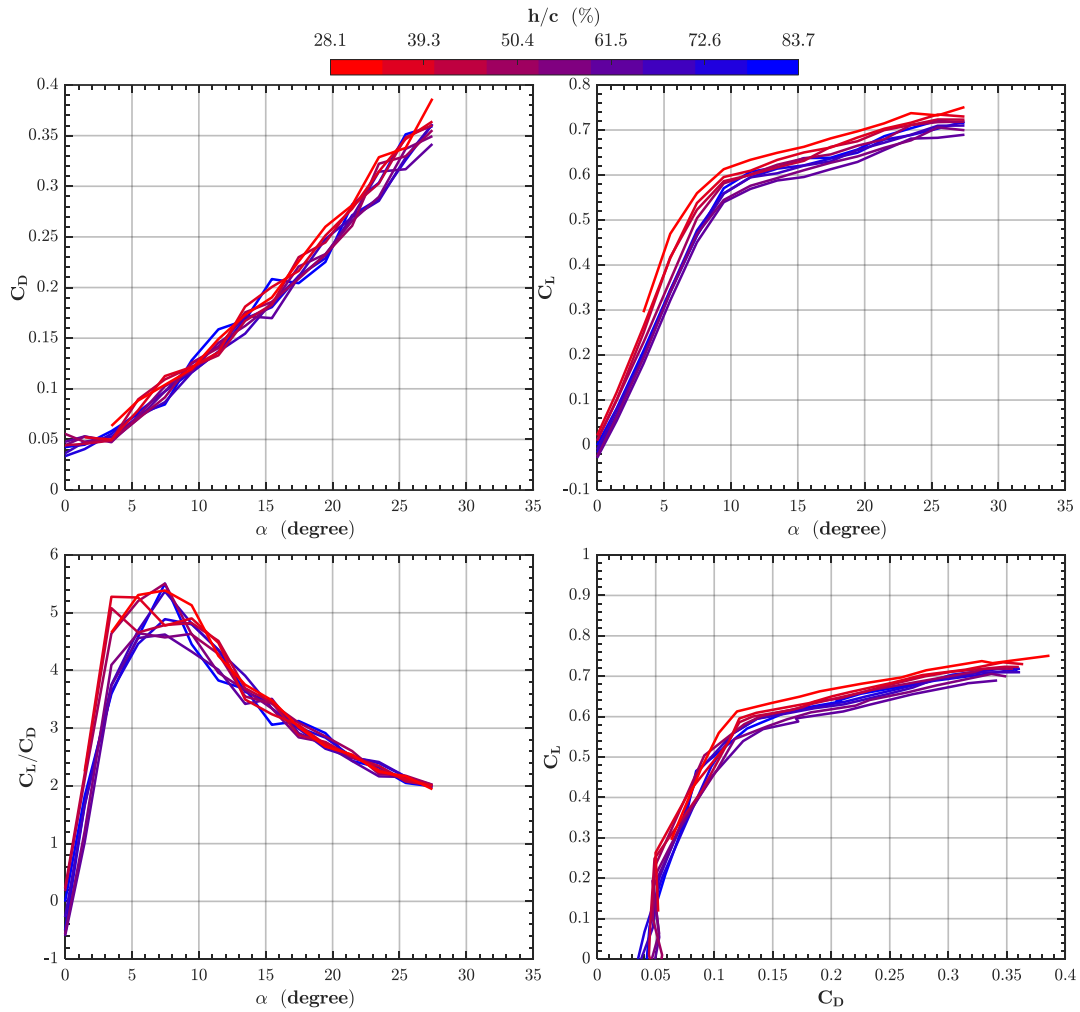

Figure 5-3 Variation of Drag coefficient C_D, Lift-to-Drag ratio C_L/C_D, Lift coefficient C_L as a function of angle of attack and Drag Polar for the reverse delta wing 2e

Considering the drag coefficient C_D shown in the upper left chart, drag values are increasing with increasing angle of attack and ground effect intensity whereas there is no clear evidence of stall considering all height values including OGE condition. The increase in drag curve slope is more pronounced after $\alpha = 14^o$.

Considering the lift coefficient C_L shown in upper right chart, lift curve slope decreases significantly after stall. However, lift increase is persistent and the decrease in slope does not become more significant with increasing GE intensity, which is the case for static ground condition. The reverse delta wing has a stall angle of $\alpha_s = 9^o$ for OGE condition whereas stall onset is not much affected by increasing GE intensity, which is quite similar with the static ground condition. However, increase in lift coefficient is observed for all angles with increasing GE intensity in both low and high angles. The lift curve slope for small angles increases with decreasing height and is the highest for the smallest height, hence the rate of increase in C_L increases significantly with increasing angle of attack as the wing approaches to the ground. After the stall angle, lift curves shift as the ground effect intensity increases, while they preserve the same slope.

Considering C_L/C_D distribution shown in the lower left chart, the performance of the wing is improved at small angles up to $\alpha = 7^o$, which is due to the higher lift increase compared to drag increase. In addition, the peak values of C_L/C_D for the delta wing is seen between $\alpha = 3^o$ and $\alpha = 8^o$, where the angles for the peak values for different heights change with decreasing heights. Comparing the peak values C_L/C_D values, the maximum performance values are inconclusive with ground effect, but the area under each curve increases with increasing ground effect intensity. This is particularly observed for angles smaller than $\alpha = 12^o$.

Considering the drag polar shown at the lower right chart, the curves shift upward yielding higher lift for the same drag after $C_D = 0.11$ with increasing ground effect intensity. In addition, increasing ground effect intensity results in higher lift values particularly between $C_D = 0.05$ and $C_D = 0.11$.

In Figure 5-4, variation of moment coefficient C_M at trailing-edge (TE) and center of gravity (CG) as functions of angle of attack and lift coefficient C_L, and non-dimensional center of pressure coordinate X_P as a function of angle of attack for the reverse delta wing 2e are given for different height values.

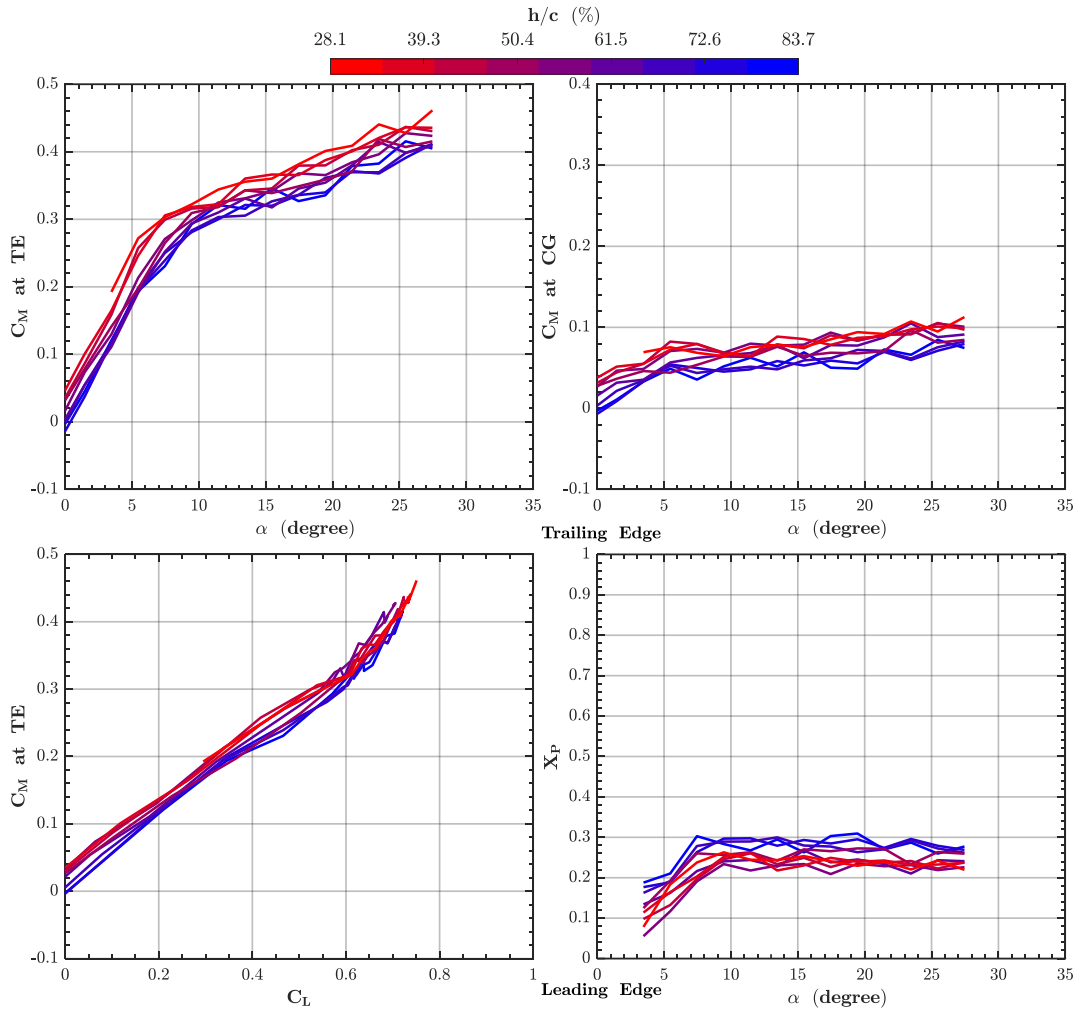

Figure 5-4 Variation of Moment coefficient C_M at trailing-edge (TE) and center of gravity (CG) as a function of angle of attack and Lift coefficient C_L, and Non-Dimensional Pressure Center coordinate X_P as a function of angle of attack for the reverse delta wing 2e

Considering the distribution of C_M at trailing-edge shown in the upper left chart, the moment coefficients at all angles increase as the height decreases and the rate of change of the pitch-up moment is also increasing with GE intensity up to stall angles and after which sudden pitch moment curve slope decrease occurs for all heights, which is quite similar with the static ground condition. After stall, pitch moment curve slope remains the same with increasing GE intensity, whereas curves shift in positive y axis.

The distribution of C_M at the trailing-edge as a function of C_L is demonstrated in the bottom left chart. The slope of the curve decreases up to $C_L = 0.26$ value with increasing ground effect intensity. After this point, slope increase is observed for the high ground effect curves whereas decrease in slope is valid for low ground effect intensity cases after $C_L = 0.19$.

Considering the C_M at wing center of gravity (CG) as a function of α shown at upper right corner, all curves at different heights pose slightly positive slopes and positive C_M values. As the height of the wing decreases $C_{M_{cg}}$ is increased monotonically, but slopes of the curves remain quite similar for all heights.

Considering the X_P as function of angle of attack demonstrated in lower right corner, GE shifts the center of pressure X_P toward leading-edge of the wing, whereas decreasing angle of attack results in even more fore-positioned X_P for all cases, which is particularly observed for angles less than $\alpha = 8^o$, which is significantly different than the static ground condition. The movement of the X_P with decreasing angle of attack is even more remarkable with increasing ground effect intensity, whereas movement of X_P is getting lower and lower with increasing ground effect intensity as the angle of attack decreases towards $\alpha = 0^o$ for the static ground condition.

5.1.2 Results of Longitudinal Static Stability

In this chapter, longitudinal static stability assessment with dynamic ground condition is made for the delta wing 1a and the reverse delta wing 2e.

5.1.2.1 Results of Longitudinal Static Stability for the Delta Wing 1a

The longitudinal static stability characteristics of the delta wing 1a are examined by constructing the height stability, H.S. and utilizing the aerodynamic center in pitch, X_a and aerodynamic center in height, X_h. In Figure 5-5, the X_a distribution is provided with respect to non-dimensional height, whereas the X_h is given with respect to angle of attack in Figure 5-6. In Figure 5-7, height stability contours with respect to angle of attack and non-dimensional height for the delta wing are provided by utilizing Eqn. 3.

Considering Figure 5-5, there is no considerable movement of the X_a until $h/c = 54\%$ excluding the fore shift of the X_a at $h/c = 68.9\%$. Further decrease in height after $h/c = 54\%$ results in downstream movement of the X_a. The maximum aft position of the X_a is observed at $x/c = 0.41$. The overall movement of the X_a with respect to height can be considered as quite linear. However, the wing is unstable in terms of the H.S. since the X_a is always positioned at a more fore position with respect to X_{CG} and Relation 4 is violated for all heights.

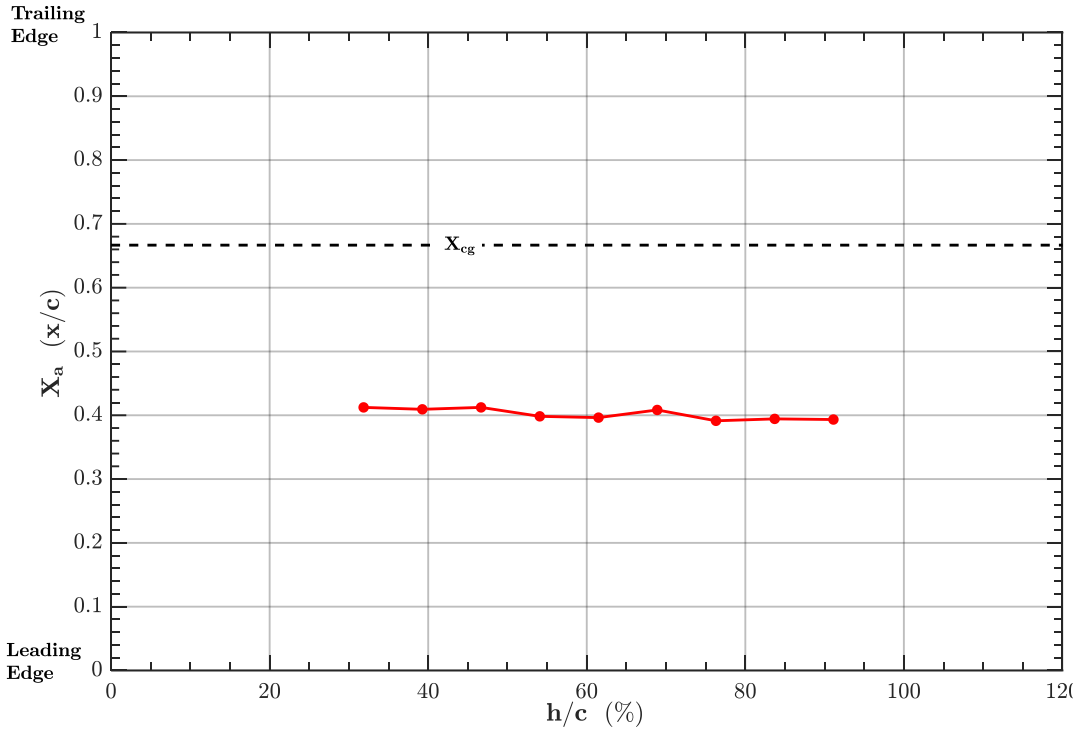

Figure 5-5 Aerodynamic center in pitch X_a with respect to non-dimensional height h/c for the delta wing 1a

Considering Figure 5-6, the movement of the X_h in longitudinal axis is quite non-linear. For the low angle of attack region between $0^o \leq \alpha \leq 7^o$, the X_h moves downstream from $x/c = 0.45$ to $x/c = 0.65$. Then, it moves upstream to $x/c = 0.61$ between $5^o \leq \alpha \leq 9^o$ whereas it is accompanied by sudden aft movement occurs at $\alpha \leq 11^o$. From this angle up to the angle $\alpha = 15^o$, it travels significantly back towards trailing-edge up to $x/c = 0.29$, whereas the downstream movement is reiterated until the stall angle $\alpha = 21^o$ to the location of $x/c = 0.77$, whereas its direction changes sign after stall, which is quite similar to the reversal seen at $\alpha = 11^o$, and it moves toward $x/c = 0.5$ location. Since the upstream shift of the X_h is desired for the H.S. and the relative positions of the X_h and X_{CG} require that X_h has to be positioned in more upstream position, the overall trend observed for the X_h in $0^o \leq \alpha \leq 22^o$ interval is not desired except for the region between angles $\alpha = 11^o$ and $\alpha = 15^o$. However, relative positions of the X_h and X_{CG} at these specific angles

show that X_h lies behind X_{CG} at more aft positions, which also violates stability requirements.

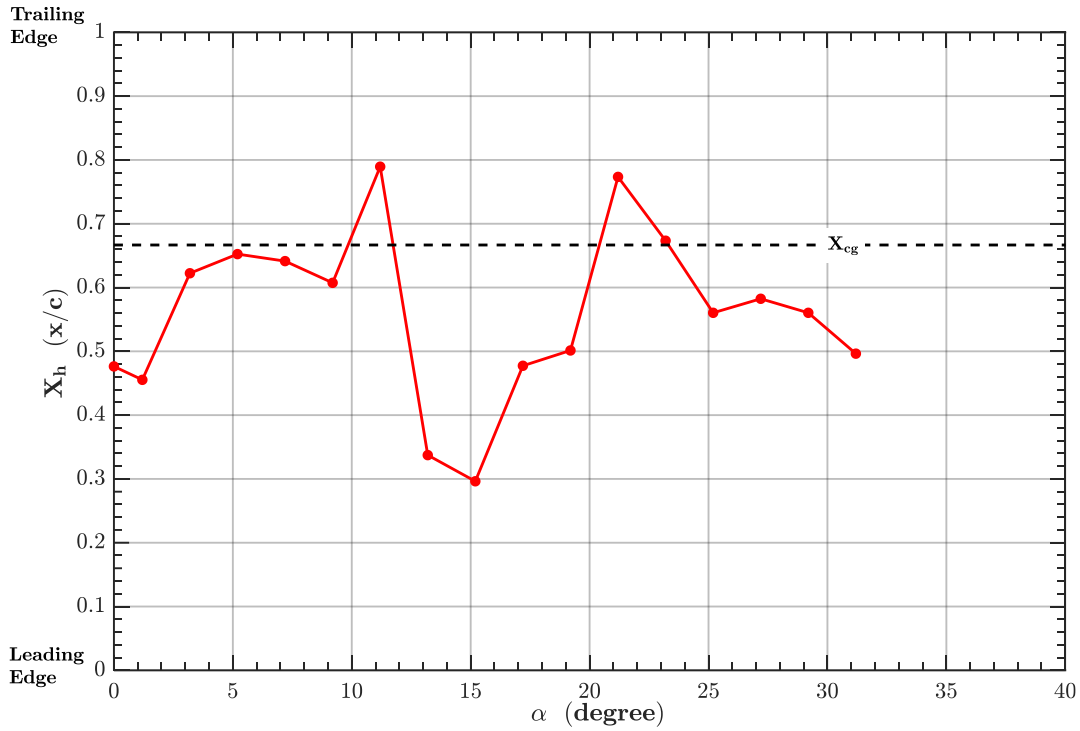

Figure 5-6 Aerodynamic center in height X_h with respect to angle of attack α for the delta wing 1a

Considering the sole effect of the H.S, hence combined behavior of the two aerodynamic centers in Figure 5-7, the wing is unstable for the majority of the test envelop, whereas it becomes stable as the angle of attack is increased from $\alpha = 11^o$ to $\alpha = 15^o$, which is primarily driven by the movement of the X_h toward the leading-edge.

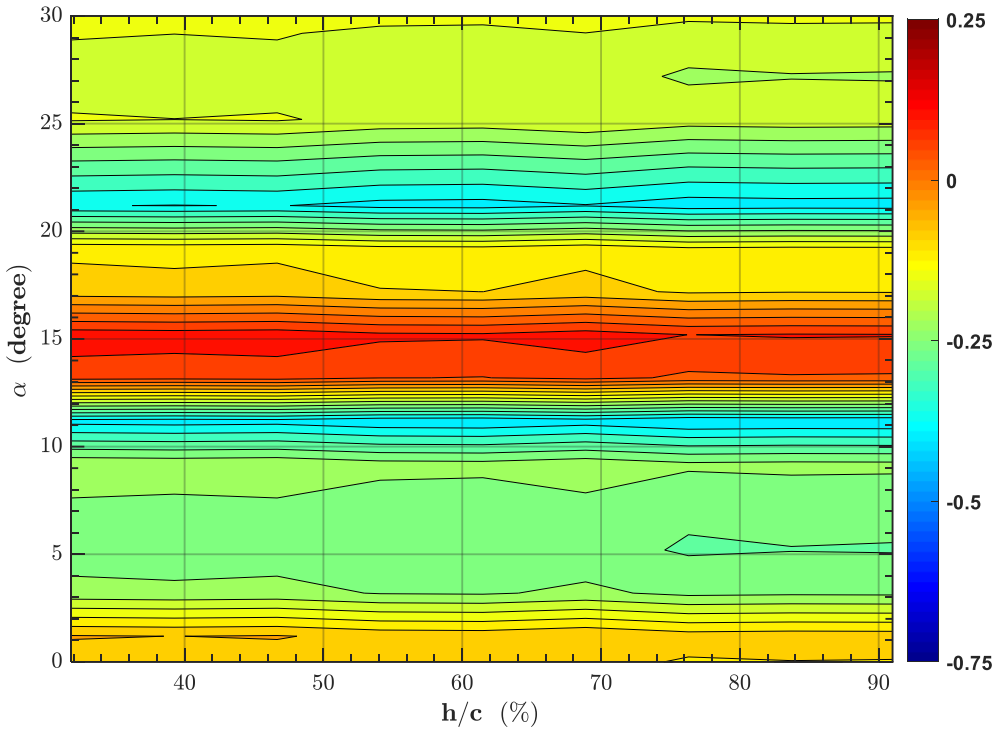

Figure 5-7 Height stability H.S. with respect to angle of attack and non-dimensional height for the delta wing 1a

5.1.2.2 Results of Longitudinal Static Stability for the Reverse Delta Wing 2e

The longitudinal static stability characteristics of the reverse delta wing 2e are examined. In Figure 5-8, the X_a distribution is provided with respect to non-dimensional height, whereas the X_h is given with respect to angle of attack in Figure 5-9. In Figure 5-10, height stability contours with respect to angle of attack and non-dimensional height for the delta wing are provided by utilizing Eqn. 3.

Considering Figure 5-8, the X_a travels between $x/c = 0.27$ to $x/c = 0.31$ interval and as the height decreases X_a tends to shift downstream, which becomes more pronounced after $h/c = 61\%$. However, the wing is unstable in terms of the H.S. since the X_a is always positioned at a more fore position with respect to X_{CG} and Relation 4 is violated for all heights.

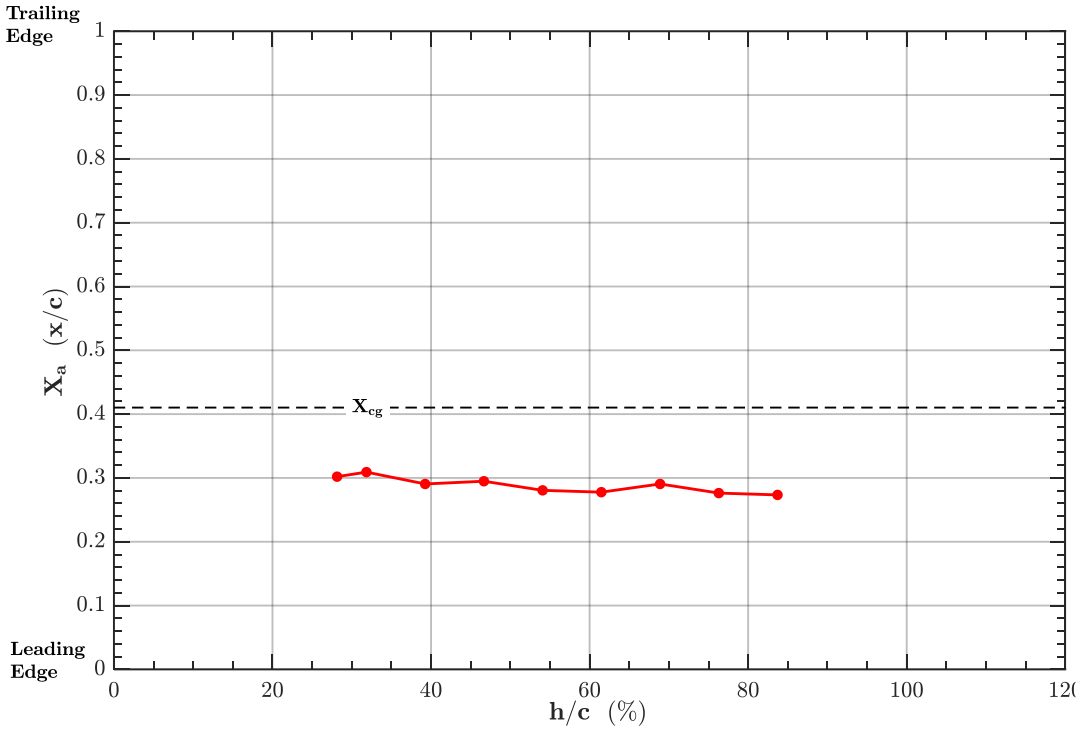

Figure 5-8 Aerodynamic center in pitch X_a with respect to non-dimensional height h/c for the reverse delta wing 2e

Considering Figure 5-9, the reversals are observed for the movement of the X_h in longitudinal axis at several angles. For the low angle of attack region $\alpha \leq 11.5^o$, the X_h is positioned well forward positions with respect to X_{CG} with increasing margin with respect to the decreasing angle of attack. At lower angles, the X_h even becomes negative, yielding more upstream positions with respect to the leading-edge of the wing. With increasing angle of attack values, the stabilizing character is particularly observed for the region between $11.5^o \leq \alpha \leq 19.5^o$ with increasing margin. In addition, back and forth movement is observed for the angles greater than $\alpha = 19.5^o$. The relative positions of the X_h and the X_{CG} show that X_h is always positioned upstream of the X_{CG} but showing stabilizing character with increasing angle of attack only in the region between $11.5^o \leq \alpha \leq 19.5^o$.

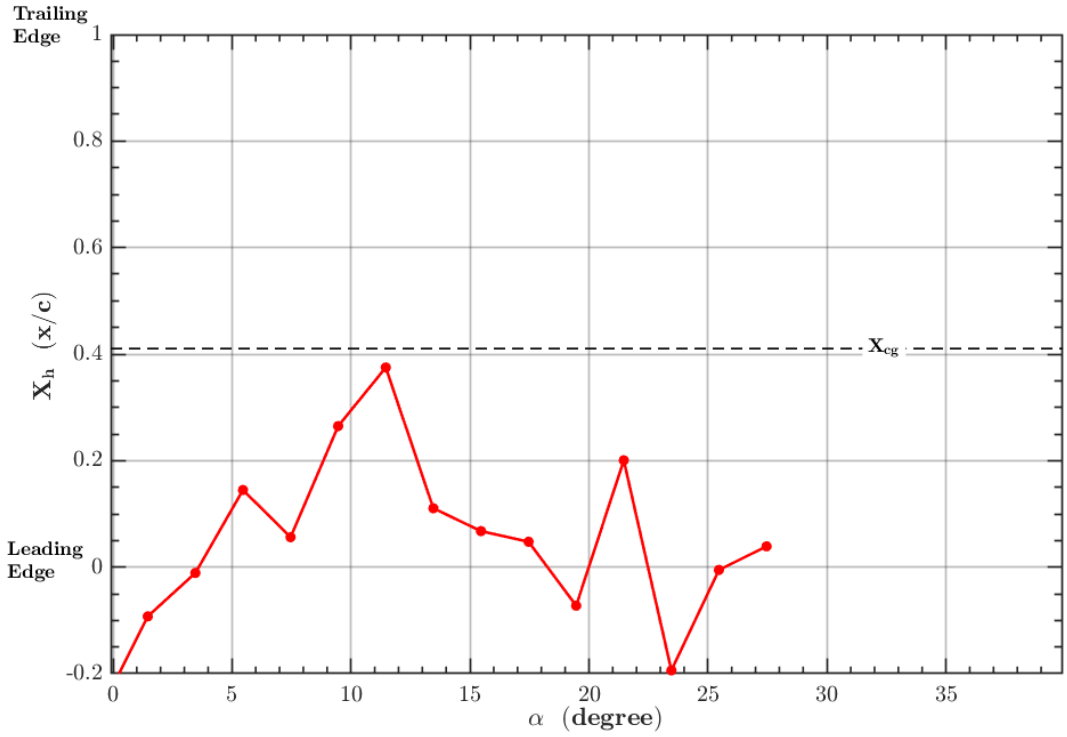

Figure 5-9 Aerodynamic center in height X_h with respect to angle of attack α for the reverse delta wing 2e

Considering the sole effect of the H.S., hence combined behavior of the two aerodynamic centers in Figure 5-10, the wing is stable for the majority of the test envelop, whereas it becomes slightly unstable around the angle of attack $\alpha = 11.5^{o}$, which is primarily driven by the movement of the X_h toward the trailing-edge.

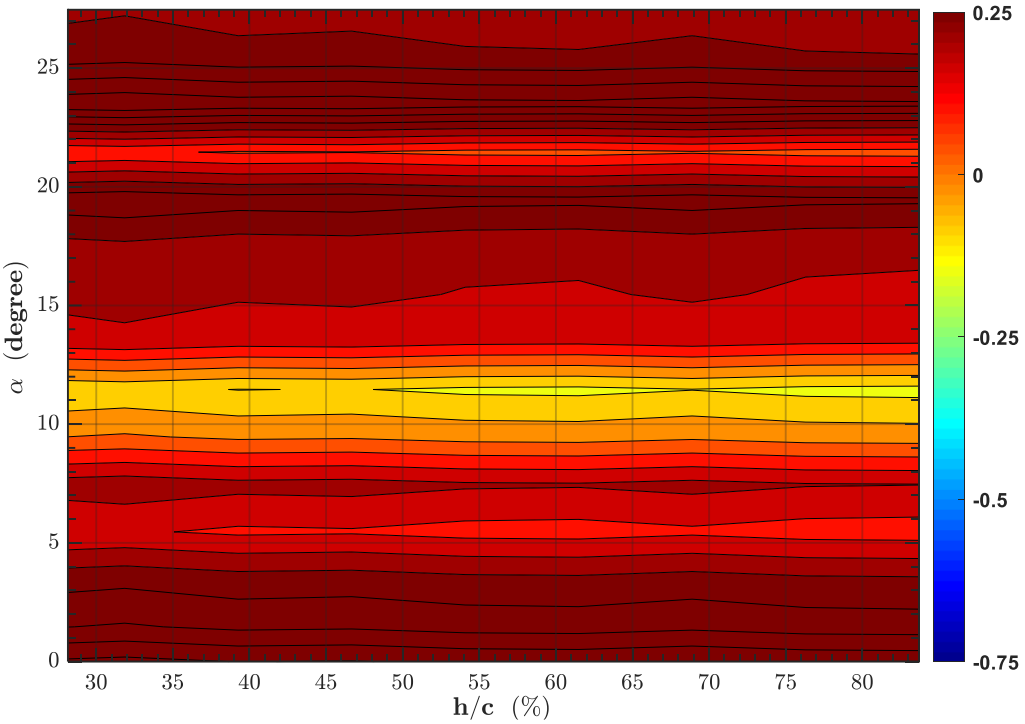

Figure 5-10 Height stability H.S. with respect to angle of attack and non-dimensional height for the reverse delta wing 2e

5.1.3 Static versus Dynamic Ground Condition

In this chapter, static and dynamic ground conditions are compared for the delta wing 1a and the reverse delta wing 2e considering force measurements for the OGE and the available most intense ground effect case for the dynamic ground case height values. Further, longitudinal static stability comparison is also made by comparing the with aerodynamic centers.

5.1.3.1 Comparison of Force Measurements of the Delta Wing 1a

In Figure 5-11, aerodynamic force coefficients for the delta wing 1a are provided for the selected cases from the static and dynamic ground conditions. In this figure, solid lines show the results for the static ground condition, whereas dashed lines show the results dynamic ground condition. Since the height values are not exactly the same, the closest values are selected among the available height values for this comparison. The OGE condition for the static ground condition is at $h/c = 88.2\%$, whereas the OGE condition for the dynamic ground condition is at $h/c = 91.1\%$. The highest ground effect intensity case, which is available for the dynamic ground condition, is also compared where the static and dynamic ground conditions are plotted at $h/c = 28.9\%$ and $h/c = 31.9\%$, respectively.

Considering the drag curve on the upper left chart, the curves are almost identical up to $\alpha \leq 10^{o}$ except for the dynamic ground condition, which shows slightly lower drag values. The drag curve slope is higher than the static ground condition for the dynamic ground case between $10^{o} \leq \alpha \leq 22^{o}$ for both OGE and IGE conditions, whereas drag values are less for the dynamic ground case again for both OGE and IGE conditions after $\alpha \geq 22^{o}$ where the slopes are quite similar for both the static and dynamic ground conditions.

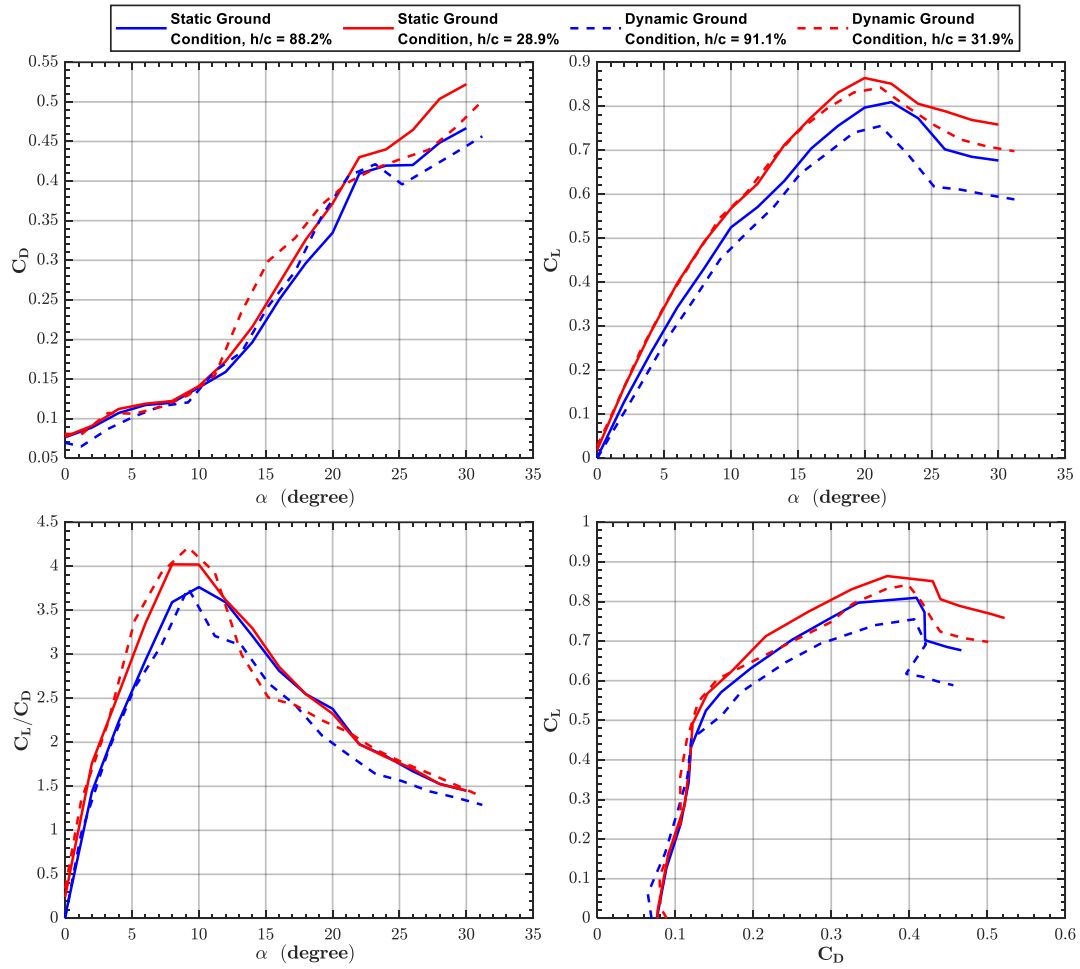

Figure 5-11 Variation of Drag coefficient C_D, Lift-to-Drag ratio C_L/C_D, Lift coefficient C_L as a function of angle of attack and Drag Polar for the delta wing 1a at OGE and IGE conditions with respect to Static and Dynamic Ground Conditions

Considering the lift curve, OGE condition for the dynamic case has an apparent smaller lift curve slope with respect to the static ground case. For all angles, the dashed blue line poses lesser lift values than the solid blue line. The difference is also larger at higher angles, whereas stall angles are quite similar. This situation is not observed for the IGE case, where solid and dashed red lines are coincident up to $\alpha = 16^o$. After this angle, lift decreases for the dynamic ground condition more than the static ground case.

Considering the lift-to-drag curves on the lower left plot, the static and dynamic ground conditions show quite similar trends and values up to the angles $\alpha \leq 9^o$.

Further increase in angle results in smaller lift-to-drag values for the dynamic ground condition for both OGE and IGE cases, where the decrease in lift-to-drag is more pronounced for the IGE case.

Considering the drag polar on the lower right plot, the curves are coincident up to $C_D = 0.12$ for OGE and $C_D = 0.17$ for IGE cases, respectively. This is accompanied by drag polar curve slope decrease for the dynamic ground condition for both OGE and IGE cases, whereas reversals on the drag polar occurs at the same C_D position for OGE case, although dynamic ground condition shows slightly earlier reversal with respect to the static ground condition.

In Figure 5-12, aerodynamic moment coefficients as well as the X_P locations for the delta wing 1a are provided for the selected cases from the static and dynamic ground conditions.

Considering the variation of moment coefficient C_M at trailing-edge with respect to angle of attack of the upper left chart, both OGE and IGE cases show smaller slopes for the dynamic ground conditions with respect to the static cases. After $\alpha = 15^o$, moment is significantly lower for the dynamic ground IGE case with respect to the static ground condition IGE, whereas this angle is postponed to $\alpha = 21^o$ for OGE cases. For the whole angle of attack range, dynamic ground condition results in more pitch-down characteristics with respect to the static ground conditions, which is valid for both OGE and IGE cases.

The distribution of C_M at the trailing-edge as a function of C_L is demonstrated in the bottom left chart. The slope of the curves for the static ground condition is higher with respect to the dynamic ground condition for both OGE and IGE. OGE and IGE curves for the static ground condition are almost identical for the static ground case up to $C_L = 0.49$, whereas IGE condition shows smaller slope as well as smaller pitch-up values with respect to OGE condition for the dynamic ground condition.

Considering the C_M at wing center of gravity (CG) as a function of α shown at upper right corner, all curves at different heights pose positive slopes and positive C_M

values. For the dynamic ground case, both the slopes and values are smaller than the static ground case considering IGE and OGE curves. However, significant increase in moment occurs for the dynamic ground IGE case up to $\alpha = 15^o$ after which decrease in moment is more intense than other curves. Finally, reversal in slope is more pronounced for the dynamic ground cases as seen in OGE (blue dashed) and IGE (red dashed) conditions.

Considering the X_P as function of angle of attack demonstrated in lower right corner, X_P is positioned at more downstream positions for the dynamic ground condition with respect to the static ground condition at all angles. Among all cases, the most aft position is seen for the dynamic ground condition IGE case, whereas the most fore position is seen for the static ground condition OGE case. The difference between X_P locations is higher for the IGE cases comparing the static (red dashed) and the dynamic (red dashed) ground conditions. This effect is more pronounced at lower angles $\alpha \leq 8^o$.

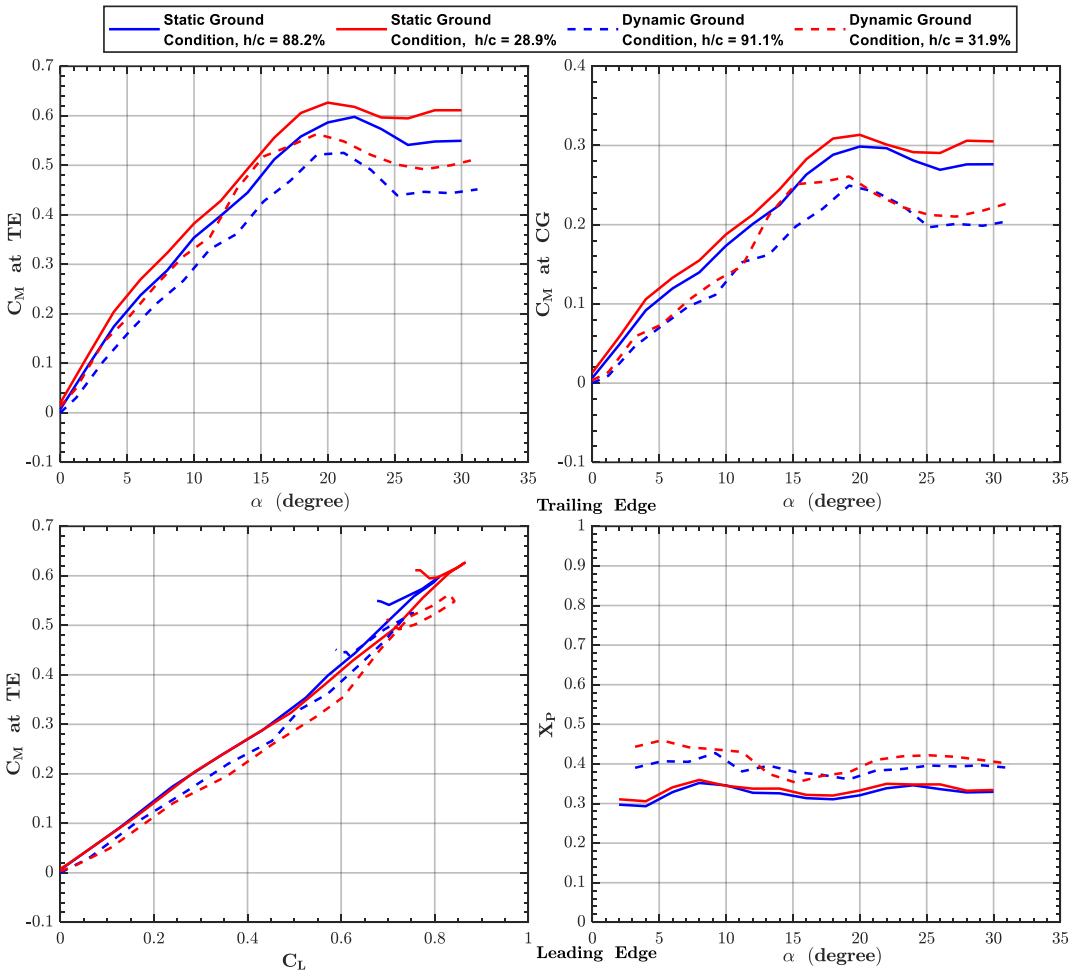

Figure 5-12 Variation of Moment coefficient C_M at trailing-edge (TE) and center of gravity (CG) as a function of angle of attack and Lift coefficient C_L, and Non-Dimensional Pressure Center coordinate X_P as a function of angle of attack for the delta wing 1a at OGE and IGE conditions with respect to Static and Dynamic Ground Conditions

5.1.3.2 Comparison of Force Measurements of the Reverse Delta Wing 2e

In Figure 5-13, aerodynamic force coefficients for the reverse delta wing 2e are provided for the selected cases from the static and dynamic ground conditions. In this figure, solid lines show the results for the static ground condition, whereas dashed lines show the results dynamic ground condition. The height values are exactly the same for the OGE comparison, but the closest values are selected among the available height values from the dynamic ground condition IGE case. The OGE condition for the static and dynamic ground conditions are at $\mathrm{h/c} = 83.7\%$. The highest ground effect intensity case, which is available for the dynamic ground condition, is also compared where the static and dynamic ground conditions are plotted at $\mathrm{h/c} = 24.4\%$ and $\mathrm{h/c} = 28.1\%$, respectively.

Considering the drag curve on the upper left chart, the drag curve slope is lesser for the dynamic ground condition cases for both OGE and IGE. Comparing the static and dynamic cases for IGE condition, latter one results in higher drag values between $3^o \leq \alpha \leq 7^o$, whereas drag is always smaller than the static ground condition IGE case for higher angles. For the OGE case, $0^o \leq \alpha \leq 9.5^o$ interval shows that dynamic ground condition results in higher drag values, although further increment in angle of attack results in similar or less drag values with respect to the static ground condition. There exists a clear drag curve difference between OGE and IGE cases for the static condition, but this is not the case for the dynamic ground condition cases as it can be seen from interchanging slopes of the blue and red dashed lines.

Considering the lift curve, IGE condition for the dynamic case has an apparent smaller lift curve slope with respect to the static ground case for all angle of attack interval, although there is no lift curve slope decrease for the dynamic ground condition the OGE case up to stall angle. For all angles, the dashed red line poses lesser lift values than the solid red line. The difference is also larger at higher angles, whereas stall angles are quite similar. This situation is not observed for the OGE case, where solid and dashed blue lines are coincident up to $\alpha = 9.5^o$. After this

angle, lift decreases for the dynamic ground condition more than the static ground case.

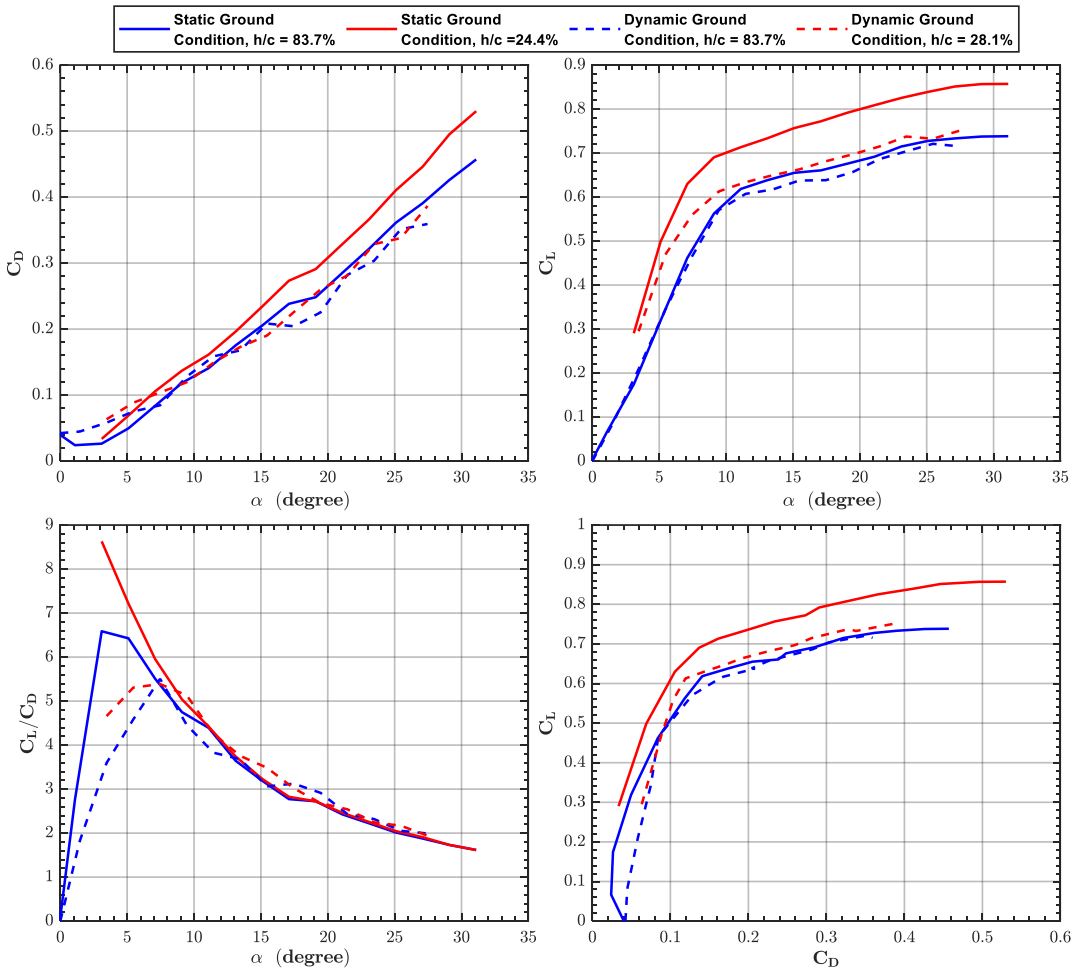

Figure 5-13 Variation of Drag coefficient C_D, Lift-to-Drag ratio C_L/C_D, Lift coefficient C_L as a function of angle of attack and Drag Polar for the reverse delta wing 2e at OGE and IGE conditions with respect to Static and Dynamic Ground Conditions

Considering the lift-to-drag curves on the lower left plot, the differences are more obvious for small angles. Static ground condition for the OGE case results in higher lift-to-drag ratio up to the angle $\alpha = 7.5^o$ due to the small drag values in this interval since lift values are almost identical for both cases. Comparing IGE cases, lift-to-drag is also smaller for the dynamic ground condition. This time both drag and lift contribute to loss in lift-to-drag ratio and there is a marginal gap between red solid

and dashed lines up to the angle $\alpha = 7.5^{o}$. Further increase in angle of attack results in higher drag increase for the static ground condition and similar lift curve slopes for both cases, hence combined effect results in similar lift-to-drag ratio between the static and dynamic cases. The peak values are quite similar for OGE and IGE cases of the dynamic ground condition, whereas the ground effect augmentation in terms of maximum achievable lift-to-drag ratio is tremendous for the static ground condition. However, ground effect augmentation for the dynamic ground condition shows itself as an expanded angle of attack region considering the area underneath of red and blue dashed lines.

Considering the drag polar on the lower right plot, apparent slope increase between red and blue solid lines are not observed between the dashed lines. The dashed curves are coincident up to $C_D = 0.1$, which is not seen for the static ground condition the OGE and IGE curves. However, the shift in drag polars between IGE and OGE conditions for the static ground condition is also observed for the dynamic ground condition, whereas this shift is milder for the dynamic ground condition.

In Figure 5-14, aerodynamic moment coefficients as well as the X_P locations for the reverse delta wing 2e are provided for the selected cases from the static and dynamic ground conditions.

Considering the variation of moment coefficient C_M at trailing-edge with respect to angle of attack of the upper left chart, both OGE and IGE cases show smaller slopes for the dynamic ground conditions with respect to the static cases. After $\alpha = 7^{o}$, moment is lower for the dynamic ground IGE case with respect to the static ground condition IGE, whereas this angle is postponed to $\alpha = 15^{o}$ for OGE cases. For the small angle of attack range $\alpha \leq 7^{o}$, dynamic ground condition results in more pitch-up characteristics with respect to the static ground conditions, which is valid for both OGE and IGE cases.

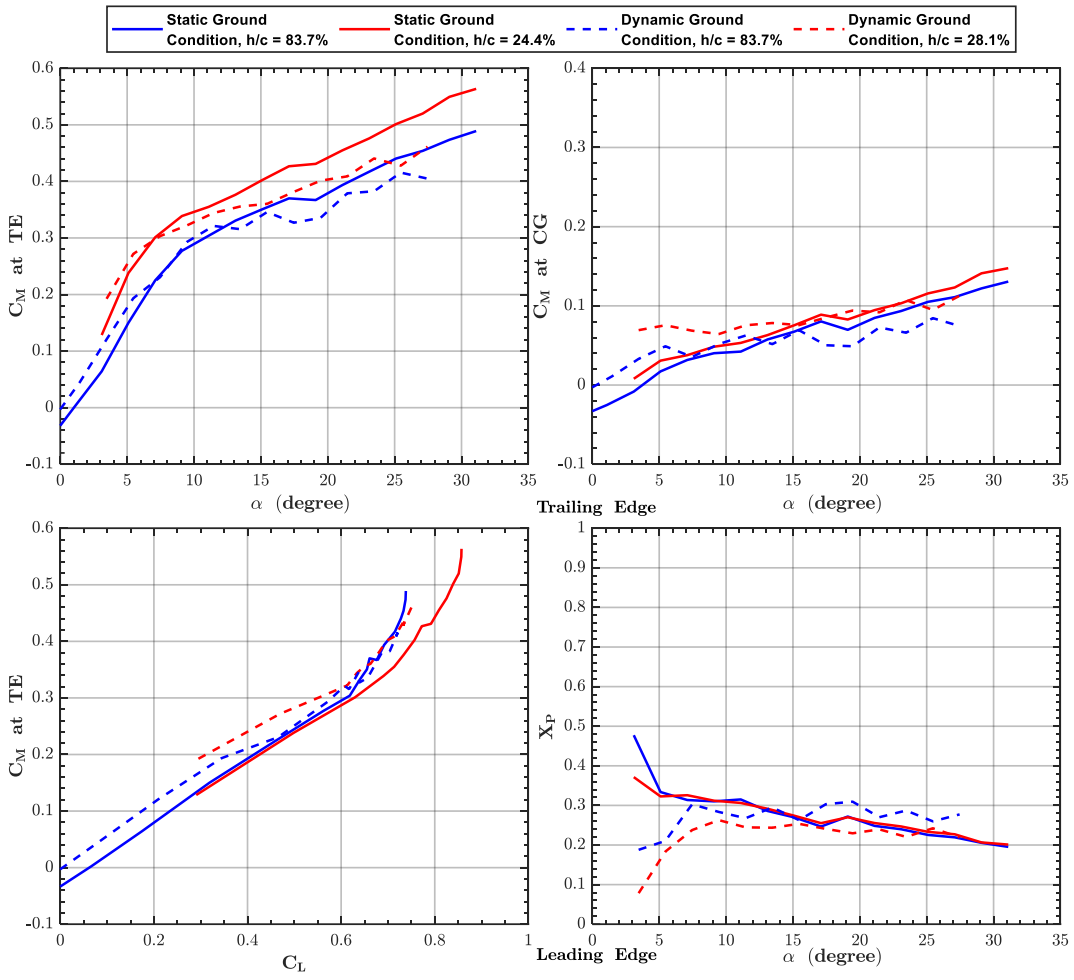

Figure 5-14 Variation of Moment coefficient C_M at trailing-edge (TE) and center of gravity (CG) as a function of angle of attack and Lift coefficient C_L, and Non-Dimensional Pressure Center coordinate X_P as a function of angle of attack for the reverse delta wing 2e at OGE and IGE conditions with respect to Static and Dynamic Ground Conditions

The distribution of C_M at the trailing-edge as a function of C_L is demonstrated in the bottom left chart. The dynamic ground condition curves are positioned at higher C_M positions for the same C_L. The slope of the dynamic ground condition OGE case is significantly reduced after $C_L = 0.34$. Although, static ground condition for OGE and IGE curves are almost identical, IGE case for the dynamic ground condition shows higher pitch-up moment with respect to the OGE case. The reversal observed in solid blue line around $C_L = 0.6$ is also steeper than the reversal of dashed blue line, which is observed at smaller C_L and has a gradual increase in slope.

Considering the C_M at wing center of gravity (CG) as a function of α shown at upper right corner, all curves at different heights pose positive slopes. For the dynamic ground case, both the slopes are smaller than the static ground case considering the IGE and OGE curves. The difference between OGE and IGE cases are such that red lines are always positioned at higher moment values for the same angle and slopes are quite similar. However, this pitch-up difference between IGE and OGE cases is more pronounced for the dynamic ground condition as it can be observed from the difference between dashed red and blue lines.

Considering the X_P as function of angle of attack demonstrated in lower right corner, as the angle of attack increases, X_P tends to shift toward the leading-edge for the static ground condition OGE and IGE cases, whereas this effect is not observed since slopes of the dashed curves change continuously for the angles of attack range between $7.5^o \leq \alpha \leq 25^o$. Between $0^o \leq \alpha \leq 7.5^o$, X_P shifts towards the trailing-edge of the wing for the static ground condition OGE and IGE cases, whereas just the opposite travel direction exists for the dynamic ground condition cases. Up to the angle of attack $\alpha \leq 15^o$, X_P tends to be positioned at more fore locations towards to the leading-edge for the dynamic ground condition cases. This tendency is more obvious for IGE cases, since the difference red solid and dashed lines are larger than the one between solid and dashed blue lines.

5.1.3.3 Comparison of Aerodynamic Center Locations of the Delta Wing 1a

In this chapter, the aerodynamic centers in static and dynamic ground conditions of the delta wing 1a are compared. In Figure 5-15, aerodynamic center in pitch X_a and in Figure 5-16 aerodynamic center in height X_h are given with solid and dashed lines, which show the static and dynamic conditions, respectively.

Considering Figure 5-15, the distinct feature of the dynamic ground condition appears as more aft positioned X_a for all heights. Therefore, it shows a more favorable H.S. characteristics since the margin between X_{CG} and X_a is smaller for the dynamic ground condition with respect to the static ground condition. However, X_a does not lie at more aft position with respect to X_{CG}, hence it also shows unstable longitudinal characteristics.

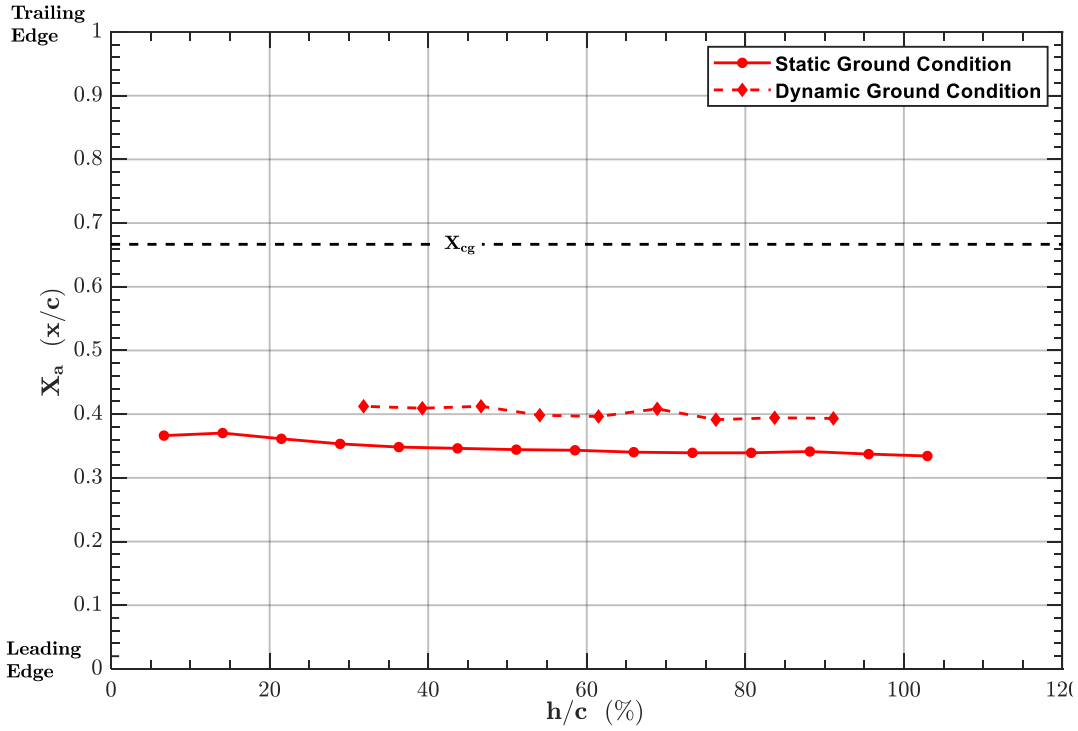

Figure 5-15 Comparison of aerodynamic center in pitch X_a at static and dynamic ground conditions with respect to non-dimensional height h/c for the delta wing 1a

Considering Figure 5-16, X_h shows considerably different characteristics for the dynamic case with respect to the static ground condition. Excluding the $11^o \leq \alpha \leq 21^o$ interval, X_h is also positioned at more aft positions for the dynamic ground condition with respect to the static ground condition. Therefore, dynamic ground condition shows an undesired characteristic since it significantly shifts X_h well aft positions with respect to X_a. In $11^o \leq \alpha \leq 21^o$ interval, even it is shifted to more aft positions with respect to X_{CG} at $\alpha = 11^o$ and $\alpha = 21^o$, which violates H.S. requirements, solely. However, dynamic ground condition shows a distinct stabilizing characteristic in this interval with respect to static ground condition up to the angle $\alpha = 15^o$, whereas it destabilizes quickly with further increase in angle of attack up to the angle $\alpha = 21^o$.

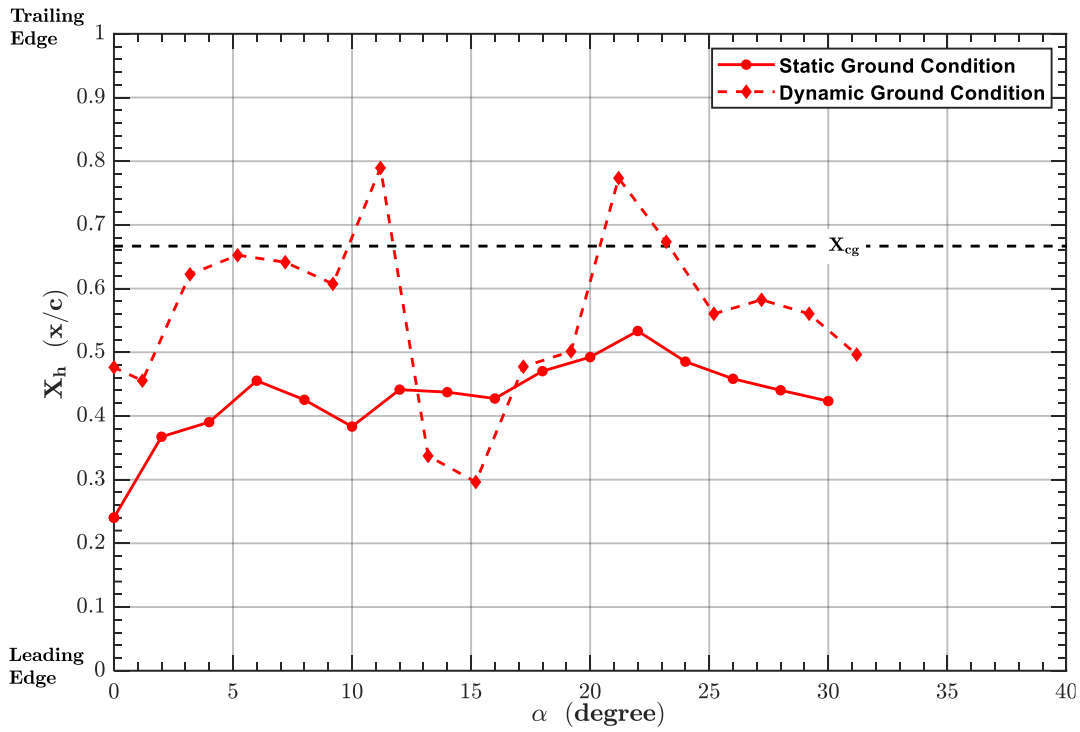

Figure 5-16 Comparison of aerodynamic center in height X_h at static and dynamic ground conditions with respect to angle of attack α for the delta wing 1a

5.1.3.4 Comparison of Aerodynamic Center Locations of the Reverse Delta Wing 2e

In this chapter, the aerodynamic centers in static and dynamic ground conditions of the delta wing 1a are compared. In Figure 5-17, aerodynamic center in pitch X_a and in Figure 5-18 aerodynamic center in height X_h are given with solid and dashed lines, which show the static and dynamic conditions, respectively.

Considering Figure 5-17, the same characteristic is also observed for the reverse delta wing 2e such that a more aft positioned X_a for all heights exists. Therefore, it also shows a more favorable H.S. characteristics. However, X_a does not lie at more aft position with respect to X_{CG}, hence it also shows unstable longitudinal characteristics, although the non-dimensional margin ($\Delta x/c$) is around 0.1.

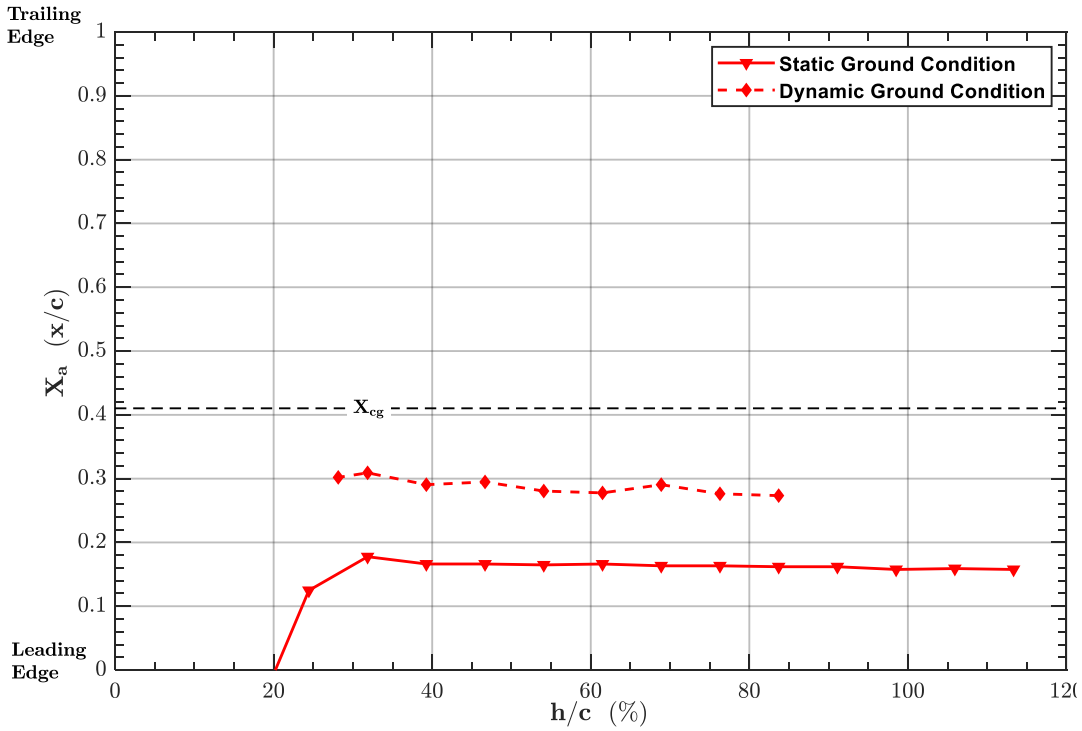

Figure 5-17 Comparison of aerodynamic center in pitch X_a at static and dynamic ground conditions with respect to non-dimensional height h/c for the reverse delta wing 2e

Considering Figure 5-18, X_h shows a more favorable characteristics for the dynamic ground condition with respect to the static case at lower angles $\alpha \leq 10^o$. Excluding the point around $\alpha = 12^o$, dynamic ground condition shows always a more aft positioned X_h with respect to the static ground condition, hence it provides more margin in terms of the distance between X_{CG} and X_h.

Considering the X_h characteristics between static and dynamic ground conditions, the reverse delta wing 2e shows both different trend and magnitude with respect to the delta wing 1a, which can be due to the different mechanism of the ground boundary layer on aerodynamics of delta and reverse delta wings as well as different aspect ratio values of those wings.

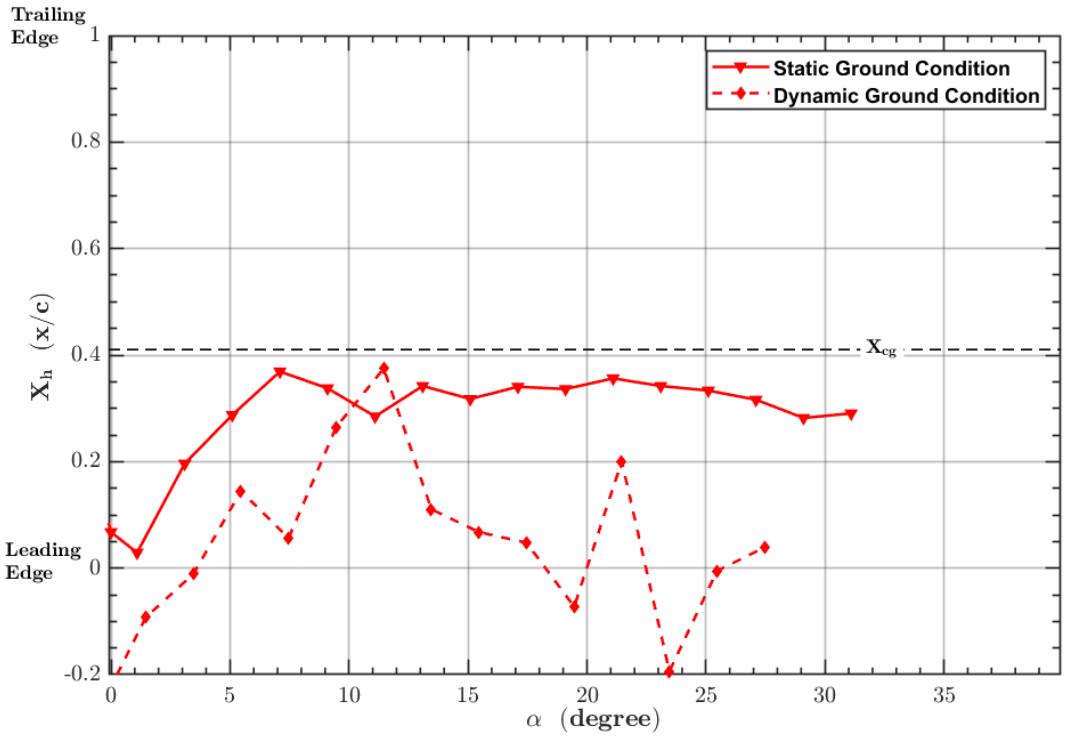

Figure 5-18 Comparison of aerodynamic center in height X_h at static and dynamic ground conditions with respect to angle of attack α for the reverse delta wing 2e

5.1.4 Comparison of Belt Status for Dynamic Ground Condition

In this chapter, dynamic ground condition is examined considering the belt status. For that purpose, belt was purposely switched off (Belt Off) for some cases during dynamic ground condition tests particularly for OGE and high intensity IGE runs for the delta wing 1a and the reverse delta wing 2e. Belt Off cases represent the lowest fidelity ground effect simulation due to the boundary layer of the wind tunnel test section, which is expected to be larger in size and more turbulent than the boundary layer of the static ground condition case.

5.1.4.1 Comparison of Force Measurements of the Delta Wing 1a

In Figure 5-19 and Figure 5-20, aerodynamic forces and moments as well as center of pressure for OGE and IGE cases are compared for Belt On and Belt Off conditions of the delta wing 1a. In these charts, OGE case is at $h/c = 91.1\%$ while two IGE cases are given at $h/c = 39.3\%$ and $h/c = 31.9\%$. The Belt On cases are given in solid lines, whereas Belt Off cases are provided with dashed lines.

Considering Figure 5-19, drag comparison on the upper left chart shows that Belt Off cases tend to have lesser drag, whereas drag values are quite similar for low angles $\alpha \leq 10^o$. For OGE case, Belt Off case results in lesser $10^o \leq \alpha \leq 30^o$ with respect to the Belt On case, although the difference gets smaller up to the angle $\alpha = 17^o$ and gets bigger with further increase in angle of attack. Similar behavior is also seen for the $h/c = 31.9\%$ case where dashed and solid red curves are identical up to $\alpha = 13^o$, whereas Belt Off case results in smaller drag values up to the angle $\alpha = 30^o$ with respect to the Belt On case. Likewise, the difference becomes minimum at $\alpha = 19^o$. For $h/c = 39.3\%$, drag values are the same for Belt On and Belt Off cases up to the angle $\alpha = 17^o$, whereas Belt Off case results in smaller drag values with further increase in angle of attack with respect to the Belt On case.

Considering lift curves on the upper right charts in Figure 5-19, OGE cases shows similar lift curve slope and similar maximum lift value, whereas Belt Off case is shifted approximately 2 deg in positive x axis direction. However, considering the two ground effect results, Belt Off cases result in lift curve slope and maximum lift decrease with respect to the Belt On cases.

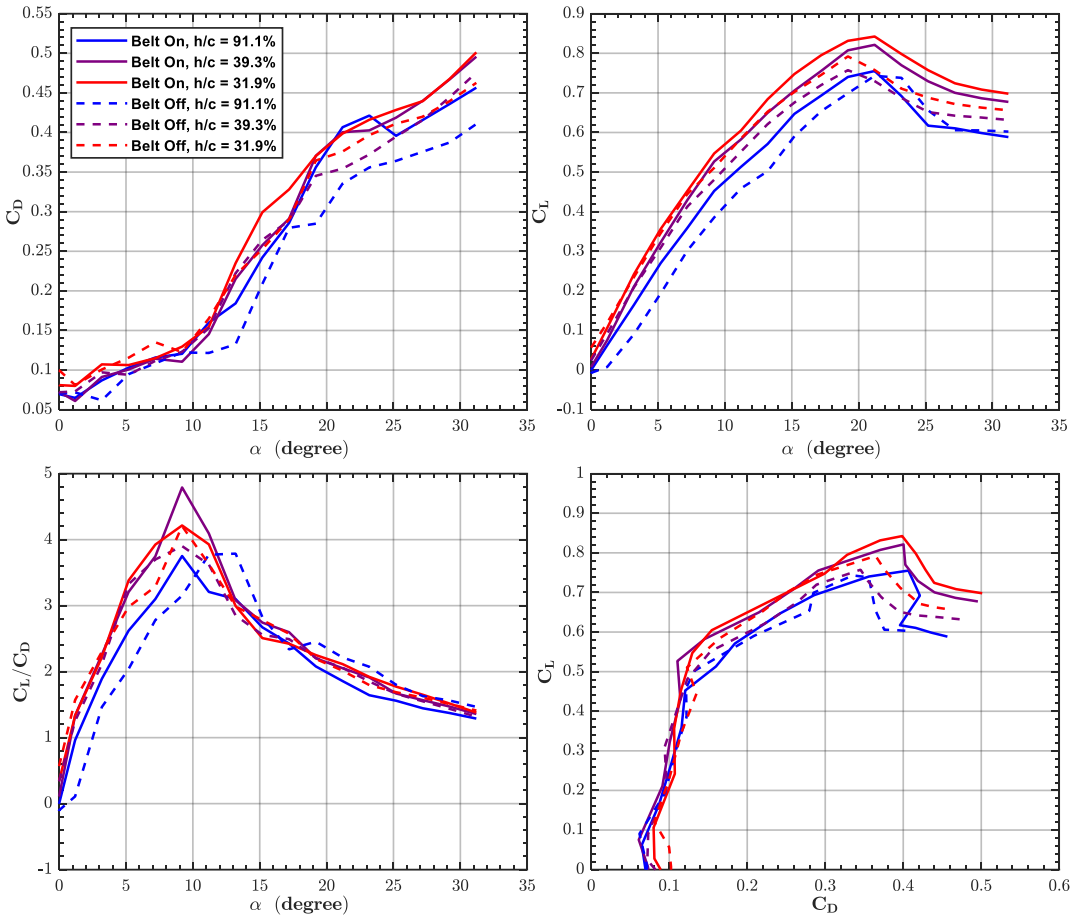

Figure 5-19 Variation of Drag coefficient C_D, Lift-to-Drag ratio C_L/C_D, Lift coefficient C_L as a function of angle of attack and Drag Polar for the delta wing 1a at OGE and IGE conditions with respect to Moving Belt Status

Considering lift-to-drag curves on the lower left charts in Figure 5-19, similar observation is valid such that Belt Off case is shifted approximately 2 deg in positive x axis direction. For $h/c = 39.3\%$ case, difference occurs around the peak values of the lift-to-drag curves such that Belt Off case results in lesser lift-to-drag peak value around $\alpha = 9^o$, whereas the curves are almost identical for other angles. For $h/c = 31.9\%$ case, lift-to-drag curves are quite similar, whereas area under dashed red curve is smaller for Belt Off case with respect to Belt On case for the low angle of attack region $\alpha \leq 10^o$.

Considering drag polars on the lower right charts in Figure 5-19, OGE cases show similar trends and magnitudes up to the reversal points such that it occurs $C_D = 0.4$ for Belt On case, whereas earlier reversal is seen at $C_D = 0.36$ for Belt Off case. For $h/c = 39.3\%$ case, Belt On and Belt Off cases are quite similar up to $C_L = 0.42$ whereas slope decrease occurs Belt Off case after this point with respect to the Belt On case, which results in lesser lift for the same drag values at higher angles for Belt Off case. Considering the $h/c = 31.9\%$ case, Belt On and Belt Off curves are quite similar up to $C_D = 0.29$, which is followed by slope decrease and lesser lift values for Belt Off case with respect to Belt On case.

Considering Figure 5-20 and upper left chart of C_M at trailing-edge (TE) with respect to angle of attack, Belt Off case results in lesser pitch-up moment for the same angle with respect to Belt On case up to the angle $\alpha = 15^o$ with interchanging slope. There is no remarkable difference for higher angles and blue dashed and solid curves are quite similar to each other. For IGE cases, difference occurs at high angles and curves are coincident for solid and dashed lines. For both heights, Belt Off cases results in smaller slopes and lesser pitch moment values with respect to Belt On cases.

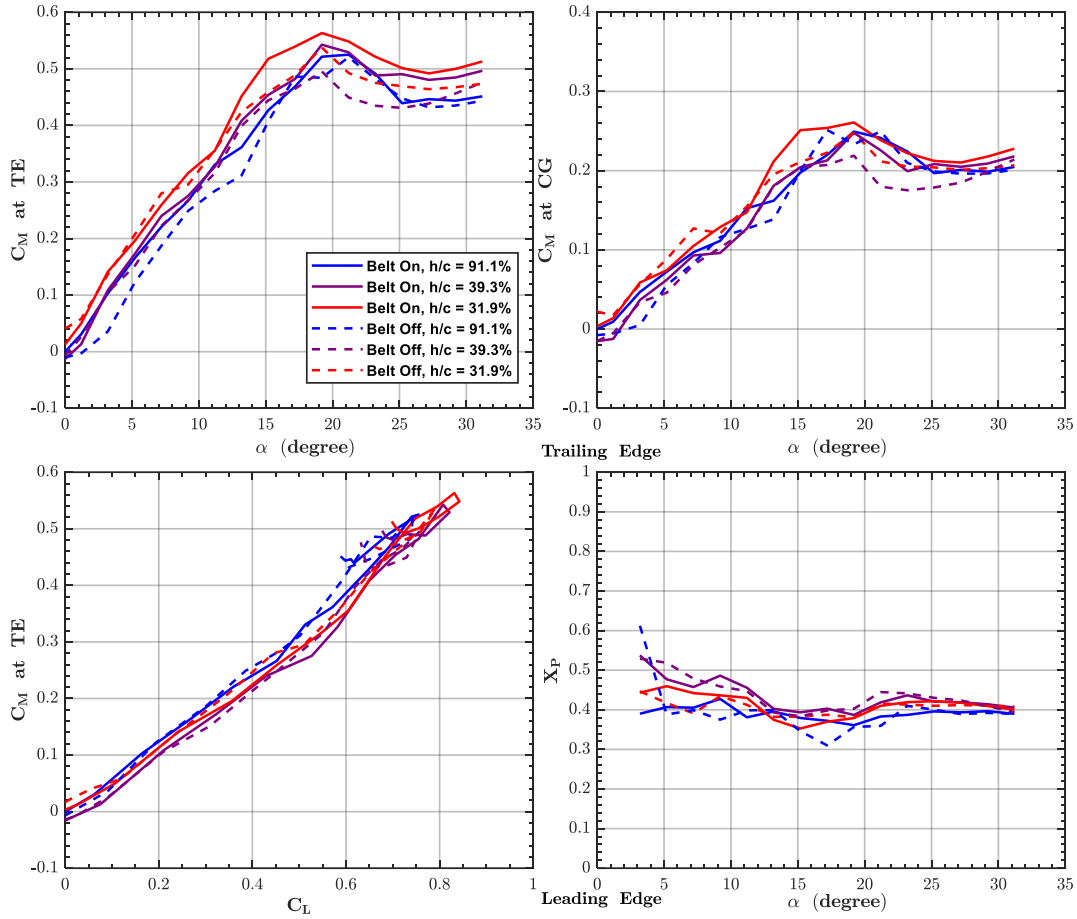

Figure 5-20 Variation of Moment coefficient C_M at trailing-edge (TE) and center of gravity (CG) as a function of angle of attack and Lift coefficient C_L, and Non-Dimensional Pressure Center coordinate X_P as a function of angle of attack for the delta wing 1a at OGE and IGE conditions with respect to Moving Belt Status

The distribution of C_M at the trailing-edge as a function of C_L is demonstrated in the bottom left chart. For all cases, dashed and solid lines are quite similar and no remarkable differences are observed.

Considering the C_M at wing center of gravity (CG) as a function of α shown at upper right corner, all curves at different heights pose positive slopes. For OGE case, Belt Off case results in lesser $C_{M_{cg}}$ up to $\alpha = 15^o$ with respect to Belt On case, whereas further increase in angle of attack results in similar $C_{M_{cg}}$ values. For $h/c =$

39.3% case, Belt Off case results in lesser $C_{M_{cg}}$ with respect to Belt On case after $\alpha = 17^o$, whereas this angle is reduced to $\alpha = 13^o$ for $h/c = 31.9\%$ case. The differences between solid and dashed lines are quite small for the angles lesser than $\alpha = 17^o$ and $\alpha = 13^o$, respectively.

Considering the X_P as function of angle of attack demonstrated in lower right corner, neither a remarkable movement nor a monotonic trend of the X_P is observed considering Belt On and Belt Off cases. IGE cases are almost identical, whereas differences in X_P locations between Belt On and Belt Off cases are more pronounced for OGE case such that Belt Off case results in more aft positioned X_P at lower angles and more fore positioned X_P around $\alpha = 17^o$.

5.1.4.2 Comparison of Force Measurements of the Reverse Delta Wing 2e

In Figure 5-21 and Figure 5-22, aerodynamic forces and moments as well as center of pressure for OGE and IGE cases are compared for Belt On and Belt Off conditions of the reverse delta wing 2e. In these charts, OGE case is at $h/c = 83.7\%$ while two IGE case is at $h/c = 28.1\%$. The Belt On cases are given in solid lines, whereas Belt Off cases are provided with dashed lines.

Considering Figure 5-21, drag comparison on the upper left chart shows that Belt Off and Belt On cases do not show a consistent trend such that dashed and solid lines intersect each other at several angles. Although, differences of drag values are smaller, Belt Off case results in lesser drag values with respect to Belt On case between $9.5^o \leq \alpha \leq 16^o$ interval for OGE case.

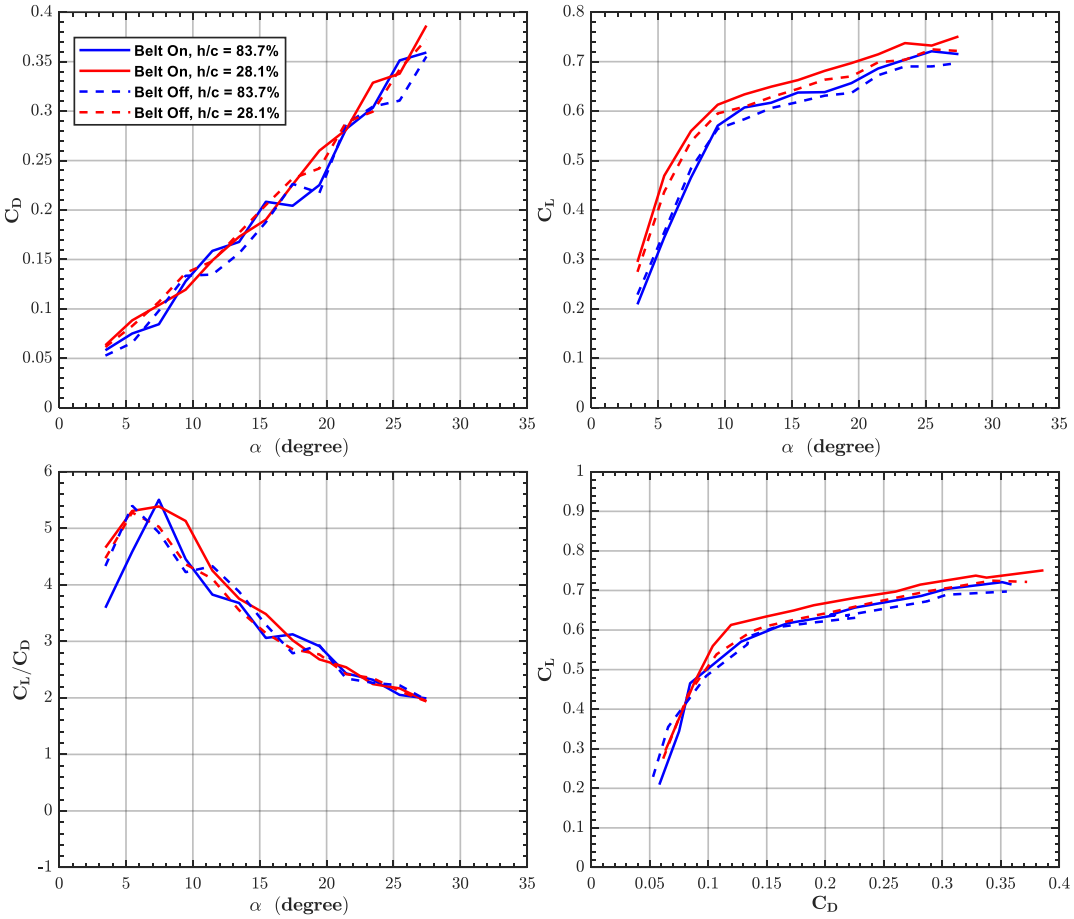

Figure 5-21 Variation of Drag coefficient C_D, Lift-to-Drag ratio C_L/C_D, Lift coefficient C_L as a function of angle of attack and Drag Polar for the reverse delta wing 2e at OGE and IGE conditions with respect to Moving Belt Status

Considering lift curves on the upper right charts in Figure 5-21, OGE cases shows similar lift curve slope and similar maximum lift value up to the angle $\alpha = 10^o$, whereas lift curve slope is reduced for Belt Off case with respect to Belt On case with further increase in angle. There is a slight decrease in lift curve slope for Belt Off IGE case with respect to Belt On IGE case up to the angle $\alpha = 10^o$, whereas lift curve slope decrease for higher angles observed in OGE cases are much more pronounced for IGE case since reduction in red dashed line slope is bigger than the reduction in blue dashed line compared to associated Belt On cases given with solid red and blue lines, respectively.

Considering lift-to-drag curves on the lower left charts in Figure 5-21, Belt Off case is shifted approximately 2 deg in negative x axis direction, which is just opposite direction for the same case of the delta wing 1a. For IGE case, lift-to-drag curves are quite similar, whereas area under dashed red curve is smaller for Belt Off case with respect to Belt On case for the angle of attack region $\alpha \geq 5.5^{o}$.

Considering drag polars on the lower right charts in Figure 5-21, Belt Off case is slightly shifted leftward and has smaller slope for the region $C_D \geq 0.08$ with respect Belt On case for OGE condition. For IGE case, Belt On and Belt Off curves are identical up to $C_D = 0.1$. At higher C_D values, Belt Off cases result in lesser C_L with respect to Belt On case.

Considering Figure 5-22 and upper left chart of C_M at trailing-edge (TE) with respect to angle of attack, Belt Off case has similar slope and magnitude up to the angle $\alpha = 10^{o}$ for OGE case with respect to Belt On case, whereas increasing angle of attack results in pitch-up moment for the same angle with respect to Belt On case with interchanging slope. For IGE cases, both slope and magnitude is reduced for Belt Off case with respect to Belt On case, whereas differences increase with increasing angle of attack.

The distribution of C_M at the trailing-edge as a function of C_L is demonstrated in the bottom left chart. For OGE case, dashed and solid lines are quite similar in magnitude and no distinct characteristic is seen, whereas the curve is shifted in negative y axis for red dashed line with respect to red solid line whereas slopes are quite similar for C_L values $C_L \leq 0.6$. Further increase in C_L results in approximately identical curves for Belt On and Belt Off IGE cases.

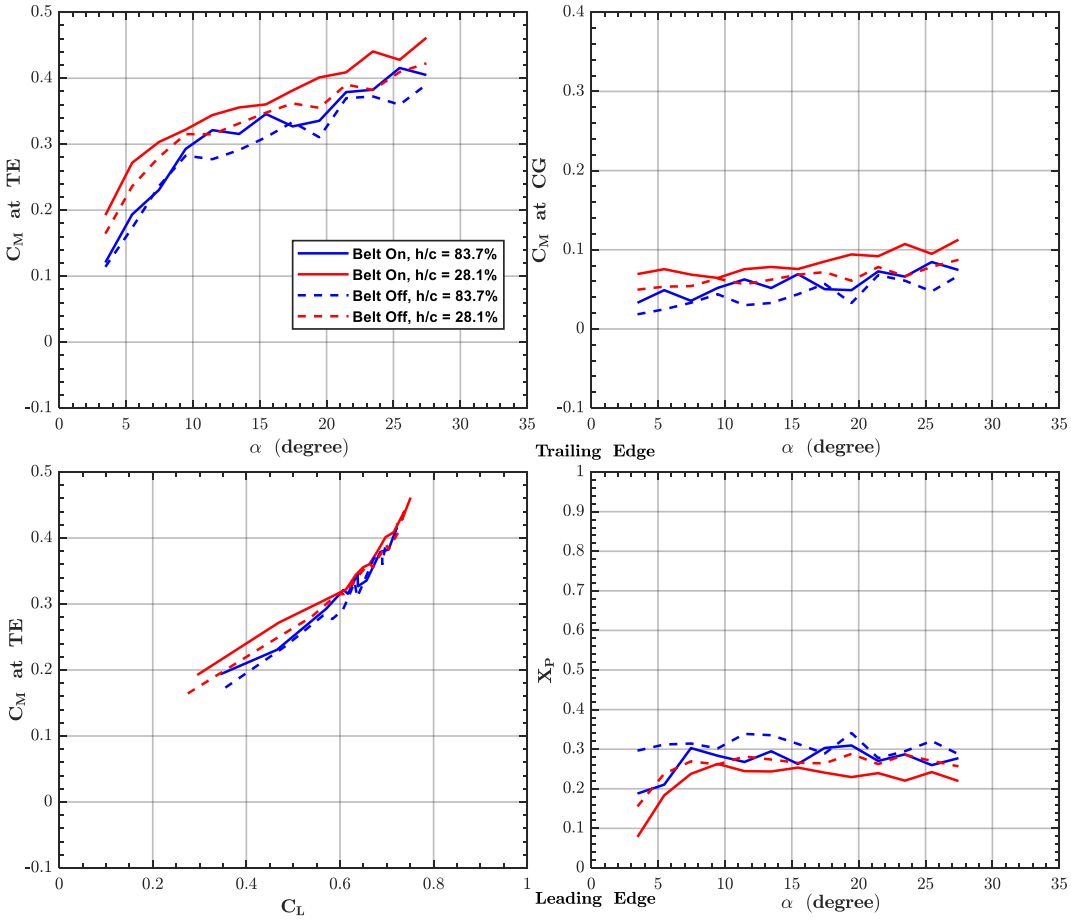

Figure 5-22 Variation of Moment coefficient C_M at trailing-edge (TE) and center of gravity (CG) as a function of angle of attack and Lift coefficient C_L, and Non-Dimensional Pressure Center coordinate X_P as a function of angle of attack for the reverse delta wing 2e at OGE and IGE conditions with respect to Moving Belt Status

CONCLUSION

The principal findings throughout this study is provided in this chapter. The conclusions are drawn considering the static and and dynamic ground condition, their comparison as well as the effect of belt status.

6.1 Effect of Static Ground Condition

6.1.1 Out of Ground Effect Results

Considering the combined assessments of the pressure and force measurements, the principal findings are as follows:

- Considering the effect of wing thickness on aerodynamic performance of delta and reverse delta wings, aerodynamic characteristics of delta wings and reverse delta wings and their corresponding dependence on wing thickness are substantially different. The thick delta wing 1a with symmetric bevel at the leading-edge could maintain a strong vortex structure up to $\alpha = 20^{o}$ and $\alpha = 22^{o}$ and achieve maximum C_L value close to the thin delta wing 1b. The thin reverse delta wing 2b generates higher lift at low angles of attack with higher maximum efficiency compared to the thin delta wing 1b. However, this is not witnessed when the thickness of the wing is increased. In addition, the reverse delta wings 2a, 2b have aerodynamic and pressure centers closer to the leading-edge and have better longitudinal static stability characteristics with higher stability margin when compared to the delta wings 1a, 1b. The stability margin of reverse delta wing increases significantly with increasing wing thickness whereas the wing thickness has negligible effect on it for delta wings.
- Considering the effect of geometrical modifications on aerodynamic performance of reverse delta wings, the sole effect of wing anhedral has

deteriorating impact on the performance of reverse delta wings since it increases drag penalty, decreases the lift and lift curve slope and efficiency, although it promotes longitudinal static stability and shifts the aerodynamic and pressure centers towards the trailing-edge. Cropping of the anhedraled wings tremendously improves the deteriorated performance characteristics resulting in improvement in lift and efficiency, additional shift of aerodynamic and pressure centers towards the trailing-edge and further enhancement in longitudinal static stability and stability margin. This might be due to elimination of the wing portion with cropping which neither contributes to lift generation capability nor creates nose-down pitch moment. Anhedraled and cropped wing 2e with $\delta = 15^{o}$ and $Cr = 30\%$ possesses the highest C_L/C_D with slight loss in lift at high angles of attack and the best longitudinal static stability characteristics.

6.1.2 In Ground Effect Results of the Static Ground Condition

Considering the combined assessments of the pressure and force measurements, the principal findings are as follows:

- Considering the influence of the presence of the ground on the LEV as well as aerodynamic performance of the delta wing 1a, the observed effects are substantially different at different heights and angles of attack. The GE intensity is favorable for aerodynamic performance at all angles of attack and quite effective on both vortex reattachment and vortex strength at moderate angles of attack around $\alpha = 13^{o}$. The pressure and force measurements confirm that the observed effects increase in an exponential manner such that the change in flow features such as vortex behavior as well as force, moment and pressure results are more significant at both higher angles of attack as well as lower heights values. The delta wing 1a could maintain a strong

vortex structure up to $\alpha = 20^o$ and $\alpha = 22^o$ for OGE condition whereas the stall onset is earlier for the lower heights. Although, both drag and lift forces increase with GE at all angles, the performance improvements come from the higher rate of increase in lift force at lower angles of attack, which is not witnessed for higher angles. The maximum C_L/C_D value shifts toward to lower angles of attack as the height decreases and maximum 24% increase in performance with GE is observed considering the lowest height value in the present study with respect to the OGE case.

- Ground effect with static ground condition results in earlier stall for the delta wings 1a and 1b as well as the reverse delta wing 2a, whereas this effect is either not observed or negligibly small for the reverse delta wings 2b, 2c, 2d, 2e, and 2f. The peak values of the lift-to-drag ratio are observed at smaller angle of attack with ground effect for both the delta wings 1a and 1b, whereas none of the reverse delta wings show this behavior.
- Presence of the static ground results in downstream shift of the center of pressure for all the wings, whereas this effect is smaller for the reverse delta wings 2e and 2f and may even change sign at low angles of attack such that ground effect may result in upstream shift of the X_P.
- Considering the longitudinal static stability characteristics of the delta wing 1a, GE results in increased slopes for C_L and C_M, which in turn results in aft movement of pressure center X_P as well as aerodynamic center in pitch X_a. However, the movements on the longitudinal axis of these centers remain in a limited range over the wing chord whereas aerodynamic center in height X_h exhibits significant back and forth movement on the longitudinal axis resulting in interchanging stability characteristics varying with both height and angle of attack. Although, height stability H.S. is ensured for $\alpha \leq 3^o$, the location of the aerodynamic center in pitch is not desired since it violates that it has to be positioned at a more aft position with respect to the X_{CG}, hence the usage of the delta wing as a WIG vehicle is not feasible. However, inclusion of horizontal tail or incorporation of blended wing body concept

such as wing twist and camber variations might be considered to position the X_a at a more aft location.

- Considering different planforms for the delta and reverse delta wings, the X_a trends are quite similar for delta wings 1a and 1b, whereas former one (thick) has a more fore positioned X_a at different heights. The reverse delta wings 2a and 2b show also similar trends with respect to the height, but this time thick reverse delta wing 2a has a more aft positioned X_a at different heights. Considering the aerodynamic center in height X_h, thin delta wing 1b has more aft positioned X_h with respect to the thick delta wing 1a, whereas interchanging relative positions are observed between the reverse delta wing 2a and 2b. Considering the sole effect of anhedral angle, inclusion of anhedral angle first shifts the X_a to the more aft positions for the reverse delta wing 2c, but further increase in anhedral for the reverse delta wing 2d results in similar X_a locations with respect to the reverse delta wing 2b without anhedral. The effect of anhedral also shifts the X_h to aft positions at high angles of attack for the reverse delta wing 2c, but further increase in anhedral causes reversal in shift direction and results in significantly fore positioned X_h for the reverse delta wing 2d with respect to the reverse delta wing 2b. Considering the sole effect of cropping on anhedraled reverse delta wings, inclusion of $\mathrm{Cr} = 30\%$ to the 15^o anhedraled reverse delta wing 2c results in similar X_a for the reverse delta wing 2e, whereas significant aft shift of X_a is observed for the reverse delta wing 2f with the inclusion of cropping to the anhedraled reverse delta wing 2d. Cropping also results in aft shift of X_h for the reverse delta wing 2e compared to the reverse delta wing 2c, whereas it results in significant forward shift for the reverse delta wing 2f with respect to the reverse delta wing 2d at low and moderate angles of attack between $5^o \leq \alpha \leq 10^o$.
- Among reverse delta wing planforms, the reverse delta wing 2e, which incorporates 15^o anhedral and $\mathrm{Cr} = 30\%$ cropping, results in good

longitudinal static stability characteristics as well as remarkable performance characteristics IGE for the static ground condition.

6.2 Effect of Dynamic Ground Condition and Ground Boundary Condition

Considering the combined assessments of the force measurements of the dynamic ground condition and corresponding cases with the static ground condition, the principal findings are as follows:

- Considering the influence of the ground boundary condition for the dynamic case, the GE intensity is favorable for aerodynamic performance, but its effect cannot be generalized to all angles of attack, which is different from the static ground condition case. Aerodynamic improvements are observed in terms of increased area under lift-to-drag versus angle of attack curve rather than increased peak values, which is the obvious effect of the static ground condition. Increased C_L value is the primary source of performance improvements observed for IGE cases with respect to OGE cases.
- Compared to the static ground condition case, slopes for C_D, C_L and C_M are generally reduced for the dynamic ground case. The combined effects may result in similar and improved performance values for OGE and IGE cases, respectively, which is seen from the delta wing 1a results or significant performance losses for both OGE and IGE conditions as deduced from the reverse delta wing 2e results.
- Considering the longitudinal static stability characteristics for dynamic ground case, dynamic ground condition resulted in quite similar aerodynamic center in pitch X_a behavior with respect to the height, whereas it is positioned at more aft positions with respect to the static ground condition. Movement of pressure center X_P is affected by the ground boundary condition, whereas it is also positioned at more aft positions for the different angles of attack and height values. However, X_P movement with respect to the angle of attack at both IGE and OGE cases are quite different from the static ground condition.

Aerodynamic center in height X_h exhibits significantly different characteristics for the dynamic ground case with respect to the static ground case. For the delta wing 1a, it is generally positioned at more aft positions with respect to the angle of attack, whereas it is positioned at more forward positions for the reverse delta wing 2e. Therefore, the longitudinal static stability characteristics are dependent both on ground boundary condition as well as the planform. Considering the H.S. for the dynamic ground condition, the combined effect of aft positioned X_a for the delta wing 1a and significantly forward shifted X_h for the reverse delta wing are the primary reasons for the improved longitudinal static stability characteristics of both wings.

- The belt status for the dynamic ground condition has two different effects, which are common for both the delta wing 1a and the reverse delta wing 2e. Compared to the Belt On case, Belt Off case results in lesser slope for the aerodynamic coefficients, which can be interpreted as dynamic pressure loss or angularity change. The latter one decreased or increased angle of attack for the peak values of the lift-to-drag ratio. Although, decreased slopes are common for both the delta wing 1a and the reverse delta wing 2e, the effect of Belt Off case on X_P are different in terms of wing planforms. For the delta wing 1a, Belt On and Belt Off cases generally show similar X_P distribution with respect to the angle of attack at IGE and OGE conditions, whereas Belt Off case results in clear aft shift of X_P for all angles of attack at both IGE and OGE cases for the reverse delta wing 2e.

6.3 Recommendations for Future Work

In this thesis, the effect of ground on flow structure of non-slender delta and reverse delta wings as well as the effects of thickness-to-chord ratio, anhedral angle, and cropping on the aerodynamics and longitudinal static stability of non-slender reverse delta wings in comparison to non-slender delta wings have been investigated experimentally. It is suggested that the following extensions and items can be employed as future work:

- The characterization of ground and its effect on aerodynamics and stability of the delta and reverse delta wings are based on pressure and force measurements. The experiments with other measurements techniques such as laser-illuminated flow visualization and particle image velocimetry (PIV) can be conducted to understand the global flow field that would help to explain the different mechanisms affecting the aerodynamic and stability characteristics of delta and reverse delta wings.
- The experiments for force and pressure measurements were conducted with pitch and pause technique. The model positioning system design can be improved by utilizing servo motors for pitch and height adjustments of the model. The automatic pitch and height control would allow smaller increments for angle of attack and height between consecutive runs, which further improves the accuracy of the stability derivative estimation as well as accelerate the experiments by eliminating the human effort from the process and better resolution in angle of attack and height dimensions.
- The moving belt mechanism can be further upgraded with the inclusion of the suction slot. The necessity of the suction slot regarding to the parameters such as wing planform and Reynolds number can be constructed utilizing force measurements.
- The boundary layer characterization with different ground conditions can be examined by utilizing laser doppler anemometry (LDA) measurements. Particularly, boundary layer measurements at different longitudinal positions

on the tunnel flow, on the ground plate, and on the moving belt would be helpful to understand the limitations of the different ground effect testing methods and further improvements for reflecting the physically correct boundary condition.

- The reverse delta wing 2e can be further investigated with the inclusion of horizontal tail as a complete aerodynamic configuration. The overall design can be tested IGE and OGE to reveal the potential of the base planform as a WIG vehicle.

REFERENCES

[1] Graves, S. S. *Investigation of a Technique for Measuring Dynamic Ground Effect in a Subsonic Wind Tunnel*. Hampton, Virginia, 1999.

[2] Cui, E., and Zhang, X. "Ground Effect Aerodynamics." *Encyclopedia of Aerospace Engineering*, No. 1927, 2010, pp. 1–12. doi:10.1002/9780470686652.eae022.

[3] Rozhdestvensky, K. V. "Wing-in-Ground Effect Vehicles." *Progress in Aerospace Sciences*, Vol. 42, No. 3, 2006, pp. 211–283. doi:10.1016/j.paerosci.2006.10.001.

[4] Qu, Q., Lu, Z., Liu, P., and Agarwal, R. K. "Numerical Study of Aerodynamics of a Wing-in-Ground-Effect Craft." *Journal of Aircraft*, Vol. 51, No. 3, 2014, pp. 913–924. doi:10.2514/1.C032531.

[5] Gursul, I. "Recent Developments in Delta Wing Aerodynamics." *Aeronautical Journal*, Vol. 108, No. 1087, 2004, pp. 437–452. doi:10.1017/S0001924000000269.

[6] Gursul, I., Gordnier, R., and Visbal, M. "Unsteady Aerodynamics of Nonslender Delta Wings." *Progress in Aerospace Sciences*, Vol. 41, No. 7, 2005, pp. 515–557. doi:10.1016/j.paerosci.2005.09.002.

[7] Taylor, G., Kroker, A., and Gursul, I. "Passive Flow Control over Flexible Non-Slender Delta Wings." *43rd AIAA Aerospace Sciences Meeting and Exhibit - Meeting Papers*, No. January, 2005, pp. 14389–14405. doi:10.2514/6.2005-865.

[8] ROCKWELL, D. "Three-Dimensional Flow Structure on Delta Wings at High Angle-of-Attack - Experimental Concepts and Issues." 1993. doi:10.2514/6.1993-550.

[9] Earnshaw, P. B., and Lawford, J. A. “Low-Speed Wind-Tunnel Experiments on a Series of Sharp-Edged Delta Wings.” *Ministry of Aviation Aeronautical Research Council, Reports and Memoranda*, No. 3424, 1964.

[10] Yavuz, M. M., and Rockwell, D. “Identification and Control of Three-Dimensional Separation on Low Swept Delta Wing.” *AIAA Journal*, Vol. 44, No. 11, 2006, pp. 2805–2811. doi:10.2514/1.24756.

[11] Breitsamter, C. “Unsteady Flow Phenomena Associated with Leading-Edge Vortices.” *Progress in Aerospace Sciences*, Vol. 44, No. 1, 2008, pp. 48–65. doi:10.1016/j.paerosci.2007.10.002.

[12] Gad-El-Hak, M., and Black welder, R. F. “The Discrete Vortices from a Delta Wing.” *AIAA Journal*, Vol. 23, No. 6, 1985, pp. 961–962. doi:10.2514/3.9016.

[13] Delery, J. M. “Aspects of Vortex Breakdown.” *Progress in Aerospace Sciences*, Vol. 30, No. 1, 1994, pp. 1–59. doi:10.1016/0376-0421(94)90002-7.

[14] Yaniktepe, B., and Rockwell, D. “Flow Structure on a Delta Wing of Low Sweep Angle.” *AIAA Journal*, Vol. 42, No. 3, 2004, pp. 513–523. doi:10.2514/1.1207.

[15] Yaniktepe, B., and Rockwell, D. “Flow Structure on Diamond and Lambda Planforms: Trailing-Edge Region.” *AIAA Journal*, Vol. 43, No. 7, 2005, pp. 1490–1500. doi:10.2514/1.7618.

[16] Bulent, Y., Coskun, O., Besir, S., and Serkan, C. “Experimental Investigation of Surface Flow Structure over Non-Slender Diamond Wing.” *Green Energy and Technology*, 2018, pp. 319–331. doi:10.1007/978-3-319-62572-0_22.

[17] Tumse, S., Tasci, M. O., Karasu, I., and Sahin, B. “Effect of Ground on Flow Characteristics and Aerodynamic Performance of a Non-Slender Delta Wing.” *Aerospace Science and Technology*, Vol. 110, 2021, p. 106475. doi:10.1016/j.ast.2020.106475.

[18] Canpolat, C., Yayla, S., Sahin, B., and Akilli, H. “Observation of the Vortical Flow over a Yawed Delta Wing.” *Journal of Aerospace Engineering*, Vol. 25, No. 4, 2012, pp. 613–626. doi:10.1061/(asce)as.1943-5525.0000163.

[19] Lee, T., and Ko, L. S. “Experimental Study of the Vortex Flow and Aerodynamic Characteristics of a Reverse Delta Wing.” *Proceedings of the Institution of Mechanical Engineers, Part G: Journal of Aerospace Engineering*, Vol. 230, No. 6, 2016, pp. 1126–1138. doi:10.1177/0954410015604653.

[20] Gursul, I., Allan, M. R., and Badcock, K. J. “Opportunities for the Integrated Use of Measurements and Computations for the Understanding of Delta Wing Aerodynamics.” *Aerospace Science and Technology*, Vol. 9, No. 3, 2005, pp. 181–189. doi:10.1016/j.ast.2004.08.007.

[21] Anderson, J. D. *Fundamentals of Aerodynamics*. McGraw-Hill, Singapore, 1991.

[22] Werlé, H. “Quelques Résultats Expérimentaux Sur Les Ailes En Flèche, Aux Faibles Vitesses, Obtenus En Tunnel Hydrodynamique.” *La Recherche Aéronautique*, No. 41, 1954, pp. 15–21.

[23] Bird, J. D. *Tuft-Grid Surveys at Low Speeds for Delta Wings*. WASHINGTON, D.C., 1969.

[24] Polhamus, E. C. “Predictions of Vortex-Lift Characteristics by a Leading-Edge Suction Analogy.” *Journal of Aircraft*, Vol. 8, No. 4, 1971, pp. 193–199. doi:10.2514/3.44254.

[25] Erickson, G. E. “Water-Tunnel Studies of Leading-Edge Vortices.” *Journal of Aircraft*, Vol. 19, No. 6, 1982, pp. 442–448. doi:10.2514/3.57414.

[26] Gursul, I., Wang, Z., and Vardaki, E. Review of Flow Control Mechanisms of Leading-Edge Vortices. *Progress in Aerospace Sciences*. 7–8. Volume 43, 246–270.

[27] Karasu, I., Sahin, B., Tasci, M. O., and Akilli, H. “Effect of Yaw Angles on Aerodynamics of a Slender Delta Wing.” *Journal of Aerospace Engineering*, Vol. 32, No. 5, 2019, p. 04019074. doi:10.1061/(asce)as.1943-5525.0001066.

[28] Sahin, B., Yayla, S., Canpolat, C., and Akilli, H. “Flow Structure over the Yawed Nonslender Diamond Wing.” *Aerospace Science and Technology*, Vol. 23, No. 1, 2012, pp. 108–119. doi:10.1016/j.ast.2011.06.008.

[29] Ol, M. V., and Gharib, M. “Leading-Edge Vortex Structure of Nonslender Delta Wings at Low Reynolds Number.” *AIAA Journal*, Vol. 41, No. 1, 2003, pp. 16–26. doi:10.2514/2.1930.

[30] Gursul, I., Taylor, G., and Wooding, C. Vortex Flows over Fixed-Wing Micro Air Vehicles. 2002.

[31] Gordnier, R. E., and Visbal, M. R. “Compact Difference Scheme Applied to Simulation of Low-Sweep Delta Wing Flow.” *AIAA Journal*, Vol. 43, No. 8, 2005, pp. 1744–1752. doi:10.2514/1.5403.

[32] Taylor, G., Schnorbus, T., and Gursul, I. An Investigation of Vortex Flows over Low Sweep Delta Wings. 2003.

[33] Wang, J. J., and Zhang, W. “Experimental Investigations on Leading-Edge Vortex Structures for Flow over Non-Slender Delta Wings.” *Chinese Physics Letters*, Vol. 25, No. 7, 2008, pp. 2550–2553. doi:10.1088/0256-307X/25/7/060.

[34] Widmann, A., and Tropea, C. “Reynolds Number Influence on the Formation of Vortical Structures on a Pitching Flat Plate.” *Interface Focus*, Vol. 7, No. 1, 2017, p. 20160079. doi:10.1098/rsfs.2016.0079.

[35] Earnshaw, P. B. “An Experimental Investigation of the Structure of a Leading Edge Vortex.” *Ministry of Aviation Aeronautical Research Council, Reports and Memoranda*, No. 2740, 1961, p. 11.

[36] Yavuz, M. M., Elkhoury, M., and Rockwell, D. “Near-Surface Topology and Flow Structure on a Delta Wing.” *AIAA Journal*, Vol. 42, No. 2, 2004, pp. 332–340. doi:10.2514/1.3499.

[37] Özgören, M., Sahin, B., and Rockwell, D. “Vortex Structure on a Delta Wing at High Angle of Attack.” *AIAA Journal*, Vol. 40, No. 2, 2002, pp. 285–292. doi:10.2514/2.1644.

[38] RILEY, A. J., and LOWSON, M. V. “Development of a Three-Dimensional Free Shear Layer.” *Journal of Fluid Mechanics*, Vol. 369, No. (ed.), Amsterdam, The Netherlands, Elsevier Sci. Publishers B.V., 1984, pp.327-332. (ISBN 0-444–87594, 1998, pp. 49–89. doi:10.1017/S0022112098001712.

[39] Nelson, R. C., and Pelletier, A. “The Unsteady Aerodynamics of Slender Wings and Aircraft Undergoing Large Amplitude Maneuvers.” *Progress in Aerospace Sciences*, Vol. 39, Nos. 2–3, 2003, pp. 185–248. doi:10.1016/S0376-0421(02)00088-X.

[40] Gursul, I. “Review of Unsteady Vortex Flows over Slender Delta Wings.” *Journal of Aircraft*, Vol. 42, No. 2, 2005, pp. 299–319. doi:10.2514/1.5269.

[41] Lucca-Negro, O., and O’Doherty, T. “Vortex Breakdown: A Review.” *Progress in Energy and Combustion Science*, Vol. 27, No. 4, 2001, pp. 431–481. doi:10.1016/S0360-1285(00)00022-8.

[42] Taylor, G. S., and Gursul, I. “Buffeting Flows over a Low-Sweep Delta Wing.” *AIAA Journal*, Vol. 42, No. 9, 2004, pp. 1737–1745. doi:10.2514/1.5391.

[43] Payne, F. M., Ng, T., Nelson, R. C., and Schiff, L. B. “Visualization and Wake Surveys of Vortical Flow over a Delta Wing.” *AIAA Journal*, Vol. 26, No. 2, 1988, pp. 137–143. doi:10.2514/3.9864.

[44] Lowson, M. V. “Some Experiments with Vortex Breakdown.” *The Journal of the Royal Aeronautical Society*, Vol. 68, No. 641, 1964, pp. 343–346. doi:10.1017/s036839310007944x.

[45] Yavuz, M. M. *Origin and Control of the Flow Structure and Topology on Delta Wings*. Lehigh University, Pennsylvania, 2006.

[46] Honkan, A., and Andreopoulos, J. “Instantaneous Three-Dimensional Vorticity Measurements in Vortical Flow over a Delta Wing.” *AIAA Journal*, Vol. 35, No. 10, 1997, pp. 1612–1620. doi:10.2514/2.20.

[47] Taylor, G. S., and Gursul, I. “Unsteady Vortex Flows and Buffeting of a Low Sweep Delta Wing.” *AIAA Paper*, No. January, 2004, pp. 6627–6635. doi:10.2514/6.2004-1066.

[48] Gursul, I., and Wang, Z. “Flow Control of Tip/Edge Vortices.” *AIAA Journal*, Vol. 56, No. 5, 2018, pp. 1731–1749. doi:10.2514/1.J056586.

[49] Zhang, X., Wang, Z., and Gursul, I. “Control of Multiple Vortices over a Double Delta Wing.” *47th AIAA Fluid Dynamics Conference, 2017*, No. June, 2017, pp. 1–27. doi:10.2514/6.2017-4122.

[50] Gu, W., Robinson, O., and Rockwell, D. “Control of Vortices on a Delta Wing by Leading-Edge Injection.” *AIAA Journal*, Vol. 31, No. 7, 1993, pp. 1177–1186. doi:10.2514/3.11749.

[51] Çetin, C., Çelik, A., and Yavuz, M. M. “Control of Flow Structure over a Nonslender Delta Wing Using Periodic Blowing.” *AIAA Journal*, Vol. 56, No. 1, 2018, pp. 90–99. doi:10.2514/1.J056099.

[52] Zharfa, M., Ozturk, I., and Yavuz, M. M. “Flow Structure on Nonslender Delta Wing: Reynolds Number Dependence and Flow Control.” *AIAA Journal*, Vol. 54, No. 3, 2016, pp. 1–18. doi:10.2514/1.J054495.

[53] Taylor, G., Wang, Z., Vardaki, E., and Gursul, I. “Lift Enhancement over Flexible Nonslender Delta Wings.” *AIAA Journal*, Vol. 45, No. 12, 2007, pp. 2979–2993. doi:10.2514/1.31308.

[54] Celik, A., and Yavuz, M. M. “Effect of Edge Modifications on Flow Structure of Low Swept Delta Wing.” *AIAA Journal*, Vol. 54, No. 5, 2016, pp. 1789–1797. doi:10.2514/1.J054587.

[55] Furman, A., and Breitsamter, C. “Delta Wing Steady Pressure Investigations for Sharp and Rounded Leading Edges.” *Notes on Numerical Fluid Mechanics and Multidisciplinary Design*, Vol. 92, 2006. doi:10.1007/978-3-540-33287-9_10.

[56] Canpolat, C., Yayla, S., Sahin, B., and Akilli, H. “Effects of Trailing-Edge Attachment on the Flow Structure over a Generic Delta Wing.” *Journal of Aerospace Engineering*, Vol. 30, No. 5, 2017, p. 06017003. doi:10.1061/(asce)as.1943-5525.0000766.

[57] Yayla, S., Canpolat, C., Sahin, B., and Akilli, H. “The Effect of Angle of Attack on the Flow Structure over the Nonslender Lambda Wing.” *Aerospace Science and Technology*, Vol. 28, No. 1, 2013, pp. 417–430. doi:10.1016/j.ast.2012.12.007.

[58] Yayla, S., Canpolat, C., Sahin, B., and Akilli, H. “Yaw Angle Effect on Flow Structure over the Nonslender Diamond Wing.” *AIAA Journal*, Vol. 48, No. 10, 2010, pp. 2457–2461. doi:10.2514/1.J050380.

[59] Kawazoe, H., Nakamura, Y., Ono, T., and Ushimaru, Y. “Static and Total Pressure Distributions around a Thick Delta Wing with Rounded Leading Edge.” *AIAA Fluid Dynamics Conference, 1994*, 1994. doi:10.2514/6.1994-2321.

[60] Sharifi Ghazijahani, M., and Yavuz, M. M. “Effect of Thickness-to-Chord Ratio on Aerodynamics of Non-Slender Delta Wing.” *Aerospace Science and Technology*, Vol. 88, 2019, pp. 298–307. doi:10.1016/j.ast.2019.03.033.

[61] Gülsaçan, B., Şencan, G., and Yavuz, M. M. “Effect of Thickness-to-Chord Ratio on Flow Structure of a Low Swept Delta Wing.” *AIAA Journal*, Vol. 56, No. 12, 2018, pp. 4657–4668. doi:10.2514/1.J057083.

[62] Çelik, A., Çetin, C., and Yavuz, M. M. “Effect of Passive Bleeding on Flow Structure over a Nonslender Delta Wing.” *AIAA Journal*, Vol. 55, No. 8, 2017, pp. 2555–2565. doi:10.2514/1.J055776.

[63] Kestel, K., Ramazanlı, B., and Yavuz, M. M. “Control of Flow Structure over a Non-Slender Delta Wing Using Passive Bleeding.” *Aerospace Science and Technology*, Vol. 106, 2020, p. 106136. doi:10.1016/j.ast.2020.106136.

[64] Gibson, B. T., and Gerhardt, H. A. “Natural Laminar Flow Wing Concept for Supersonic Transports.” *Journal of Aircraft*, Vol. 32, No. 1, 1995, pp. 130–136. doi:10.2514/3.46693.

[65] Gerhardt, H. A., Kerswell, J. F., Priestley, R. T., and Gibson, B. T. Laminar Supersonic Transport Aircraft, US5842666A, 1998.

[66] Gerhardt, H. A. Supersonic Natural Laminar Flow Wing, US5538201AJul, 1996.

[67] Gerhardt, H. A., Seho, K., Nolan, J., and Mrdeza, M. N. Aircraft with Variable Forward-Sweep Wing, US5984231A, 1999.

[68] Elsayed, O. A., Asrar, W., and Omar, A. A. Reverse Delta Wing Trailing Vortex Characteristics by Particle Image Velocimetry (PIV). 2008.

[69] Altaf, A., Omar, A. A., Asrar, W., and Jamaluddin, H. B. L. “Study of the Reverse Delta Wing.” *Journal of Aircraft*, Vol. 48, No. 1, 2011, pp. 277–286. doi:10.2514/1.C031101.

[70] Lee, T., and Ko, L. S. “Vortex Flow and Lift Generation of a Non-Slender Reverse Delta Wing.” *Proceedings of the Institution of Mechanical Engineers, Part G: Journal of Aerospace Engineering*, Vol. 231, No. 13, 2017, pp. 2438–2451. doi:10.1177/0954410016671342.

[71] Lee, T. “Impact of Gurney Flaplike Strips on the Aerodynamic and Vortex Flow Characteristic of a Reverse Delta Wing.” *Journal of Fluids Engineering, Transactions of the ASME*, Vol. 138, No. 6, 2016, pp. 1–9. doi:10.1115/1.4032301.

[72] Lee, T., Ko, L. S., and Tremblay-Dionne, V. “Effect of Anhedral on a Reverse Delta Wing.” *Proceedings of the Institution of Mechanical Engineers, Part G: Journal of Aerospace Engineering*, Vol. 232, No. 12, 2018, pp. 2317–2325. doi:10.1177/0954410017715047.

[73] Lee, T., and He, S. M. “The Trailing Vortices Generated by a Reverse Delta Wing with Different Wing Configurations.” *Aerospace Science and Technology*, Vols. 82–83, No. xxxx, 2018, pp. 378–393. doi:10.1016/j.ast.2018.08.022.

[74] Palaviccini, M. Review: Grizzly Bean Bag. http://mrpalaviccini.blogspot.com/2013/05/review-grizzly-bean-bag.html. Accessed Oct. 20, 2019.

[75] Nebylov, A., Nebylov, V., and Fabre, P. “WIG-Craft Flight Control above the Waved Sea.” *IFAC-PapersOnLine*, Vol. 28, No. 9, 2015, pp. 102–107. doi:10.1016/j.ifacol.2015.08.067.

[76] Urquhart, S. R., Prince, S. A., and Khodagolian, V. “Aerodynamic Study of Reversed-Delta Wing Surface Craft in Ground Effect.” *Collection of Technical Papers - 44th AIAA Aerospace Sciences Meeting*, Vol. 5, No. January, 2006, pp. 3067–3081. doi:10.2514/6.2006-253.

[77] Jones, B. L. *Experimental Investigation Into the Aerodynamic Ground Effect of a Tailless Chevron-Shaped Ucav*. Air Force Institute of Technology Air University, 2005.

[78] Wang, H., Teo, C. J., Khoo, B. C., and Goh, C. J. “Computational Aerodynamics and Flight Stability of Wing-In-Ground (WIG) Craft.” *Procedia Engineering*, Vol. 67, 2013, pp. 15–24. doi:10.1016/j.proeng.2013.12.002.

[79] Nebylov, A., Sharan, S., and Elangovan, G. *Intelligent Control Systems for Wing-in-Ground Effect Vehicles*. IFAC, 2009.

[80] Qin, Y., Qu, Q., Liu, P., Tian, Y., and Lu, Z. DDES Study of the Aerodynamic Forces and Flow Physics of a Delta Wing in Static Ground Effect. *Aerospace Science and Technology*. Volume 43, 423–436.

[81] Manshadi, M. D., Eilbeigi, M., Sobhani, M. K., Bazaz Zadeh, M., and Vaziry, M. A. “Experimental Study of Flow Field Distribution over a Generic Cranked Double Delta Wing.” *Chinese Journal of Aeronautics*, Vol. 29, No. 5, 2016, pp. 1196–1204. doi:10.1016/j.cja.2016.08.002.

[82] Qu, Q., Lu, Z., Guo, H., Liu, P., and Agarwal, R. K. “Numerical Investigation of the Aerodynamics of a Delta Wing in Ground Effect.” *Journal of Aircraft*, Vol. 52, No. 1, 2015, pp. 329–340. doi:10.2514/1.C032735.

[83] Lee, T., and Ko, L. S. “Ground Effect on the Vortex Flow and Aerodynamics of a Slender Delta Wing.” *Journal of Fluids Engineering*, Vol. 140, No. 7, 2018, pp. 1–9. doi:10.1115/1.4039232.

[84] Qin, Y., Liu, P., Qu, Q., and Guo, H. Numerical Study of Aerodynamic Forces and Flow Physics of a Delta Wing in Dynamic Ground Effect. *Aerospace Science and Technology*. Volume 51, 203–221.

[85] Ishide, T., and Itazawa, M. "Aerodynamic Improvement of a Delta Wing in Combination with Leading Edge Flaps." *Theoretical and Applied Mechanics Letters*, Vol. 7, No. 6, 2017, pp. 357–361. doi:10.1016/j.taml.2017.11.010.

[86] Kumar, A. A., Manoj, N., Onkar, A. K., and Manjuprasad, M. "Fluid-Structure Interaction Analysis of a Cropped Delta Wing." *Procedia Engineering*, Vol. 144, 2016, pp. 1205–1212. doi:10.1016/j.proeng.2016.05.102.

[87] Lee, T., and He, S. M. "The Trailing Vortices Generated by a Reverse Delta Wing with Different Wing Configurations." *Aerospace Science and Technology*, Vols. 82–83, No. xxxx, 2018, pp. 378–393. doi:10.1016/j.ast.2018.08.022.

[88] Musaj, M., and Prince, S. A. "Numerical and Experimental Investigation of the Aerodynamics of an Unconventional W-Leading Edge Reversed Delta Wing in Ground Effect." *ICAS Secretariat - 26th Congress of International Council of the Aeronautical Sciences 2008, ICAS 2008*, Vol. 6, 2008, pp. 665–674.

[89] Wu, J., and Zhao, N. "Ground Effect on Flapping Wing." *Procedia Engineering*, Vol. 67, 2013, pp. 295–302. doi:10.1016/j.proeng.2013.12.029.

[90] Mivehchi, A., Dahl, J., and Licht, S. "Heaving and Pitching Oscillating Foil Propulsion in Ground Effect." *Journal of Fluids and Structures*, Vol. 63, 2016, pp. 174–187. doi:10.1016/j.jfluidstructs.2016.03.007.

[91] Cheng, H., Ming, F. R., Sun, P. N., Wang, P. P., and Zhang, A. M. "Towards the Modeling of the Ditching of a Ground-Effect Wing Ship within the Framework of the SPH Method." *Applied Ocean Research*, Vol. 82, No. September 2018, 2019, pp. 370–384. doi:10.1016/j.apor.2018.09.014.

[92] Sun, C., and Dai, C. *Experimental Study on Ground Effect of a Wing with Tip Sails*. Elsevier B.V., 2015.

[93] Tavakoli Dakhrabadi, M., and Seif, M. S. "Influence of Main and Outer Wings on Aerodynamic Characteristics of Compound Wing-in-Ground Effect." *Aerospace Science and Technology*, Vol. 55, No. June, 2016, pp. 177–188. doi:10.1016/j.ast.2016.06.002.

[94] Zerihan, J., and Zhang, X. "Force Enhancement of Gurney Flaps on a Wing in Ground Effect." *Fluids 2000 Conference and Exhibit*, Vol. 39, No. 5, 2000. doi:10.2514/6.2000-2241.

[95] Zhang, X., Toet, W., and Zerihan, J. "Ground Effect Aerodynamics of Race Cars." *Applied Mechanics Reviews*, Vol. 59, Nos. 1–6, 2006, pp. 33–48. doi:10.1115/1.2110263.

[96] Irodov, R. D. *Criteria of the Longitudinal Stability of the Ekranoplan*. Ohio, 1974.

[97] Kornev, N., and Matveev, K. "Complex Numerical Modeling of Dynamics and Crashes of Wing-In-Ground Vehicles." *41st Aerospace Sciences Meeting and Exhibit*, No. January, 2003, pp. 1–9. doi:10.2514/6.2003-600.

[98] Hahn, T., Drewelow, W., Dewitz, D., Kolewe, B., and Lampe, B. *Analysis of Wing-in-Ground-Effect Vehicle with Regard to Safety Ensuring Control*. IFAC, 2014.

[99] Aminzadeh, A., and Khayatian, A. "Stability Analysis for Time-Varying WIG Craft Dynamics in the Presence of Wavy Boundary and Gust." *Ocean Engineering*, Vol. 145, No. August, 2017, pp. 148–157. doi:10.1016/j.oceaneng.2017.08.031.

[100] Barber, T. "Aerodynamic Ground Effect: A Case Study of the Integration of CFD and Experiments." *International Journal of Vehicle Design*, Vol. 40, No. 4, 2006, pp. 299–316. doi:10.1504/IJVD.2006.009068.

[101] Yoshioka, S., Kikuchi, S., Ohta, F., Kato, T., Song, J., and Kohama, Y. "Measurement of Ground Effect and Boundary-Layer Transition by Towing Wind Tunnel." *Fluid Dynamics Research*, Vol. 41, No. 2, 2009. doi:10.1088/0169-5983/41/2/021408.

[102] Lee, P.-H., Lan, C. E., and Muirhead, V. U. "Experimental Investigation of Dynamic Ground Effect." *Journal of Aircraft*, Vol. 26, No. 6, 1989, pp. 497–498. doi:10.2514/3.45793.

[103] Schweikhard, W. A Method for In-Flight Measurement of Ground Effect on Fixed-Wing Aircraft. *Journal of Aircraft*. 2. Volume 4, 101–104.

[104] Çetin, C. *Control Of Flow Structure On Low Swept Delta Wing Using Unsteady Leading Edge Blowing*. Middle East Technical University, 2016.

[105] Wheeler, A. J., and Ganji, A. R. *Introduction to Engineering Experimentation*. Pearson, New Jersey, 2010.

APPENDICES

A. Appendix A

Wing configurations and some geometric parameters are summarized in Table 3-1. In this table, Anh and Crp denote anhedraled and cropped configurations, respectively. The other parameters such as effective chord length (c_{eff}), effective wing span (b_{eff}), base wing area (A_{BW}), projected area (A), area ratio and aspect ratio (AR) are found using the following formulas.

$$c_{eff} = c \cdot (100 - Cr\%) / 100 \quad \text{A-1}$$

$$b_{eff} = 2 \cdot \frac{C}{\tan(\Lambda)} \cdot \cos(\delta) \quad \text{A-2}$$

$$A_{BW} = \frac{1}{2} \cdot c \cdot \frac{b_{eff}}{\cos(\delta)} \quad \text{A-3}$$

$$A = \frac{1}{2} \cdot C_{eff} \cdot b_{eff}\left(\frac{Cr\%}{100} + 1\right) \quad \text{A-4}$$

$$\text{Area Ratio} = \frac{A}{A_{BW}} \quad \text{A-5}$$

$$\text{Aspect Ratio, (AR)} = \frac{b_{eff}^2}{A} \quad \text{A-6}$$

Further, another parameter called “effective angle of attack” (α_{eff}) is also explained. Since the WIGE vehicles land and takeoff from ground surface, which can be either soil or water, the angle of attack, which is affected by the anhedral angle (δ_A) of the

wing, is important in terms of longitudinal stability of the aircraft during these flight phases. Combined effects of the pressure center, aerodynamic center in pitch, and center of gravity may result in degraded controllability character and excessive loads on the hull of the vehicle. Therefore, the effective angle of attack is formulized considering the anhedral angle and the sweep angle (Δ) of the wing. In addition, the height of the wing at zero angle of attack value is also given since anhedral wings cannot operate below this level due to the possibility of the wing tip contact with the ground.

In Figure A - 1 and Figure A - 2, isometric and front views of the anhedraled reverse delta wing are given. The angle of attack is defined as the angle between the chord line, which is shown by the letter “c”, and free-stream velocity. The sweep angle is the angle between the trailing-edge and leading-edge. The anhedral angle shown by “anh” is the droop angle of the wing from the chord line.

In Figure A - 3, side view of the anhedraled reverse delta wing at effective angle of attack value is given. The effective angle of attack is the angle between the chord line and free-stream velocity when the wing trailing-edges are parallel to the ground surface. Since the trailing-edges of the wing are in contact with the ground surface during landing and takeoff conditions, the angle of attack value is equal to the effective angle of attack value of the wing.

In Figure A - 4, side view of the anhedraled reverse delta wing at zero angle of attack value is provided. At zero angle attack value, the anhedraled reverse delta wing height, which is shown by the letter “h”, is the minimum heigh (h_{min}) at which the wing can operate IGE. Therefore, it is the minimum height at which WIG vehicles can cruise above the ground surface without contacting the physical boundary of the ground.

The following relations are used for the calculation of the effective angle of attack (α_{eff}) and minimum height (h_{min}) at zero angle of attack value (α_0).

$$\tan(\alpha_{eff}) = \frac{\sin(\delta)}{\tan(\Delta)} \qquad \text{A-7}$$

$$h_{min} = c \cdot \frac{\sin(\delta)}{\tan(\Delta)} = c \cdot \tan(\alpha_{eff}) \qquad \text{A-8}$$

Isometric View

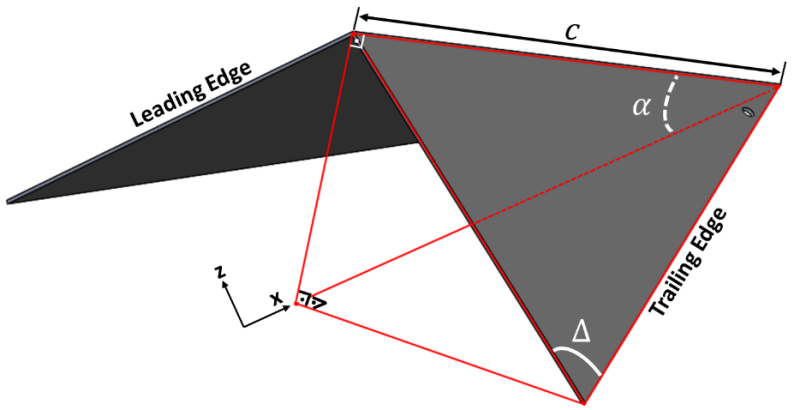

Figure A - 1 Isometric view of the anhedraled reverse delta wing

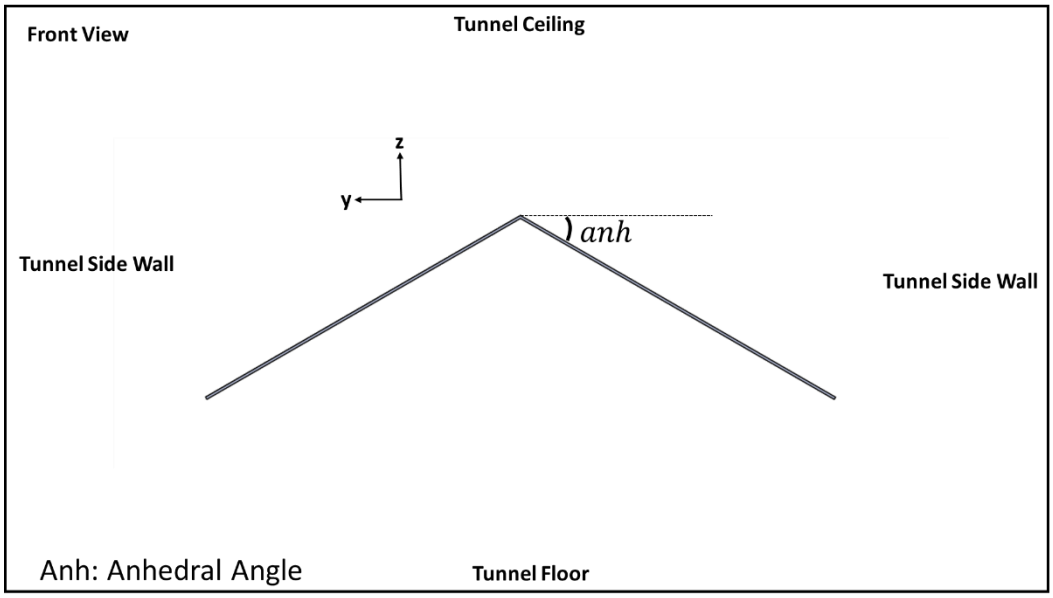

Figure A - 2 The front view of the anhedraled reverse delta wing

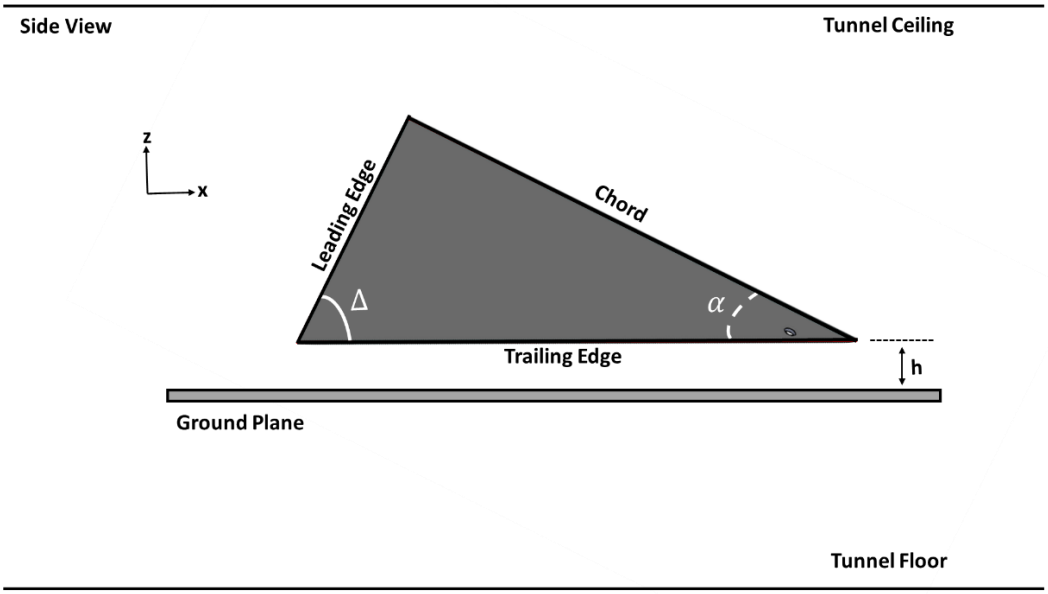

Figure A - 3 Side view of the anhedraled reverse delta wing at effective angle of attack value

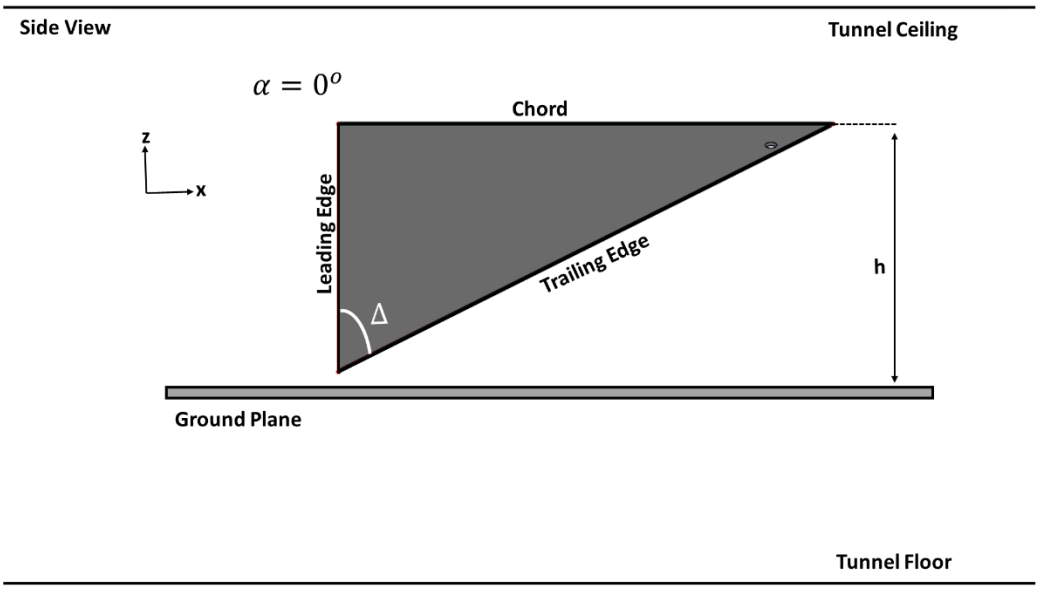

Figure A - 4 Side view of the anhedraled reverse delta wing at zero angle of attack value

B. Appendix B

The wings, which were examined in parametric study are given below. The sweep angle (45^o) and thickness (1 mm) of these wings are the same. “Anh” and “cr” denotes anhedral angle and cropping percentage, respectively.

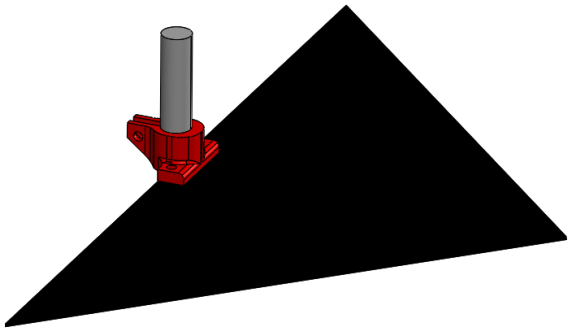

Figure B - 1 The delta wing 1b, ($\Lambda = 45^o, \mathrm{t/c} = 1.1\%, \delta = 0^o, \mathrm{Cr} = 0\%$)

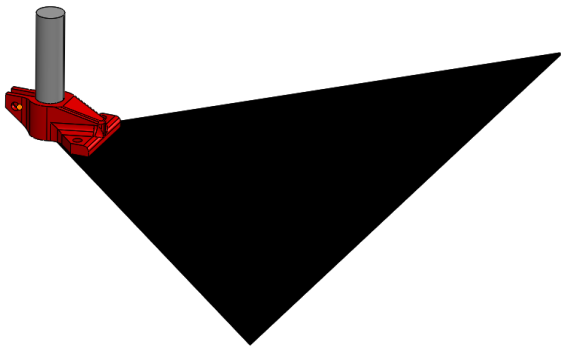

Figure B - 2 The reverse delta wing 2b, ($\Lambda = 45^o, \mathrm{t/c} = 1.1\%, \delta = 0^o, \mathrm{Cr} = 0\%$)

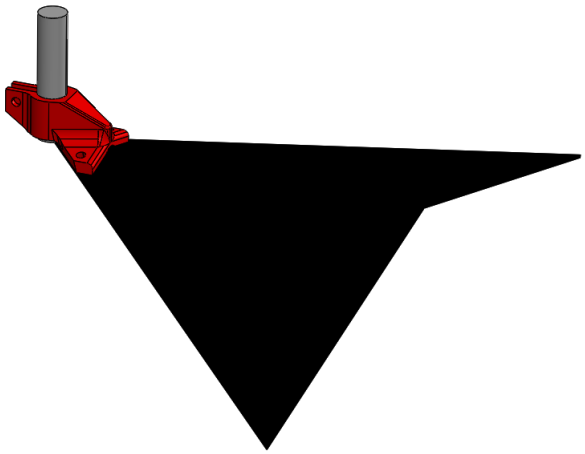

Figure B - 3 The reverse delta wing 2c, ($\Lambda = 45^o, \mathrm{t/c} = 1.1\%, \delta = 15^o, \mathrm{Cr} = 0\%$)

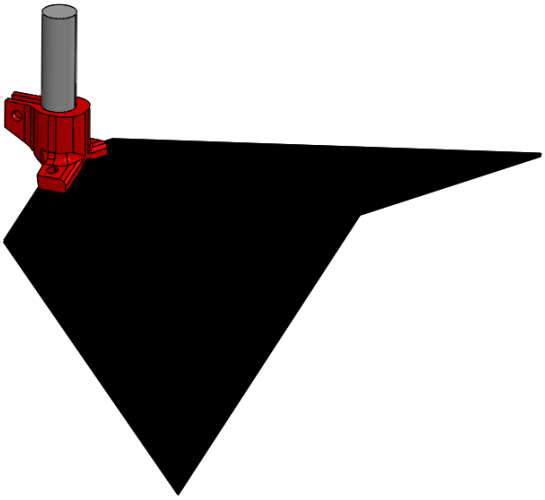

Figure B - 4 The reverse delta wing 2e, ($\Lambda = 45^o, \mathrm{t/c} = 1.1\%, \delta = 15^o, \mathrm{Cr} = 30\%$)

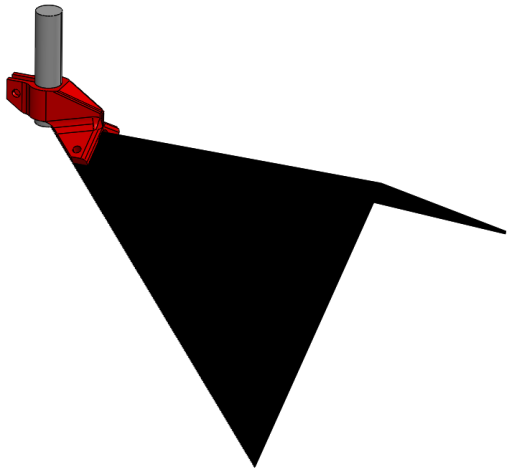

Figure B - 5 The reverse delta wing 2d, ($\Lambda = 45^o, \mathrm{t/c} = 1.1\%, \delta = 30^o, \mathrm{Cr} = 0\%$)

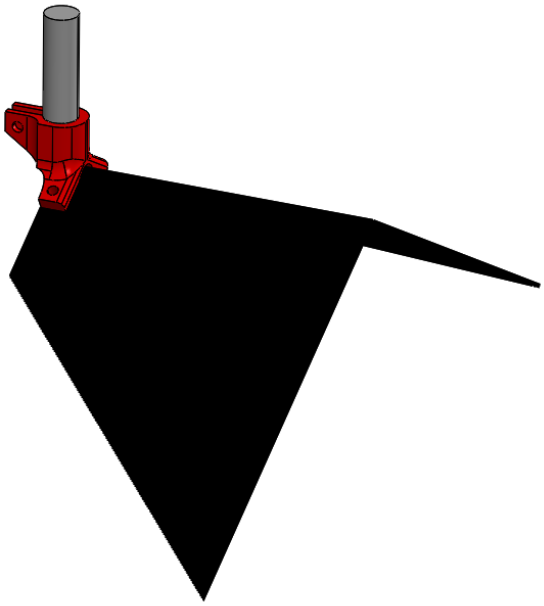

Figure B - 6 The reverse delta wing 2f, ($\Lambda = 45^o, \mathrm{t/c} = 1.1\%, \delta = 30^o, \mathrm{Cr} = 30\%$)

The Wing-Strut Connection Brackets for the Thin Wings

The mounting of the wings to the MPS strut poses difficulties, particularly for the thin wings, which incorporate anhedral angle and cropping since these thin wings do not have any surface at the trailing-edge for fastener penetration due to the thickness of the wings. This problem is solved by designing the wing specific brackets. These brackets were manufactured with Polylactic Acid, commonly known as (PLA) using a commercial 3D printer. The side view of the six different brackets with their associated wings and the strut is given in Figure B - 7. In this figure, the red dashed lines show the strut center line. These brackets are designed such that the rotation axis of the MPS (shown in the red dashed line in Figure 3-16) and trailing-edge of the wing are coincident. Therefore, the models rotate about the trailing-edge when the angle of attack is changed since it is crucial for the height accuracy of the ground effect tests, which permits any change in model height during the angle of attack change. This is achieved by placing the strut center line shown by red dashed lines in Figure B - 7 and with the trailing-edge of the wing.

The schematic representation of the wing and strut connection is further discussed in Figure B - 8 over the reverse delta wing (5) with 30 degrees anhedral since it shows all the details, which have been addressed during the design of the brackets. The bracket is connected to the MPS strut (1) through a hole. A fastener penetrating to a blind hole (3) and a nut are used to fit the strut to the bracket tightly. The angle between the legs of the brackets is equal to the anhedral angle of the associated wing. At the edge of these legs, there are two holes (4) where two fasteners are used to mount the bracket to the wing. The main body, to which bracket legs are connected, is designed according to the anhedral angle, and cropping percentage of the associated wing. The size of this frame is minimized since it occupies a certain space close to the trailing-edge of the wing and may distort the flow field to some extent. The distortion level is not constant but higher at low angle of attack and maximum at the negative angle of attack values. In addition, a chamfer is applied at the bottom

surface of the bracket close to the blind hole (3) to minimize the flow distortion at high angle of attack values since the bracket may block the flow between the wing and the ground surface, which can be either static or dynamic. The chamfer of the delta wing bracket can be seen in Figure B - 9 during a ground effect test of the delta wing 1b at angle of attack value of 24^o and h/c = 11%. In Figure B - 10, 3D printed brackets for thin delta wings are given.

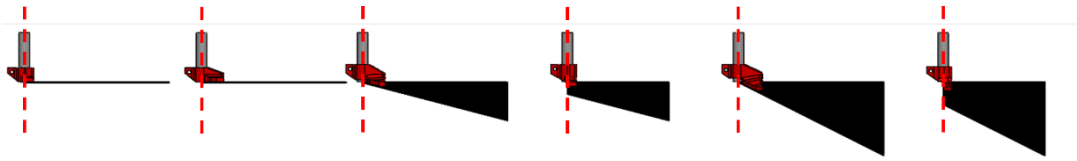

Figure B - 7 The wings, struts and model brackets. The wings from left to right are delta, reversed delta, reverse delta with 15-degree anhedral, reverse delta with 15-degree anhedral and 30% cropping, reverse delta with 30-degree anhedral, and reverse delta with 30-degree anhedral and 30% cropping

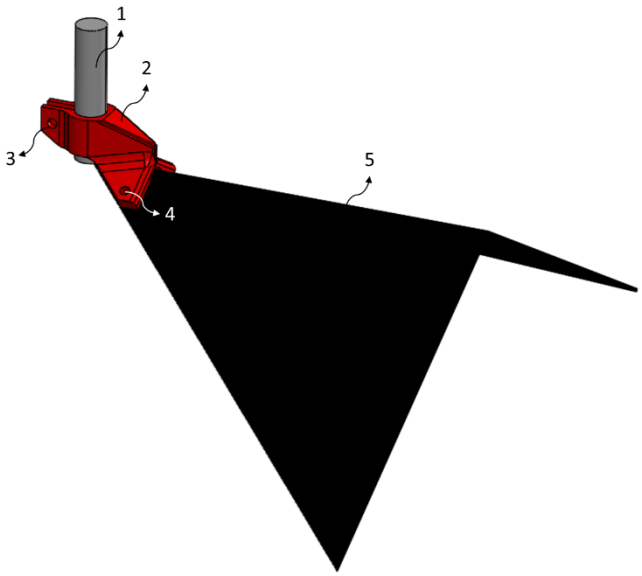

Figure B - 8 Schematic representation of the wing-strut connection, 1) the MPS strut, 2) bracket, 3) lock fastener hole, 4) wing-bracket connection fastener hole, 5) reverse delta wing with 30 degrees anhedral

Figure B - 9 The side view of the ground effect test of the delta wing 1b

Figure B - 10 Top and perspective views of the 3D printed brackets for thin wings

Details of the Ground Elevation System

The stand-alone picture of the ground elevation system is also given in Figure B - 11. In addition, the subcomponents of the elevated ground test rig are further explained in this figure. The ground plane (1) angle alignment in pitch and roll channels is conducted by adjusting the lengths of the threaded aluminum rods (3), which are connected to the ground plane with spherical joints (2). These rods are mounted to the dynamic chassis (5), which can move up and down on the 1D transvers shaft (6). The system is fixed to a stationary chassis (4), which consists of aluminum sigma profiles. The operator adjusts the height of the ground plane by rotating the traverse wheel in clockwise and counterclockwise directions. All components below the red dashed line in Figure B - 11 are located outside the wind tunnel. Therefore, their impact on the flow field is eliminated. As the ground plane approaches to the wing model, which simulates the ground effect intensity increase, the distortion due to height struts (3) on the wind tunnel flow field increases. However, this distortion occurs beneath the stationary ground plane. In this way, it is aimed that the minimal interference on the overall flow field due to these struts occurs since the oncoming flow between the wing and ground plane remains the same as the ground plane approaches to the wing and the distorted flow is channeled to the bottom of the ground plane with the help of the beveled leading-edge of the ground plane.

In Figure B - 12, the integrated ground elevation system of the wind tunnel is also shown with the MPS (1). In this figure, other subcomponents such as stationary ground plane (2), leading-edge bevel (3), 1D traverse shaft (4), and dynamic chassis (5) are shown. The red dashed area shows the effective stationary ground plane inside the wind tunnel.

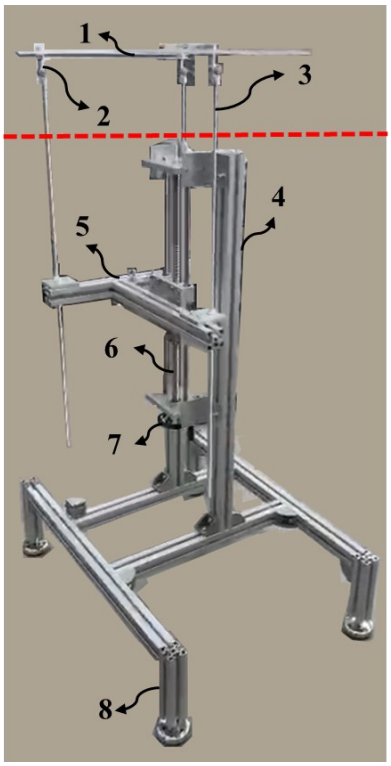

Figure B - 11 The elevated ground test rig components, 1) plexiglass ground plane, 2) spherical joints, 3) height struts with threaded aluminum rods, 4) stationary chassis located outside of the wind tunnel, 5) dynamic chassis for height adjustment, 6) 1D traverse shaft, 7) volant wheel, 8) ground legs, red dashed line indicates the wind tunnel bottom floor

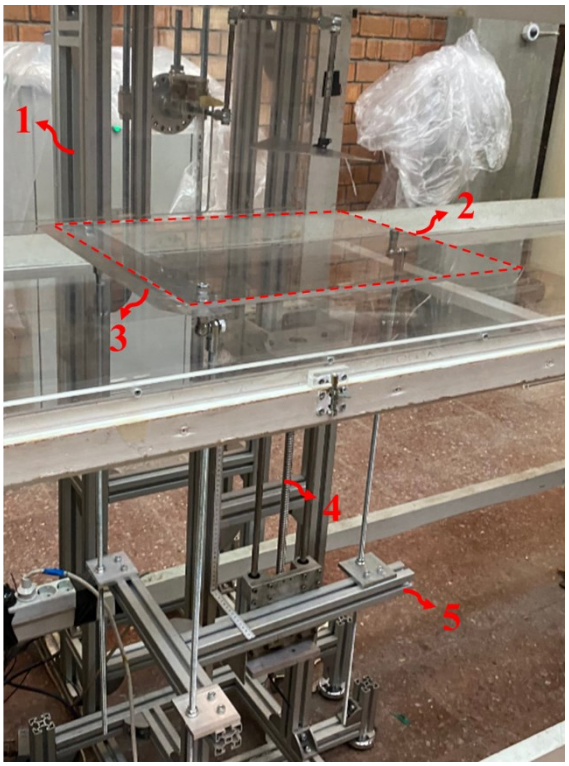

Figure B - 12 The elevated ground test rig integrated to the wind tunnel, the red dashed area indicates the effective stationary ground plane, 1) The model positioning system (MPS), 2) stationary ground plane, 3) leading-edge bevel of the stationary ground plane, 4) 1D traverse shaft, 5) dynamic chassis

The Wing and Strut Components

In Figure B - 13, the wing and strut components are shown inside the dashed lines. In this figure, any component inside the red dashed line produces both inertial and aerodynamic loads whereas components inside the green dashed lines produce only inertial load since these components are positioned outside the wind tunnel.

The model, which is shown inside the red dashed lines in the first picture in Figure B - 13, represents the wing, a bracket, 2 fasteners and 2 nuts. The strut represents the components such as model mount rod, fasteners, and tooling adaptor, which is connected to the sensor. They are shown in the second picture in Figure B - 13 inside the red and green dashed lines. The combination of model components and strut components are named as “wing-strut”, which represent all components in the red and dashed lines shown in first and second pictures in Figure B - 13.

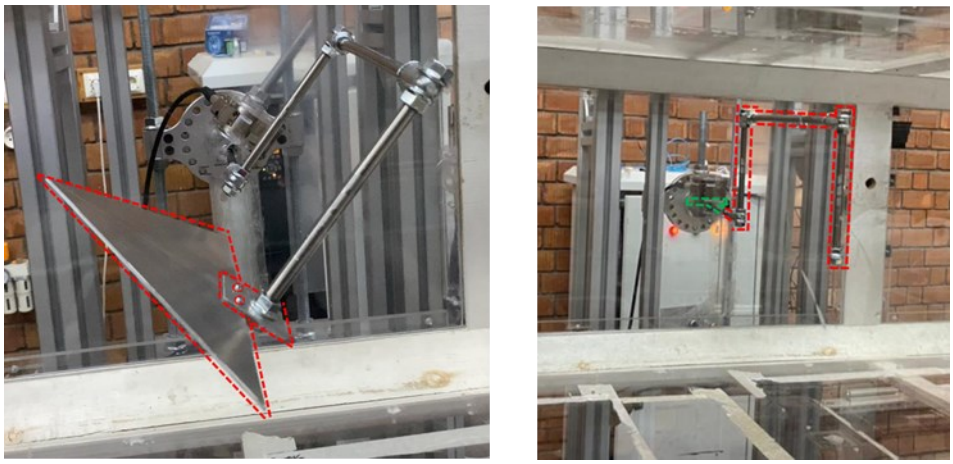

Figure B - 13 Wing and strut components

C. Appendix C

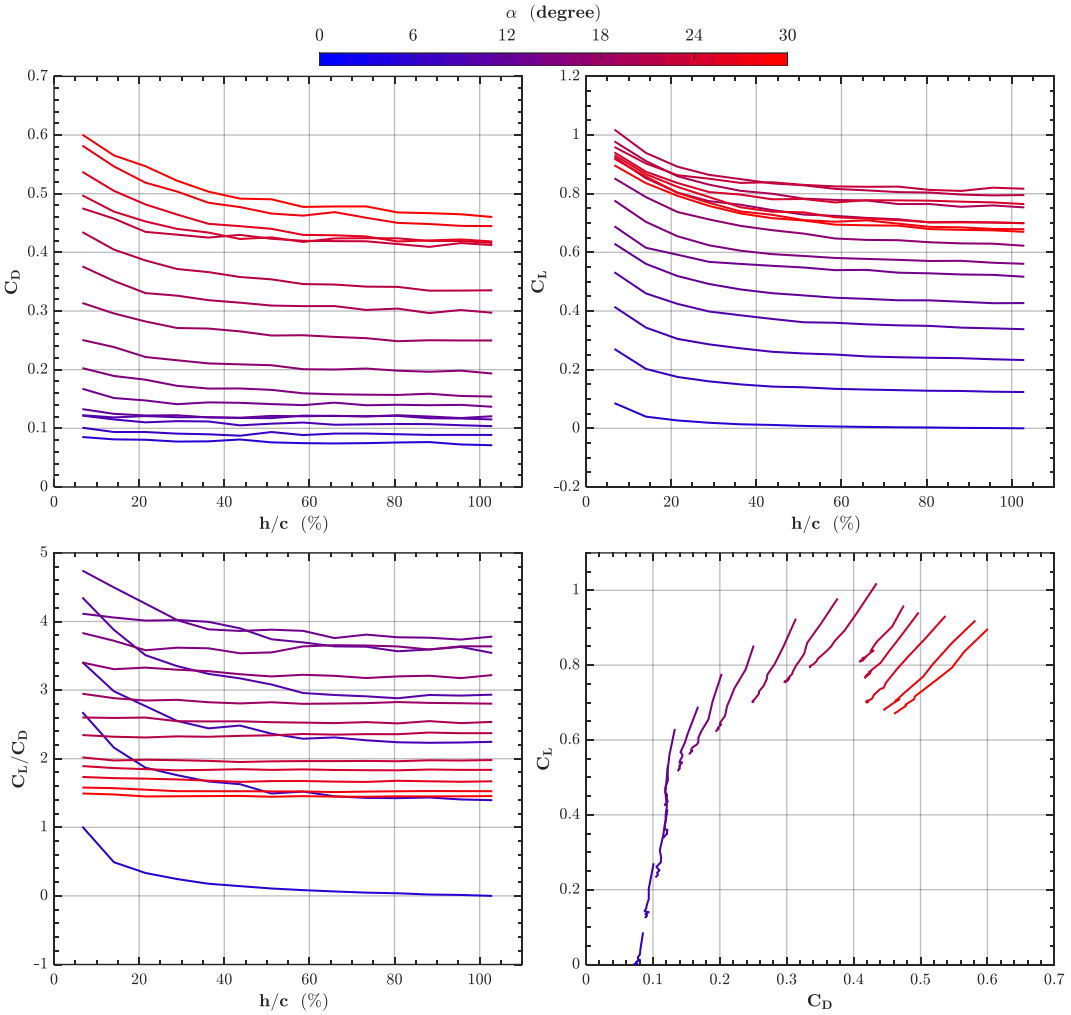

Figure C - 1 Variation of Drag coefficient C_D, Lift-to-Drag ratio C_L/C_D, Lift coefficient C_L as a function of non-dimensional height values and Drag Polar for the delta wing 1a

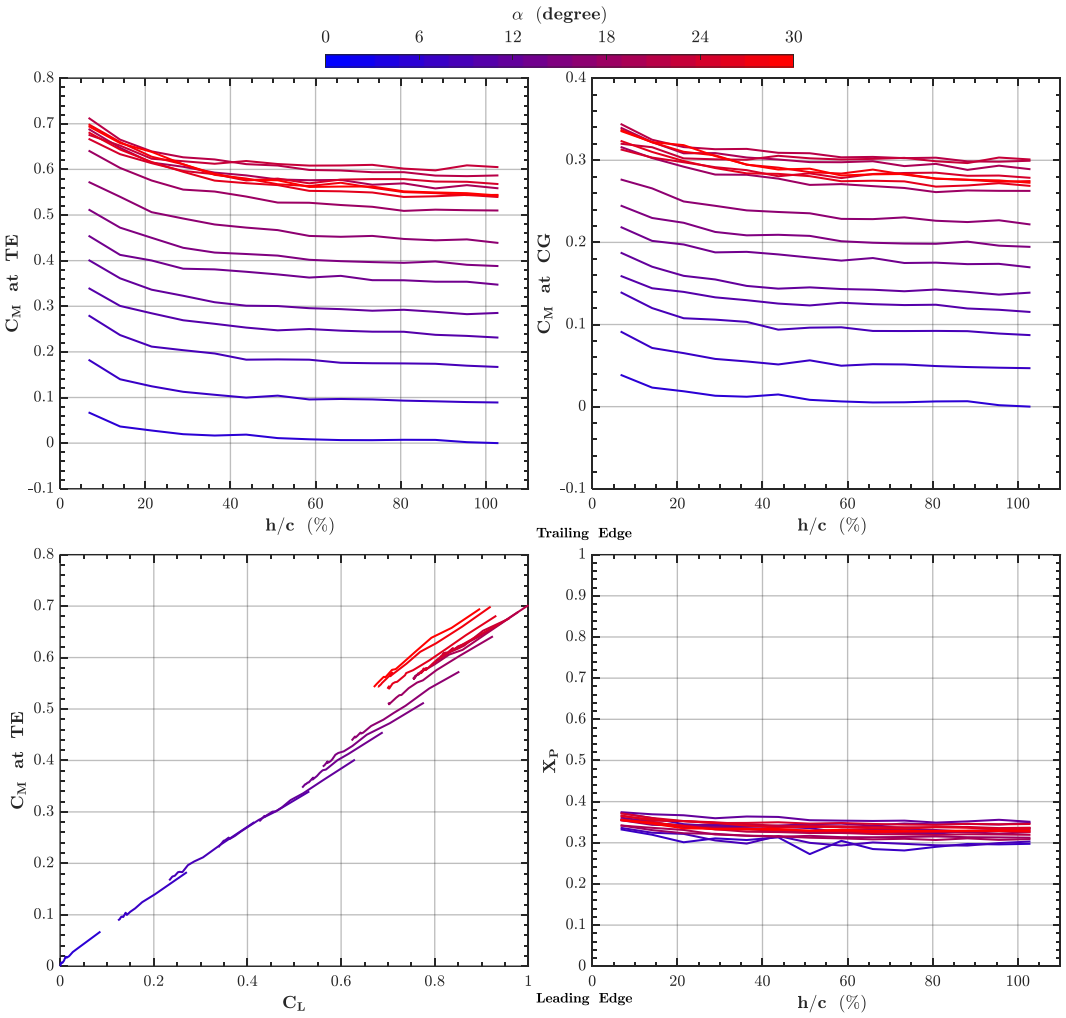

Figure C - 2 Variation of Moment coefficient C_M at trailing-edge (TE) and center of gravity (CG) as a function of function of non-dimensional height values and Lift coefficient C_L, and Non-Dimensional Pressure Center coordinate X_P as a function of non-dimensional height values for the delta wing 1a

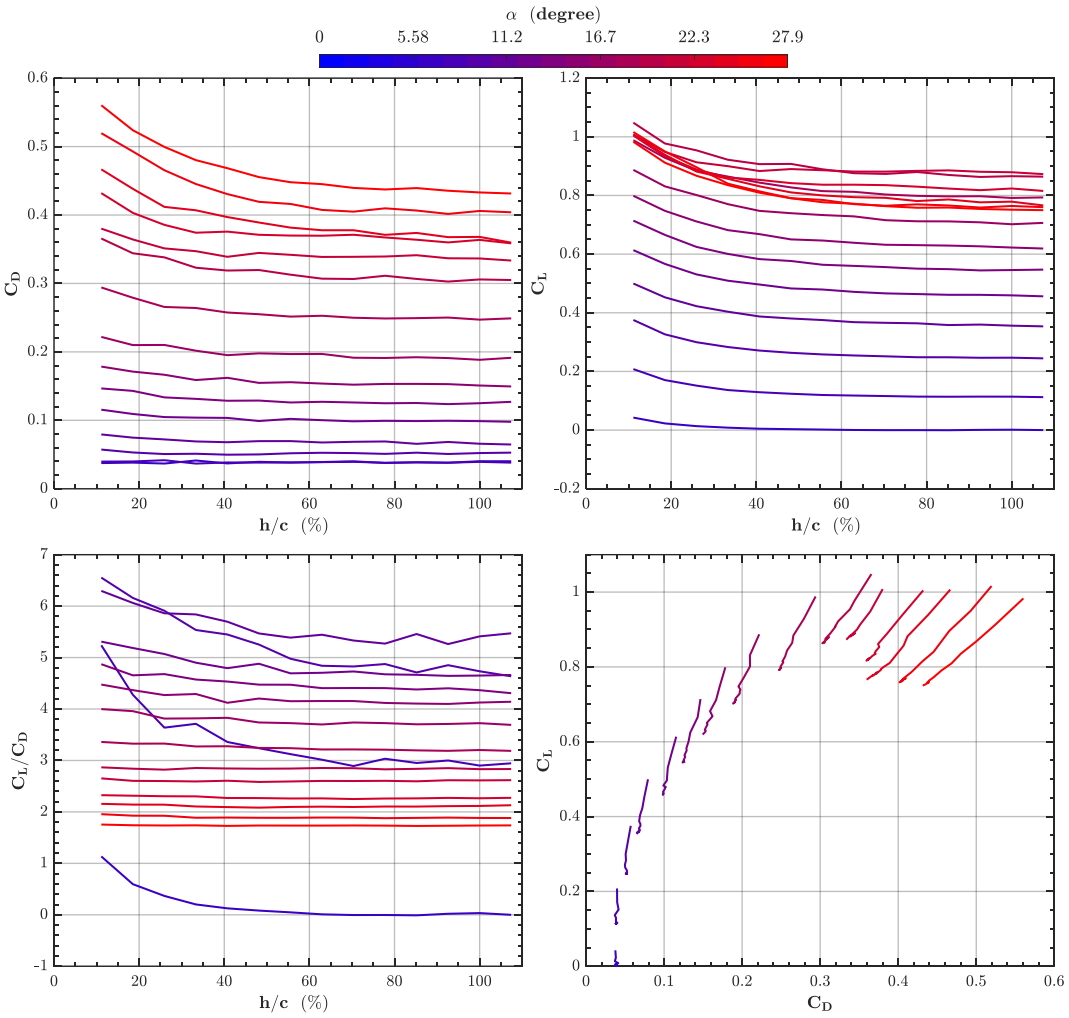

Figure C - 3 Variation of Drag coefficient C_D, Lift-to-Drag ratio C_L/C_D, Lift coefficient C_L as a function of non-dimensional height values and Drag Polar for the delta wing 1b

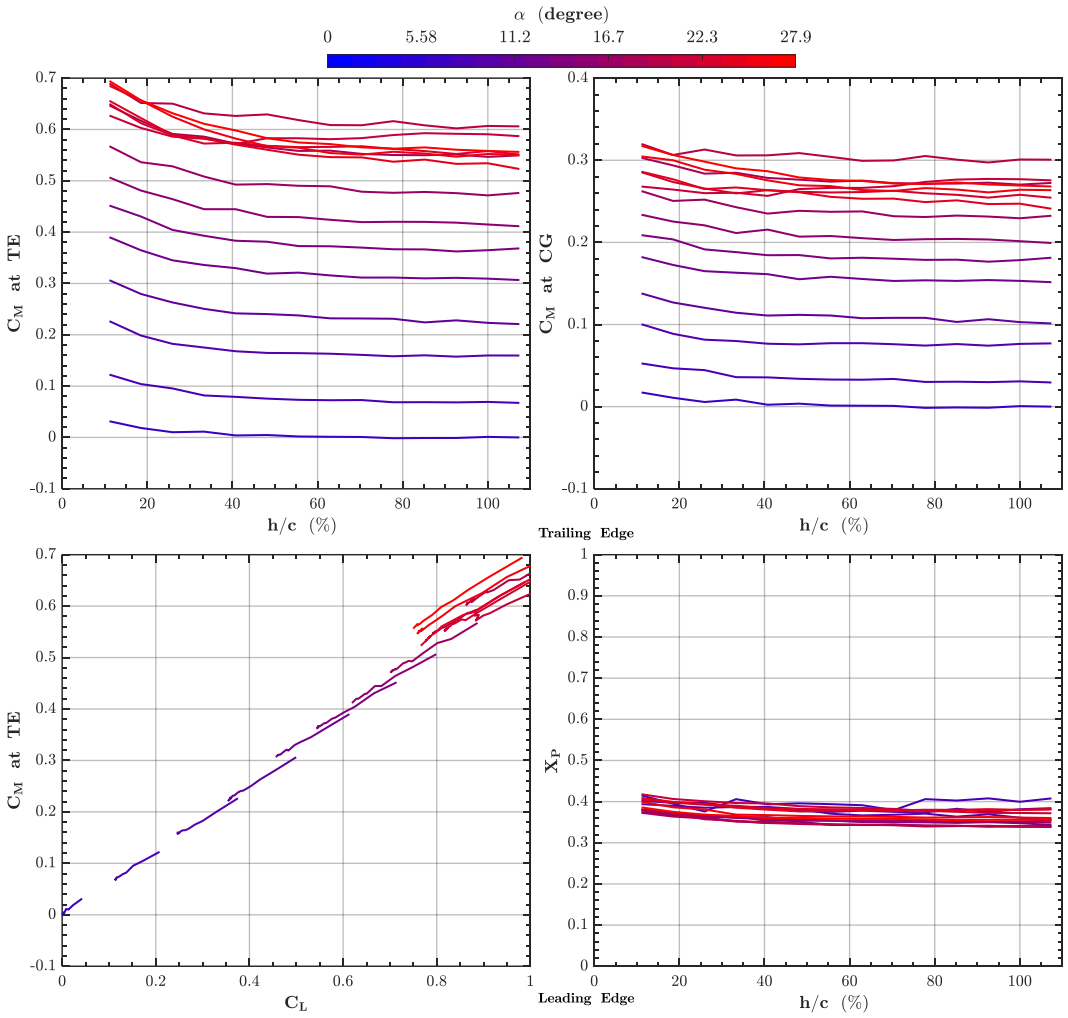

Figure C - 4 Variation of Moment coefficient C_M at trailing-edge (TE) and center of gravity (CG) as a function of function of non-dimensional height values and Lift coefficient C_L, and Non-Dimensional Pressure Center coordinate X_P as a function of non-dimensional height values for the delta wing 1b

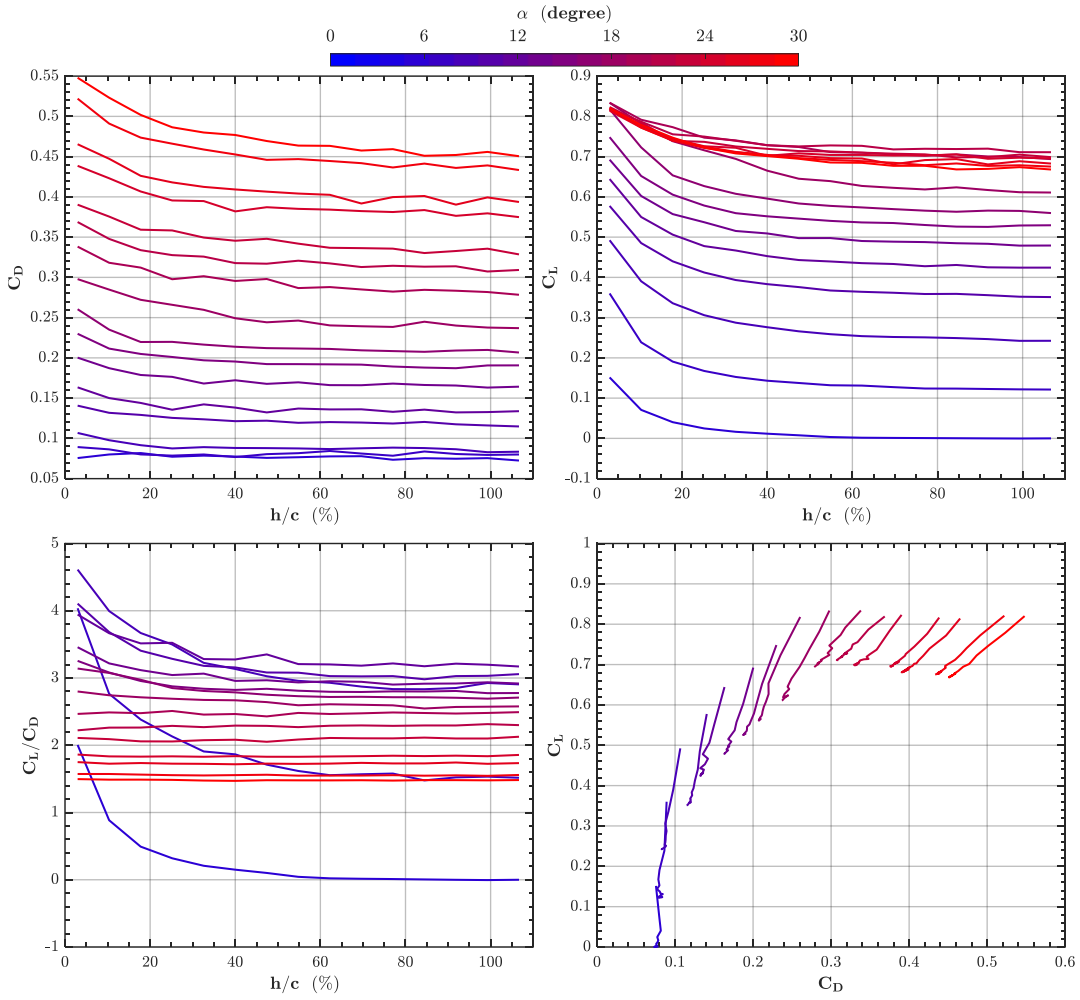

Figure C - 5 Variation of Drag coefficient C_D, Lift-to-Drag ratio C_L/C_D, Lift coefficient C_L as a function of non-dimensional height values and Drag Polar for the reverse delta wing 2a

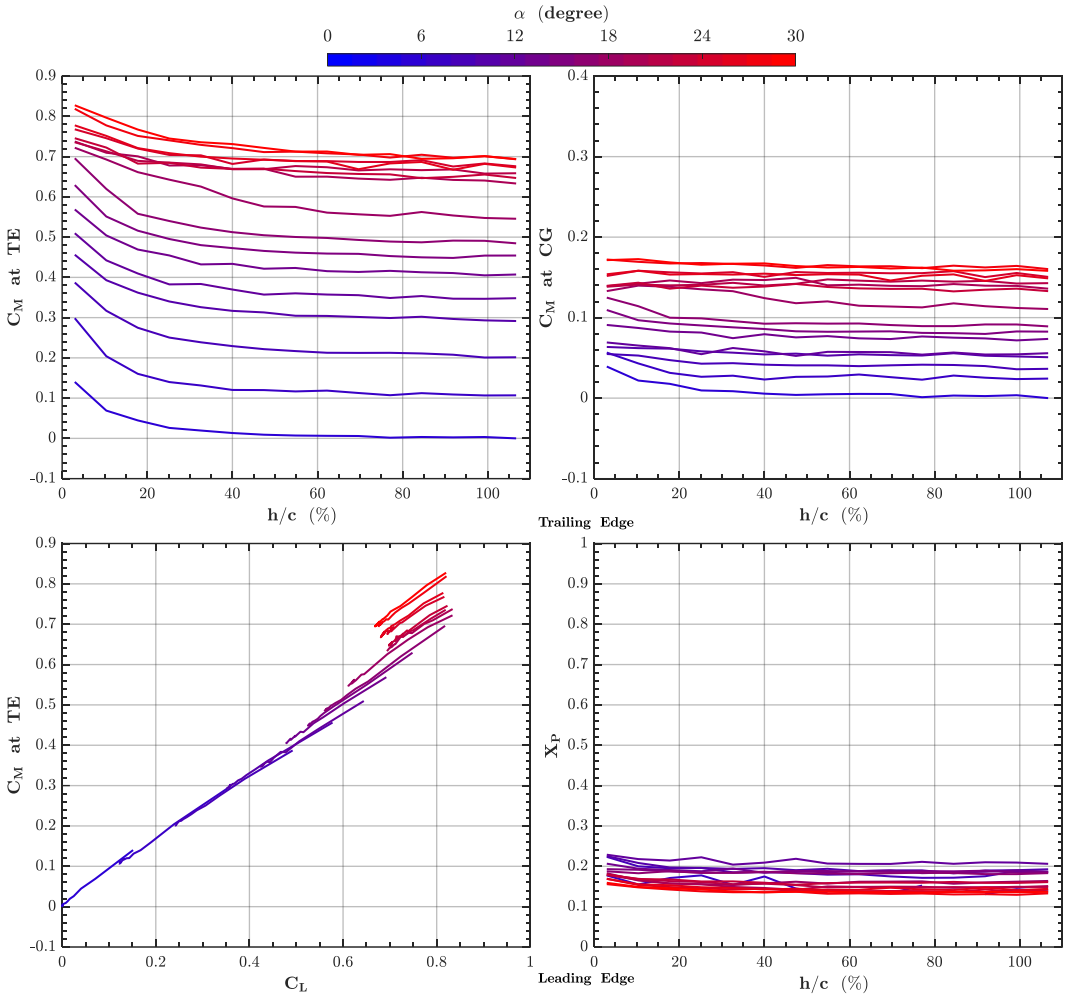

Figure C - 6 Variation of Moment coefficient C_M at trailing-edge (TE) and center of gravity (CG) as a function of function of non-dimensional height values and Lift coefficient C_L, and Non-Dimensional Pressure Center coordinate X_P as a function of non-dimensional height values for the reverse delta wing 2a

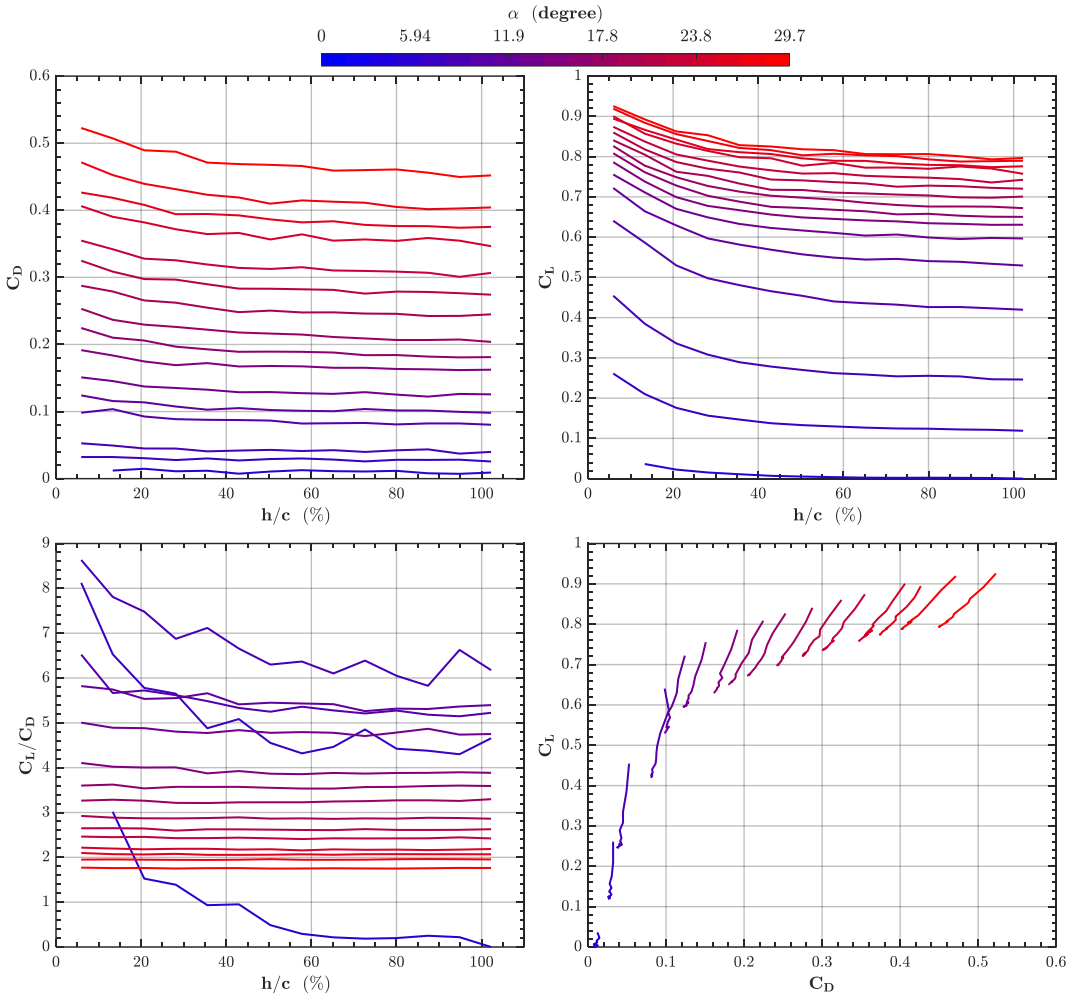

Figure C - 7 Variation of Drag coefficient C_D, Lift-to-Drag ratio C_L/C_D, Lift coefficient C_L as a function of non-dimensional height values and Drag Polar for the reverse delta wing 2b

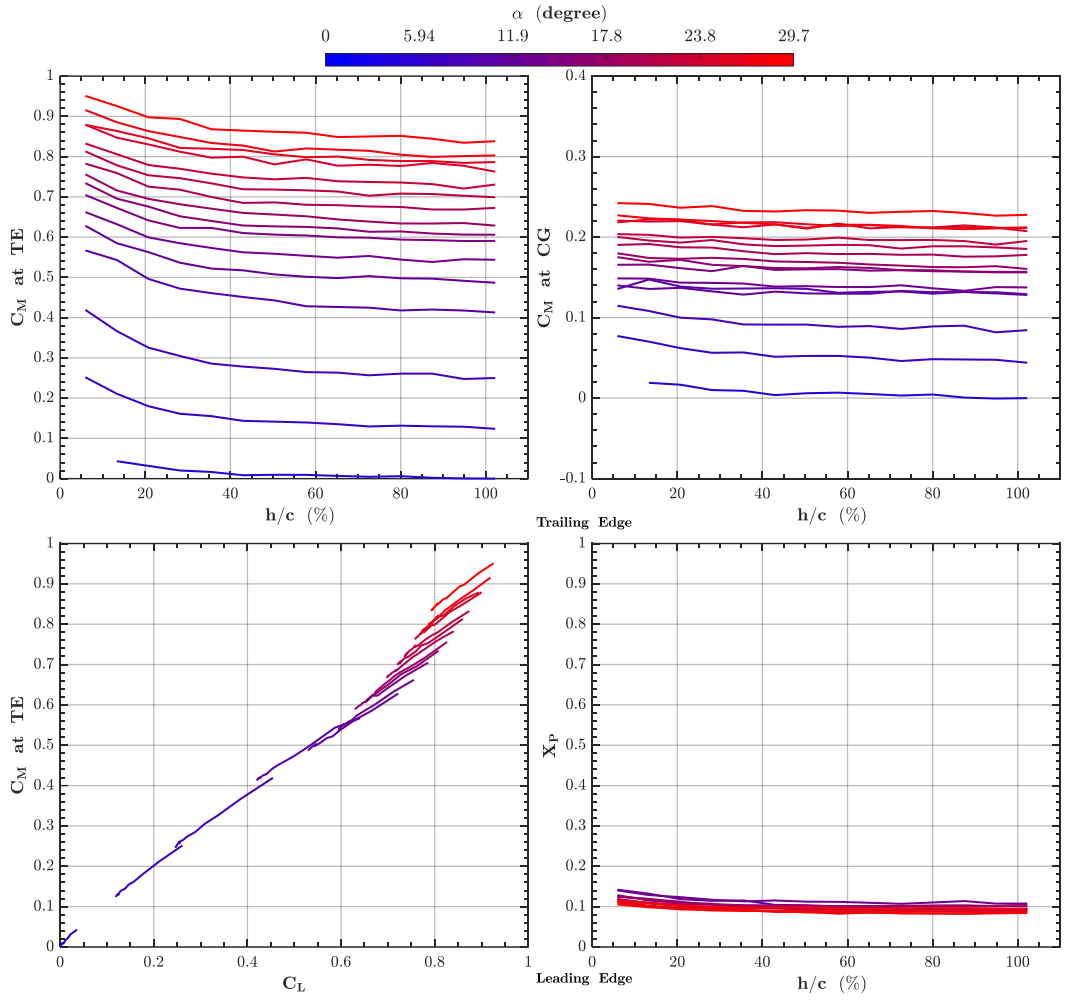

Figure C - 8 Variation of Moment coefficient C_M at trailing-edge (TE) and center of gravity (CG) as a function of function of non-dimensional height values and Lift coefficient C_L, and Non-Dimensional Pressure Center coordinate X_P as a function of non-dimensional height values for the reverse delta wing 2b

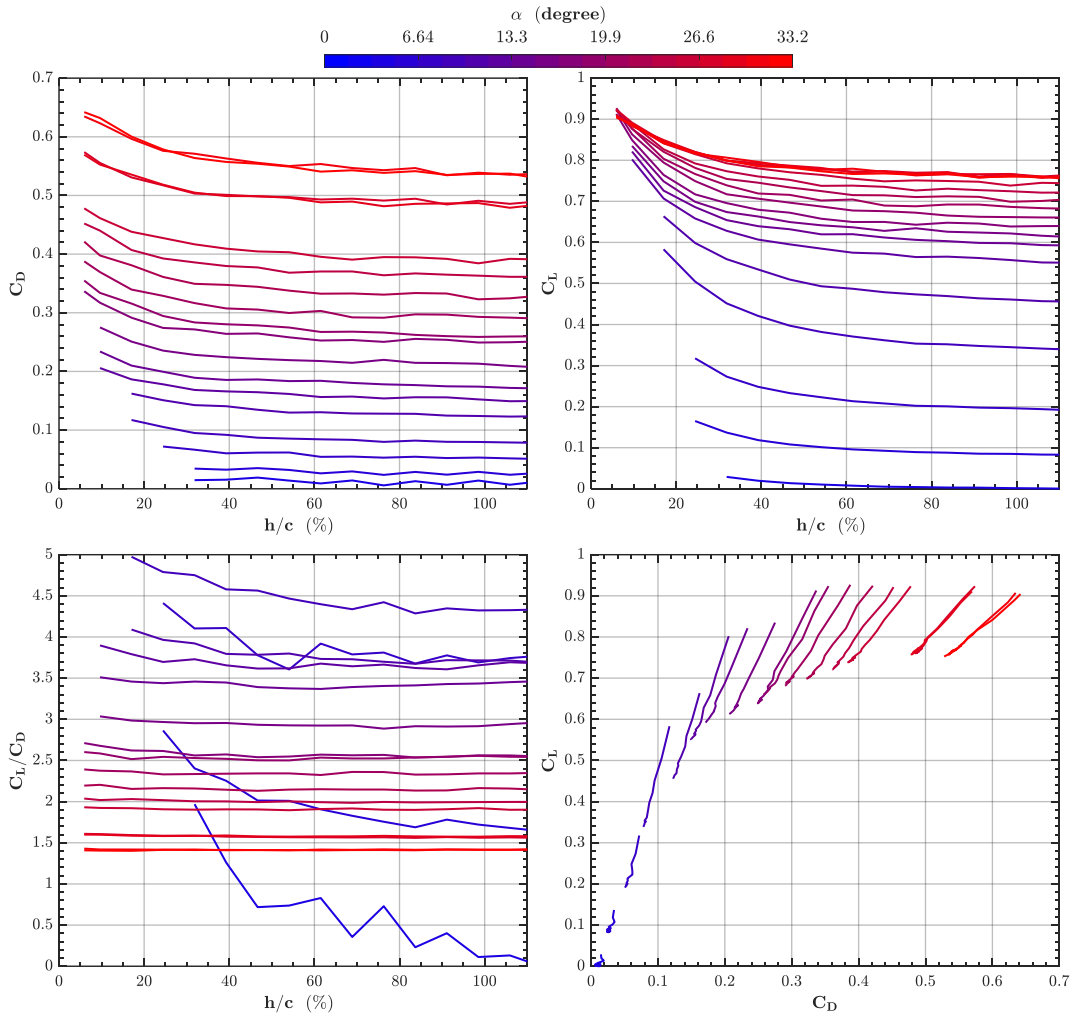

Figure C - 9 Variation of Drag coefficient C_D, Lift-to-Drag ratio C_L/C_D, Lift coefficient C_L as a function of non-dimensional height values and Drag Polar for the reverse delta wing 2c

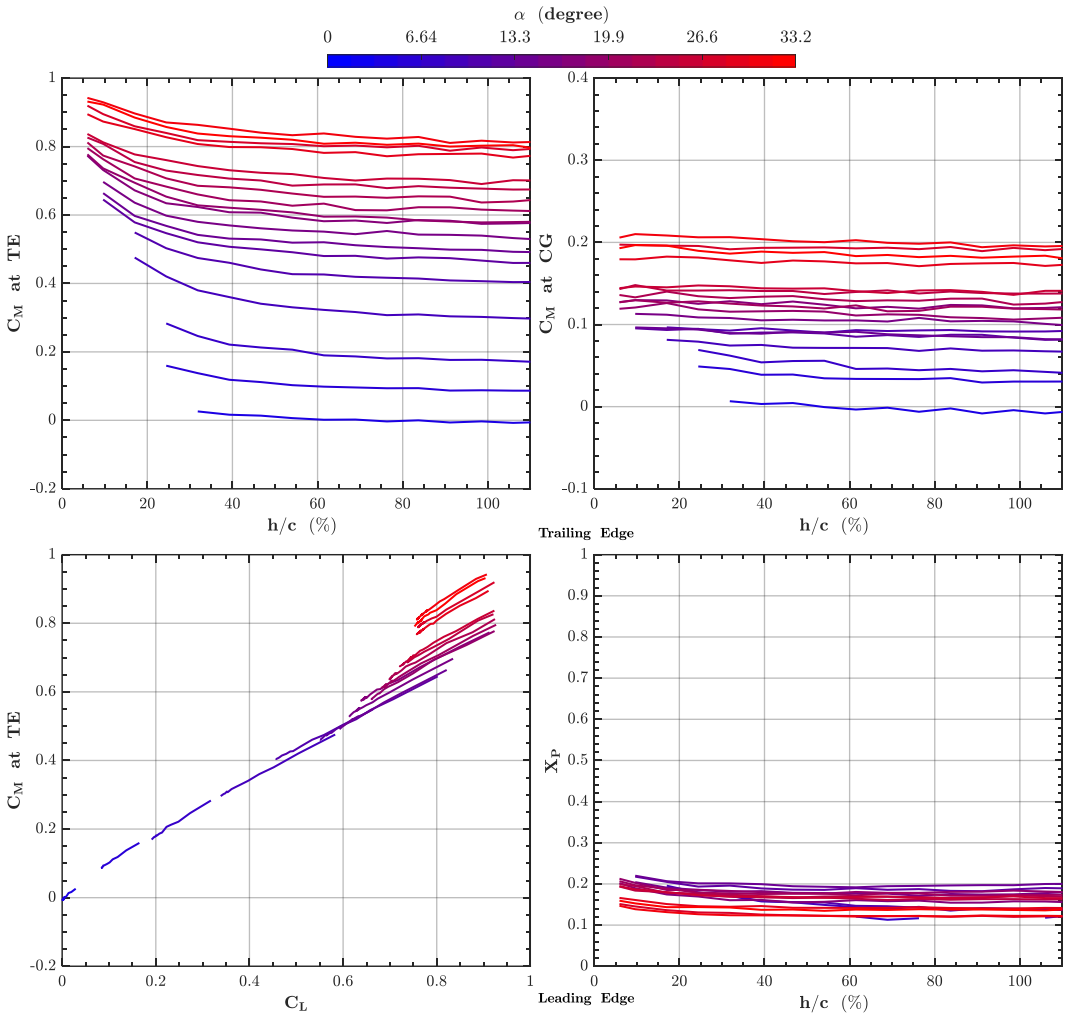

Figure C - 10 Variation of Moment coefficient C_M at trailing-edge (TE) and center of gravity (CG) as a function of function of non-dimensional height values and Lift coefficient C_L, and Non-Dimensional Pressure Center coordinate X_P as a function of non-dimensional height values for the reverse delta wing 2c

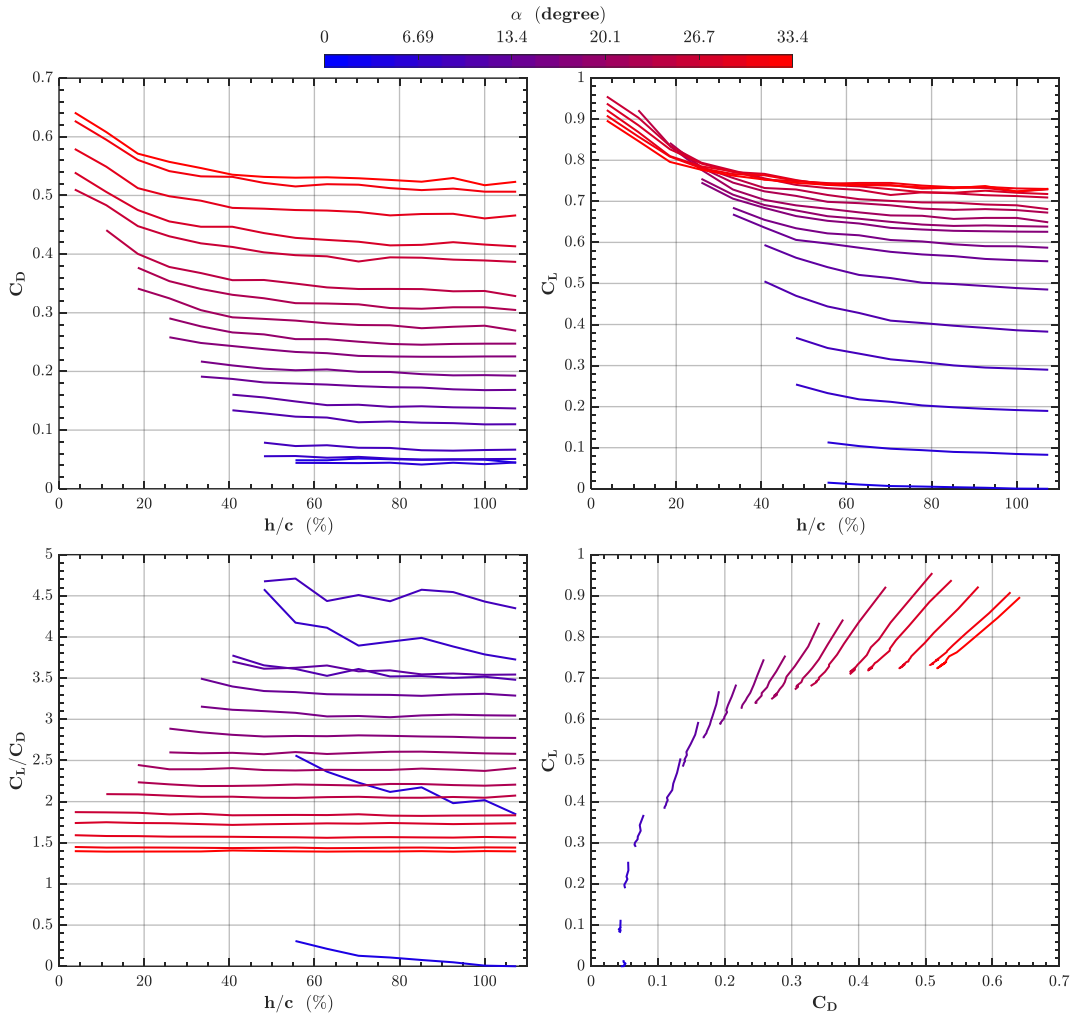

Figure C - 11 Variation of Drag coefficient C_D, Lift-to-Drag ratio C_L/C_D, Lift coefficient C_L as a function of non-dimensional height values and Drag Polar for the reverse delta wing 2d

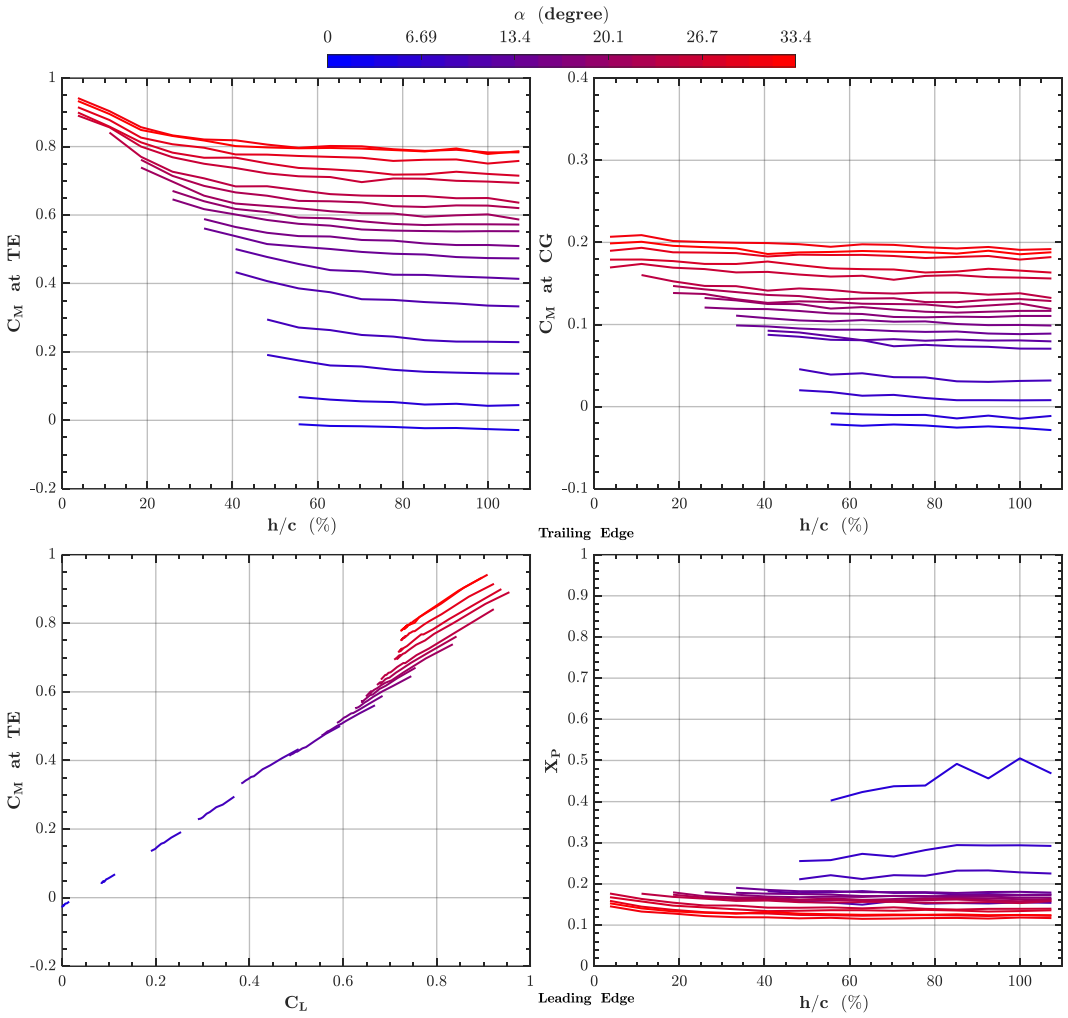

Figure C - 12 Variation of Moment coefficient C_M at trailing-edge (TE) and center of gravity (CG) as a function of function of non-dimensional height values and Lift coefficient C_L, and Non-Dimensional Pressure Center coordinate X_P as a function of non-dimensional height values for the reverse delta wing 2d

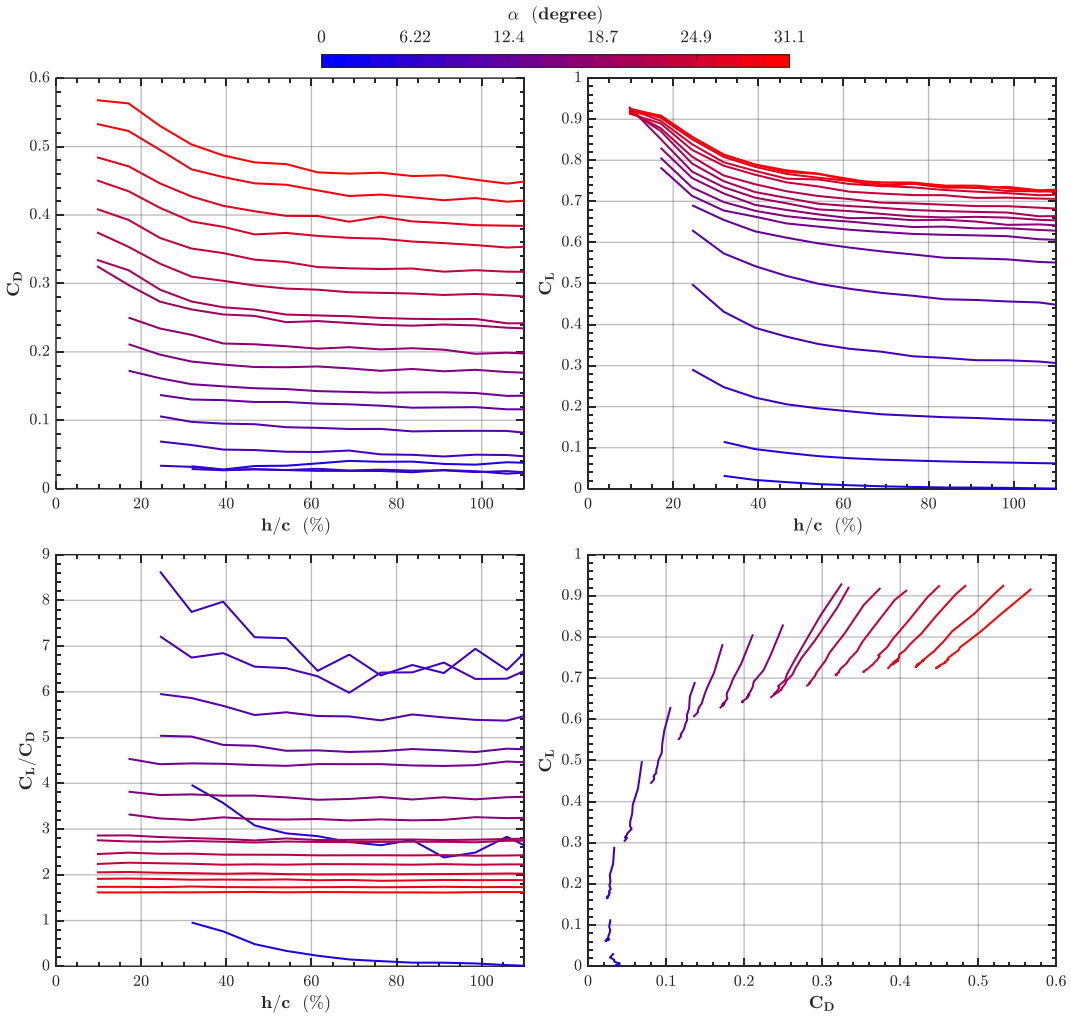

Figure C - 13 Variation of Drag coefficient C_D, Lift-to-Drag ratio C_L/C_D, Lift coefficient C_L as a function of non-dimensional height values and Drag Polar for the reverse delta wing 2e

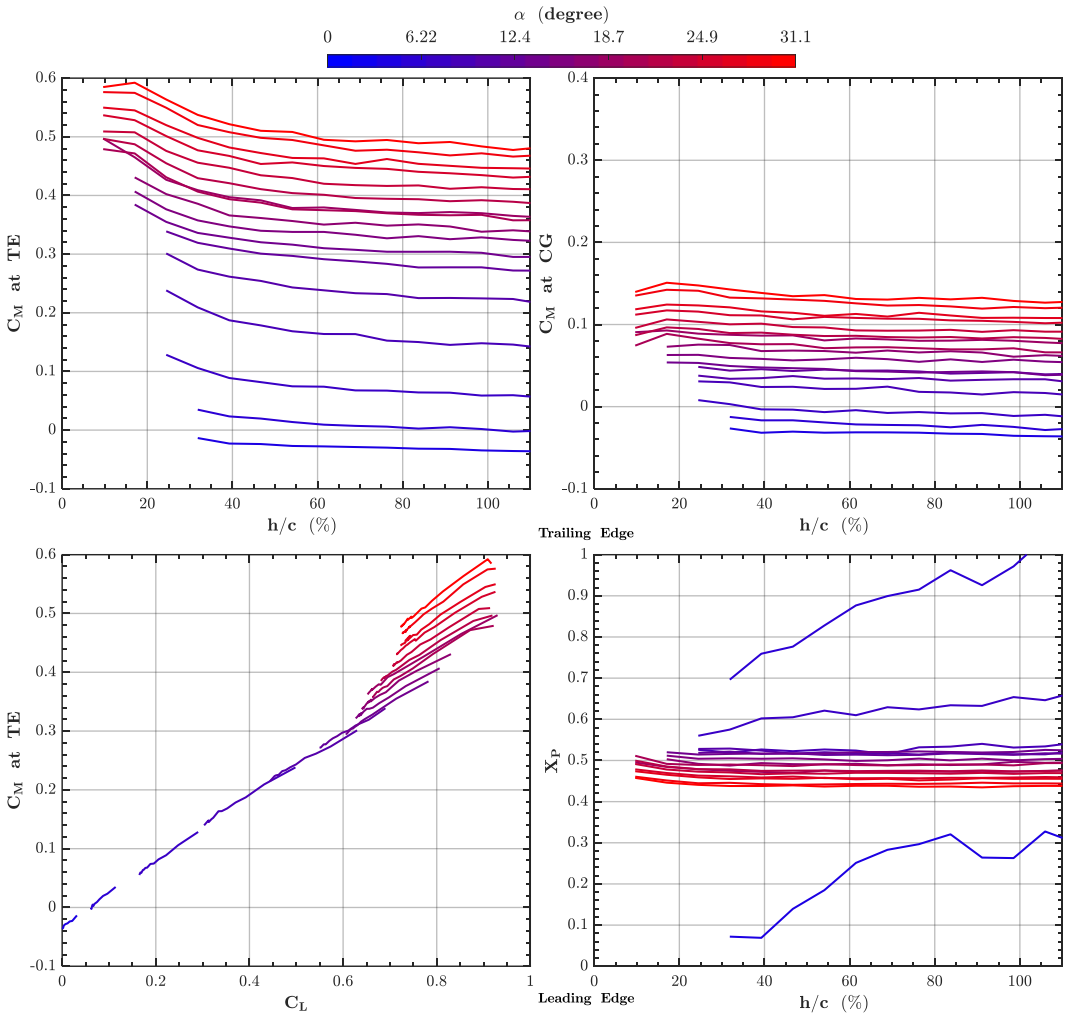

Figure C - 14 Variation of Moment coefficient C_M at trailing-edge (TE) and center of gravity (CG) as a function of function of non-dimensional height values and Lift coefficient C_L, and Non-Dimensional Pressure Center coordinate X_P as a function of non-dimensional height values for the reverse delta wing 2e

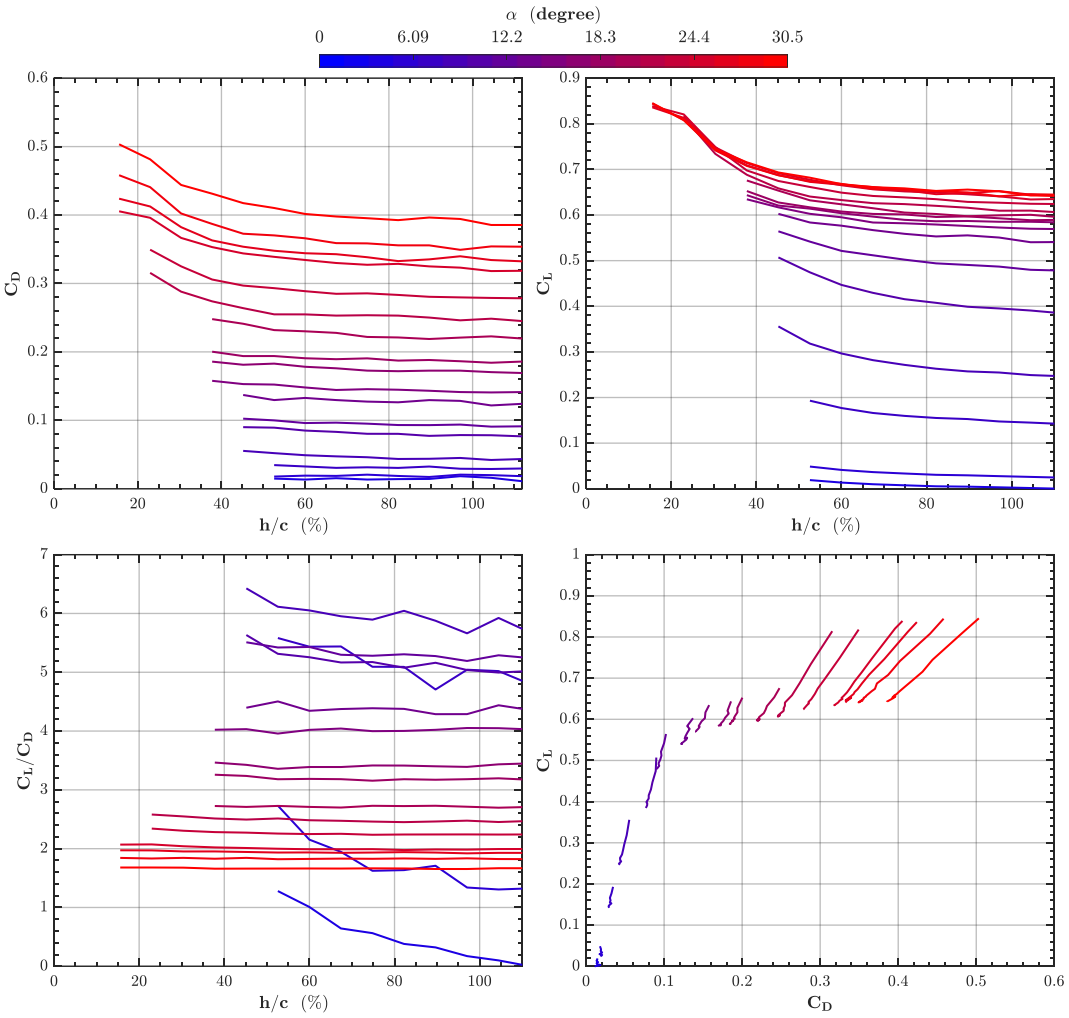

Figure C - 15 Variation of Drag coefficient C_D, Lift-to-Drag ratio C_L/C_D, Lift coefficient C_L as a function of non-dimensional height values and Drag Polar for the reverse delta wing 2f

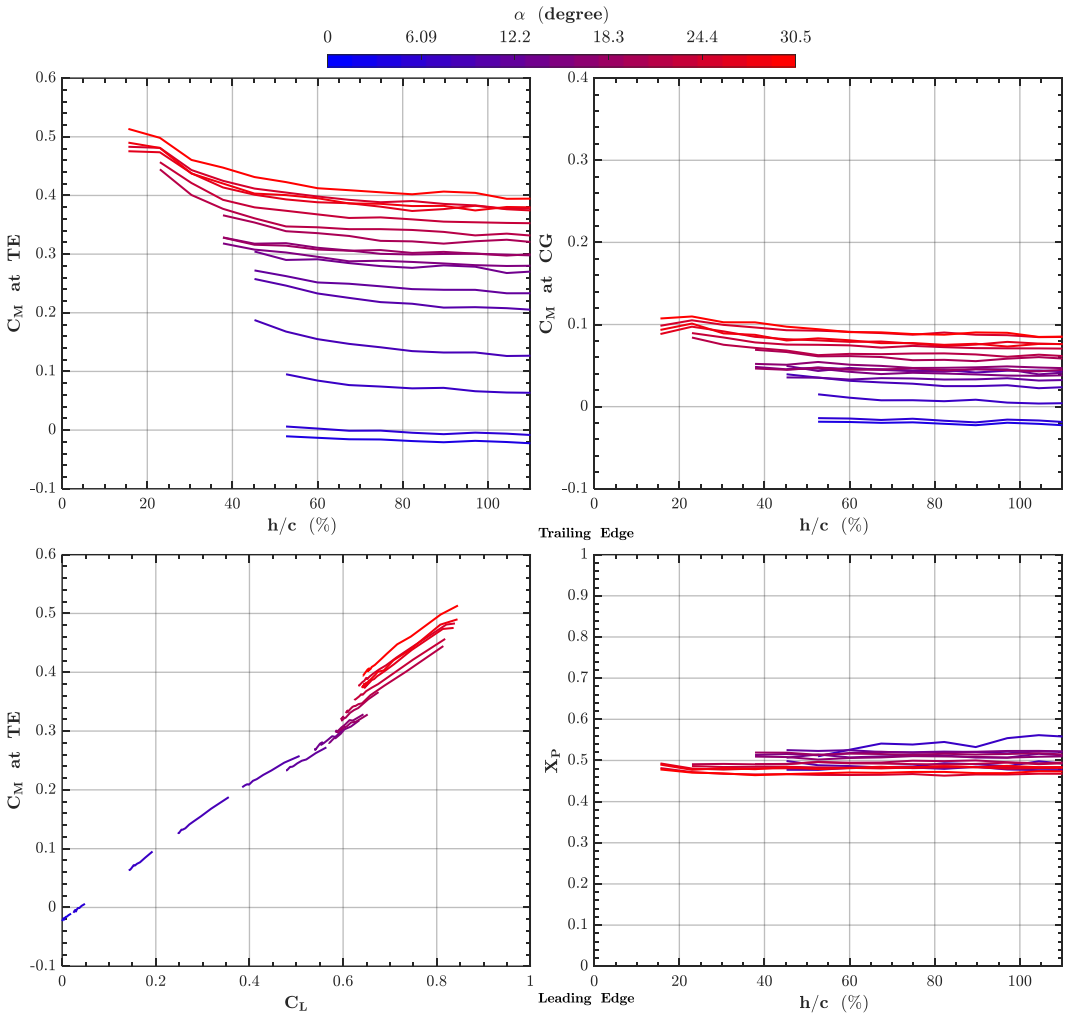

Figure C - 16 Variation of Moment coefficient C_M at trailing-edge (TE) and center of gravity (CG) as a function of function of non-dimensional height values and Lift coefficient C_L, and Non-Dimensional Pressure Center coordinate X_P as a function of non-dimensional height values for the reverse delta wing 2f

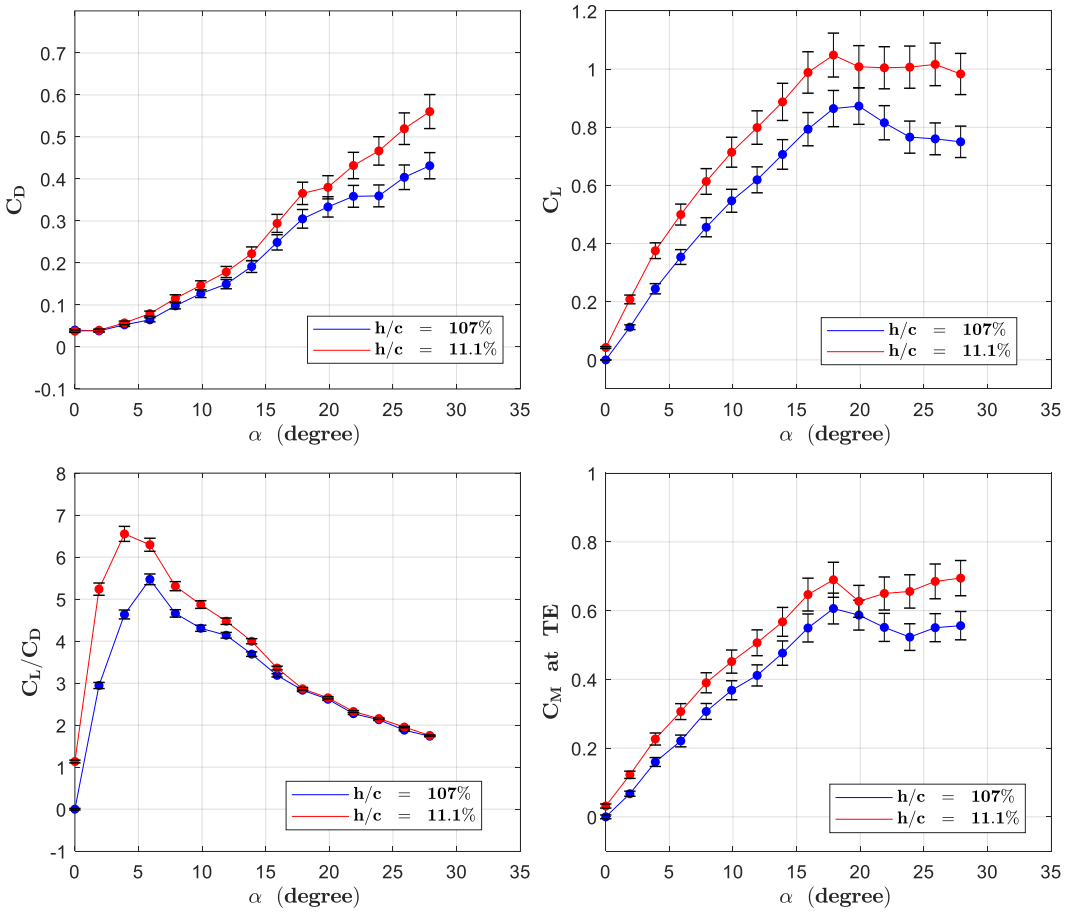

Figure C - 17 The absolute uncertainty levels of C_D, C_L, C_L/C_D, and C_M of the delta wing 1b as a function of angle of attack for the static ground condition

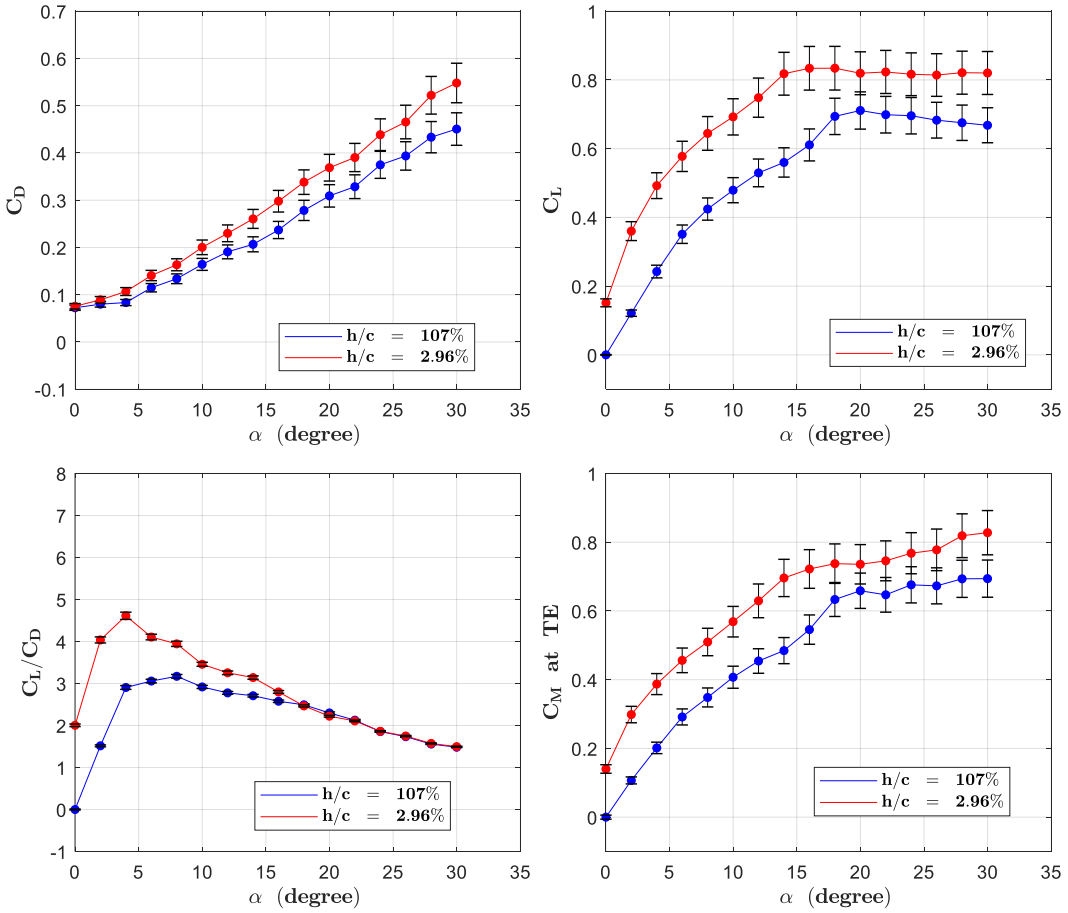

Figure C - 18 The absolute uncertainty levels of C_D, C_L, C_L/C_D, and C_M of the reverse delta wing 2a as a function of angle of attack for the static ground condition

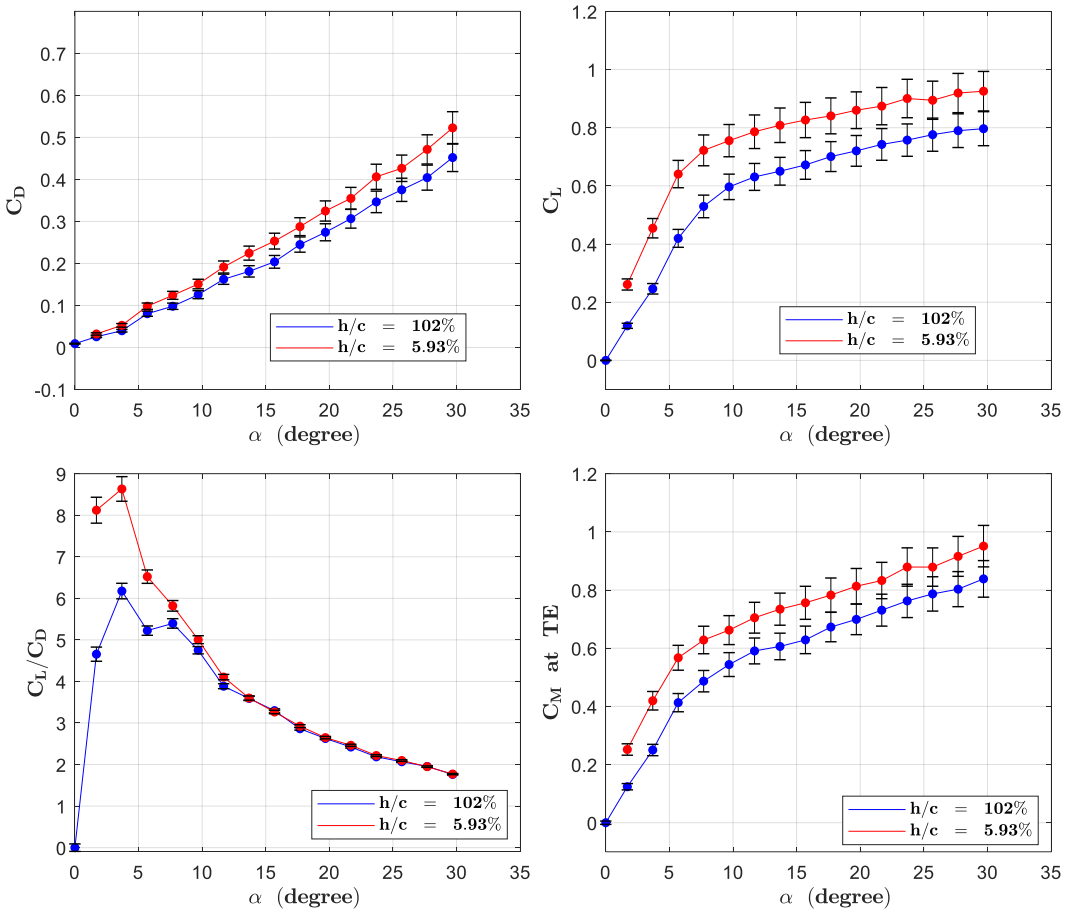

Figure C - 19 The absolute uncertainty levels of C_D, C_L, C_L/C_D, and C_M of the reverse delta wing 2b as a function of angle of attack for the static ground condition

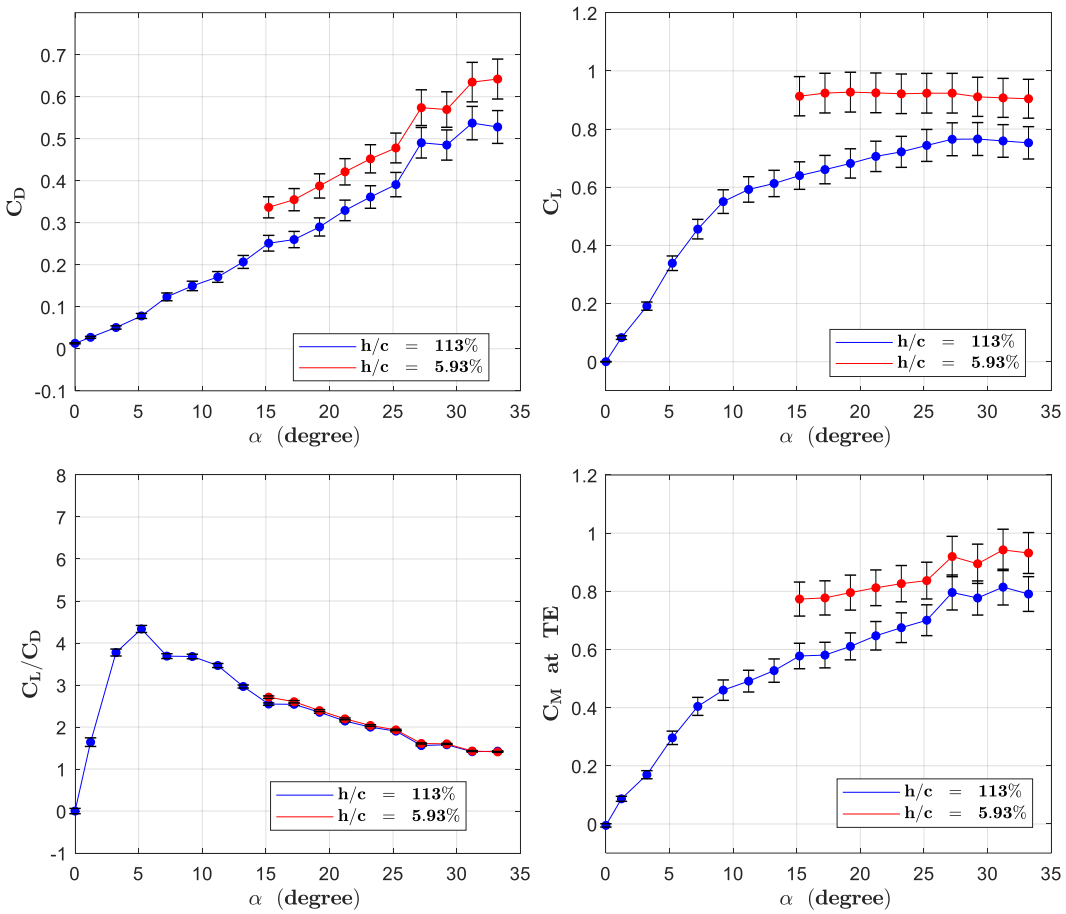

Figure C - 20 The absolute uncertainty levels of C_D, C_L, C_L/C_D, and C_M of the reverse delta wing 2c as a function of angle of attack for the static ground condition

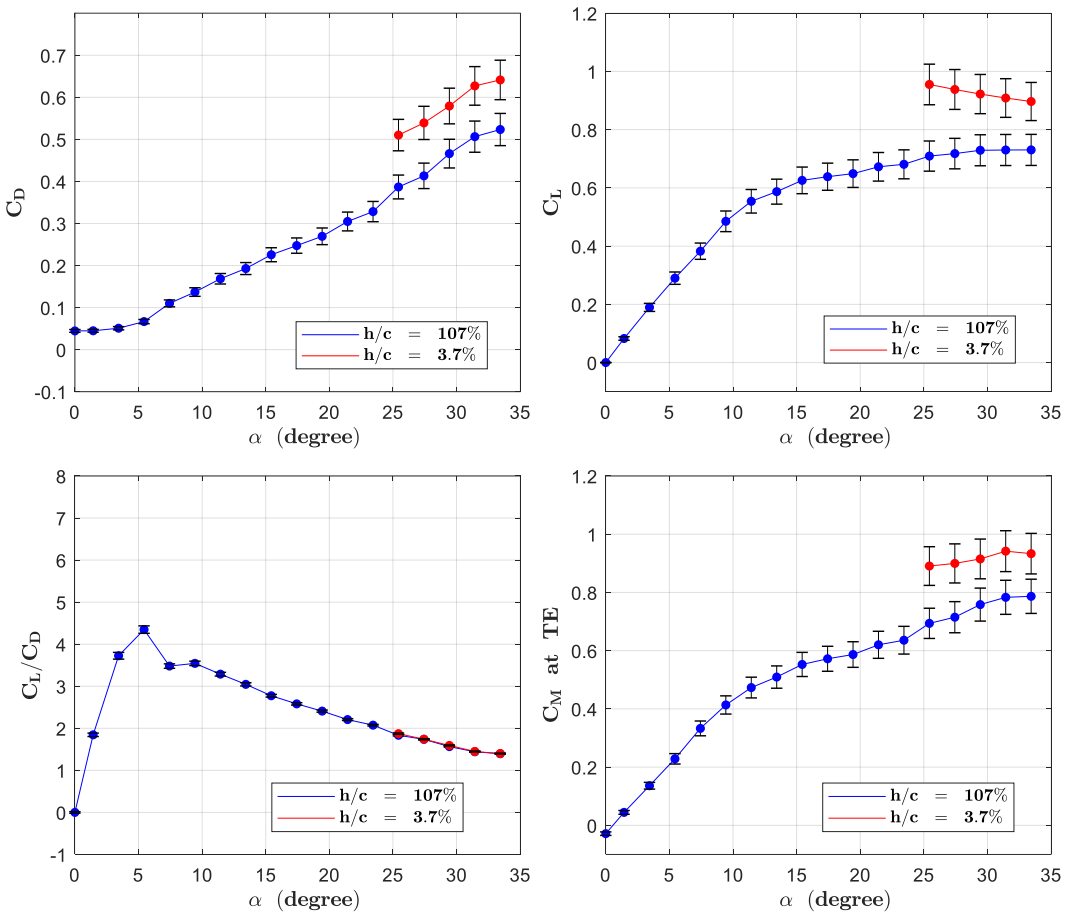

Figure C - 21 The absolute uncertainty levels of C_D, C_L, C_L/C_D, and C_M of the reverse delta wing 2d as a function of angle of attack for the static ground condition

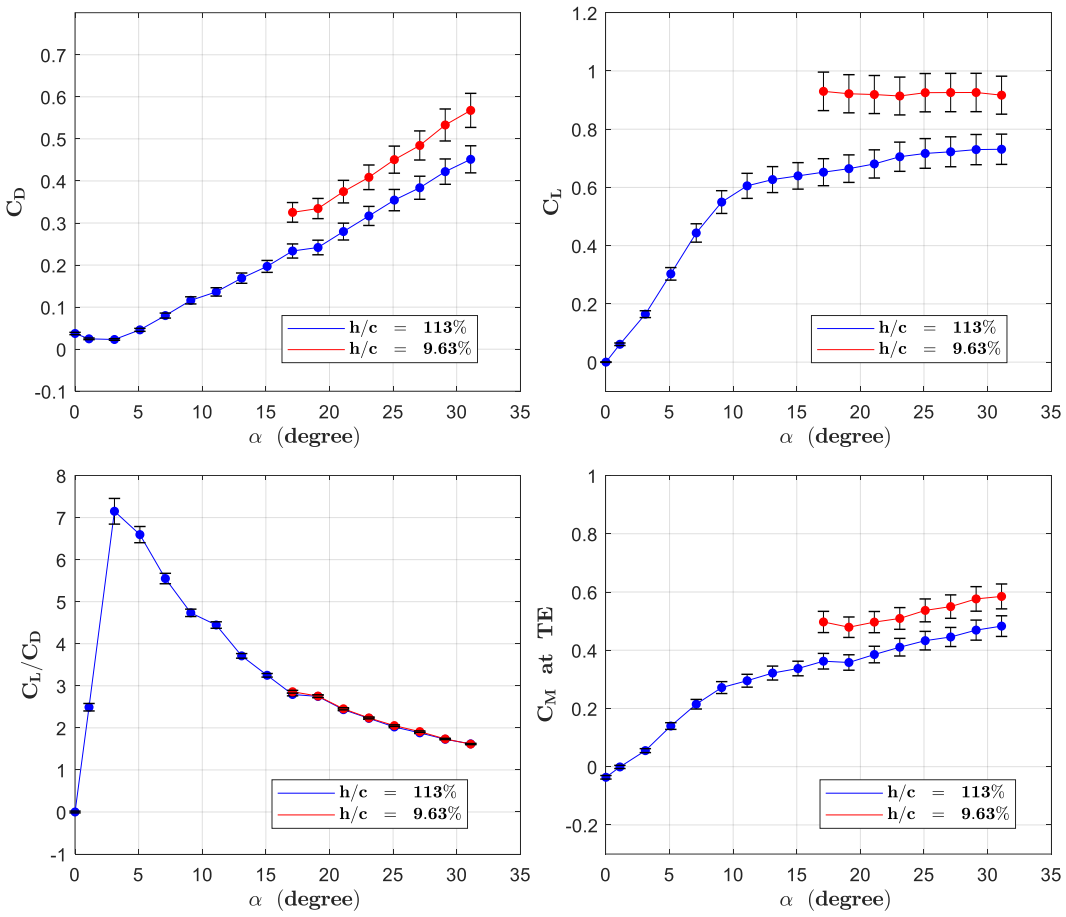

Figure C - 22 The absolute uncertainty levels of C_D, C_L, C_L/C_D, and C_M of the reverse delta wing 2e as a function of angle of attack for the static ground condition

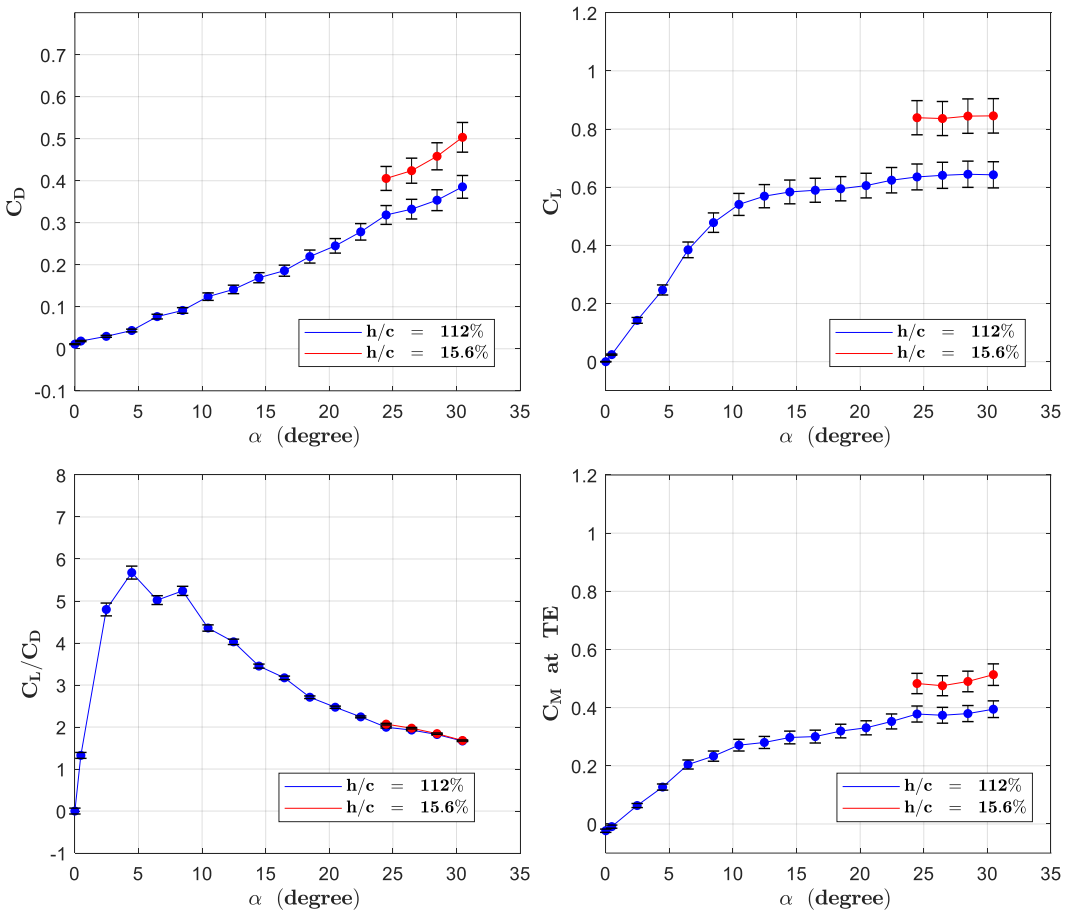

Figure C - 23 The absolute uncertainty levels of C_D, C_L, C_L/C_D, and C_M of the reverse delta wing 2f as a function of angle of attack for the static ground condition

Table C - 1 Maximum uncertainty values at OGE, the closest height to the static ground and for all heights for static ground condition of the delta wing 1a

		OGE	IGE	Max
Wing 1a	C_D	0.0337	0.044	0.044
	C_L	0.0596	0.0744	0.0744
	C_L/C_D	0.0581	0.0871	0.0871
	C_M	0.0453	0.0533	0.0533
	Suction side C_P	0.0509	0.0524	0.0562
	Pressure side C_P	0.0275	0.0223	0.0275

Table C - 2 Maximum uncertainty values at OGE, the closest height to the static ground and for all heights for static ground condition of the delta wing 1b

		OGE	IGE	Max
Wing 1b	C_D	0.0312	0.0405	0.0405
	C_L	0.0629	0.0755	0.0755
	C_L/C_D	0.1278	0.1789	0.1789
	C_M	0.0448	0.0513	0.0513

Table C - 3 Maximum uncertainty values at OGE, the closest height to the static ground and for all heights for static ground condition of the delta wing 2a

		OGE	IGE	Max
Wing 2a	C_D	0.0344	0.0418	0.0418
	C_L	0.0541	0.0635	0.0635
	C_L/C_D	0.0453	0.0863	0.0863
	C_M	0.0541	0.0644	0.0644

Table C - 4 Maximum uncertainty values at OGE, the closest height to the static ground and for all heights for static ground condition of the delta wing 2b

		OGE	IGE	Max
Wing 2b	C_D	0.0333	0.0418	0.0418
	C_L	0.0585	0.0635	0.0679
	C_L/C_D	0.1867	0.0863	0.3119
	C_M	0.0629	0.0644	0.0713

Table C - 5 Maximum uncertainty values at OGE, the closest height to the static ground and for all heights for static ground condition of the delta wing 2c

		OGE	IGE	Max
Wing 2c	C_D	0.0398	0.0475	0.0475
	C_L	0.0566	0.0685	0.0685
	C_L/C_D	0.0833	0.03	0.0966
	C_M	0.0615	0.0711	0.0711

Table C - 6 Maximum uncertainty values at OGE, the closest height to the static ground and for all heights for static ground condition of the delta wing 2d

		OGE	IGE	Max
Wing 2d	C_D	0.0383	0.0469	0.0469
	C_L	0.0533	0.0697	0.0697
	C_L/C_D	0.088	0.0161	0.1027
	C_M	0.0588	0.0702	0.0702

Table C - 7 Maximum uncertainty values at OGE, the closest height to the static ground and for all heights for static ground condition of the delta wing 2e

		OGE	IGE	Max
Wing 2e	C_D	0.0322	0.0405	0.0405
	C_L	0.052	0.0661	0.0661
	C_L/C_D	0.3055	0.0328	0.3322
	C_M	0.0354	0.0427	0.0433

Table C - 8 Maximum uncertainty values at OGE, the closest height to the static ground and for all heights for static ground condition of the delta wing 2f

		OGE	IGE	Max
Wing 2f	C_D	0.0271	0.0354	0.0354
	C_L	0.0451	0.0592	0.0592
	C_L/C_D	0.1545	0.0189	0.1756
	C_M	0.0287	0.0371	0.0371

D. Appendix D

Figure D - 1 The reverse delta wing 2a in extreme ground effect for static ground condition

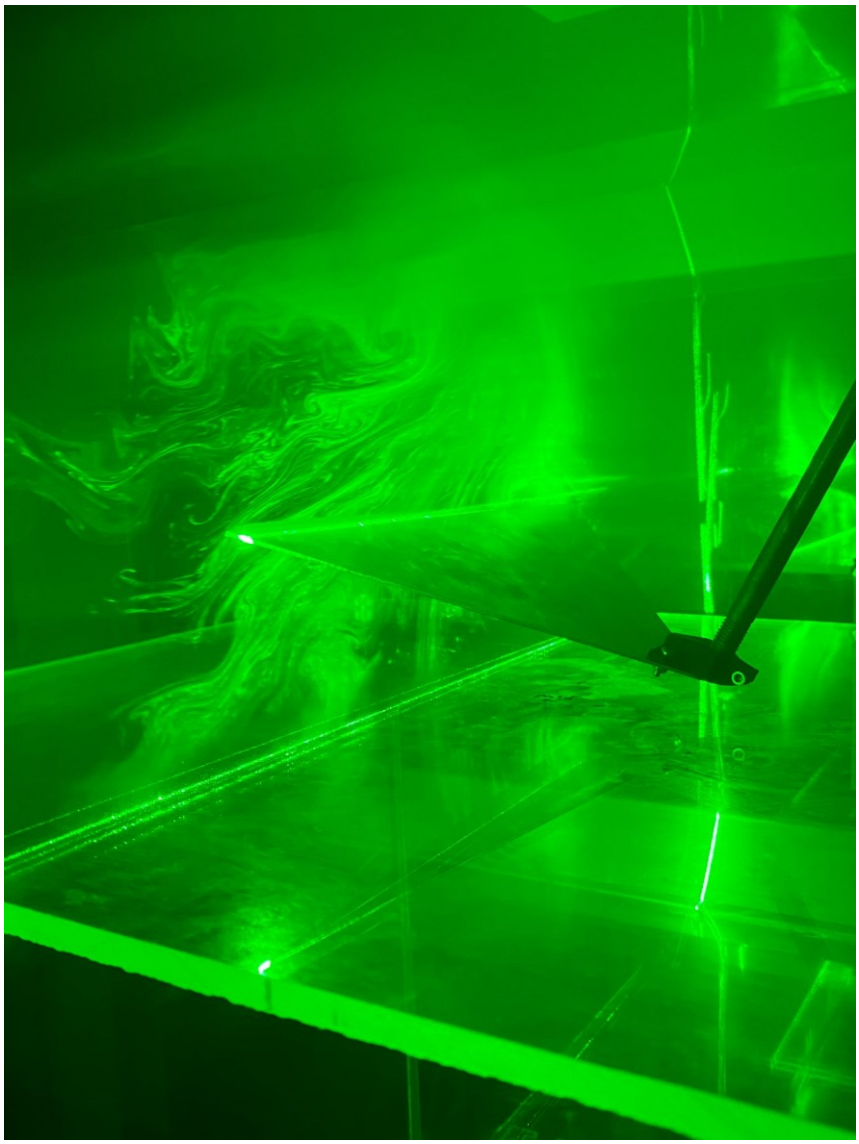

Figure D - 2 Laser illuminated smoke visualization for the reverse delta wing 2b IGE at static ground condition for an aribtrary low Re number

Figure D - 3 The delta wing 1a and tunnel test section with moving belt system

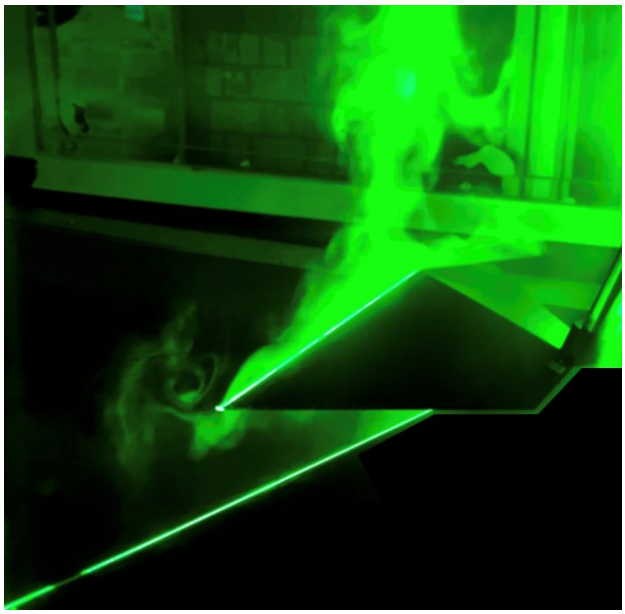

Figure D - 4 Tip vortex observed in dynamic ground condition for the reverse delta wing 2e

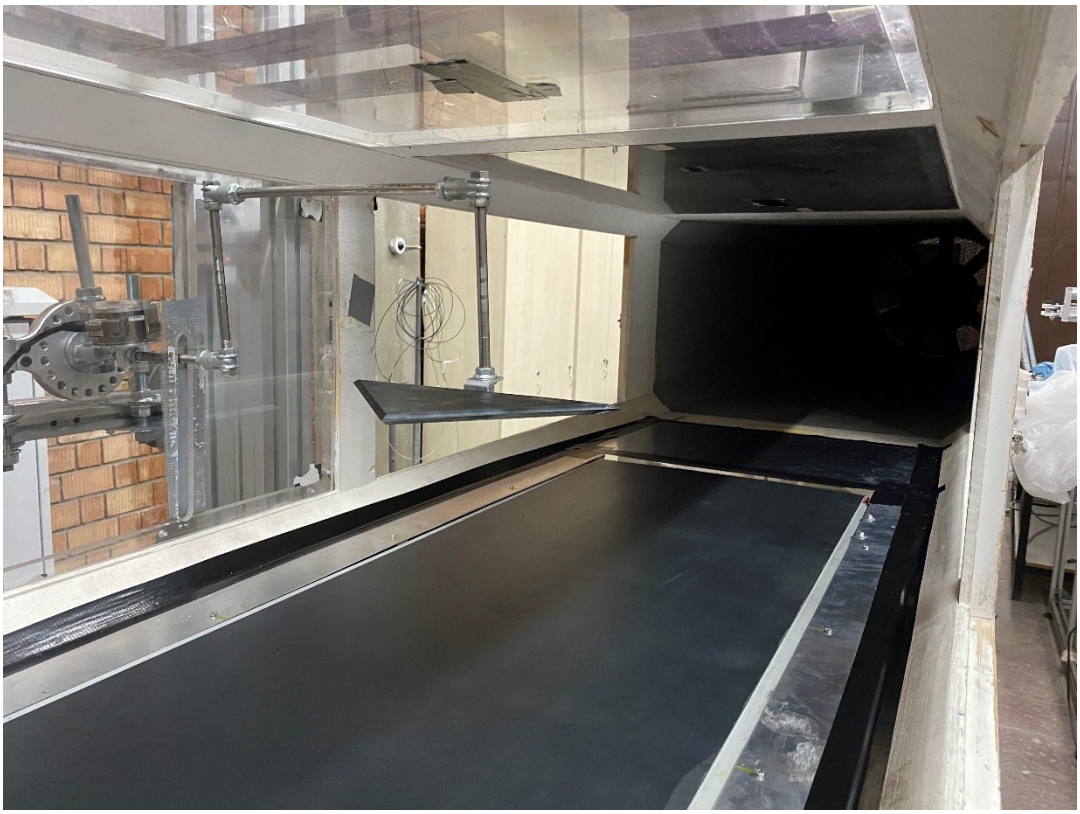

Figure D - 5 The delta wing 1a and tunnel test section with moving belt system

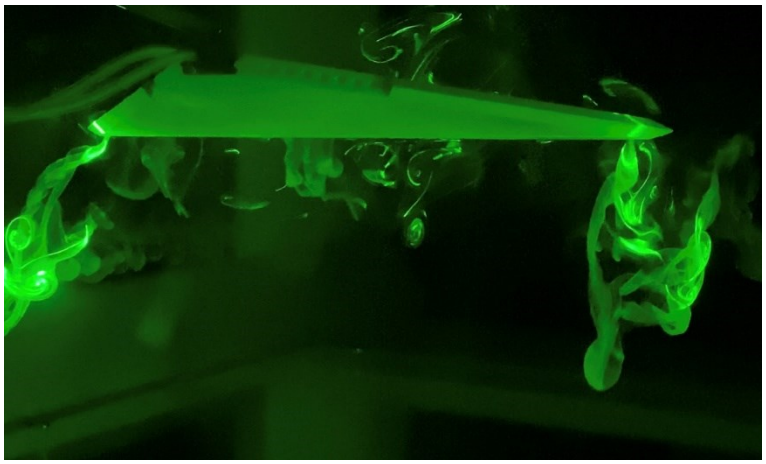

Figure D - 6 Vortical structures emating from the wing tips of the reverse delta wing 2a

Figure D - 7 The reverse delta wing 2e, modified MPS and moving belt system

Figure D - 8 The reverse delta wing 2e, modified MPS and moving belt system

Figure D - 9 Control unit of the moving belt mechanism

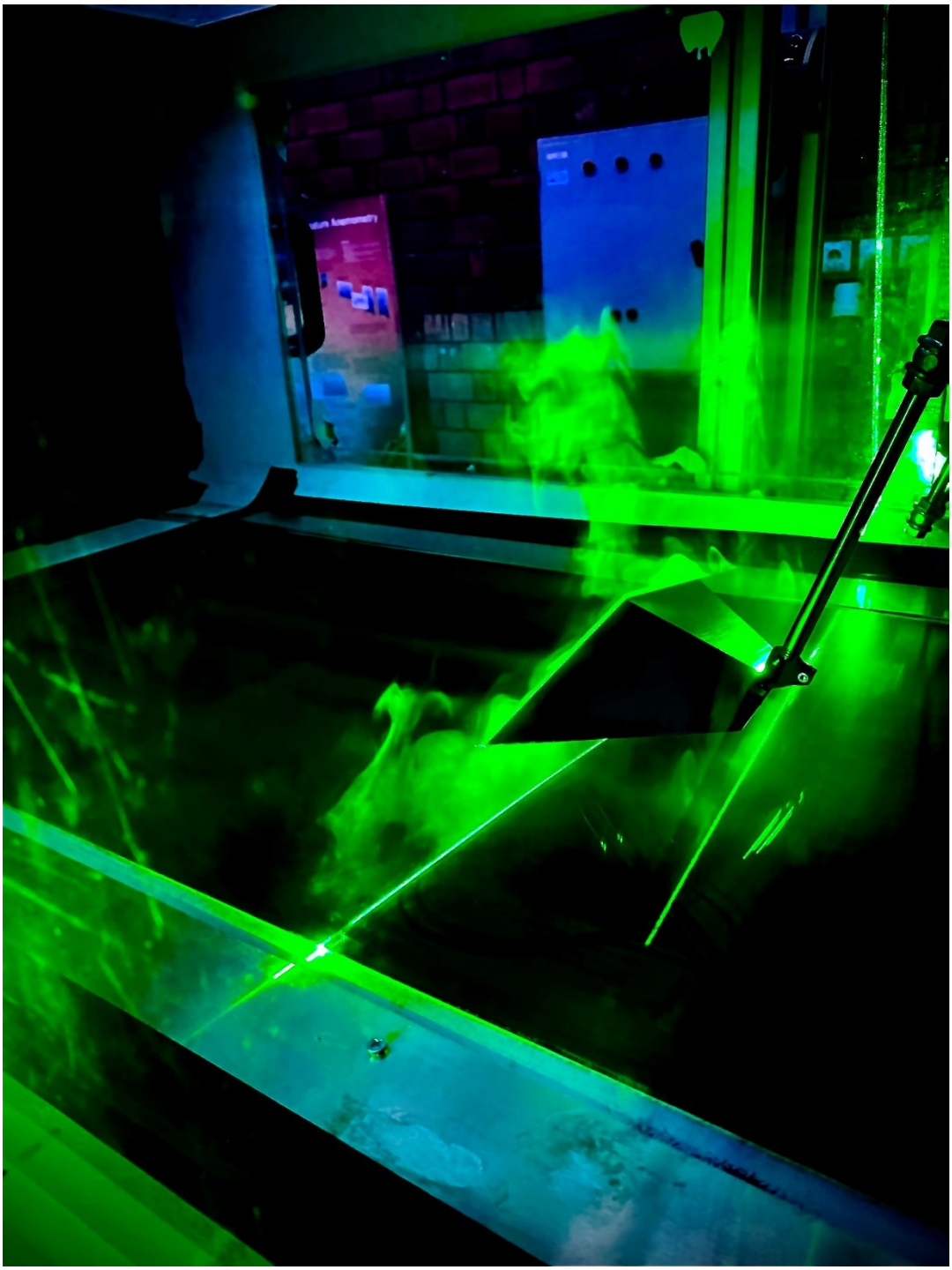

Figure D - 10 Laser illuminated smoke visualization for the reverse delta wing 2e IGE at dynamic ground condition for Re $= 9x10^4$

Figure D - 11 Moving belt mechanism inside the wind tunnel test section

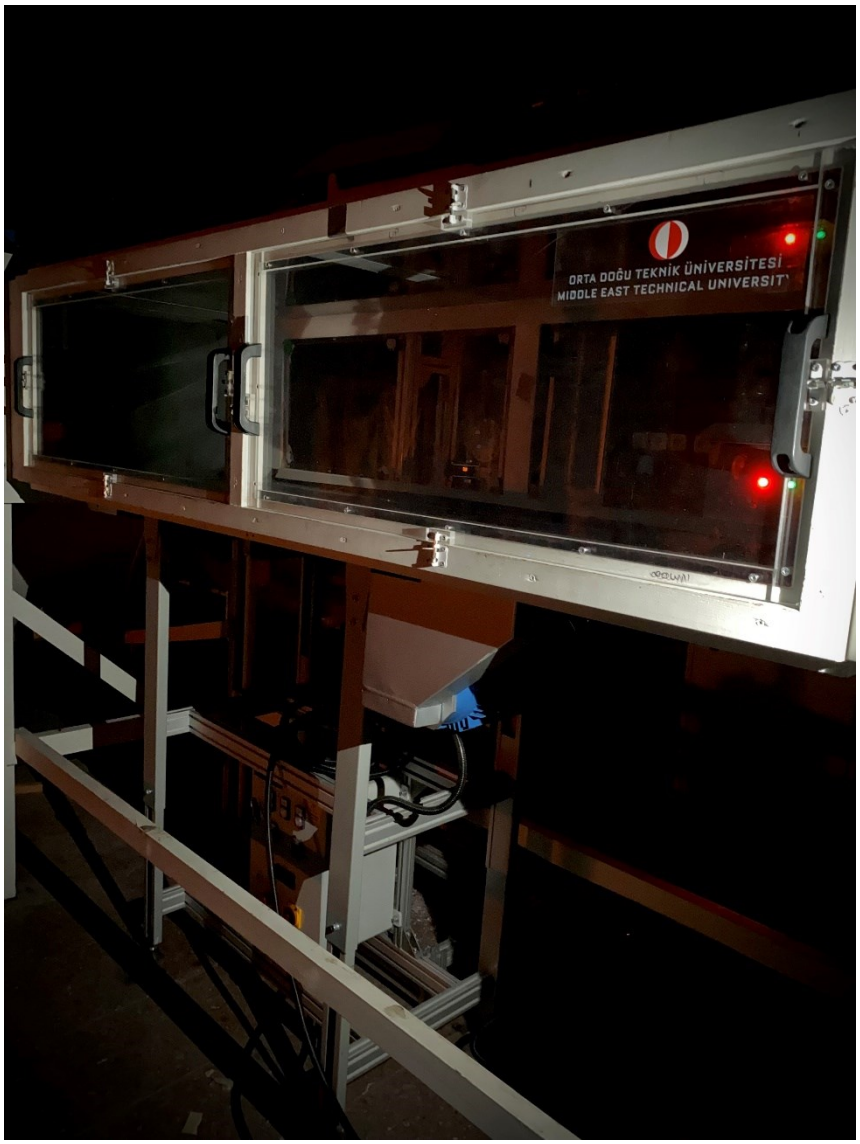

Figure D - 12 Wind tunnel test section with moving belt mechanism

CURRICULUM VITAE

Surname, Name: Koçak, Göktuğ

CONTACT INFORMATION

Address: Mechanical Engineering Department / METU

E-mail:

EDUCATION

2016-2023 Ph.D., METU- Mechanical Engineering Department

Effect of Ground on Flow Structure of Non-Slender Delta and Reverse Delta Wings

2013-2016 M.Sc., METU- Mechanical Engineering Department

Flow Characterization of Full, Partial, and Inclined Ground Effect

2008-2013 B.S., METU- Mechanical Engineering Department

JOURNAL PUBLICATIONS

1. **Koçak, G.**, Yavuz, M. M., 2022, "Aerodynamics of non-slender delta and reverse delta wings: Wing thickness, anhedral angle and cropping ratio", *In Print - Chinese Journal of Aeronautics, 2022*.
   doi: https://doi.org/10.1016/j.cja.2022.06.015
2. **Koçak, G.**, Yavuz, M. M., 2022, "Effect of Ground on Aerodynamics and Longitudinal Static Stability of a Non-Slender Delta Wing", *Aerospace Science and Technology, Vol. 130, 2022*.
   doi: https://doi.org/10.1016/j.ast.2022.107929

PRESENTATIONS

1. **Koçak, G.**, Nalbantoğlu, V., Yavuz, M. M., 2017, "Flow Characterization of Full, Partial, and Inclined Ground Effect", ICMAE 2017, Prag, CZ.

2. **Koçak, G.**, Nalbantoğlu, V., Yavuz, M. M., 2017, "Effect of Different Ground Scenarios on Flow Structure of a Rotor at Hover Condition", APS 2017, Denver, CO, US.
3. Şansal, K., **Koçak, G.**, Kargin, V., 2018, "Multi-objective Horizontal Stabilizer Optimization Using Genetic Algorithm", AHS 2018, Phoenix, AZ, US.
4. **Koçak, G.**, Şansal, K., Sağıroğlu, S., Kargin, V., 2018, "A Generic Ground Dynamics Model for Ground Handling Evaluations", ERF 2018, Delft, NL.

NATIONAL CONFERENCE

1. **Koçak, G.**, Nalbantoğlu, V., Yavuz, M. M., 2016, "Döner Kanatlar için Yer Etkisinin Deneysel Olarak İncelenmesi", UHUK 2016 (National Aeronautical and Aerospace Conference), Kocaeli.
2. Çetin C., **Koçak, G.**, Yavuz, M. M., 2022, "Yeni Bir Pasif Akıtma Tasarımı İle Düşük Ok Açılı Delta Kanat Akışının Kontrolü", UHUK 2022 (National Aeronautical and Aerospace Conference), İzmir.
3. **Koçak, G.**, Yavuz, M. M., 2022, "Düşük Ok Açılı Delta Ve Ters Delta Kanatların Aerodinamiği: Kanat Kalınlığı Etkisi", UHUK 2022 (National Aeronautical and Aerospace Conference), İzmir.

WORK EXPERIENCE

1. Aerodynamics Chief Engineer at TF-X (Turkish Fighter) Program of Turkish Aerospace Industries, Inc. since April 2022. Responsible of aerodynamic design and development of TF-X.
2. Design Specialist at Flight Mechanics and Autopilot Systems in Helicopter Group of Turkish Aerospace Industries, Inc. from 2013 to 2022.
3. Presentation assistant of university, university representative in education fairs of METU Public Relations Office since 2008 to 2010 and involved in 100+ sessions and one-to-one consulting.